



Levens, Peter James (2018) Diagnostics of solar tornado-like prominences.
PhD thesis.

<http://theses.gla.ac.uk/8684/>

Copyright and moral rights for this work are retained by the author

A copy can be downloaded for personal non-commercial research or study, without prior permission or charge

This work cannot be reproduced or quoted extensively from without first obtaining permission in writing from the author

The content must not be changed in any way or sold commercially in any format or medium without the formal permission of the author

When referring to this work, full bibliographic details including the author, title, awarding institution and date of the thesis must be given

Enlighten:Theses
<http://theses.gla.ac.uk/>
theses@ gla.ac.uk

Diagnosics of solar tornado-like prominences

Peter James Levens

B.Sc.

Astronomy and Astrophysics Group
School of Physics and Astronomy
Kelvin Building
University of Glasgow
Glasgow, G12 8QQ
Scotland, U.K.



University
of Glasgow

Presented for the degree of
Doctor of Philosophy
University of Glasgow
January 2018

This thesis is my own composition except where indicated in the text.
No part of this thesis has been submitted elsewhere for any other degree
or qualification.

Copyright © 2018 by Peter J. Levens

17 January 2018

FOR JIM

Abstract

Solar tornado-like prominences have been observed for over 90 years, but their true nature has recently been one of the most hotly debated aspects of prominence research. They have been linked to prominence eruptions, so understanding their stability and the plasma motions seen could provide a link between these dynamic features and the Sun-Earth space weather, which is important to fully understand in modern-day society. This thesis aims to answer some of the open questions on solar ‘tornadoes’, specifically on the plasma behaviour at different temperatures and the magnetic field structure of these apparently-rotating phenomena. Using a range of spectral diagnostic techniques and data from space-based and ground-based instruments, a more complete picture of solar tornadoes is built here.

Optically thin emission at coronal temperatures (~ 1.5 MK) has previously been shown to give anti-symmetric Doppler velocity patterns in a tornado, indicative of rotation. Using the same data set, from 13 September 2014, it has been possible to show that the Doppler pattern is visible in all spectral lines formed above 1 MK, but at lower plasma temperatures the pattern is not present. Electron densities are calculated from density-sensitive line pairs, and it is found that the electron density is lower in the tornado than the surrounding corona. Non-thermal line widths are calculated, showing that there is some additional broadening at the tornado compared to the surrounding corona, which could be due to a turbulent magnetic field component or the presence of unresolved Kelvin-Helmholtz instabilities at the tornado-corona boundary. The temperature structure along an observed line of sight is calculated using the technique of Differential Emission Measure, and this indicates that tornadoes are part of the larger prominence structure that is seen in some wavebands.

A dedicated coordinated observation was designed to study tornadoes at lower plasma temperatures (< 1 MK), and to investigate their unknown magnetic structure.

An observation of two tornadoes from 15 July 2014 is presented, from which the Mg II h and k lines and the magnetic field are analysed in detail. The optically thick Mg II lines, formed at chromospheric temperatures, show no velocity patterns similar to those seen at higher temperatures. The Mg II lines show a mix of reversed and non-reversed profiles in the prominence. This is the first report of strong central reversal of the h and k lines in a prominence. Comparing to a grid of isothermal isobaric Mg II models reveals that the large central reversals seen in the 15 July 2014 prominence indicates high optical thicknesses and pressures in the prominence slab.

The magnetic field in the tornadoes on 15 July 2014 has been measured using spectropolarimetry of the He I D₃ line, which gives the magnetic field strength and orientation. Field strengths of up to 60 G are found in places, but the average field strength is around 20 – 30 G. The inclination of the magnetic field indicates that it is horizontal, parallel to the solar surface. These observations suggest that the tornado magnetic field is not twisted, but instead horizontal with plasma suspended in dips.

An attempt has been made to find correlations between plasma parameters and the observed magnetic field parameters. No correlations are found, but this study has allowed a clearer, statistical investigation into the parameters available from this coordinated observation. These statistics are useful for comparing observations to models, in order to better understand the physical conditions that created the observed line profiles.

Finally, this thesis contains an update to a radiative transfer prominence modelling code, PROM, to include calculations of the emergent intensities of Mg II lines. This step was taken to have the ability to freely explore models for larger ranges of model parameters than presented by previous authors, with the scope to investigate more complex (1D, 2D) multi-thread models. The output of the updated code is compared to the results of another Mg II modelling code, finding good agreement in the recovered optical thickness, but integrated intensities are found to vary by 30–40% for some models. An extended grid of isothermal isobaric and PCTR models is then explored in order to understand the links between observable Mg II h and k line parameters and model parameters. A number of correlations are found, meaning that observed Mg II h and k lines can be used to identify physical parameters in a prominence. These models are compared to observations from 15 July 2014, finding that they can explain some of the observed line profiles, but more complex models are required to fully explain the observations.

Contents

Abstract	iii
List of Figures	ix
List of Tables	xiii
Acknowledgements	xiv
1 Introduction	1
1.1 The Sun and its atmosphere	2
1.2 Solar prominences	8
1.2.1 Discovery and historical observations	12
1.2.2 Recent observations	16
1.2.3 Prominence types	21
1.2.4 Plasma conditions	22
1.2.5 Magnetic fields	25
1.2.6 Neutral atom support	29
1.3 Solar “Tornadoes”	30
2 Observations and diagnostics	39
2.1 Spectral lines	39
2.1.1 Observing spectral lines	41
2.2 Optically thin plasma emission	42
2.2.1 Direct spectral inversion	44
2.2.2 Electron density diagnostics	46
2.2.3 Differential emission measure	48
2.2.4 Emission measure distribution	51
2.3 Optically thick plasma emission	52

2.3.1	The Mg II h and k lines	52
2.3.2	Mg II in the chromosphere and flares	58
2.4	Instruments	59
2.4.1	Hinode	59
2.4.1.1	Extreme-ultraviolet Imaging Spectrometer	61
2.4.1.2	Solar Optical Telescope	62
2.4.2	Interface Region Imaging Spectrograph	63
2.4.3	THEMIS	64
2.4.4	Solar Dynamics Observatory	66
3	Plasma diagnostics of tornado-like prominences	69
3.1	14 September 2013 – Observational overview	70
3.1.1	Description of the event	71
3.1.2	Data reduction	72
3.1.3	Spectral lines used for analysis	74
3.1.3.1	Fe X 184 Å blend	75
3.1.3.2	Fe XI 188 Å blend	75
3.1.3.3	Fe XI and O V 192 Å blend	75
3.1.3.4	Fe XII 195 Å blend	77
3.1.3.5	He II 256 Å blend	78
3.2	Plasma diagnostics	80
3.2.1	Line-of-sight velocity measurements	81
3.2.2	Density diagnostics	86
3.2.2.1	Fe XI diagnostics	86
3.2.2.2	Fe XII diagnostic	86
3.2.3	Non-thermal line widths	88
3.2.4	Differential emission measure	92
3.3	15 July 2014 – Coordinated observations	98
3.3.1	SDO AIA observations	99
3.3.2	IRIS observations	102
3.3.3	Hinode SOT observations	103
3.3.4	Hinode EIS observations	104
3.4	Plasma parameters	104
3.4.1	AIA time-distance analysis	104

3.4.2	<i>IRIS</i> spectral analysis	107
3.4.3	Doppler shifts	112
3.4.4	Gas pressure and optical thickness	113
3.5	Conclusion	116
4	Relationship between magnetic field and plasma in tornadoes	121
4.1	THEMIS observations	122
4.1.1	Magnetic field	123
4.2	Comparing magnetic field and plasma parameters	127
4.2.1	Co-aligning data sets	127
4.2.1.1	<i>IRIS</i> with <i>SDO</i> AIA	129
4.2.1.2	<i>Hinode</i> SOT with <i>IRIS</i>	130
4.2.1.3	THEMIS with <i>Hinode</i> SOT	131
4.2.1.4	<i>Hinode</i> EIS with <i>SDO</i> AIA	134
4.3	Correlation between THEMIS and <i>IRIS</i> data	135
4.3.1	Mg II k_2/k_3 ratio	138
4.3.2	Mg II k/h ratio	143
4.3.3	Mg II k_3 Doppler shift	143
4.4	Correlation between THEMIS and EIS data	145
4.5	Correlation between <i>IRIS</i> and EIS data	148
4.6	Conclusion	150
5	Modelling of Mg II lines in prominences	156
5.1	Radiative transfer in prominences	158
5.1.1	Statistical equilibrium	162
5.2	The PROM prominence models	164
5.3	The model Mg II atom	166
5.4	Incident radiation	168
5.5	Isothermal isobaric models	173
5.5.1	The HVA grid of models	173
5.5.2	Extended grid of models	180
5.6	PCTR models	188
5.7	Results from modelling	193
5.7.1	Correlations	193
5.7.2	Comparison to observations	200

5.8 Conclusion	202
6 Conclusions	206
Bibliography	217

List of Figures

1.1	Examples of solar atmospheric features from DOT and AIA.	4
1.2	Temperature of the solar atmosphere with height.	6
1.3	A solar prominence from <i>Hinode</i> /SOT.	9
1.4	Full disc H- α image from the Kanzelhöhe Observatory.	11
1.5	Prominences observed during the eclipse of 1860 from Secchi (1875)	15
1.6	Three possible prominence PCTR thread arrangements from Pojoga (1994)	24
1.7	Injection models for plasma into the prominence magnetic field from Mackay et al. (2010)	28
1.8	Examples of tornado prominences in H- α from Pettit (1932, 1943a)	31
1.9	Sketches of the two tornado sub-classes from Pettit (1943a)	32
1.10	Multi-wavelength view of solar tornadoes from Su et al. (2012)	34
2.1	Electron density sensitivity curve for two Fe XI lines.	47
2.2	Prominence DEM from Parenti & Vial (2007)	50
2.3	Mg II five-level term diagram.	53
2.4	Averaged <i>IRIS</i> Mg II quiet-sun and prominence spectra.	56
2.5	Mg II k profile.	57
3.1	Tornado on 14 September 2013 as viewed by AIA and SMART.	71
3.2	Filament observations on 11 September 2013.	72
3.3	EIS and AIA intensity maps from 14 September 2013.	73
3.4	Density curve for the O V 192 Å lines.	77
3.5	Fitted EIS 192 Å spectral window.	78
3.6	Density curve for the Fe XII 195 Å lines.	79
3.7	Fitted EIS 195 Å spectral window.	80
3.8	Velocity maps of the Fe XII 195.119 Å line.	82

3.9	Velocity maps of four ionised iron lines formed at different plasma temperatures.	83
3.10	Line-of-sight velocity vs. position across tornado for six ionised iron lines.	84
3.11	Electron density map from Fe XI line ratio.	87
3.12	Electron density maps from the Fe XII line ratio.	88
3.13	Electron density measured along cuts through the tornado axis.	89
3.14	NTLW maps for Fe XII 195 Å and Fe XIII 202 Å lines.	90
3.15	NTLW measured along parallel cuts through the tornado.	91
3.16	DEM and EMD for a tornado pixel.	94
3.17	DEM and EMD for a pixel in the main prominence body.	95
3.18	DEM and EMD for a pixel in the corona (tornado altitude).	96
3.19	DEM and EMD for a pixel in the corona (prominence body altitude).	96
3.20	H- α observation of filament on 11 July 2014.	99
3.21	H- α observation of prominence on 15 July 2014.	100
3.22	AIA 171 Å image from 15 July 2014 with FOV context of other instruments.	101
3.23	AIA 304 Å and 193 Å images of the prominence on 15 July 2014.	102
3.24	Time-distance diagrams for the two tornadoes on 15 July 2014.	106
3.25	Time-averaged intensity profiles of Mg II, Si IV, and C II from IRIS.	108
3.26	IRIS Mg II k spectra from the raster at 10:21 UT.	109
3.27	Mg II profiles from the prominence on 15 July 2014.	110
3.28	Four Mg II k Doppler velocity maps from the IRIS raster study.	112
3.29	Time-distance plots of Mg II k intensity and l.o.s. velocity.	114
3.30	Raster maps made using different parts of the Mg II k line.	117
4.1	Raw intensity images from the two THEMIS rasters on 15 July 2014.	123
4.2	Magnetic field strength, inclination and azimuth images from THEMIS.	124
4.3	Histogram of magnetic field inclination from Levens et al. (2016a)	126
4.4	AIA and IRIS maps of the prominence on 15 July 2014.	129
4.5	SOT Ca II image from 15 July 2014 at 10:21 UT.	130
4.6	THEMIS intensity, field strength, inclination and azimuth maps.	133
4.7	SOT Ca II image with disc mask and threshold applied.	134
4.8	AIA 193 Å and EIS 195 Å images from 10:34 UT on 15 July 2014.	136

4.9	Composite plot showing co-alignment of data sets.	137
4.10	THEMIS/ <i>IRIS</i> masks showing overlap area	138
4.11	Mg II k_2/k_3 ratio vs. magnetic field parameters for tornado points and rest-of-prominence points.	140
4.12	Histograms of magnetic field parameters from THEMIS.	141
4.13	Histograms of k_2/k_3 , k/h and v_{k3} from <i>IRIS</i>	142
4.14	Mg II k/h ratio vs. magnetic field parameters for tornado points and rest-of-prominence points.	144
4.15	Mg II k_3 Doppler shift vs. magnetic field parameters for tornado points and rest-of-prominence points.	146
4.16	Density map of the prominence on 15 July 2014 made using EIS.	147
4.17	THEMIS/EIS masks showing overlap area.	148
4.18	Electron density vs. magnetic field parameters for tornado points and rest-of-prominence points.	149
4.19	Histograms of electron density from EIS.	150
4.20	Electron density vs. Mg II parameters.	151
5.1	Prominence geometry for the 1D radiative transfer problem.	158
5.2	Two-level atom for atomic transitions	163
5.3	Sun-centre spectrum indicating Mg II lines.	170
5.4	Mg II h and k observed half line profiles.	171
5.5	Averaged and smoothed Mg II h and k half line profiles.	172
5.6	Emergent Mg II h and k line profiles for 200 km slab models.	177
5.7	Emergent Mg II h and k line profiles for 1000 km slab models.	178
5.8	Emergent Mg II h and k line profiles for 5000 km slab models.	179
5.9	Relative difference plots for the Mg II h and k lines.	180
5.10	Mg II h and k relationships between observables for isothermal isobaric models.	182
5.11	Integrated intensity vs. optical thickness for the Mg II h and k lines.	182
5.12	Reversal level vs. optical thickness for the Mg II h and k lines.	183
5.13	Emergent Mg II k profiles for the 252 isothermal isobaric models.	184
5.14	Half-line Mg II h and k profiles for high temperature models.	185
5.15	Integrated intensity vs. temperature for the Mg II h and k lines.	186

5.16	Integrated intensity vs. pressure and slab thickness for the Mg II h and k lines.	187
5.17	Mg II h vs. k relationships between observables for models with a PCTR.	190
5.18	Mg II h and k integrated intensity vs. optical thickness for models with a PCTR.	191
5.19	Emergent Mg II k profiles for PCTR models.	192
5.20	Mg II k/h ratio vs. T , P , D , and τ_h for isothermal isobaric models.	194
5.21	Mg II h and k reversal level vs. T , P , and D for isothermal isobaric models.	196
5.22	Reversal level vs. optical thickness for the Mg II h and k lines for models with a PCTR.	197
5.23	Mg II k/h ratio vs. T_{cen} , P_{cen} , M , and τ_h for PCTR models.	198
5.24	Mg II h and k reversal level vs. T_{cen} , P_{cen} , and M for PCTR models.	199
5.25	Observed Mg II h vs. k line parameter relationships from <i>IRIS</i>	200

List of Tables

1.1	Prominence classifications by Pettit	21
1.2	Usual prominence parameters for the core and the PCTR.	23
3.1	EIS spectral lines used in the analysis of the tornado on 14 September 2013.	74
3.2	Spectral lines used in DEM analysis on 14 September 2013	93
3.3	Main spectral lines visible in the EIS <code>madj_qs</code> study	105
3.4	Line parameters measured for the Mg II k and h lines at points in the tornadoes.	115
4.1	Instruments and observations used for co-alignment.	128
4.2	Mg II line parameters measured previously in prominences	138
4.3	Moments of the distributions of parameters from THEMIS, <i>IRIS</i> and EIS.	152
5.1	Comparison of atomic and prominence parameters to those of HVA.	169
5.2	Table 2 from Heinzel et al. (2014)	175
5.3	HVA grid of models using the PROM code.	176
5.4	Parameters for the extended grid of 1D models.	181
5.5	Parameters for the PCTR models.	189

Acknowledgements

In what seems like the blink of an eye, it was four years later. There are probably more people than I can realistically thank here who have helped me through this, but here goes.

First and foremost, this whole thing would not have been possible without the constant help and guidance from Nic Labrosse, my supervisor. Be it an encouraging word, a prod in the right direction, picking me up when I'm down, or just being there to listen to every little question I've had about physics, thank you. He also deserves a medal for proof reading this thesis (twice).

Huge thanks to my examiners, Lucie Green and Eduard Kontar, for suggesting alterations to add much needed clarity to parts of this thesis. Thanks also to Giles Hammond, exam convenor, for organising my viva and scheduling the viva day. I must also acknowledge the financial support of the STFC grant that has funded this research, as well as trips to many conferences and my LTA to Paris.

Special thanks also go to my second supervisor, Lyndsay Fletcher, without whom I doubt I'd even be doing a PhD. Despite (seemingly) being the busiest person on the planet, she has always made time to check over my papers, with suggestions and useful comments, and has always been an inspiring figure throughout my time here.

My sincerest thanks go to Brigitte Schmieder for taking me under her wing during my trip to Paris, and for always asking 'where is the paper?' I'd also like to thank my friends and colleagues from my time in Paris (both at the observatory and outside of it) who made my four months there one of the most memorable times of my life. I grew to love that city, and everyone there helped me go from feeling like a lost traveller to feeling like I truly belonged. Thanks also to Arturo for providing all the THEMIS data, helping with observations, and interpretation of the results (and teaching me basically everything I know about polarimetry). My other paper co-authors deserve thanks too: thanks!

To all the people here in the Glasgow astronomy group, you are amazing. The friendships made here will last a lifetime, and the support has been unreal throughout, especially from those in 604, 614 and latterly 616 – Duncan, Stephen, Al, Graham, Ben, Dave, Tony, Paul, Tash, Ewan, Dina, Andrew, Gerrard, Kyle, Nicolina, Tom, you've all helped me in more ways than I can comprehend. Long live the group chat. Thanks to Rachael for forever helping with travel arrangements. Gail, thanks for football! And I will miss 4pm coffee!

There are two people who deserve far more credit than I can put into words: Mum and Dad. For always being there, putting a roof over my head (thanks Tom for that too!), encouraging me, supporting me, teaching me, and putting up with my weird, hermit-like tendencies whilst I was writing at home, thank you. Thank you, thank you, thank you, and I love you. My granny deserves a special thank you, too; trips to visit you have always given me a small, but much needed escape from work, and I love every minute of my time with you. Huge thanks also to the rest of my family and friends who have kept me somewhat sane during these final few months.

And to Katie – It's not been easy, but we did it. Together. Thank you for being there to keep me grounded and sane and alive. Thank you for being the support I needed, and for the all the fun, laughs, camping, food, road trips, treats, nights out, good times, and so so much more that we've shared. You've taught me so much. I could not have done this without you.

Thank you.

“Light thinks it travels faster than anything but it is wrong. No matter how fast light travels, it finds the darkness has always got there first, and is waiting for it.”

– Sir Terry Pratchett

REAPER MAN

*“O snail,
Climb Mount Fuji,
But slowly, slowly!”*

– Kobayashi Issa

HAIKU, EDO ERA

Chapter 1

Introduction

Solar prominences are one of the oldest observed solar phenomena. The first accounts of them date back to 1185, when a total solar eclipse made prominences above the solar limb visible from Earth (Sviatsky 1923; Vyssotsky 1949). These accounts, which were recorded by Christian scholars in Russian chronicles dating from the thirteenth century, describe the appearance of a “glow similar to that of red-hot charcoals” upon the totality of the eclipse. At that time in Russia any astronomical anomaly, such as an eclipse or aurora, was taken to be a sign from higher powers regarding the politics of the time or even as a sign of anger from their deity, and a description of the event would duly be noted in the records. Unbeknownst to them, these records were to be the first written description of a solar prominence. The origin of this “red glow” remained somewhat of a mystery until the mid-nineteenth century, when it was discovered that they were clouds of hot plasma in the solar atmosphere (Grant 1852). Despite huge advances in the field of prominence research since then a great deal of their true nature is still unknown today.

Of course, it is now widely known that prominences are solar in origin, and their links with other solar phenomena are slowly becoming better and better understood. Due to the intrinsic link between prominences and the rest of the Sun it is important to begin this thesis with an overview of the Sun itself. The Sun is (one of) the most important factors in the evolution and continued success of life on Earth. It warms the Earth’s surface, which in turn heats the atmosphere to a comfortable level for life to flourish – not too hot, not too cold (on average). It allows plants to photosynthesize, in turn giving sustenance to most forms of life and replenishing oxygen in the Earth’s atmosphere in order that the cycle of life can carry on. The

Sun is the life-giver of this planet, but the Earth itself has very little impact on the Sun (other than a small gravitational perturbation). The fact that life has developed and bloomed here on Earth is little more than a happy coincidence on the sidelines of the solar system, the main part of which is the enormous ball of gas and plasma at its centre. It is easy, from a terrestrial perspective, to lose sight of what the Sun actually is – an active star that is over 300 000 times more massive than the Earth, and an efficient nuclear fusion reactor – and become complacent that it will continue to rise every morning and set every evening, just like it has always done. That is because, unless anything truly unexpected happens, it *will* continue to rise every morning and set every evening for at least another 5 billion years. Nevertheless it is important that we learn to understand the Sun and all of its peculiarities, because the Sun can have profound impacts on modern life on Earth. Global Positioning System networks, telecommunications satellites, national power-grids, and many other aspects of today's society can be directly affected by *solar storms* – energetic particles that have been ejected from the Sun and can impact the Earth. Being able to predict solar storms and fully prepare for their societal impacts is becoming more of an imperative, and a new division of the Met Office in the UK dedicated to *space weather* has now been established¹ in order to understand and forecast these effects.

This chapter continues with an overview of the Sun and our present understanding of it from an astrophysical point of view, before going into a deeper introduction to the field of solar prominences that is relevant for this thesis. Previous observations of solar 'tornadoes' are also introduced, beginning with the original classification and early attempts to quantify the plasma motions seen, through to modern observations using satellites and ground-based observatories.

1.1 The Sun and its atmosphere

The Sun is a fairly average G-type main-sequence star, meaning that the light we see from it originates from the nuclear fusion of hydrogen into helium in its core. The outward radiative pressure caused by the huge number of photons and particles produced as a result of this fusion is perfectly balanced by the inward force of gravity. As a result it is in a stable state, and will remain so for at least another 5 billion years when it will run out of hydrogen fuel in its core and migrate off the main sequence.

¹<http://www.metoffice.gov.uk/services/public-sector/emergencies/space-weather>

The close proximity of the Sun allows for detailed observations of its features, which provide a wealth of information to astronomers. It has been studied for over two millennia (Stephenson 1990) and over time, through the continuous development of telescopes capable of probing all parts of the electromagnetic spectrum, our understanding of the Sun has grown. However, with every technological development and new observation there come further questions to be answered about the nature of the Sun.

The Sun consists of distinct layers. The visible surface of the Sun, the *photosphere*, acts as the boundary between the solar interior and the solar atmosphere. Internal to the Sun is the *core*, the *radiative zone*, and the *convective zone*, which ends at the photosphere. The atmosphere consists of the *chromosphere*, the *transition region*, and the *corona*. Each of these layers are described in more detail in the following:

Solar interior: Internally the Sun consists of a *core* where temperatures reach 15 million Kelvin (K), electron densities are extremely high (on the order of 10^{34} cm^{-3}), and the temperature and pressure are high enough to allow nuclear fusion of hydrogen into helium, releasing a huge number of photons (γ radiation) and neutrinos as a by-product (Ambastha 2010). The core is surrounded by a *radiative zone*, where the main energy transport mechanism is via radiation, through *Thompson scattering* of photons by electrons. Temperature and density drop off through the radiative zone, and as they do so the ionisation of the plasma decreases, meaning that the number of neutral hydrogen atoms increases. This causes the opacity of the plasma to increase, where photons can now be absorbed more easily by atoms, to a critical point where energy can no longer be transported freely by radiation. At this point the radiative zone ends and the *convective zone* begins, where the density is too low for the radiation to transport the energy outwards. Instead convective cells form which are heated at the boundary of the radiative zone, expand and move outwards, before cooling near the solar surface and falling back into the interior to be heated again, continuing the cycle. The magnetic fields that penetrate the solar surface are also believed to originate from the boundary between the radiative and convective zones – a region called the *tachocline* (Gilman 2000). These magnetic fields are then forced upwards, through the convection zone and into the solar atmosphere, where they are responsible for most of the observed phenomena that are described in the following sections.

Photosphere: The ‘surface’ of the Sun is the layer called the *photosphere*, which is at

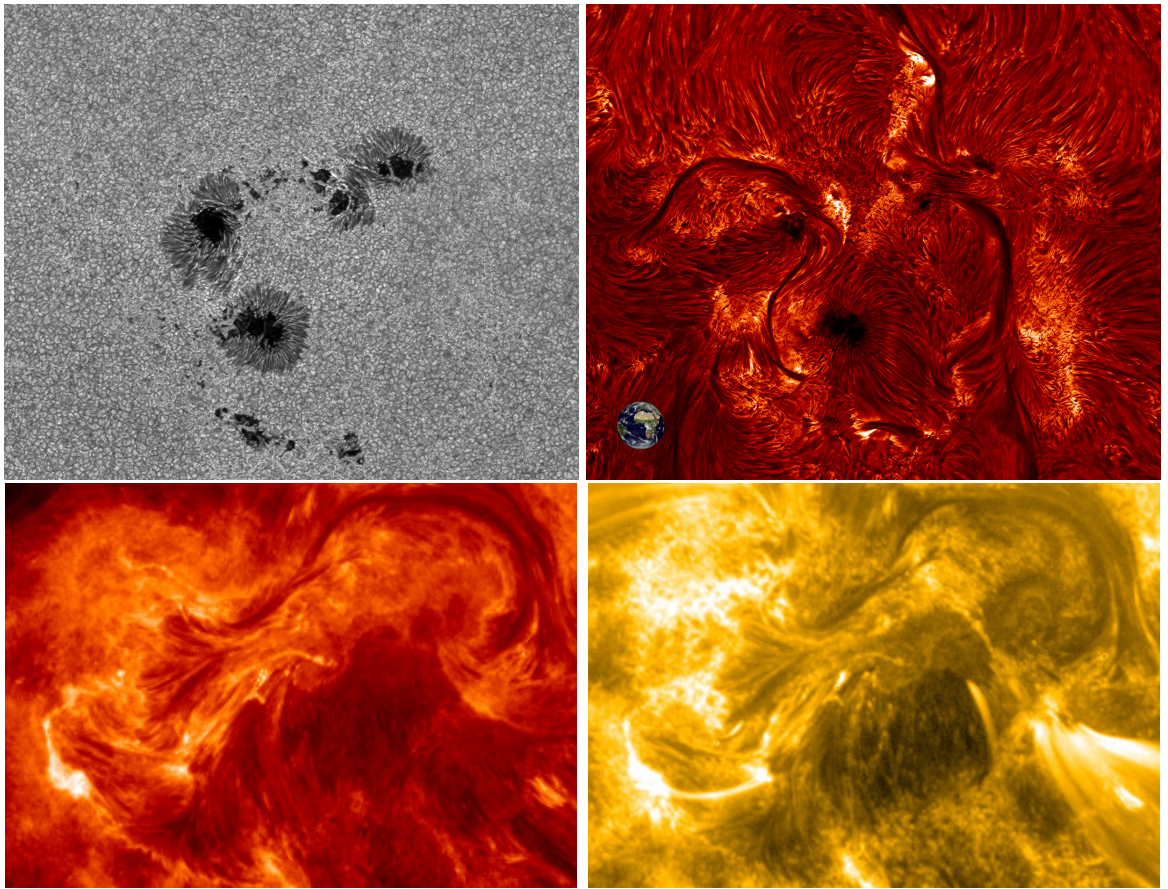


Figure 1.1: Images from DOT and SDO/AIA showing the different layers of the solar atmosphere. DOT images (*top*) are from 8 July 2005 and AIA images (*bottom*) are from 12 July 2012. *Top left:* DOT G-band image of sunspots on the solar surface. Also visible in the image are granulation cells. Image is quoted as having a field of view of $182'' \times 133''$. ²*Top right:* DOT H- α image of the same region as the G-band image. Filaments and fibrils are visible in H- α . Earth is shown for scale. *Bottom left:* AIA 304 Å image of an active region, showing the upper chromosphere. Image was made with a field of view of $182'' \times 133''$. *Bottom right:* AIA 171 Å image of an active region, showing the corona. Field of view is the same as in the 304 Å image.

the very top of the convective zone. Convective cells in the photosphere are seen as *granulation* on the visible surface, with the granulation cells having a bright centre and darker edges. These granulation cells can be seen around the edge of Figure 1.1

²DOT images from: <http://www.staff.science.uu.nl/~rutte101/dot/albums/images/album.html>

(*top left panel*), which is a G-band (continuum) image taken by the Dutch Open Telescope (DOT, Rutten et al. 1997). The photosphere is not a solid surface – it is instead the layer above which the solar plasma becomes optically thin to light in the visible part of the solar spectrum at ~ 5000 Ångstrom ($1 \text{ Å} = 0.1 \text{ nm}$) and these photons can freely escape without being re-absorbed. On average it takes a photon emitted in the core of the Sun 100 000 years to reach the photosphere and escape into space, as it will be scattered millions of times inside the Sun. The photosphere approximately emits as a *blackbody* (an object that absorbs all incident light and does not reflect any) with a temperature of around 5800 K and an emission spectrum that is peaked in the green part of the visible spectrum.

Besides granulation, the photosphere has other notable characteristics. *Sunspots* are the most conspicuous of these. Appearing as dark patches on the bright solar surface, sunspots are a visual manifestation of the Sun's internal magnetic field breaking through the surface layers from below – Figure 1.1 (*top left panel*) shows examples of sunspots in an *active region*. They are darker due to the fact that they are cooler than their surroundings – the temperature is inhibited by the strong magnetic field (> 1000 Gauss) in these regions. Due to this intense magnetic flux the areas around and above sunspots can be incredibly active, with localised plasma heating and strong flows. In quiet-sun regions, too, there are magnetic fields penetrating through the solar surface into the atmosphere, which is important for the formation of prominences.

Chromosphere: The photosphere also marks the lowest boundary of the solar atmosphere. Above this, the electron and hydrogen densities drop enormously (from $\sim 10^{16} \text{ cm}^{-3}$ to $\sim 10^{11} \text{ cm}^{-3}$) over a distance of a few thousand kilometres, before further dropping to $\sim 10^9 \text{ cm}^{-3}$ in the *corona*. The atmospheric temperature dips slightly to around 5700 K in the *temperature minimum region* at 500 km above the surface, before rising to $\sim 20000 - 30000$ K at the base of the *transition region* above. This temperature structure is shown in Figure 1.2, which shows the atmospheric temperature against height above the photosphere. Many models of the solar atmosphere have been constructed, and Figure 1.2 shows the resulting temperature structure of an updated Vernazza et al. (1981) semi-empirical model. The layer directly above the photosphere is the *chromosphere*, with typical temperatures in the range 10000 – 20000 K, where many of the absorption lines in the visible solar spectrum (the *Fraunhofer lines*) are formed by species of hydrogen (H), helium (He),

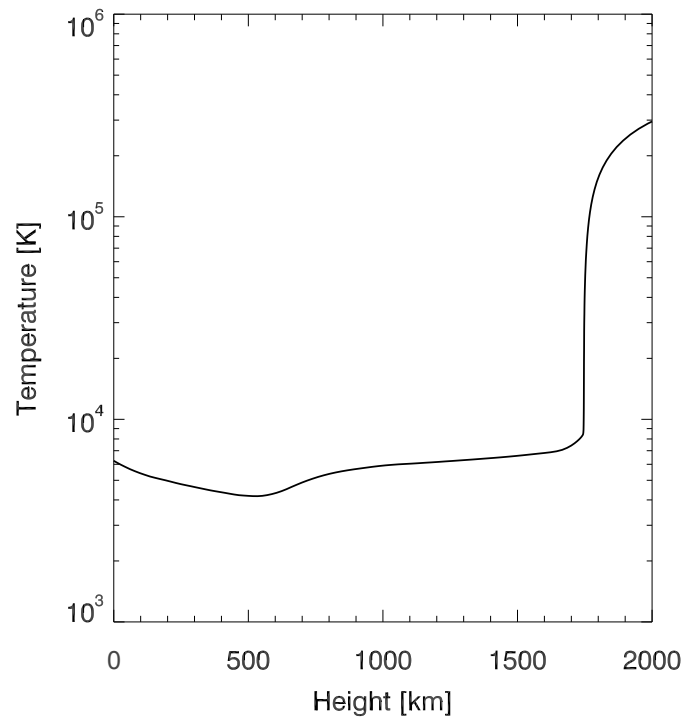


Figure 1.2: Temperature of the solar atmosphere, plotted against height above the photosphere. This plot was made using an updated [Vernazza et al. \(1981\)](#) atmosphere model. Data provided by S. Brown.

calcium (Ca), and sodium (Na) amongst others. The Fraunhofer ‘C’ line at 6562 \AA (red in colour), caused by hydrogen-alpha ($H-\alpha$) absorption in the chromosphere, is a notable example as it is one of the strongest lines in the solar spectrum. Other notable chromospheric lines are hydrogen-beta ($H-\beta$) at 4861 \AA , which is green in colour, and the ‘H’ and ‘K’ lines of singly-ionised calcium (Ca II), at 3968 \AA and 3933 \AA respectively, which are prominent in the violet part of the optical spectrum. Applying a narrow filter around one of these lines, blocking out the bright light from the photosphere, it is possible to view the chromosphere directly, and it appears visually completely different to the photosphere below it. Figure 1.1 (*top right panel*) shows the same active region as the top left panel, but instead using the $H-\alpha$ filter of DOT. Immediately noticeable is the fact that the chromosphere is active and dynamic, with *spicules* and *fibrils* (e.g. [Hansteen et al. 2006](#); [de Pontieu et al. 2007](#)) in quiet regions being an example of the dynamic chromosphere. Also visible in Figure 1.1

(*top right panel*) are a number of dark *filaments* – see §1.2. The chromosphere is also the place where much of the energy released during a *solar flare* is deposited (Fletcher et al. 2011) – flares are the sudden release of energy stored in the magnetic field above the solar surface, causing particle acceleration and extreme brightenings in many parts of the electromagnetic spectrum.

As well as being observable at optical wavelengths, the chromosphere is also extremely bright in the *ultraviolet* (UV) part of the solar spectrum, with many UV spectral lines being formed at chromospheric temperatures. Notable examples are the Lyman lines of neutral hydrogen (with Ly- α = 1216 Å, Ly- β = 1026 Å, and higher order lines at shorter wavelengths), and the h and k lines of ionised magnesium (Mg II) at 2803 Å and 2796 Å respectively. Figure 1.1 (*bottom left panel*) shows an image of an active region from the *Atmospheric Imaging Assembly* on the *Solar Dynamics Observatory*, taken with the 304 Å filter. That filter is dominated by emission from He II lines, which are formed in the upper chromosphere.

Transition region: At a height of around 2000 km above the solar surface the temperature of the atmosphere sharply increases from around 20000 K up to ~ 1 million K (MK). This is called the *transition region* (TR), and it links the chromosphere to the hot and tenuous corona above. Despite being an extremely thin region, only a few hundred kilometers thick, it is an important piece of the solar atmosphere as the temperature range that it covers is where many ion species are created, and consequently there are many spectral lines formed in this region too.

Corona: At the top of the transition region lies the *corona* – a hot ($T \geq 1$ MK) tenuous ($n_e \sim 10^9 \text{ cm}^{-3}$) region that extends out to several solar radii before becoming the *solar wind* in the *heliosphere*. The quiet corona is generally considered to be around 1 – 2 MK, however parts of the corona can be heated to temperatures in excess of 10 or even 20 MK. The corona was discovered during total solar eclipses, where a diffuse white-light glow was seen around the Sun when the moon had entirely obscured the bright solar disc. High coronal temperatures allow for extreme levels of ionisation in heavy elements like iron (Fe), silicon (Si), and sulfur (S), amongst others, with anywhere from eight to 25+ electrons typically being lost. Ions of iron create some of the most prominent lines observable in the corona. Many of these ions emit at *extreme ultraviolet* (EUV) and *X-ray* wavelengths, with $\lambda < 1000$ Å. That spectral range is completely absorbed by the Earth's atmosphere, so in order to observe lines formed in the EUV, satellites, rockets, or balloon missions must be employed in

order to get above the Earth's atmosphere. Figure 1.1 (*bottom right panel*) shows an active region in the 171 Å filter of the Atmospheric Imaging Assembly, which mostly samples emission from Fe IX, formed at ~ 1 MK.

The extreme temperatures found in the solar corona pose one of the biggest mysteries of solar research. With temperatures of a few thousand Kelvin at the photosphere, one might expect the temperature to drop off through the solar atmosphere, so why does the temperature suddenly increase by several orders of magnitude? The answer to this problem is not definitively known, but different proposals have been made in attempt to resolve the issue, for example small-scale reconnection events ('nano flares', Parker 1988) or heating caused by plasma waves which are transported from the photosphere in spicules (Uchida & Kaburaki 1974; Wentzel 1974).

The corona is the hottest part of the solar atmosphere, and it is one of the most dynamic parts as well. *Coronal mass ejections*, loops above active regions, and flares are some of the most striking features seen in the corona, and waves and heating can be seen throughout the region. Solar prominences also reside in the corona, where cool plasma is suspended in the hot atmosphere by the magnetic field. Prominences can lead to some of the most dramatic eruption events known, *prominence eruptions*, and can be associated with *coronal mass ejections* (CME), which release huge numbers of particles into the heliosphere which can impact the Earth, causing aurora and potentially affecting telecommunications, GPS satellites, and national power grids. Understanding the onset of such eruptions is therefore an important problem in modern solar-terrestrial physics, and so studying all aspects of prominences can help with understanding these potentially damaging eruption events.

1.2 Solar prominences

Prominences are one of the most striking phenomena in the solar atmosphere. Formed of cool plasma ($T \sim 10^4$ K) suspended in the hot corona by magnetic fields, prominence plasma is generally around 100 times denser than that of the surrounding corona (Labrosse et al. 2010). They can remain stable in the solar atmosphere for days, or even weeks, before either dramatically erupting into space in a *prominence eruption* or fading gradually over time. The presence and longevity of this plasma in the context of the hot corona raises questions about how the cool plasma is transported into the atmosphere, and also how it maintains its energy balance in a hot

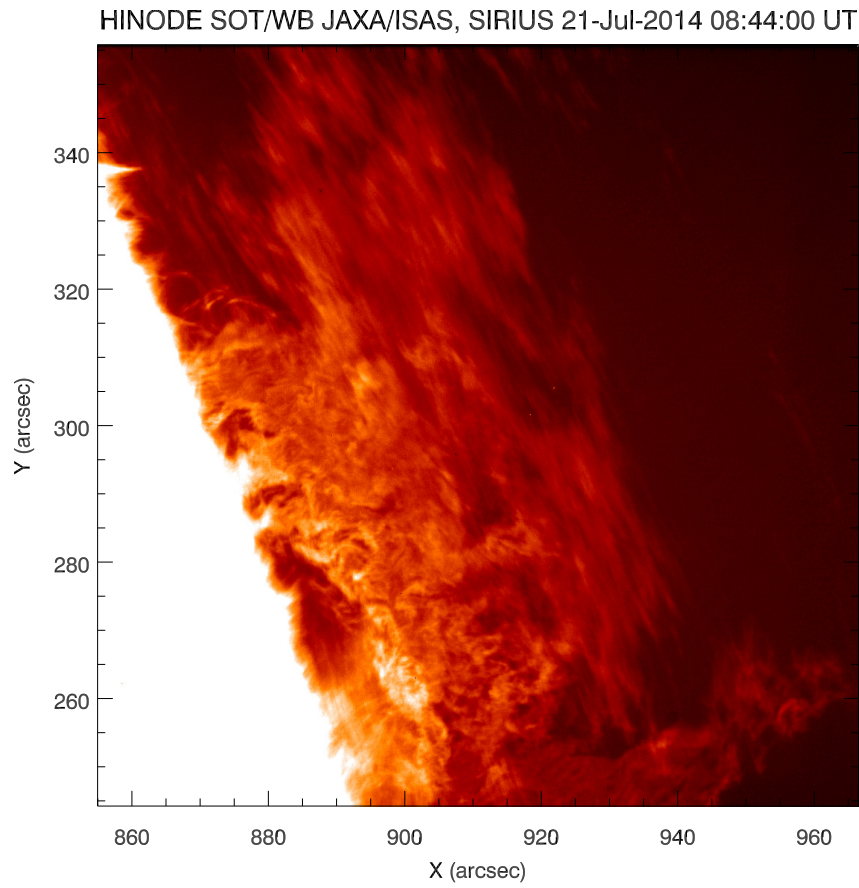


Figure 1.3: An example of a solar prominence from *Hinode*/SOT. The image was made using the Ca II H (3968 \AA) filter. The solar disc is visible in the lower-left of the image.

surrounding for such long periods of time. Prominences always form above a *polarity inversion line* (PIL) on the solar surface, where regions of opposite magnetic polarity border one another (Mackay et al. 2010). In these regions the magnetic field above the surface can become sheared along the PIL, allowing for the suspension of cool material above the surface by the magnetic field.

Prominences can be distinguished into two main types based on where on the Sun they form – *quiescent* and *active*. *Quiescent prominences* are those that are found far from any regions of activity, generally forming in areas of weak magnetic fields, and are usually the longest lasting. Figure 1.3 shows a quiescent prominence observed by the *Solar Optical Telescope* on the *Hinode* spacecraft, using the Ca II H line at 3968 \AA . Quiescent prominences are able to form anywhere on the Sun in quiet-

sun regions, including latitudes close to the solar poles (within $\pm 30^\circ$). They can remain visible for weeks at a time, and are not prone to erupt unless there is some trigger nearby, such as a flare or CME. Despite their name suggesting that they are inactive and quiet, quiescent prominences show dynamic fine structures (seen in Figure 1.3) which evolve on a timescale of minutes. *Active prominences* form in active regions, as the name suggests. In active regions the magnetic field strength can be thousands of times that of quiet-sun regions, and prominences that form in or around active regions are normally smaller in height and shorter lived than their quiescent counterparts. Active-region prominences are also much more likely to erupt into prominence eruptions, and can provide material that becomes part of a CME. There is a third type of prominence that is somewhere in between the quiescent and active cases, known as *intermediate* prominences. These intermediate prominences generally form around and between active regions, but not within the active regions themselves.

There is another distinction to be made between *prominences* and *filaments*. Prominences are viewed in profile above the solar limb, and are seen brightly in emission in spectral lines such as hydrogen H- α or Ca II H and K lines due to illumination from the solar disc below. They can also be seen as dark structures above the limb in coronal emission lines formed above 1 MK, where the cool plasma in the prominence absorbs emission coming from behind it. Filaments, on the other hand, are viewed from above on the solar disc. They appear as dark features on the disc in chromospheric lines, most clearly seen in H- α . A number of filaments are visible on the solar disc in the H- α image shown in Figure 1.4 (from Kanzelhöhe Observatory), most notably the large filament in the northern hemisphere near disc centre. Prominences can also be seen faintly in Figure 1.4 at the south-west limb (lower right). The reason that filaments appear darker than the rest of the solar disc is due to the fact that the filamentary plasma scatters the light illuminating it from below in all directions, meaning that photons are scattered out of the line of sight, so less photons are observed than there would be in the absence of the filament. Filaments and prominences are, however, the same structures viewed from different angles. The terms are sometimes used interchangeably, but in this thesis ‘filament’ will only be used to refer to these structures when viewed on disc, and ‘prominence’ will be used to describe them above the solar limb.

Prominences and filaments are usually characterised and identified as having

Kanzelhohe H-alpha 18-May-2014 08:26:16 UT

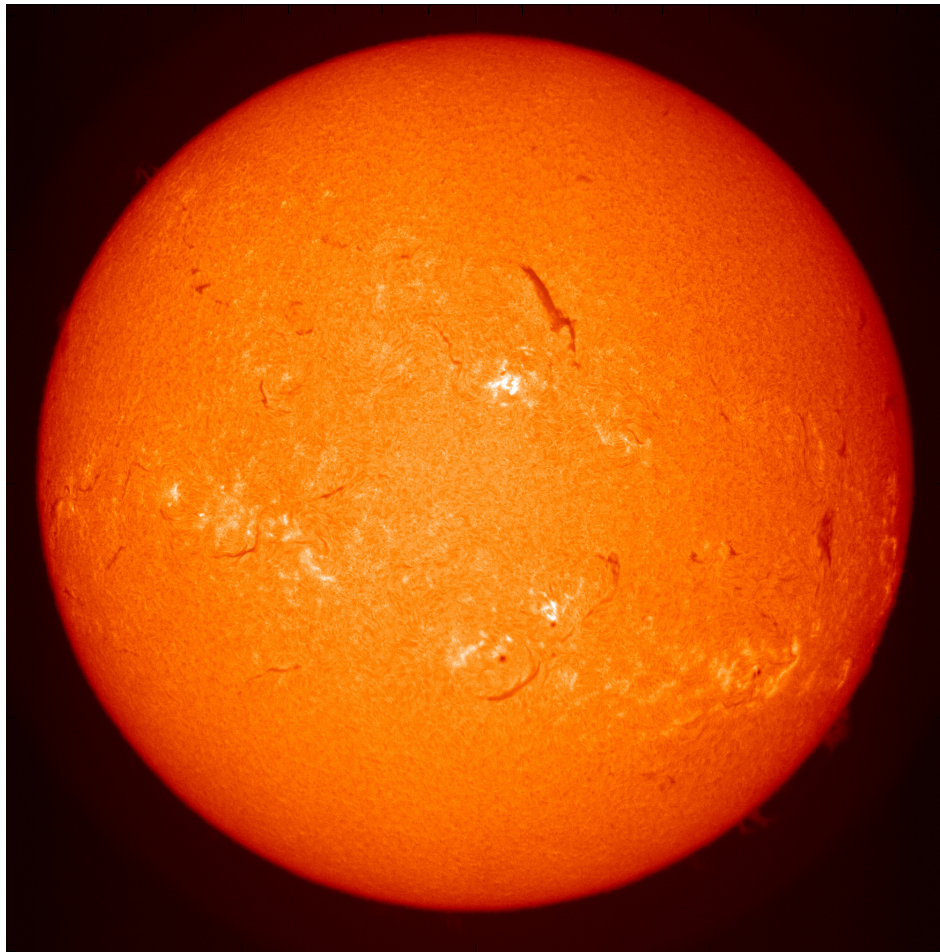


Figure 1.4: Full disc H- α image from the Kanzelhöhe Observatory on 18 May 2014. Image shows a number of filaments on the solar disc. Prominences can be seen faintly at the south-west limb.

two main observable features – a horizontal *spine*, suspended above the solar surface, and ‘vertical’ *barbs* (or *legs*), which appear to reach down from the spine towards the solar surface (Mackay et al. 2010). Spines and barbs are most easily identifiable when viewed as filaments on disc in the H- α line, such as in Figure 1.4. The spine appears as the main body of the filament, and the barbs stick out to either side. In some cases the spine is invisible, and only barbs can be seen – this can give the impression of many small filaments instead of one big one. When viewed as a prominence, the barbs appear to extend down to the solar surface, giving the impression that they are columns supporting the spine. These are general terms, of course, and many

different classes and sub-classes of prominences/filaments have been identified based on observable features (see §1.2.3 for an outline of the various classifications).

Another prominence feature that should be outlined is the *prominence to corona transition region* (PCTR). Analogous to the transition region that exists between the chromosphere and the corona in the solar atmosphere, it is natural to consider that a similar transition region might exist between the cool, dense prominence plasma and the hot, tenuous coronal plasma that surrounds it. It is well documented that prominences are primarily made of hydrogen gas, with spectral lines formed at ~ 6000 K, but they are also seen to emit in a large range of other spectral lines formed at much higher plasma temperatures. Chromospheric temperatures ($\sim 10000 - 20000$ K), transition region temperatures ($\sim 20000 - 800000$ K) and even coronal temperatures (> 800000 K) have been reported in association with prominences. This indicates that prominences, too, have some transition region (both in temperature and pressure), which is called the PCTR. The exact structure of the PCTR within prominences is not precisely known (see §1.2.4), but it appears that the PCTR changes with viewing angle (Heinzel & Anzer 2001) and orientation of the magnetic field (Schmieder et al. 2007). Prominence models are generally found to match observed spectra better when a PCTR is included (Anzer & Heinzel 1999; Labrosse & Gouttebroze 2001; Heinzel & Anzer 2001; Heinzel et al. 2014, 2015).

1.2.1 Discovery and historical observations

Prominences were first observed long before they were understood to be solar plasma suspended in the Sun's atmosphere by magnetic fields. As mentioned previously, the first recorded observations of prominences occurred during total solar eclipses, the first of which was noted during the eclipse of 1185 by scholars in Russian 'CHRONICLES OF NOVGOROD' (Vyssotsky 1949). Although these chronicles were written in the thirteenth century, each author was believed to have faithfully recounted the work of their forebears which dated back hundreds of years. They described the sky becoming dark and that "the sun became like a crescent of the moon, from the horns of which a glow similar to that of red-hot charcoals was emanating." It is thought that this account is describing a prominence above the limb (Sviatsky 1923; Vyssotsky 1949), which appeared red in colour due to the strength of the H- α emission line. The accounts of the eclipse of 1185 are corroborated by several

chronicles from different areas at the time, so it is believed that they are accurately recorded. However, as noted in a footnote of [Vyssotsky \(1949\)](#) the red colour could be caused by chromospheric light instead of a prominence, but the account in the chronicle is generally taken to be an observation of prominence light.

Throughout the 1700s there are numerous reports of total solar eclipses, several of which reported observations of phenomena which are now thought to be prominences. Many of the early accounts of prominences are described in the book 'HISTORY OF PHYSICAL ASTRONOMY. FROM THE EARLIEST AGES TO THE MIDDLE OF THE 19TH CENTURY' by [Grant \(1852\)](#). Interestingly, this book makes no mention of the astronomical observations in the early Russian chronicles, despite their publication in the early nineteenth century. Dedicated translations of the astronomical parts of the chronicles were collected in the twentieth century by [Sviatsky \(Vyssotsky 1949\)](#). In the eighteenth century there were numerous reports of light seen above the solar/lunar limb during the totality of the eclipse. Some early accounts from 1706 and 1715 allude to "red light" seen just before or just after the totality of the eclipse, which were possibly prominences, although this light could also be chromospheric in origin and nothing more descriptive is written about them. Most notable is the eclipse of 1733 which was reported at the time by Vassenius, and then later by Celsius in 1735 ([Grant 1852](#); [Tandberg-Hanssen 1974](#)). Vassenius described seeing three or four "reddish spots which appeared in the lunar atmosphere," a suggestion that was paralleled by Celsius and others ([Grant 1852](#)) – at that time they believed that they were seeing clouds suspended in the lunar atmosphere (and indeed that the moon may have an atmosphere capable of supporting clouds of gas). On this theory, [Grant](#) notes that it is unlikely that they are lunar in origin, and that the moon does not support an atmosphere, or at least not one that could support "clouds of such enormous magnitude." A later eclipse observation in 1778 by Ulloa noted a "point of red light" at the edge of the lunar disc, near where the Sun was to emerge from occultation. He thought that this light was coming from the Sun, unlike the supposition of Vassenius and Celsius, and was visible due to a "hole in the body of the moon" – it is thought that this was probably a prominence which became visible before the Sun emerged from the eclipse, but it could also be the appearance of *Baily's beads* (e.g. [Herald 1976](#)) caused by craters on the lunar limb.

In 1842 another eclipse was observed where reports of prominences were made, however the general consensus at the time was that they were some sort of mountain-

ous structure on the Sun (Grant 1852; Pettit 1943b). One observer, Mayette, called them “beautiful sheaves of flame,” whilst Baily noted that “the luminous protuberances had the appearance of mountains of a prodigious elevation.” A common theme was that they were red, or rose, in colour, and many observers mentioned that they resembled mountains. However, it seems that no accounts of prominences during the 1842 eclipse considered them to be lunar in origin, unlike those in the previous century. Instead there was a consensus that they were related to the Sun. Grant agrees on this, however he does not admit to agreeing with the mountain analogy. He says on the matter: “if they be admitted to be clouds suspended in the solar atmosphere, the explanation of the various facts relating to them becomes more consistent and probable.”

After 1850 some dedicated work was done in order to observe and identify prominences during eclipses (Nasmyth 1852; Schweizer 1853). At that time it was generally thought that prominences were related to *faculae* on the solar disc – bright patches on the solar surface – but that statement was questioned by Schweizer (1853). Schweizer then went on to attempt to link prominences with sunspots, but was unable to find any consistent results. The idea that prominences and faculae were linked persisted for some time (Brayely 1869), but we now know that prominences are not related to brightenings on the solar disc at any visible wavelengths – instead filaments are actually darker than the surrounding solar disc in lines which show prominences brightly in emission.

In the 1860s a large amount of important work was done regarding prominences. The first came during the eclipse of 1860 when photographic techniques were first used to image prominences. Figure 1.5 is from the first volume of the seminal work ‘LE SOLEIL’ by Secchi (1875), showing an image taken during that eclipse. Secchi identified seven prominence structures in that image, visible as white patches above the occulted solar disc, which are labelled with letters A through K. The dark strip labelled XY in Figure 1.5 represents the solar equator, and was used to identify the relative positions of the prominences.

Significant developments came during the eclipse of 1868 when Janssen (1869a,b) made observations of a prominence using a spectroscope, hence performing the first spectral examination of prominences. It was found in that work that prominences appeared brightly in emission in certain lines that are normally viewed in absorption on the solar disc, which were known at the time to be lines of hydrogen. Janssen

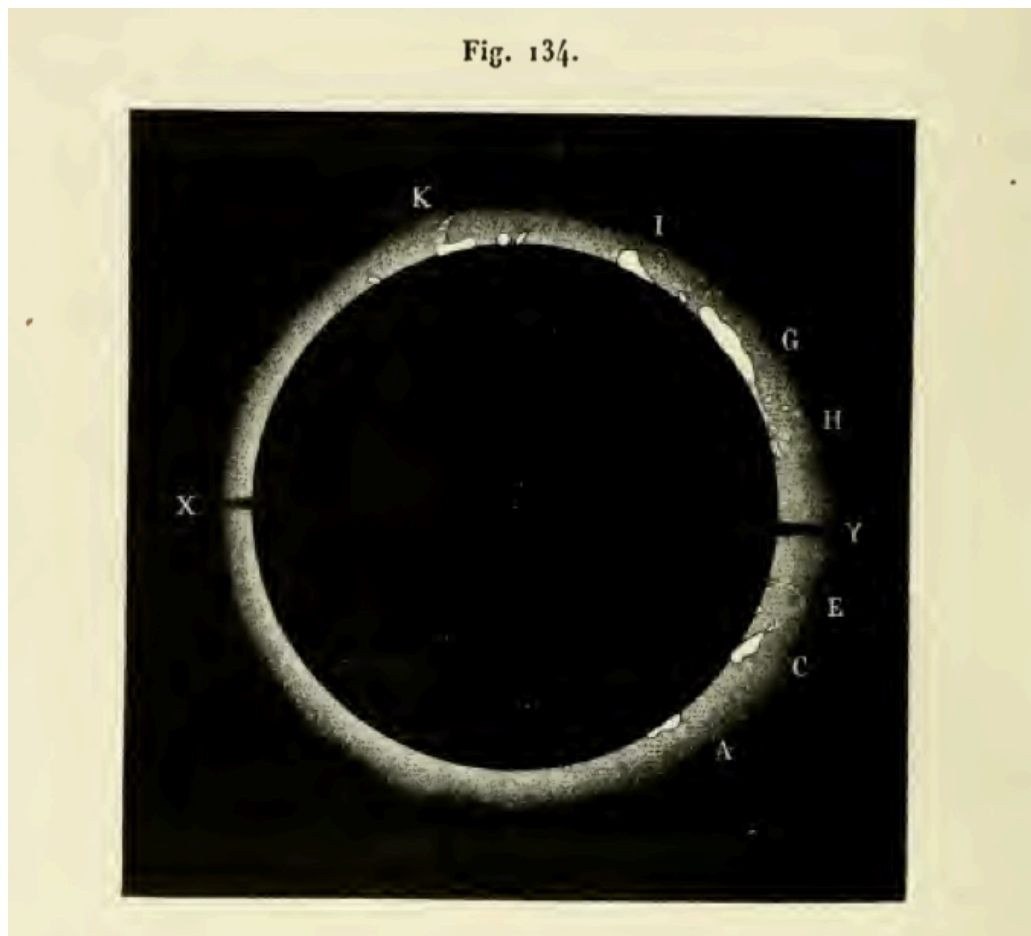


Figure 1.5: The first image of solar prominences, taken during the total eclipse of 1860. The prominences appear as white patches above the occulted solar limb and are denoted by letters A through K. The dark strip XY was used to identify positions of the prominences relative to the solar equator. This image is taken from 'LE SOLEIL' (Secchi 1875).

(1869a,b) was therefore able to determine that prominences were gaseous in nature, due to the presence of these bright emission lines. Further to this Janssen (1869b) thought that, due to the brightness of the emission lines seen in prominences during the eclipse, he may be able to observe them with the spectroscope without an eclipse blocking light from the solar disc. He was able to do this, observing the Fraunhofer 'C' line ($H-\alpha$) in emission in the prominence at the same time as in absorption on the disc (later repeating this to observe the 'F' line, or $H-\beta$). These observations allowed

Janssen to state, without doubt, that prominences belonged to the Sun, and that they are primarily made of hydrogen. He also managed to determine that prominences are large-scale, highly dynamic structures, which change form on a time scale of minutes. These ideas were revolutionary as they allowed prominences to be observed outside of eclipses, which are relatively rare occurrences. Some attempts were subsequently made to view prominences without a spectrometer by using coloured filters alone (de La Rue 1869; Huggins 1869). By the time 'LE SOLEIL' was written (Secchi 1875, Volume I, and Secchi 1877, Volume II) the field of prominence study had well and truly taken off, with many spectroscopic and photographic observations having been made.

From the late nineteenth century through the start of the twentieth century, countless studies of prominences were made. The advancement of telescope and photographic technology meant that observations of prominences became easier, and more detailed spectral studies were also made possible. Authors were able to begin categorising prominences into different morphological types, mapping their features in great detail (Secchi 1875, 1877; Pettit 1919, 1925, 1932, 1943a) – see §1.2.3. In the early 1900s, spectroscopic and filtered photographic techniques had become accurate enough to distinguish dark filaments on the solar disc (Hale & Ellerman 1903). It also became known that prominences could erupt (Secchi 1875; Young 1896). Pettit (1919) measured and photographed prominences erupting on two occasions, plotting graphs of prominence height over time – noting that erupting prominences appeared to accelerate in stages as they rose – and he also measured internal motions in one of these eruptions. Since then a significant amount of work has been done on prominences, and the field of prominence physics is now well established. Further advancements came with the development of space-based observatories, many of which will be discussed in §1.2.2.

1.2.2 Recent observations

Since the 1960s, the use of rocket and satellite experiments for solar research has been commonplace, with a string of dedicated solar space missions creating the possibility for continuous solar monitoring. Many of these space-borne missions focussed on spectroscopy of the UV and EUV parts of the solar spectrum, as these are blocked by the Earth's atmosphere. The UV/EUV solar spectrum is extremely

rich in spectral lines, providing a great wealth of information on all parts of the Sun's atmosphere, including prominences. Many ions created at chromospheric and transition region temperatures, as well as the Lyman series of neutral hydrogen, emit lines in the UV and EUV, so studying these spectral ranges in prominences allows for a more detailed understanding of their temperature and density structure.

Some of the earliest dedicated remote solar observatories were the *Orbiting Solar Observatory* (OSO) satellites, which observed from the 1960s until the 1980s. A total of eight OSO spacecrafts were launched, with OSO-4, OSO-6 (Noyes et al. 1972), and OSO-8 (Vial et al. 1979; Vial 1982a) being used to study prominences. Noyes et al. (1972) found that prominences emit strongly in lines formed up to a temperature of 3×10^5 K, and measured electron densities to be 2×10^9 cm⁻³. Vial et al. (1979) and Vial (1982a) studied the behaviour of optically thick emission lines (Ly- α , Ly- β , Mg II h and k, Ca II H and K) with OSO-8. From the 1970s, numerous UV and EUV studies of prominences were made using the *Apollo Telescope Mount* (ATM) on board *Skylab* (Moe et al. 1979; Mariska et al. 1979; Orrall & Schmahl 1980; Kanno et al. 1981; Widing et al. 1986). The analysis done with ATM data provided many physical parameters for prominence plasma, such as temperature structure, emission measure, line-of-sight velocities, electron densities and pressures using line ratios and other techniques. See Chapter 2 for an outline of many of the techniques used for plasma diagnostics. For example, Widing et al. (1986) used ATM data of an eruptive prominence, which had measured plasma velocities of 400 km s⁻¹, and a large range of possible electron densities, from 8×10^9 – 3×10^{11} cm⁻³. In the 1980s and 1990s, satellites and rocket experiments were continually employed to study prominences. Observations from the *Solar Maximum Mission* (SMM) satellite (Poland & Tandberg-Hanssen 1983; Schmieder et al. 1984) and the *High Resolution Telescope and Spectrograph* (HRTS) sounding rocket (Wiik et al. 1993) were used in extensive prominence studies. Extremely high prominence electron densities ($\geq 10^{11}$ cm⁻³) were found from both SMM and HRTS studies, and emission measures were found to be consistent with previous results.

The launch of the *Solar Heliospheric Observatory* (SOHO, Domingo et al. 1995) in 1995 allowed for a new era of prominence observations (Patsourakos & Vial 2002). Two of the instruments on SOHO, the *Solar Ultraviolet Measurement of Emitted Radiation* (SUMER, Wilhelm et al. 1995) and the *Coronal Diagnostics Spectrometer* (CDS, Harrison et al. 1995), were particularly well suited to observing prominences

in the UV and EUV. Both SUMER and CDS are spectrometers, meaning that a large spectral range is available by using a combination of the instruments – SUMER observed from 500 – 1610 Å and CDS observed from 150 – 800 Å. Throughout the operational lifetime of *SOHO* a large number of prominence studies were made with SUMER and CDS. Due to the selection of lines available, SUMER and CDS were prime for measuring prominence densities and temperature structures. In early studies using *SOHO* instruments, plasma properties in quiescent (Madjarska et al. 1999) and eruptive (Wiik et al. 1997) prominences were recovered, with electron densities similar to those found previously ($\sim 10^9 - 10^{10} \text{ cm}^{-3}$). Heinzel & Anzer (2001) used an observation of the SUMER Lyman lines in a prominence in comparison to models, determining that the inclusion of a PCTR was necessary to explain the observed profiles. Kucera & Landi (2006) and Parenti & Vial (2007) utilised the strength of the SUMER spectral range to try and analyse this PCTR, calculating the emission measure at a range of temperatures to try and quantify the PCTR observationally. Electron densities in the range $5 \times 10^8 - 3 \times 10^9 \text{ cm}^{-3}$ were recovered in quiescent prominences. Parenti & Vial (2007) also provided a complete spectral atlas of emission lines visible by SUMER in prominences. Further to the work of Heinzel & Anzer (2001), Schmieder et al. (2007) determined that the orientation of the magnetic field in the prominence had an effect on the observed Lyman line profiles from SUMER. Combined with the earlier result, this suggests that the structure of the PCTR is linked to the magnetic field orientation. A complementary study was performed by Gunár et al. (2007) using the Lyman lines observed by SUMER, where they found, using a 2D multi-thread model, that the observed line profiles were best replicated as the result of integrating along many fine threads of plasma. These model threads also each included a PCTR on both sides, as in Heinzel & Anzer (2001). An extensive study was made by Heinzel et al. (2008) using *SOHO* (SUMER and CDS), along with the *Transition Region and Coronal Explorer* (TRACE) and *Hinode* satellites, where they managed to measure the absorption and volume blocking of coronal emission caused by the presence of cool prominence material along the line of sight. Using this combination of instruments they measured the number density of hydrogen in a prominence to be around $1 \times 10^{19} - 5 \times 10^{19} \text{ cm}^{-3}$. TRACE is a UV/EUV imager (Handy et al. 1999) and was itself used to study active region filaments (Chae 2003), determining high transverse speeds of $80 - 250 \text{ km s}^{-1}$ and electron densities of $0.7 \times 10^{10} - 1.9 \times 10^{10} \text{ cm}^{-3}$.

2006 saw the launch of the *Hinode* satellite (Kosugi et al. 2007). *Hinode* has three science instruments on board (covered in more detail in §2.4.1) – the *Extreme-ultraviolet Imaging Spectrometer* (EIS, Culhane et al. 2007), the *Solar Optical Telescope* (SOT, Suematsu et al. 2008), and the *X-Ray Telescope* (XRT, Golub et al. 2007). SOT is a high-resolution imager, with filters for the Ca II H (3968 Å) and H- α (6562 Å) lines, both of which emit brightly in prominences, meaning it is useful for studying prominence fine structure and dynamics (Berger et al. 2008; Ning et al. 2009; Schmieder et al. 2010). The EIS instrument has been used to study prominences too. EIS is a slit (or slot) spectrometer, observing in the EUV, which is capable of observing several lines that are bright in prominences. A detailed multi-wavelength prominence study using EIS was performed by Labrosse et al. (2011), where they found particularly that the He II 256 Å resonance line can provide useful diagnostics, but it is not easy to interpret due to the presence of line blends. Labrosse et al. (2011) also found that EIS observed several higher-temperature transition region lines emitting in prominences, which can be useful for studying the PCTR, and confirmed that prominences appear dark against a bright background in EIS coronal lines. A tornado prominence was observed using EIS by Su et al. (2014), where a velocity pattern indicative of rotation was found in the tornado at temperatures of over 1.5×10^6 K. This Doppler pattern was later found to be present at lower temperatures observed by EIS (Levens et al. 2015, and Chapter 3).

The *Solar Dynamics Observatory* (SDO, Pesnell et al. 2012) was launched in 2010 and includes a full-disc solar imager: the *Atmospheric Imaging Assembly* (AIA, Lemen et al. 2012). AIA has ten filters, mostly in the UV/EUV, many of which are dominated by coronal emission lines where prominences sometimes appear as dark features that absorb/block background coronal emission. One filter, however, is dominated by emission from the He II 304 Å line, which is a resonance line that is strongly in emission in prominences. This alone makes it a good instrument for context images. Due to its large field of view and its high temporal and spatial resolution, AIA has been used to study prominence motions by multiple authors (Li et al. 2012; Su et al. 2012; Williams et al. 2013; Landi et al. 2013; Mghebrishvili et al. 2015). Li et al. (2012) and Su et al. (2012) reported tornado-like motions in AIA images – these reports will be discussed in detail in §1.3. Parenti et al. (2012) used AIA to investigate the emission in prominences at EUV wavelengths, finding that some spectral lines formed at PCTR temperatures were observable in two of the AIA coronal filters.

The latest dedicated UV solar observatory was launched in 2013. The *Interface Region Imaging Spectrograph* (*IRIS*, De Pontieu et al. 2014) is a UV spectrometer and imager that is designed to study lines formed in the solar chromosphere (see §2.4.2). It observes several lines that are visible in prominences, and its high spatial and spectral resolution make it a very powerful instrument for investigating prominence dynamics. Schmieder et al. (2014) used *IRIS* to study a quiescent prominence using the Mg II h and k lines, finding that line-of-sight velocities of up to 80 km s^{-1} were observable, even in a quiescent prominence. That study prompted an update in Mg II prominence models to be made (Heinzel et al. 2014, 2015), as the observation of these fast flows and unusual profiles could not be accounted for by previous models. Harra et al. (2014) and Liu et al. (2015a) observed prominence eruptions using *IRIS*, with the latter giving an extremely detailed analysis of the erupting plasma. They found extremely high velocities ($\sim 1200 \text{ km s}^{-1}$ in the plane of sky, $\sim 460 \text{ km s}^{-1}$ along the line of sight) and that the eruption appeared to have two components. Liu et al. (2015a) also found that *Doppler dimming* had a large effect in that eruption – Doppler dimming occurs when emitting plasma has a large radial velocity, and the observed spectral line is weaker than it would be from a stationary plasma. Vial et al. (2016) observed a polar crown prominence with the Mg II h and k lines from *IRIS*, finding that it displayed velocities on the order of 10 km s^{-1} , and compared their observations to the model of Heinzel et al. (2014). Analysis presented in Levens et al. (2016a, and in Chapters 3 and 4) showed tornado-like prominence legs as observed by *IRIS*. That observation is covered in detail in this thesis, from §3.3.2 onwards. Recent work by Schmieder et al. (2017a) used *IRIS* and *Hinode/SOT* observations to measure the real trajectories of plasma ‘blobs’ in a prominence. That analysis showed that the plasma was following horizontal paths, tracing the magnetic field, despite the projection in the plane of sky suggesting that the plasma was flowing along a curved path. High plasma velocities were again found by Schmieder et al. (2017a), up to 65 km s^{-1} .

The sheer quantity of modern prominence observations, and the wealth of information available through them, means that our understanding of solar prominences is constantly improving. The plasma conditions in prominences is well studied, but questions remain open as each new observation that improves understanding also raises new questions about the nature of the plasma in prominences. This will be discussed further in §1.2.4. Magnetic fields play an extremely important role in

Table 1.1: The five main prominence classifications defined by [Pettit \(1932\)](#). Descriptions are quoted directly from that paper.

Class	Name	Description
I	Active	“appear to be torn apart by an area of attraction or by a neighboring sun-spot”
II	Eruptive	“ascend in a more or less vertical direction”
III	Spot	“often have the appearance of closed loops of a fountain or of spikes with external wings”
IV	Tornado	“appear like vertical spirals or tightly twisted ropes”
V	Quiescent	“show only minor changes from minute to minute”

prominence physics, and alongside the development in interpretation of observed prominence plasma (outlined here) has come improvements in the understanding of prominence magnetic fields – these will be discussed in §1.2.5.

1.2.3 Prominence types

The classification of prominences into different types has been attempted for nearly as long as prominences have been studied in any detail. [Secchi \(1875, 1877\)](#) began dividing prominences into different types, with two main categories of ‘quiescent’ and ‘eruptive’ (or active) prominences ([Young 1896](#)). Further sub-categories were specified based on observed morphology – clouds, cyclones, filaments, flames, horns, jets, plumes, sheafs, spikes, and stems ([Young 1896](#); [Tandberg-Hanssen 1974](#)) were all descriptive names used for different prominence appearances. Edison Pettit was responsible for some of the most well known prominence classifications throughout the twentieth century ([Pettit 1932, 1936, 1943a](#)). [Pettit](#) defined five classes for the forms of prominences – I) *active* prominences, II) *eruptive* prominences, III) *spot* prominences, IV) *tornado* prominences, and V) *quiescent* prominences. The original descriptions of these five prominence types from [Pettit \(1932\)](#) are given in Table 1.1. It was also noted that the first two classes, active and eruptive, were closely linked and often prominences of either class would display aspects of the other. Subsequently, with more refinement, [Pettit \(1943a\)](#) designated a larger range of sub-classes under each main prominence class, giving a meticulously detailed

account of the observational features of each sub-class. The classifications by [Pettit](#) were by no means exhaustive, and as observing techniques advanced so too did the classifications of prominences (see e.g. [Tandberg-Hanssen 1974](#)). Generally, however, the two main prominence types remain relatively unchanged – quiescent and active – though sub-classes show a large variation depending on the observation/author. [Newton \(1934\)](#) identified the same two main classes in filaments on disc, with [Newton's class I](#) filament defined exactly as [Pettit's class V](#) prominence (quiescent), and the other four prominence classes coming under *class II* in [Newton's](#) designation.

Many of [Pettit's](#) classifications are still used to describe prominences, although some are used less frequently than others. A few of the more modern sub-classes of quiescent prominence, as outlined in [Tandberg-Hanssen \(1974\)](#), are worth noting as they are still in common use today. So-called 'hedgerow' prominences are large, sheet-like quiescent prominences that show a large amount of fine structure, with apparent internal horizontal and vertical motions in the plane of the sky. 'Polar crown' prominences are those that are at extreme northerly or southerly latitudes, usually within $\pm 30^\circ$ of the solar poles, and being so far from the active-region belt they are always quiescent. It is worth emphasising that each prominence is unique, and the observed morphology can be different depending on the instrument used and wavelength observed. The classes and sub-classes outlined here are therefore generalisations and mostly refer to H- α prominences/filaments, but they are still extremely useful for describing each prominence in context.

1.2.4 Plasma conditions

Prominences consist of cool, dense plasma, with $T \sim 6000$ K, suspended in a hot, diffuse surrounding, which has $T \gtrsim 10^6$ K, with some transition region (PCTR) between them. The general plasma conditions are still not precisely defined, as each prominence is different, but many studies have measured values for prominence temperatures, gas pressures, and electron/ion densities, as described in §1.2.2. [Table 1.2](#) shows approximate plasma parameters for the cool 'core' region and the PCTR. This table and the values in it have been adapted from [table 1](#) of [Labrosse et al. \(2010\)](#), where those authors adapted it from [Engvold et al. \(1990\)](#). The values listed in [Table 1.2](#) come from pre-1990 measurements, which came before the results from *SOHO*, *TRACE*, *Hinode*, *IRIS*, and other instruments described in §1.2.2. Comparing

Table 1.2: Usual prominence parameters for the cool core region and the PCTR. Table adapted from Labrosse et al. (2010), where values are from pre-1990 measurements from Engvold et al. (1990). Parameters are: T = Temperature, v_T = microturbulent velocity, n_e = electron density, P = gas pressure, $N(\text{H}^+)/N(\text{H}^0)$ = hydrogen ionisation ratio, V = flow velocities.

Parameter (units)	Core	PCTR
T (K)	$4.3 \times 10^3 - 10^4$	$10^4 - 10^6$
v_T (km s^{-1})	3 – 20	30
n_e (cm^{-3})	$10^9 - 10^{11}$	$10^6 - 10^8$
P (dyne cm^{-2})	$\sim 0.02 - 1$	~ 0.2
$N(\text{H}^+)/N(\text{H}^0)$	0.2 – 0.9	
V (km s^{-1})	~ 5	~ 10

with more recent results, however, reveals that the values from Table 1.2 are still approximately correct, and provide good ball-park estimates for the expected physical parameters in a prominence. It is expected that the cool core of the prominence has temperatures from $4.3 \times 10^3 - 10^4$ K, or roughly that of the photosphere to that of the chromosphere, with the PCTR having a temperature range similar to that of the solar transition region up to around 10^6 K at the corona. Electron densities follow a similar pattern to the temperatures, analogous to the changes seen between layers of the solar atmosphere. Gas pressure and ionisation fraction are found to have a large range of possible values, which are dependent on the observation. The two velocities listed in Table 1.2 have different physical interpretations – microturbulent velocity (v_T) is a parameter that describes random, small-scale, unresolved motions within the plasma that is often invoked in prominence modelling, which has the effect of broadening the emergent spectral lines, whereas the flow velocity (V) describes the observable bulk motions seen in prominences.

The internal structure of the plasma in prominences is not precisely known. At low resolution, prominences appear to be sheet-like and relatively uniform, with thicknesses of around 2000 – 5000 km. However, with the advent of higher resolution imaging and spectroscopy it became clear that prominences had a much more complex structure. Prominences are now observed to have extremely fine structures, being made up of numerous thin threads, with individual threads of plasma hav-

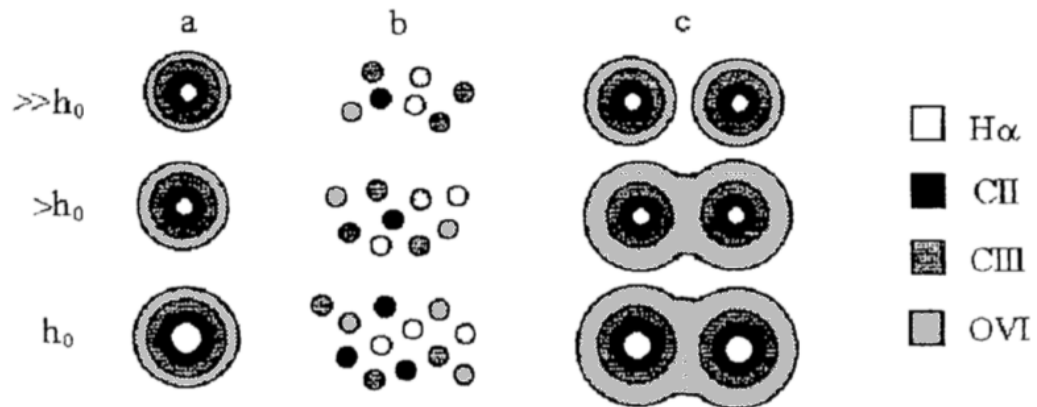


Figure 1.6: Three possible arrangements of prominence fine-structure threads, showing possible cross-sections of threads with regions of different temperature. The models are: (a) Cold cores surrounded by progressively hotter PCTR sheaths, (b) isothermal threads each with a different temperature, (c) cold cores and progressively hotter sheaths, with the hottest layers enveloping several threads. Model behaviour is shown at three different heights above the photosphere (h_0). Figure adapted from Pojoga (1994).

ing scales that are smaller than the highest resolution imagery currently possible ($\sim 100 - 150$ km). Several suggestions have been made to describe the temperature structure across a prominence consisting of multiple threads, which are nicely described by Pojoga (1994). Three scenarios for the relationship between the cool core plasma and the hotter PCTR plasma are shown in figure 4 of Pojoga (1994), which is recreated here as Figure 1.6. This diagram shows cross-sections of individual threads, and the thread length is not specified. In that paper Pojoga used *Skylab* ATM data in the $H\alpha$, $C II$, $C III$, and $O VI$ lines, which are each formed at increasingly large temperatures, from the cool core ($H\alpha$) to the outer part of the PCTR ($O VI$). Due to the intensity and temperature structures seen in the prominence at this range of temperatures, Pojoga was able to infer the three possible thread arrangements at different heights above the photosphere (h_0) that are shown in Figure 1.6. The three model thread arrangements can be summarised as follows: (a) Individual cool cores surrounded by successively hotter sheaths, (b) many isothermal threads, each with a

different temperature, (c) cool cores and progressively hotter sheaths and a hot envelope, similar to (a) but with the hottest layers enveloping several threads. The results of [Gunár et al. \(2007\)](#) suggest that the arrangements (a) and (c) are more likely than (b). [Gunár et al.](#) replicated the observed profiles of the first seven lines in the Lyman series of hydrogen in a quiescent prominence by using a 2D multi-thread model, which included a PCTR similar to model (a) of [Pojoga \(1994\)](#). The success of the models investigated by [Gunár et al. \(2007\)](#) points to the integrity of the multi-thread with PCTR model of prominence fine structure. [Gunár et al. \(2008\)](#) went further to this to show that asymmetries in the observed Lyman lines could be explained by the inclusion of random, small ($\lesssim 10 \text{ km s}^{-1}$) line-of-sight velocities to each thread in the prominence model.

The plasma in prominences can be well modelled by multiple thin threads, each with a PCTR, which create the overall observed prominence structure when viewed together as an ensemble. This represents the most likely model for most prominence types. There is, however, still value in investigating simple 1D slab models of prominences, as complex 2D multi-thread models like those by [Gunár et al. \(2008\)](#) are much more computationally intensive.

1.2.5 Magnetic fields

Possibly the most important aspect of solar prominences is the magnetic field supporting the plasma in the solar atmosphere – without the magnetic field there would be no prominences at all. It was found by [Babcock & Babcock \(1955\)](#) that prominences and filaments form above *polarity inversion lines* (PIL), where two regions of opposite magnetic field polarity border one another. In those regions the magnetic field arches between areas with positive and negative magnetic field direction (here ‘positive’ and ‘negative’ are relative terms that define the direction that the field is pointing, either outward from or inward to the solar surface). The PIL could be in a region of strong magnetic flux and surface field strengths exceeding 1000 G (an active region), or one of weak magnetic fields where the field strength is less than 1 G. Above a PIL the magnetic loops can become sheared due to photospheric motions, and it is in these sheared magnetic loops that prominences usually form. The main thing that is required for prominence formation is the presence of a magnetic field above a PIL.

An essential part of the support of prominence plasma in the magnetic field against gravity is the presence of magnetic ‘dips’ in the field (Aulanier & Demoulin 1998; Heinzel & Anzer 1999). These dips have been modelled as dips in the horizontal, sheared arcade field, or as part of a twisted *flux rope* – a spiral-shaped field that naturally has dips along its lower edge. Both models have been well explored in terms of prominence stability and formation (described in detail in Mackay et al. 2010). The main difference between the models in terms of plasma support is the origin of the magnetic field dips. In the flux rope model the dips appear naturally due to the twist of the magnetic field, whereas dips in the horizontal field model must be caused by either the weight of the plasma itself (Mackay et al. 2010) or through some other source such as a *parasitic polarity* at the solar surface (Aulanier & Demoulin 1998; Aulanier et al. 1998).

An important concept that should be introduced is the *plasma β* . Plasma interacts with magnetic fields, but the way in which they interact depends on the plasma β , which is defined as the ratio of gas pressure, P_{gas} , to magnetic pressure, P_{mag} . The plasma β describes whether the plasma is *gas dominated* (*high β , $P_{\text{gas}} > P_{\text{mag}}$*) or *magnetically dominated* (*low β , $P_{\text{gas}} < P_{\text{mag}}$*) – if the plasma is gas dominated then plasma motions can move the magnetic fields around, whereas if the plasma is magnetically dominated then the plasma flows along the field without perturbing it. The solar photosphere is an example of a high β plasma, where the motion of the convective cells can perturb the magnetic field. In the solar corona (and to some extent in prominences) the plasma density is lower, so generally β is low and the plasma follows the magnetic field.

With a magnetic field that is capable of supporting plasma, the question then arises about how the cool plasma comes to be suspended in the field at all. It has been known for some time that the prominence plasma cannot come directly from condensation of coronal plasma, because there is simply not enough plasma in the corona to account for the observed masses of prominences (Pikel’Ner 1971; Saito & Tandberg-Hanssen 1973; Zirker et al. 1994). The plasma must therefore come from below, from the chromosphere. A number of models for plasma injection into prominence magnetic fields have been suggested, which can be sorted into three categories: plasma injection models, levitation models, and evaporation/condensation models (Mackay et al. 2010). These models rely on different forces to lift the chromospheric plasma into the corona, either through magnetic forces directly lifting cool plasma

upwards (injection and levitation models), or through thermal pressure forces where heating and then cooling cause evaporation of chromospheric plasma which then condensates into the magnetic dips. The three models are shown in Figure 1.7 (from [Mackay et al. 2010](#)) and can be summarised as follows:

Injection: Photospheric/chromospheric material is injected to the prominence loops with high speeds at regions of flux cancellation or reconnection near the loop footpoints. The material enters the corona due to magnetic forces at (or near) its original temperature. Figure 1.7 (*top panel*) shows the plasma transport in the magnetic field for the injection model. The prominence plasma is shown in purple at the loop centre, and the injected plasma (and direction of motion) are shown in purple near the footpoint. The black lines show the prominence magnetic field, and the blue lines on the right indicate the low-lying loops where the reconnection/injection event occurs.

Levitation: Photospheric/chromospheric material is raised at the centre of the loops from the PIL region by rising magnetic fields (Figure 1.7, *middle panel*). Mass motion is slow and the mass emerges directly into the centre of the loop, it does not need to travel the length of the loop. Plasma enters the loop at its original temperature.

Evaporation/condensation: Chromospheric material at the footpoint of the prominence loop is heated (shown in red in Figure 1.7, *bottom panel*), causing the plasma to expand and evaporate along the magnetic loops (red arrows, Figure 1.7 *bottom panel*). Near the top of the loops the plasma cools and condensates into the dipped regions of the magnetic field.

Each of these models is capable of describing some observed features of prominences, but no individual model can fully explain the range of prominence types that are seen ([Mackay et al. 2010](#)).

Measuring the magnetic field in a prominence above or near the limb cannot be done in relation to the solar surface magnetic field, as the surface field cannot be seen due to the projection effect. Luckily, prominence fields can be measured in other ways. Light that is emitted in a magnetic field can be affected by the presence of that field in measurable ways – the magnetic field can create and alter polarisation of certain spectral lines by the *Zeeman* and *Hanle* effects (e.g. [López Ariste & Casini 2002](#)). The *Zeeman effect* causes the splitting of the energy levels of an atom or ion in a magnetic field, which results in the splitting of an observed spectral line into multiple components. This effect is especially noticeable in sunspots on the solar disc,

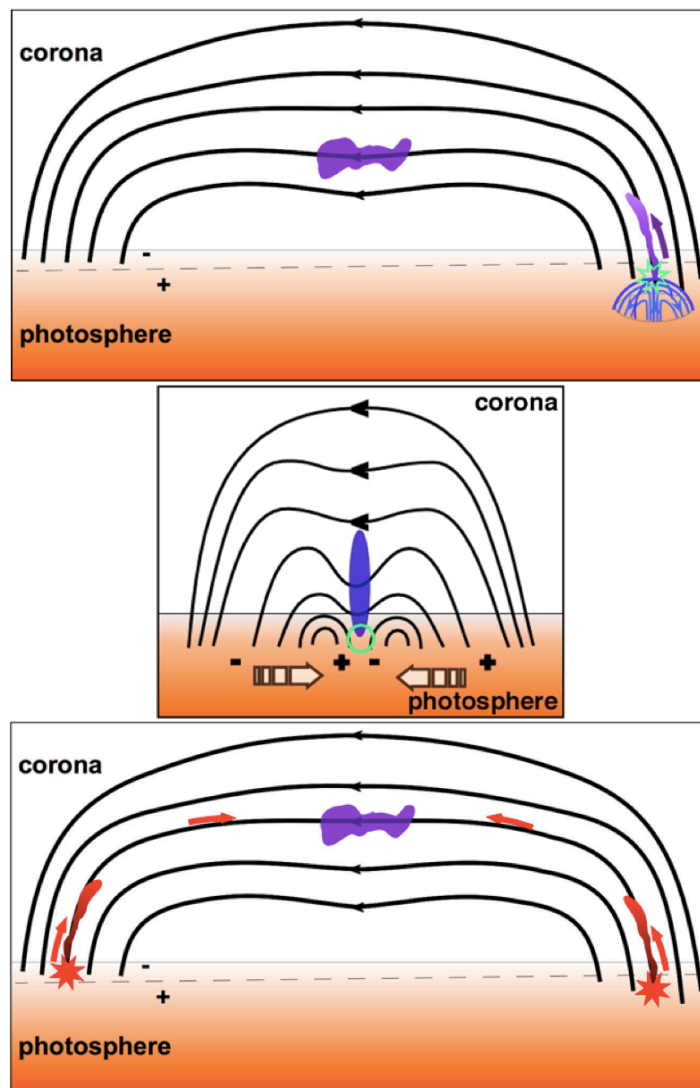


Figure 1.7: Models for the injection of cool plasma into the prominence magnetic field. Prominence magnetic field loops are shown in black, and prominence plasma is shown in purple at the loop centre. *Top:* Injection model. Reconnection near the footpoints (blue magnetic fields) launches cool plasma (shown in purple) into the loop tops. *Middle:* Levitation model. Cool plasma is raised into the loop tops by motion of the magnetic field. *Bottom:* Evaporation/condensation model. Heating of plasma at the loop footpoints causes evaporation into the loops (heated plasma shown in red). Figures taken from [Mackay et al. \(2010\)](#).

where strong magnetic fields can split a spectral line into at least three components, and the distance between the peaks depends on the strength of the field. Magnetic

fields in prominences are generally not strong enough to see this splitting, but the Zeeman effect can also create polarisation in some lines. The *Hanle effect* also has an effect on the polarisation of light emitted in a magnetic field. Although the Hanle effect does not create polarisation, it can have an effect on already polarised light. These polarisation effects can be measured in spectral lines from prominences (López Ariste & Casini 2002; Casini et al. 2003).

Polarisation of light is measurable through the *Stokes parameters*. The four Stokes parameters, called I , Q , U , and V , together describe the polarisation state of the observed light. The first, I , is the total intensity of the line, and Q , U , and V describe the polarisation, both linear and circular polarisation. Polarimetry can be done using a number of spectral lines that emit strongly in prominences, including H- α and the He I 5876 Å (D_3) and 10830 Å lines. In early attempts, Tandberg-Hanssen (1970) was able to measure the magnetic field strength in 135 quiescent prominences using the Zeeman effect in optical lines, finding an average field strength of between 3–8 G. The Stokes parameters and the effects of polarisation are still used to measure magnetic fields in prominences, although it has been found that it is important to account for the Hanle effect as well as the Zeeman effect (López Ariste & Casini 2002). Modern measurements using both Hanle and Zeeman effects have been able to reconstruct the magnetic field orientation as well as providing ever more accurate calculations of the field strength in prominences (López Ariste & Casini 2002, 2003; Casini et al. 2003; López Ariste 2015). These calculations find magnetic field strengths generally of around 10 G in quiescent prominences, a similar order as in previous estimates (Tandberg-Hanssen 1970), but it has also been shown that prominence fields can exceed 50 G in some regions, even in quiescent prominences (Levens et al. 2016b). Techniques for polarimetry in prominences continue to improve (López Ariste 2015), and as they do the measurement of prominence magnetic fields become increasingly more accurate.

1.2.6 Neutral atom support

It is common to discuss prominence plasma, as a portion of the atoms in a prominence are in the ionised state, and it is natural that the plasma can be supported by the magnetic field. However a significant fraction of the prominence material is in the neutral state, as can be seen from the emission of spectral lines of neutral hydrogen

and helium. These neutrals are not affected by the magnetic field, so the question therefore arises on how they are suspended in the solar atmosphere and do not simply drain downwards due to gravity. The answer comes in the combination of two atomic interactions. The first is friction, where downward moving neutrals collide with the magnetically trapped ions and are slowed in their descent (Mercier & Heyvaerts 1977; Gilbert et al. 2002). Gilbert et al. (2002) calculated that this effect alone could support neutral hydrogen against gravity for around 22 days. The second effect is one called *charge exchange*, where energetic hydrogen ions can capture electrons from hydrogen atoms. This process has been explored in the chromosphere (Leake et al. 2013), so it is natural to consider that the same applies in the case of prominences.

Terradas et al. (2015) brought together these two effects in a single model, finding that frictional forces reduced the downward velocity of the neutrals to around 2 m s^{-1} . The charge exchange interactions were found to reduce this velocity by a further four times, so the overall effect is a stable prominence that is essentially static in the solar atmosphere.

1.3 Solar “Tornadoes”

This thesis is primarily concerned with tornado-like prominences, or simply solar ‘tornadoes’ as they are often known. The term has been used to describe prominence types for a long time, in fact ‘tornado’ was one of the original prominence classifications used by Pettit (1932). Recently, however, with the renewed interest in tornadoes there has been some confusion surrounding the term, and that is what this section aims to discuss.

Prominences with a spiral structure, somewhat resembling a terrestrial tornado, were first shown by Secchi (1877) under the title “Flammes.” Secchi describes that the ‘flammes’ have a spiralling motion, which is only visible in projection when they are viewed above the solar limb. This description can claim to be one of the first reports of spiralling, tornado-like motions in a prominence, but it was not until later that the word ‘tornado’ was used for these types of prominence. That name was coined by Edison Pettit (1889 – 1962), who dedicated a large amount of time to studying and categorising all prominence types.

Described by Pettit (1932) as appearing “like vertical spirals or tightly twisted rope,” the earliest identifications of tornado-like prominences were in the bright H- α

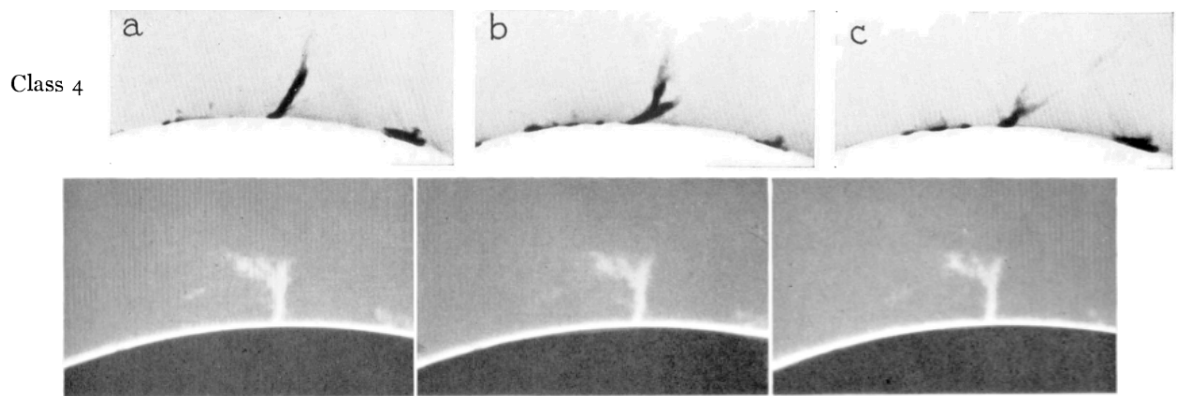


Figure 1.8: Examples of the ‘tornado’ class of prominence (*Class IV*), as defined by Pettit (1932), observed in H- α . *Top:* Observations from 5 July 1928 from Pettit (1932). These images are in negative intensity. Panels *a*, *b*, and *c* were photographed approximately 5 minutes apart. *Bottom:* Observations from 19 September 1941 from Pettit (1943a). Photographs were taken at 15 minute intervals.

emission line. The first photographs of tornadoes were presented by Pettit (1925), where observations of tornado prominences in 1910 and 1919 were shown. They were described in that paper as being “difficult to photograph,” but Pettit persevered and managed to capture images of many more tornado prominences. Figure 1.8 (*top panels*) show an example from Pettit (1932) of the tornado prominence class (*Class IV*), photographed at three times at ~ 5 minute intervals, from an observation on 5 July 1928. The bottom panels of Figure 1.8 show a later example from 19 September 1941 (Pettit 1943a), with 15 minutes between each photograph. Spiralling motions were noted a number of years earlier by the same author (Pettit 1919) with regards to an erupting prominence, where he noted that the prominence “began to show a spiral structure, as if the whole body were twisted into a giant spring” – behaviour that continued until the prominence erupted entirely. This earlier report of twisted structure appears different to the ‘tornado’ classification, which is only used to describe vertical columns of quiescent prominences. The tornado classification was further refined in Pettit (1943a), where two sub-classes were identified – ‘columnar’ tornadoes and ‘skeleton’ tornadoes (Figure 1.9). Columnar tornadoes were described as being dense, twisted columns that resembled “closely wound springs or fine-threaded screws.” Skeleton tornadoes, on the other hand, were much less tightly wound, where Pettit described them as “individual twisting streamers, which give

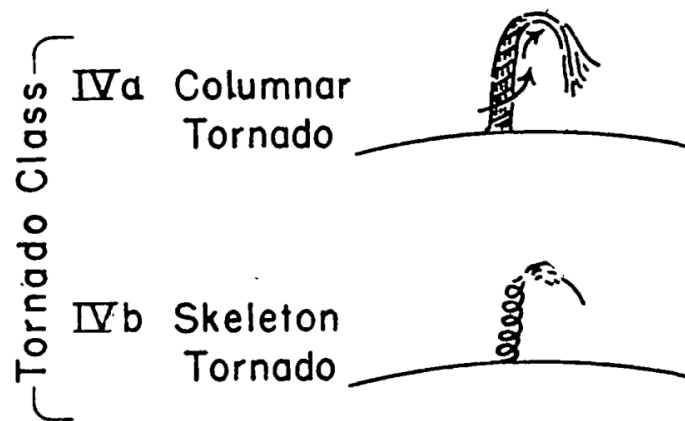


Figure 1.9: Sketches of the two tornado sub-classes, extract from figure 1 in [Pettit \(1943a\)](#). The top sketch is of a ‘columnar’ tornado, and the bottom is of a ‘skeleton’ tornado.

them the appearance of a crossed latticework.” In both cases, [Pettit](#) believed that they were rotating columns, calling them a “vortex,” and that they would dissipate if the rotational velocity became too large. It was also estimated, by using a series of images, that one tornado prominence had a rotational velocity of 54 km s^{-1} ([Pettit 1941](#)). In 1945 [Pettit \(1946\)](#) was able to observe the spectrum of a group of tornadoes using a spectroheliograph, measuring the Doppler shift of the H- α line. From that study [Pettit](#) found that each tornado column had redshift down one side, and blueshift down the other, indicating rotational motion, and he determined that each of the tornadoes was rotating with velocities of $2\text{--}4 \text{ km s}^{-1}$, much smaller than the 54 km s^{-1} he had previously estimated from images alone. In [Pettit \(1946\)](#) it is argued that the earlier tornado was much more active than the latter ones, eventually erupting, so this was the reason the calculated velocities were so much higher. Other observers reported on tornado prominences in the 1940s, with [Richardson \(1940\)](#) noting a “tornado prominence of record height” which had an impressive height of 240 Mm ($\sim 0.3R_{\odot}$), and [Nicholson \(1944\)](#) reporting an erupting tornado prominence. The observations of tornado prominences up to 1950 were well described in [Pettit \(1950\)](#), which was [Pettit](#)’s final publication on the topic. He concluded with a summary on what was known about tornado prominences up to that point, which are again summarised as the following: 1) Tornadoes had been observed using imaging and

spectroscopic techniques. 2) Some tornadoes show signs of activity, with plasma streaming from their tops back to the chromosphere. 3) They are anchored at the solar surface, unmoving in solar latitude. 4) They rotate around a central axis, and this rotation has been observed both spectroscopically and using image series. 5) They disappear when their rotational velocity becomes too large or when they erupt.

After Pettit (1950) tornado prominences were largely forgotten about for a long time. There were some reports in the 1960s of rotational motions in filaments (Öhman 1969), but these were not the same as the tornadoes described by Pettit. An observation of an eruptive prominence in 1990 at the Yunnan Observatory in China prompted some discussion of tornado-like motions (Zhong & Li 1994; Li & Zhong 1997), but this erupting prominence was not the same as the more quiescent tornado prominences that were discussed earlier. The term ‘tornado’ was used by Pike & Mason (1998) to describe rotational motions in so-called *macrospicules* observed by *SOHO*, but these did not bear any relationship to a prominence.

With the launch of the *Solar Dynamics Observatory* and its high-resolution imager, AIA, in 2010, authors became interested in tornadoes in relation to prominences again. In 2012 three letters were published that reported tornado-like motions in prominences (Li et al. 2012; Su et al. 2012; Orozco Suárez et al. 2012). Li et al. (2012) reported a helical structure in the top part of a prominence observed by AIA, which consisted of a bright prominence set within a dark cavity when viewed in coronal filters, where the prominence was bright in the AIA coronal wavebands (indicating heating) and appeared to have some horizontal vorticity. This event was also studied by Panesar et al. (2013), who noted that the activity in this prominence could have been caused by a nearby flaring region. The ‘tornado’ reported in these papers was different in structure to those classified by Pettit, however, with a horizontal cyclonic component (parallel to the solar surface) as opposed to a vertical one (perpendicular to the solar surface). Su et al. (2012) presented an observation that was more similar to the original classification of a tornado prominence. In that paper they observed a number of column-like features in a quiescent prominence that appeared dark in coronal emission filters from AIA, and found that they could be directly related to bright emission seen in H- α and Ca II. These tornadoes appeared as funnels, or columns of cool material which were wider at their tops than at their bases, and they were extremely dynamic, evolving quickly as they crossed the limb. Figure 1.10 shows figure 1 from Su et al. (2012), which shows a multi-wavelength view of the

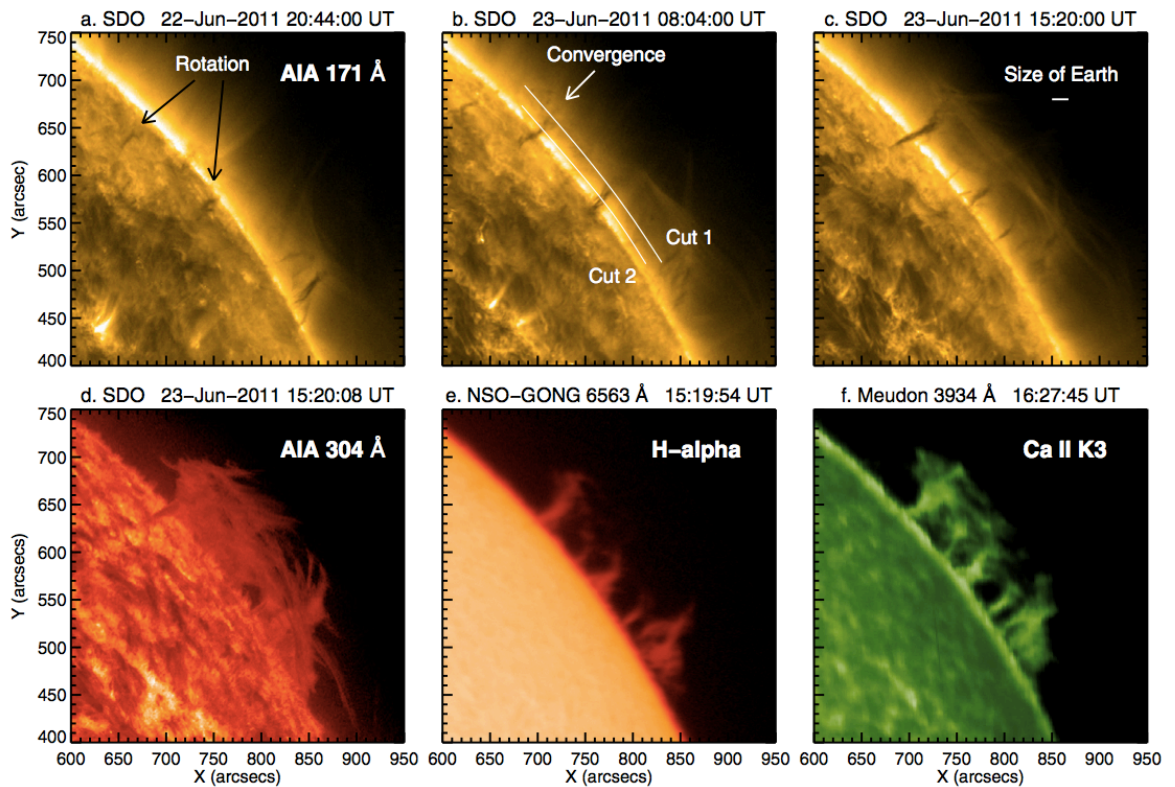


Figure 1.10: A multi-wavelength view of a group of solar prominences, taken from [Su et al. \(2012\)](#). Panels (a), (b), and (c) show *SDO/AIA* 171 Å images at three times as the tornadoes crossed the limb. Panels (d), (e), and (f) show the corresponding images in He II 304 Å (AIA), H- α (NSO), and Ca II K3 (Meudon) respectively.

group of tornadoes observed in 2010. The analysis of [Su et al. \(2012\)](#) consisted of creating time-distance diagrams by taking cuts through the tornado column, where they found oscillatory motions which they interpreted as rotation. They suggested that the magnetic field was in a twisted (or twisting) helical configuration, where plasma flowed along the field lines, giving the appearance of rotation. These features and similar analysis have been reported a number of times since then ([Orozco Suárez et al. 2012](#); [Wedemeyer et al. 2013a](#); [Su et al. 2014](#); [Levens et al. 2015](#); [Mghebrishvili et al. 2015](#); [Levens et al. 2016a](#)). AIA tornadoes like those reported by [Su et al. \(2012\)](#) were also observed by [Orozco Suárez et al. \(2012\)](#), with coordination from the *Vacuum Tower Telescope* (VTT) in Tenerife. The VTT can observe optical and near-infrared spectra, such as the He I 10830 Å line that was used by [Orozco Suárez et al. \(2012\)](#). Using that spectral line [Orozco Suárez et al.](#) were able to calculate

Doppler shifts and derived a velocity pattern in a tornado-like prominence, with velocities on the order of $\pm 3 \text{ km s}^{-1}$. The Doppler velocity pattern showed redshifts down one side of the tornado, and blueshifts down the other, indicative of rotation around a central axis, similar to that found by Pettit (1946). Wedemeyer et al. (2013a) showed tornadoes observed by AIA and the *Swedish Solar Telescope* (SST) in La Palma, calling them “giant tornadoes” and identifying them as the legs of prominences. They showed that tornadoes appeared to be rotating by using a Doppler study of the H- α line from SST, similar to Orozco Suárez et al. (2012).

To avoid confusion, it is worth noting other observations of ‘tornadoes’ in recent literature that do not relate to prominences. Wedemeyer-Böhm et al. (2012) reported on *magnetic tornadoes* which appeared on disc as apparent swirling motions in the photosphere and chromosphere, but are not related to any filamentary structure. That work was continued in Wedemeyer et al. (2013b), where these *chromospheric swirls* were characterised and classified. These features appear to be more akin to the ‘tornado’ observed by Pike & Mason (1998) – chromospheric features that are unrelated to prominences. It is therefore worth clarifying that these ‘magnetic tornadoes’ are not what are referred to by the name *tornado* in this thesis, instead the ‘giant tornadoes’ of Wedemeyer et al. (2013a) or more generally ‘solar tornadoes’ (Li et al. 2012; Su et al. 2012; Orozco Suárez et al. 2012) in relation to prominences are the topic of discussion here.

With the re-discovery and recent reports of solar tornadoes, questions were raised about the nature of the magnetic field in these structures, and on how the plasma could be supported against gravity in a tornado. Since the time of Pettit a great deal of work has been done on understanding the magnetic field structure in prominences (see §1.2.5). In nearly all cases the field was found to be horizontal, and the prominence plasma is often believed to be contained in dips in the field. The idea, then, of a vertical, twisted magnetic field outlined by Su et al. (2012) does not match the known prominence magnetic field structure. Panasenco et al. (2014) raised many counter-points to the observations of tornadoes with AIA (Li et al. 2012; Su et al. 2012; Orozco Suárez et al. 2012), arguing against the rotational tornado model and instead that the observations can be accounted for by oscillations and counter-flows in the more traditional horizontal, dipped magnetic field. Firstly, and correctly, Panasenco et al. (2014) make a distinction between the tornadoes of Li et al. and Su et al. – morphologically they are different and the reported rotation is in a different

plane. [Panasenco et al.](#) then show an observation from TRACE that indicates that tornado-like features of prominences (of the [Su et al.](#) variety) correspond directly to filament barbs when viewed on disc. Further analysis of a tornado from AIA showed that the sinusoidal motion found in the time-distance diagrams can easily be explained by oscillation and counter-streaming of prominence plasma in a horizontal magnetic field. [Panasenco et al. \(2014\)](#) state that the observed ‘rotation’ in AIA is simply an optical illusion created by the projection of these oscillations onto the plane of the sky, and that the Doppler pattern reported by [Orozco Suárez et al. \(2012\)](#) was a misinterpretation of counter-streaming flows. The tornado of [Li et al. \(2012\)](#) was explained by [Panasenco et al. \(2014\)](#) as the motion of plasma along a writhed magnetic field, viewed in projection. The debate surrounding tornadoes has shown the importance of spectroscopic observations, and coordinated observations, of tornadoes in order to more fully understand their characteristics.

In a dedicated study using EIS, [Su et al. \(2014\)](#) observed a tornado in a *raster* – an extended spectral view of a source made by taking exposures at successive slit positions – and a sit-and-stare study, finding that the tornado had a split Doppler pattern at temperatures above 1.5 MK, similar in pattern to those found at low temperatures by [Orozco Suárez et al. \(2012\)](#) and [Wedemeyer et al. \(2013a\)](#). It was again suggested by [Su et al. \(2014\)](#) that tornadoes have a twisted magnetic structure. A model by [Luna et al. \(2015\)](#) attempted to create a scenario where prominence plasma could be supported in a twisted magnetic field like the one suggested by [Su et al. \(2014\)](#). Due to the nature of the twisting of the field, their magnetic structure was vertical at the core of the tornado, becoming more twisted and horizontal further from the central axis. In this model it was found that cool plasma could be supported against gravity in a tornado-like magnetic structure, but the magnetic field would need to be extremely twisted in order to do so. The temperature range that the split Doppler pattern was seen at in the EIS observation of [Su et al. \(2014\)](#) was extended to ~ 1 MK in [Levens et al. \(2015\)](#), which is described in detail in Chapter 3. A coordinated observation of two tornadoes using *Hinode*, *IRIS*, and the *Télescope Héliographique pour l’Etude du Magnétisme et des Instabilités Solaires* (THEMIS) is presented in [Levens et al. \(2016a\)](#), which is also described in Chapters 3 and 4. These observations included measurements of the magnetic field in tornadoes using THEMIS. It was found that the magnetic field is predominantly horizontal, with some turbulent component. This suggests that tornadoes do not consist of a vertical

twisted magnetic fields, but are instead in the horizontal (dipped) magnetic field. Many tornado observations from THEMIS provide consistent results with this picture (Levens et al. 2016b). Martínez González et al. (2016) used the VTT to measure the magnetic field in tornadoes, however their results on the orientation of the magnetic field were inconclusive, finding that it seemed to change over time, going from horizontal to vertical. In a recent paper, Schmieder et al. (2017b) showed that Doppler patterns that are apparently indicative of tornadoes do not always show the true evolution of the plasma velocity. Using the Meudon Solar Tower, Schmieder et al. (2017b) show Doppler measurements of a tornado in the H- α line, which at certain times, in certain snapshots, appears to give the impression of a split Doppler pattern. However, upon examining the Doppler pattern at different times the tornado pattern is not visible, and the evolution seen suggests slow oscillation rather than rotation.

Regardless of the actual physical nature of solar tornadoes, if they are rotating or not, it is important to have an easy way to identify them visually. In this thesis the method of Su et al. (2012) is used – AIA images and movies of dark columns in coronal wavebands, which exhibit sinusoidal, oscillating motions over time. By selecting this as an identifier for tornadoes, and tracing them back as filaments on disc, it is possible to learn about their on-disc behaviour and then target them with coordinated observing campaigns.

This chapter has given an introduction to the Sun, the phenomenon of solar prominences, and the history of observed ‘tornadoes’ in prominences. Chapter 2 gives a detailed introduction to many of the observations of, and diagnostics available from, solar data (specifically for prominences). It also gives an introduction to the main science instruments that are relevant to the analysis done in later chapters. Following that are the three main research chapters of this thesis. Chapter 3 introduces plasma diagnostics of prominence observations from 2013 and 2014 using space-based observatories and a brief comparison to current prominence models. Chapter 4 investigates the prominence magnetic field for one of these dates using a ground-based telescope, and compares the magnetic field to the observed plasma parameters. Chapter 5 then goes on to introduce an updated prominence model to try and account for recent observations, and compares the resulting models with

previous ones. The final chapter, Chapter 6, contains a summary of this thesis and concluding remarks on the work in it.

Chapter 2

Observations and diagnostics

Astronomy is not a ‘typical’ physical science, in a sense. We have no laboratory to take measurements in, where we can carefully control our experiment and change parameters as we please, because the objects we study are typically millions, if not billions, of miles away. Luckily many of the objects that astronomers study are extremely bright, and can be seen at Earth. The Sun is a perfect example of this. To be bright is to emit a lot of light, and not just visible light that can be seen with the naked eye – we have the entire electromagnetic spectrum available to us, and an impressive range of specially designed instruments to study it with. To study astronomy is therefore to study light in all its forms, and it is through this electromagnetic radiation that we get most of our information about the universe.

There is a great deal that can be learnt about the physical conditions in solar prominences by studying their spectra. This chapter aims to introduce spectral line emission and what they can tell us about the plasma that is emitting them, as well as techniques that can be used for analysing the observed spectral profiles. It is also important to introduce some of the instruments that are used to observe solar spectra, both from the ground and from above the Earth’s atmosphere – these are discussed in §2.4.

2.1 Spectral lines

As was described in Chapter 1, the Sun as a whole radiates as a blackbody, with a continuum spectrum and a great number of spectral lines on top of it that are emitted or absorbed by different atoms, ions, and molecules at/above the solar surface.

Prominences, formed of cool plasma that is suspended in the solar atmosphere, also emit and absorb light in ways that are detectable at the Earth. The emission of spectral lines takes place when an electron transitions from one energy state to another in an atom or ion, emitting a photon of the appropriate energy. Several physical processes can cause these transitions, and depending on the plasma conditions at the source there could be a combination of emission processes happening simultaneously.

Solar prominences, as viewed above the solar limb, are generally seen brightly in emission (against the dark background corona) when viewed in lines formed at photospheric, chromospheric or transition region temperatures. This plasma, colder than the ambient coronal plasma, can be seen absorbing coronal emission at EUV wavelengths. The emission of specific spectral lines is closely linked with the temperature of the plasma, or rather the formation of different ions depends on the temperature of the plasma, and each ion has a unique set of spectral lines associated with it. Therefore we can associate a temperature with each spectral line that we see, based on the formation temperature of the ions in the plasma. In reality, an atom can be in a specific ionisation state over a range of temperatures, before being further ionised or undergoing recombination with a free electron.

Plasma emission occurs when an electron undergoes de-excitation from one energy state to another in an atom or ion. The difference in energy, E , between the two levels determines the wavelength, λ , of the emitted photon, and hence the wavelength of the observed spectral line, by Equation 2.1.

$$E = \frac{hc}{\lambda} \quad (2.1)$$

The constants h and c are the Planck constant and the speed of light, respectively. The emission of spectral lines from any given ion is dependent on the balance between ionisation and recombination – the fraction of each determines the amount of emitting plasma in each ionisation stage. This then helps to determine how bright each spectral line is. It is generally assumed that the rates of ionisation and recombination are constant and equal, i.e. that a plasma is usually in ionisation equilibrium. This means that the fraction of a plasma that is at a given ionisation level is a constant. Usually that process of ionisation and recombination happens over a much longer time scale than excitation caused by collisions between ions, so the two processes can be handled independently from one another – it is assumed that ionisation/recombination and excitation processes are not linked. Another sim-

plification used in understanding spectral emission is the *coronal approximation*. This approximation assumes that only two energy levels are important in the emission of a spectral line, the ground level g and the excited level j . In this case the relationship between collisional excitation from state g to state j , C_{gj} , and spontaneous decay from state j to state g , A_{jg} , is simplified to Equation 2.2, where the number densities of the levels are n_g and n_j and the electron number density is n_e . Equation 2.2 states that collisional excitation and spontaneous emission are directly proportional, meaning that each time an ion is collisionally excited it will then spontaneously decay and emit a photon.

$$n_e n_g C_{gj} = n_j A_{jg} \quad (2.2)$$

Another consideration to be made is on the *thermodynamic equilibrium* of the plasma. A plasma in thermodynamic equilibrium is isothermal, where the temperature is described by a Maxwell-Boltzmann distribution, and the *source function* of the plasma is the Planck function (source function described in Chapter 5). Plasma that is in *Local Thermodynamic Equilibrium* (LTE) can be described by thermodynamic equilibrium conditions at any given point, but the plasma as a whole cannot be described as one thermodynamic system. However, in most real plasmas LTE does not hold. This is the case in prominences, where the plasma cannot be in thermodynamic equilibrium due to the influence of the incident radiation from the solar disc below (Hirayama 1963). The incident radiation is scattered and absorbed by the prominence plasma, meaning there is a constant source of heating on the plasma. Under non-LTE conditions, the source function differs from the Planck function, so in order to accurately compute the emergent line profiles from the prominence a full consideration of the non-LTE physics must be made – see Chapter 5.

2.1.1 Observing spectral lines

To make observations of spectral lines it is common to use a *slit spectrometer*. As the name suggests, light from a source is passed through a collimating slit and is then diffracted using a prism or grating to allow observation of the spectrum of the source. In space-based spectrometers it is more common to use a grating due to weight/layout constraints, however prisms are still used in some ground-based observatories. Light incident on a grating is diffracted according to the *grating equation* (Equation 2.3), where diffraction angle θ is related to wavelength λ , d is the

slit width and m is the order of the diffraction (an integer).

$$d \sin \theta = m \lambda \quad (2.3)$$

The spectrum created is then passed to the imaging plane, where e.g. a CCD can be placed to image the spectrum. In the case of solar observatories it is common to apply filters to the incoming light in order to isolate the parts of the solar spectrum of interest.

2.2 Optically thin plasma emission

There are two regimes of plasma emission to consider – optically thin emission and optically thick emission. When observed, spectral lines are the integration of the emission along the line of sight between the source and the observer, and the optical thickness, τ , determines the amount of absorption of photons along the line of sight due to the plasma itself. In the optically thick scenario photons that are emitted are readily absorbed and re-emitted, or scattered by the plasma closer to the observer. In an optically thin plasma this re-absorption does not happen and the observed line profile is an integration of the entire line of sight, unaffected by absorption. The transition between optically thick and optically thin is somewhat fuzzy, but generally a plasma is described as optically thin if $\tau \ll 1$ and optically thick if $\tau > 1$. Most of the emission considered in the first part of Chapter 3, and some of that discussed in Chapter 4, is emitted under the optically thin regime. It is therefore important to introduce the concepts behind and equations describing optically thin plasma emission.

For optically thin emission, the *emissivity* (power per unit volume per unit solid angle), $\epsilon(\lambda_{jg})$, is given by Equation 2.4.

$$\epsilon(\lambda_{jg}) = \frac{hc}{4\pi\lambda_{jg}} n_j A_{jg} \text{ [erg cm}^{-3} \text{ s}^{-1} \text{ sr}^{-1}] \quad (2.4)$$

This corresponds to the spontaneous decay of electrons from the excited level, j , to the ground level, g , as in Equation 2.2. Integrating this across the emitting volume V (cross sectional area A , along the line of sight) gives the line intensity, $I(\lambda_{jg})$. Substituting from Equation 2.2 and integrating Equation 2.4 gives Equation 2.5 for the line intensity.

$$I(\lambda_{jg}) = \frac{hc}{4\pi\lambda_{jg}A} \int_V n_e n_g C_{gj} dV \text{ [erg cm}^{-2} \text{ s}^{-1} \text{ sr}^{-1}] \quad (2.5)$$

The number density, n_g , can be substituted for Equation 2.6 (which is essentially a clever way of multiplying by 1), allowing n_g to be written in terms of the total electron density, n_e .

$$n_g = \frac{n_g}{N_{ion}} \frac{N_{ion}}{N_{el}} \frac{N_{el}}{N_H} \frac{N_H}{n_e} n_e \quad (2.6)$$

N_{ion} is the ion number density, N_{el} is the number density of the element of interest, and N_H is the number density of hydrogen. The ratio $\frac{n_g}{N_{ion}} \sim 1$ for the assumptions made here. The elemental abundance, Ab , is given by the ratio $\frac{N_{el}}{N_H}$.

The collisional excitation rate, C_{gj} (used in Equation 2.2), is given by Equation 2.7 for a Maxwellian electron velocity distribution with temperature T .

$$C_{gj} = \frac{8.36 \times 10^{-6} \Upsilon_{gj}(T)}{\omega_g T^{1/2}} e^{-\frac{E_{gj}}{kT}} \text{ [cm}^3 \text{ s}^{-1}] \quad (2.7)$$

ω_g is the statistical weight of the ground state and E_{gj} is the energy difference between levels g and j . $\Upsilon_{gj}(T)$ is the thermally averaged collisional strength, given by Equation 2.8. The collisional strength is Ω . Note the energy used here is E_j , the specific energy of the j level.

$$\Upsilon_{gj}(T) = \int_0^\infty \Omega e^{-\frac{E_j}{kT}} d\left(\frac{E_j}{kT}\right) \quad (2.8)$$

Substituting Equations 2.6 and 2.7 into 2.5, the *contribution function*, $G(T)$, can be defined by gathering all the parameters from atomic physics (shown in Equation 2.9).

$$G(T) = \frac{8.36 \times 10^{-6} \Upsilon_{gj}(T)}{\omega_g T^{1/2}} \frac{N_{ion}}{N_{el}} \frac{N_H}{n_e} e^{-\frac{E_{gj}}{kT}} \frac{hc}{\lambda_{jg}} \quad (2.9)$$

This contribution function is peaked in temperature around the nominal formation temperature of the line. These substitutions lead to the spectral intensity in the form shown in Equation 2.10.

$$I(\lambda_{jg}) = \frac{1}{4\pi A} \int_V Ab G(T) n_e^2 dV \quad (2.10)$$

This intensity is therefore related to electron density (see §2.2.3). Equation 2.10 is a significant simplification, as the coronal approximation is not always valid, but for most optically thin plasma emission it is an acceptable simplification. The coronal approximation does not hold for plasmas where the incident radiation field plays a large role in the emission, and the plasma is not in LTE, but in the case of the PCTR

(where many spectral lines are optically thin) the coronal approximation is a useful simplification.

To calculate the emission from an optically thin plasma therefore requires knowledge of the atomic physics behind the transition forming the observed spectral line. There are a number of spectral atlases available for solar emission lines, most notably the CHIANTI atomic database (Dere et al. 1997), which is freely available. As well as containing information of most atomic transitions, CHIANTI can also create synthetic spectra for a range of scenarios, and contains abundance files and contribution functions for each. This makes it a powerful tool, especially when calculating e.g. electron densities (§2.2.2) or emission measure (§2.2.3).

2.2.1 Direct spectral inversion

As described above, spectral line emission is due to the emission of a photon by de-excitation of an atom or ion from one energy state to another. An ideal (optically thin) spectral line would be a narrow δ -function at the wavelength corresponding to the difference in energy between the upper and lower levels. This is not what is observed, however, as a number of mechanisms act to broaden spectral lines from a δ -function to a Gaussian function. The first, and most fundamental, is a natural broadening that occurs due to the Heisenberg Uncertainty Principle (Equation 2.11), which imposes uncertainties on the energy of each level of a transition.

$$\Delta t \Delta E \sim \hbar \quad (2.11)$$

Δt is the lifetime of the decaying state, and ΔE is the uncertainty in the energy (in this case the energy of the transition, E). The parameter \hbar is the Planck constant divided by 2π . This natural broadening results in spectral lines appearing Gaussian in shape, centred on the nominal wavelength of the transition. Other factors that increase the spectral line width are due to the environment local to the atom or ion itself. The ambient plasma temperature can cause thermal broadening, and collisions within the plasma can also act to broaden the line profile. Unresolved plasma motions and non-thermal processes can also cause broadening of spectral lines, as described in §3.2.3. A significant portion of the observed line width can also come from the instrument used to make the observation. This instrumental width can usually be described by a Gaussian profile, and for most space-based telescopes this is measured pre-flight, with some further estimates generally being made after

launch. The net effect of these broadening mechanisms is a spectral line that appears approximately Gaussian in shape.

Gaussian functions are described by a total of three parameters – centroid position, peak height, and Gaussian width. The Gaussian function, $f(x)$, is shown in Equation 2.12.

$$f(x) = ae^{-\frac{(x-\lambda_c)^2}{2\sigma^2}} + d \quad (2.12)$$

In Equation 2.12 a is the peak height of the Gaussian, λ_c is the centroid position (the use of λ here indicating wavelength units, and that f is a function of wavelength), σ is the Gaussian width, and d is an arbitrary background level. By fitting a spectral line with a Gaussian function, the parameters in Equation 2.12 can provide information about the plasma that emitted the light. The peak height of the Gaussian, a , directly translates to the peak intensity of the spectral line, which can be used to calculate an integrated intensity, I , of the spectral line using Equation 2.13.

$$I = \int_{-\infty}^{\infty} ae^{-\frac{(x-\lambda_c)^2}{2\sigma^2}} dx = a\sigma\sqrt{2\pi} \quad (2.13)$$

The centroid position, λ_c , can be used to calculate how much a spectral line is Doppler shifted – if a spectral line is observed to have a centroid position that is different from the nominal centroid position for that line, λ_0 , then that line is Doppler shifted. This indicates that the plasma that is emitting the line is moving, with (non-relativistic) Doppler velocity v_D along the line of sight. The difference between the observed line centroid and the nominal line centroid, $\Delta\lambda = \lambda_c - \lambda_0$, is related to the Doppler velocity through Equation 2.14. Here c is the speed of light.

$$\frac{v_D}{c} = \frac{\Delta\lambda}{\lambda_0} \quad (2.14)$$

The Gaussian line width, σ , is related to the Full Width at Half Maximum (FWHM) of the line by Equation 2.15.

$$\text{FWHM} = 2\sqrt{2\ln 2} \cdot \sigma \quad (2.15)$$

The Gaussian width can be used to calculate thermal and non-thermal motions of the plasma, which can be used to infer plasma properties. Equation 2.16 shows the calculation of the thermal line width, $\Delta\lambda_{\text{th}}$, which is related to the plasma temperature T , the atomic mass m , and the rest wavelength of the line λ_0 . Constants

k and c are the Boltzmann constant and the speed of light respectively.

$$\Delta\lambda_{\text{th}} = \frac{\lambda_0}{c} \sqrt{\frac{2kT}{m}} \quad (2.16)$$

Non-thermal line width is caused by plasma motions that are not due to the temperature, for example any motions caused by waves in the plasma or the magnetic pressure.

The technique of Gaussian fitting of optically thin spectral lines is used throughout this thesis, specifically in analysis presented in Chapters 3 and 4. Gaussian fitting can also be used to de-blend spectral lines. Sometimes multiple spectral lines can appear blended when they are close together and the spectral resolution of the instrument is not high enough to resolve them individually. In these situations it is usually possible to fit multiple Gaussians and separate the emission from each component of the blend. This is a common technique in spectral analysis, and essential when studying lines in the UV/EUV as they are extremely busy parts of the solar spectrum. §3.1.3 outlines practical methods used for de-blending lines in this way.

2.2.2 Electron density diagnostics

In order to derive electron densities from spectral data, lines formed by *forbidden* transitions must be considered. Forbidden transitions occur when the spontaneous decay rate of a level is low, so collisional processes can act to de-populate the level on a similar timescale. Such a level is called *metastable*. In forbidden transitions an atom or ion is collisionally de-excited from a metastable level to a lower level, emitting a photon. This differs from the usual *allowed* transitions, where an atom/ion spontaneously decays and emits a photon. Allowed atomic transitions create spectral lines that have intensities that are dependent on the electron density (Equation 2.10), while the population of a metastable level is also dependent on the temperature, T , of the plasma. Taking the ratio of two lines from the same ion, formed by the transition between level j to the ground state g ($I(\lambda_{jg})$ from Equation 2.5) and from a metastable level m to another level k ($I(\lambda_{mk})$) leaves Equation 2.17, assuming the same emitting volume for both lines.

$$\frac{I(\lambda_{jg})}{I(\lambda_{mk})} = \frac{n_g}{n_m} \frac{C_{gj}}{C_{mk}} \frac{\lambda_{mk}}{\lambda_{jg}} \quad (2.17)$$

It is important to point out the subtle differences between the two intensities considered here. $I(\lambda_{jg})$ is a result of transitions from level j to level g , however it is

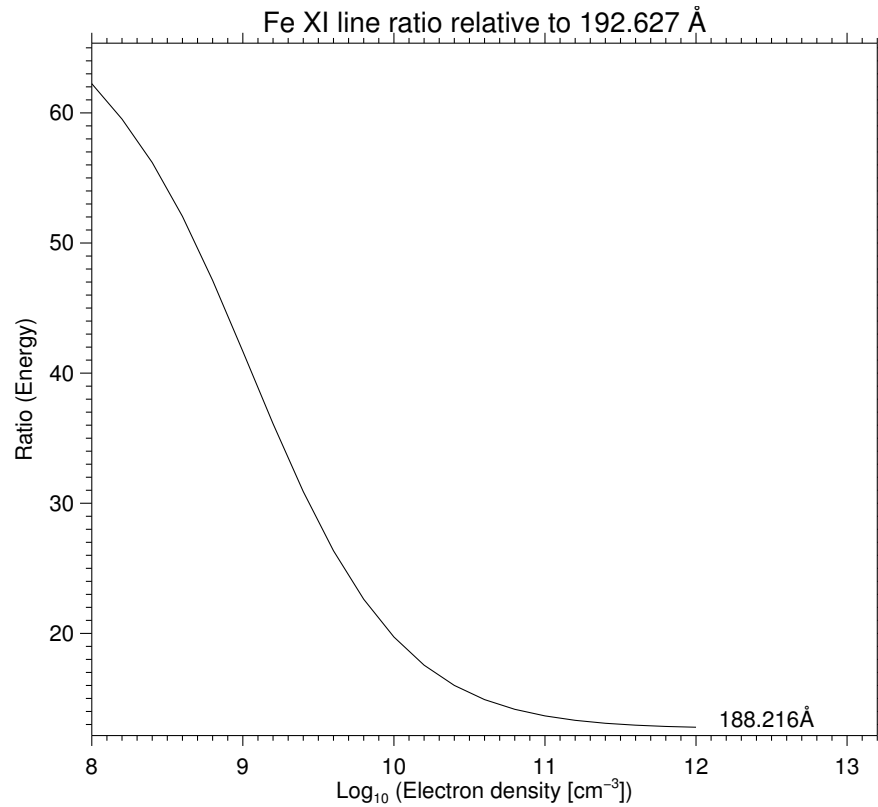


Figure 2.1: Electron density sensitivity for the intensity ratio of the 192.627 Å and 188.216 Å lines of Fe XI.

dependent on the collisional excitation from level g to level j , C_{gj} . On the other hand, $I(\lambda_{mk})$ results from the depopulation of metastable level m to level k , which is caused by collisional de-excitation from level m to level k , C_{mk} . Therefore the intensities are relative to populations of different levels – allowed transitions depend on the population of the lower level, g , whereas forbidden levels depend on the population of the upper level, m . From Equation 2.6 $n_g \propto n_e$, whereas n_m is a function of both electron density and temperature, $F(T, n_e)$. Therefore the ratio in Equation 2.17 is related to the electron density, as shown in Equation 2.18.

$$\frac{I(\lambda_{jg})}{I(\lambda_{mk})} \propto \frac{n_e}{F(T, n_e)} \quad (2.18)$$

This intensity ratio is then a measure of the electron density in the emitting volume at a certain temperature, as demonstrated in Figure 2.1 which shows the density sensitivity curve for the intensity ratio of two Fe XI lines. Figure 2.1 shows that the intensity ratio of the 192.627 Å and 188.216 Å lines changes as a function of

electron density. Therefore for each measured intensity ratio there is a unique value for electron density, for an appropriate range of densities. Ratios of line intensities from two allowed transitions would result in no density sensitivity, as the relevant $I(\lambda)$ values would both have $n_g \propto n_e$, so the ratio would be constant with n_e .

Most optically thin emission lines formed in the EUV in prominences are from the PCTR region, meaning that it is lines from the PCTR that are the best for performing density diagnostics in this way. Many previous studies have looked at the electron density of the PCTR using several instruments, and a wide range of values for n_e have been found. These observations are discussed in detail in §1.2.2. Through all of those studies a large range of possible electron densities were found, ranging from around $10^9 - 10^{11} \text{ cm}^{-3}$. These values are for a range of prominence types, with quiescent prominences generally having lower densities than active or erupting ones. The method for calculating electron densities outlined here is used in Chapters 3 (§3.2.2) and 4 (§4.4).

2.2.3 Differential emission measure

For features such as solar prominences, a cool plasma suspended in the hot solar corona, understanding the temperature structure across them is extremely useful for understanding the nature of their formation and sustainability in their hot surrounding. *Emission measure* is a method for quantifying the amount of emission at a given temperature along the line of sight. For hydrogen emission, the emission measure, $\langle \text{EM} \rangle$, which is defined at a temperature T in temperature range ΔT , along the line of sight can be calculated by Equation 2.19.

$$\langle \text{EM} \rangle = \int_h n_e^2 dh [\text{cm}^{-5}] \quad (2.19)$$

Here n_e is the electron density, and h is defined along the line of sight. When considering emission from other elements, the emission measure will be altered by the the relative abundance of that element, Ab . This emission measure quantity was introduced by Ivanov-Kholodnyi & Nikol'Skii (1961) and Pottasch (1963), and is related to the measured line intensity, $I(\lambda)$, by Equation 2.20.

$$I(\lambda) = \frac{1}{4\pi} Ab \langle \text{EM} \rangle \langle g(T) \rangle \quad (2.20)$$

In Equation 2.20 Ab is the elemental abundance with respect to hydrogen and $\langle g(T) \rangle$ is the contribution function defined by Pottasch (1963), shown in Equation 2.21,

which contains information about the atomic physics involved in the relevant transition.

$$\langle g(T) \rangle = 0.7 \text{MAX} \left(T^{-1/2} 10^{-5040W/T} \frac{N_{ion}}{N_{el}} \right) \quad (2.21)$$

In this equation, W is the excitation energy in electron volts. The logic for this form of the contribution function in Pottasch (1963) is that the value of the contribution function quickly decreases away from the maximum value, to the point that it is approximately zero at less than a third of the maximum. In their analysis it is therefore assumed that when the contribution function is non-zero, that it has a value of 0.7 times the maximum. However, for the analysis presented here it is important that the contribution function used, $G(T)$, is peaked in temperature. Equations 2.19 and 2.20 are only valid for optically thin emission. The emission measure gives a measure of the amount of contribution along the line of sight (l.o.s.) of plasma at a certain temperature. Therefore considering the contribution of lines formed at a range of plasma temperatures allows us to probe the temperature structure along the l.o.s. – this is done using the *Differential Emission Measure* (DEM).

The differential emission measure, or DEM, can be calculated when a number of lines formed at a range of plasma temperatures are observed simultaneously. This allows for the probing of the temperature structure along the line of sight – it tells us about how much plasma is at which temperatures. For optically thin emission, the differential emission measure in temperature, $\text{DEM}(T)$, is given by Equation 2.22.

$$\text{DEM}(T) = n_e^2 \frac{dh}{dT} [\text{cm}^{-5} \text{K}^{-1}] \quad (2.22)$$

The $\text{DEM}(T)$ is then related to the line intensity by Equation 2.23.

$$I(\lambda) = \frac{1}{4\pi} Ab \int_T G(T) \text{DEM}(T) dT \quad (2.23)$$

Therefore, in order to calculate $\text{DEM}(T)$ directly from integrated line intensities, Equation 2.23 must be inverted. This inversion is a complicated process, but a number of dedicated codes have been written to address the issue (e.g. Landi & Landini 1997; Hannah & Kontar 2012). Elemental abundances, Ab , can be calculated using the CHIANTI atomic database (Dere et al. 1997). The code of Hannah & Kontar (2012) calculates the contribution functions for each line used to constrain the DEM, and uses a regularisation procedure in order to fit the DEM curve. This regularisation allows the user to tweak the model in order that the resulting DEM is not over-fitted

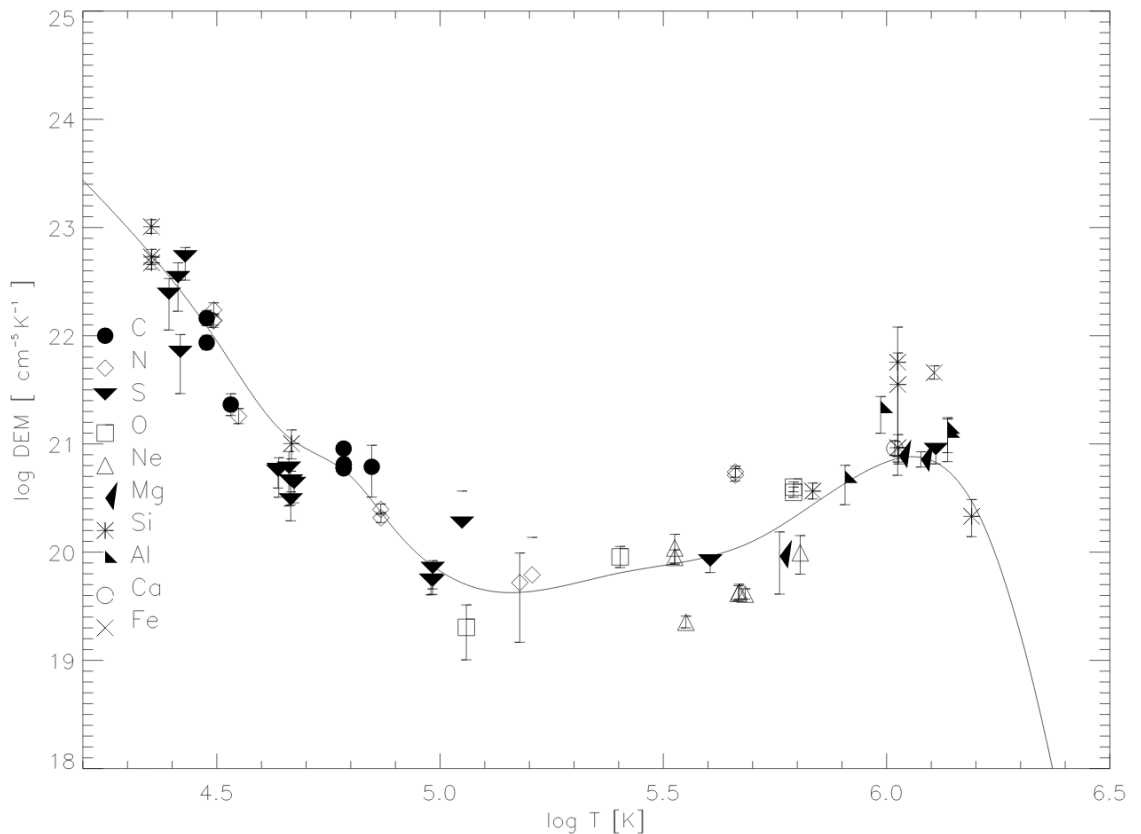


Figure 2.2: Prominence DEM from Parenti & Vial (2007). This DEM was made using spectral lines observed by the *SOHO/SUMER* instrument. Points are the data, with each symbol representing a different element. Solid line is their ‘best fit’ to the DEM data.

or under-fitted. For each optically thin emission line, the contribution function $G(T)$ is usually peaked at the formation temperature of the line (Equation 2.9). The code then uses $G(T)$ values along with observed intensities to calculate the DEM. Measuring the temperature and density gradient of the transition region between the cool prominence core and the corona is important for modelling prominences, and the DEM technique can help answer this question.

DEMs have previously been calculated in prominences by a number of authors, using a range of instruments. An example prominence DEM (taken from Parenti & Vial 2007) is shown in Figure 2.2. Some of the first were calculated using data from *Skylab* by Mariska et al. (1979), and then later by Schmahl & Orrall (1986). In Schmahl & Orrall (1986), the authors presented three possible prominence thread

geometries (cool core with hot sheath, isothermal threads and one including a PCTR parallel to the magnetic field) to explain observed features of prominence DEMs. However, they found that none of these simple models could fully account for the observed features. These early DEMs show a peak at around $\log T = 6.0 - 6.2$, with rapid drop-off to higher temperatures. Towards lower temperatures they show a steady decrease to some minimum (around $\log T = 5$) before increasing again towards $\log T = 4$. [Wiik et al. \(1993\)](#) presented a DEM from a prominence observed by the *High Resolution Telescope and Spectrograph (HRTS)*. Comparing to the DEM of [Schmahl & Orrall \(1986\)](#) they found similar results, especially at low temperatures. More recently, [Parenti & Vial \(2007\)](#) calculated prominence DEMs using lines observed by *SOHO/SUMER*, which is shown in [Figure 2.2](#). Again, similar results to those of [Schmahl & Orrall \(1986\)](#) were found, with a high temperature peak around $\log T = 6$ and a minimum at $\log T = 5$. The DEM technique is used in [§3.2.4](#) of this thesis to probe the temperature structure of a tornado-like prominence observed by *Hinode/EIS*.

2.2.4 Emission measure distribution

A useful concept to introduce is the *Emission Measure Distribution (EMD)*, which is subtly different from the DEM. Whilst the DEM (units $\text{cm}^{-5} \text{K}^{-1}$) is a direct mathematical result from the inversion of [Equation 2.23](#), the EMD (units cm^{-5}) is calculated by first performing an integration of the DEM over a small temperature range, ΔT , as shown in [Equation 2.24](#). This is the emission measure over the temperature range ΔT , defined in [Del Zanna et al. \(2002\)](#).

$$\text{EM}(T_i) = \int_{T_i - \Delta T/2}^{T_i + \Delta T/2} \text{DEM}(T) dT \quad (2.24)$$

$\text{DEM}(T)$ is calculated for a finite grid of temperatures so ΔT can be defined according to that grid. For each temperature range is a corresponding $\text{EM}(T_i)$, so considering all of these temperature bins gives the emission measure distribution in temperature, $\text{EMD}(T)$. To convert from $\text{DEM}(T)$ to $\text{EMD}(T)$ a conversion factor, f with a form shown in [Equation 2.25](#), is used ([Hannah & Kontar 2012](#)).

$$f = N 10^{\log T} \ln(10^{d \log T}) \quad (2.25)$$

N is the number of temperature bins, $\log T$ is the temperature grid in log space, with $d \log T$ between each temperature bin.

2.3 Optically thick plasma emission

Emission in an optically thick plasma is more complex than the optically thin case. Instead of sampling emission along the entire emitting volume, emission from an optically thick plasma is affected by self-absorption and re-emission processes along the line of sight, as well as the addition of photons that are scattered into the line of sight. Therefore it becomes important to consider the *radiative transfer* – the changes to the observed intensity due to absorption and emission along the line of sight. In an optically thick plasma, emitted photons are readily re-absorbed, exciting an atom/ion from the ground state up to some higher level. This atom/ion in the excited state can then decay, emitting a photon of the same frequency as the absorbed one, but not necessarily in the same direction (the process of *scattering*). The net result of this process is a reduction of the observed intensity at line centre, where the line is most optically thick. This is usually observed as a line profile with a flattened top, or a *central reversal* in a line profile – the reduction of intensity at the line centre creating an emission profile with two apparent peaks on either side of the line centre. Absorption processes reduce the intensity at line centre, but not across the whole profile of the line. This is because the absorption of photons is generally heavily wavelength dependent, with the relevant transition only possible at certain energies, whereas the overall line profile can be broadened by a number of effects, such as *Van der Waals* and *Stark* broadening mechanisms. These are described in Chapter 5. Therefore an ‘optically thick’ spectral line is really optically thickest at its core, with optical thickness decreasing towards the wings of the line.

In this thesis, the majority of analysis of optically thick spectral lines is done on the Mg II h and k lines observed by *IRIS*. Therefore it is important to introduce these lines specifically as they form a large part of the analysis presented in Chapters 3, 4, and 5. The physical processes behind optically thick plasma emission are detailed in Chapter 5, where they are directly relevant for the codes used to model the Mg II lines.

2.3.1 The Mg II h and k lines

The singly-ionised magnesium h and k lines, at 2803 Å and 2976 Å respectively, are optically thick emission lines in the UV part of the solar spectrum. They come about

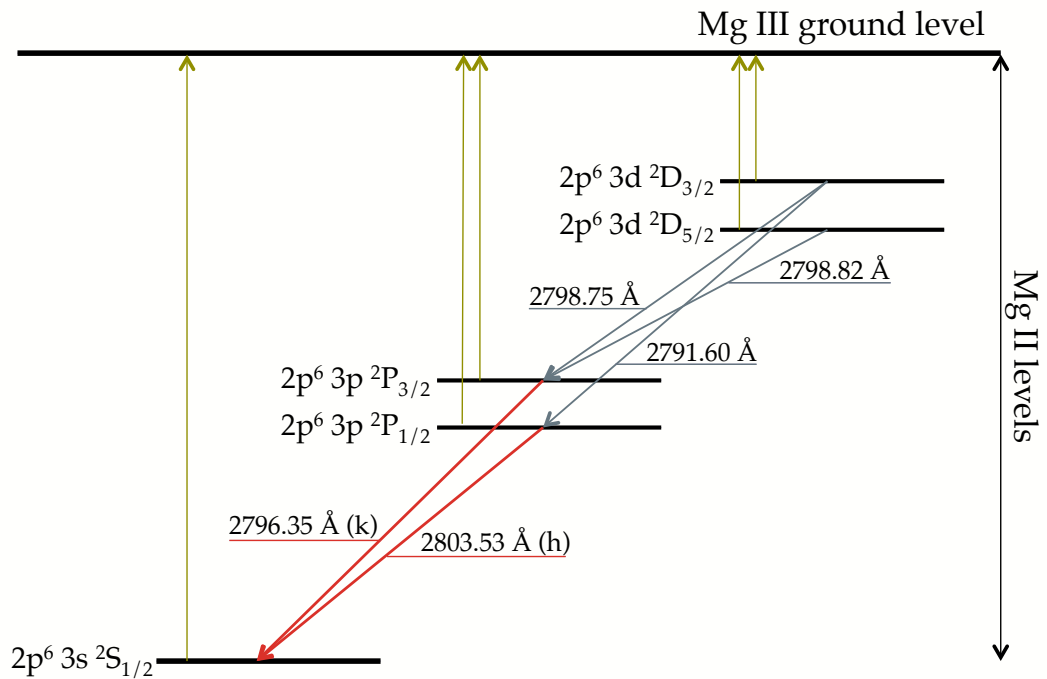


Figure 2.3: Five-level term diagram for the Mg II system. Shown in red are the (bound-bound) Mg II h and k transitions, and in grey are the UV triplet transitions. Indicated in yellow are the bound-free transitions to the Mg III ground state.

from transitions to the Mg II ground state from the second (h) and third (k) excited levels, as shown in Figure 2.3. Formed at chromospheric plasma temperatures, they are strongly in emission in prominences, and have good diagnostic potential in the prominence context (Pereira et al. 2013), however they are not observable from the ground, so satellites, sounding rockets, and balloon experiments must be employed to get above the Earth’s atmosphere. These strong resonance lines have been studied in the solar context for some time (see below), but interest in them has piqued again recently with the launch of the *Interface Region Imaging Spectrograph* satellite (*IRIS*, De Pontieu et al. 2014, see §2.4.2). The launch of *IRIS* has meant that there are currently observations of the Mg II lines being made with extremely high temporal, spatial and spectral resolutions at all times. There have been a number of dedicated prominence studies run using *IRIS*, with a number of authors analysing *IRIS* prominence data for a range of prominence types (Schmieder et al. 2014; Harra et al. 2014; Liu et al. 2015a; Vial et al. 2016; Levens et al. 2016a). *IRIS* observations

have also inspired updates to Mg II prominence models to account for some of the new observations (Heinzl et al. 2014, 2015).

The first solar observations of the Mg II UV lines came in 1948, using a V-2 rocket experiment (Hopfield & Clearman 1948). After some tentative identification of the observed UV lines by Hopfield & Clearman (1948), further detailed analysis of the V-2 spectrum was carried out by Durand et al. (1949) and Clearman (1953). Johnson et al. (1953) presented a dedicated photograph of the Mg II h and k lines (simply named the Mg II ‘doublet’ lines at that stage), followed by an in-depth review of all solar UV spectral observations presented by Tousey (1963). Further spectra were obtained by Purcell et al. (1963), with many authors up to this point noting the distinctive shape of the Mg II h and k lines, with their broad absorption profile, distinctive central emission peaks, and reversal at the line cores, very similar to the well documented Ca II H and K lines. Full disc images of the Mg II h line (Fredga 1966) and later the k line (Fredga 1969) were achieved using rocket experiments during the 1960s. In the latter paper, Fredga noted the similarities between the full disc Mg II k image and co-temporal Ca II K images. These images included on-disc filaments, which are notably much less visible in Mg II than in Ca II, bright active regions, and prominences visible above the solar limb (however the contrast of their images does not show the prominences). Fredga (1969) also began using the notation ‘H’ and ‘K’ for the Mg II doublet lines, in analogy to the Ca II H and K Fraunhofer lines – this was later adjusted to the lower case ‘h’ and ‘k’ for the Mg II lines to avoid confusion during analysis (Lemaire & Skumanich 1973). Bonnet et al. (1967) presented spectra from a rocket experiment that included the Mg II h and k lines, where they attempted to measure limb darkening. Inadvertently with those observations they also measured the first spectra of Mg II h and k in a prominence above the solar limb, noting that these lines in the prominence appear to be very broad. Further solar disc observations were made throughout the 1970s using rocket and balloon experiments (Bates et al. 1969, 1970; Lemaire & Skumanich 1973) as well as above-limb observations of quiet sun regions and active regions using *Skylab* (Feldman & Doschek 1977; Doschek & Feldman 1977). With the launch of the eighth *Orbiting Solar Observatory* (OSO-8) satellite and its *Laboratoire de Physique Stellaire et Planetaire* instrument (LPSP, Artzner et al. 1977; Bonnet et al. 1978) in 1975, high-resolution observations of the Mg II h and k lines were available consistently over a three-year period. This prompted many observations of various solar features to be

made, including quiet sun and plage (Artzner et al. 1978; Lemaire et al. 1981) and an early Mg II flare observation (Lemaire et al. 1984). Prominences were also a target of interest for OSO-8, with active (Vial et al. 1979) and quiescent (Vial et al. 1981; Vial 1982a) prominences observed. These early prominence observations in Mg II revealed profiles with no central reversal, however they did not appear as simple Gaussians either (Vial 1982a). Doppler shifts in the range ± 20 km s⁻¹ were found in these prominences, comparable to simultaneous measurements of Ca II lines, with FWHM of Mg II around 0.1 – 0.25 Å and k/h intensity ratios of around 2. The *Solar Maximum Mission* (SMM, Tandberg-Hanssen et al. 1981) had a UV spectrometer and polarimeter onboard which was capable of observing the Mg II lines, however seemingly few studies were done on those lines from SMM. Henze & Stenflo (1987) attempted polarimetry of the Mg II h and k lines from SMM solar disc observations, but no prominence studies were carried out during that mission. Further Mg II observations were made in the mid-1990s with the RASOLBA balloon experiment (Staath & Lemaire 1995), with high resolution spectra being taken at disc centre. Thereafter the Mg II lines were largely forgotten, barring some sounding rocket experiments such as *HRTS-9* (Morrill & Korendyke 2008) and the *Solar Ultraviolet Magnetograph Investigation* (SUMI, West et al. 2011), until the launch of the *IRIS* satellite in 2013.

Figure 2.4 shows example spectra of a quiet-sun region (*top panel*) and a prominence (*bottom panel*) from *IRIS*. The Mg II h and k lines, when observed on disc (Figure 2.4, *top panel*), have a number of components formed at a range of heights in the solar atmosphere. They are characterised by a deep absorption profile into the solar continuum (called h_1 , k_1), containing strong double-peaked emission (called h_2 , k_2) near line centre, and a central reversal (called h_3 , k_3) at the core of the line. These are often followed by ‘v’ or ‘r’ to distinguish the features on the blue and red sides of the line centre respectively. Figure 2.5 highlights these features for the k line (equivalently for the h line). The broad absorption features are formed at the temperature minimum region of the outer photosphere (Fredga 1969), whereas the emission and central reversal are products of the chromosphere. The emission peaks are formed in the lower chromosphere, whereas the central reversal is from the upper chromosphere. A number of absorption lines can also be seen in the top panel of Figure 2.4, which are mostly photospheric in origin. Amongst those, however, are the Mg II triplet lines at 2798.75 Å and 2798.82 Å, which form a blended absorption line

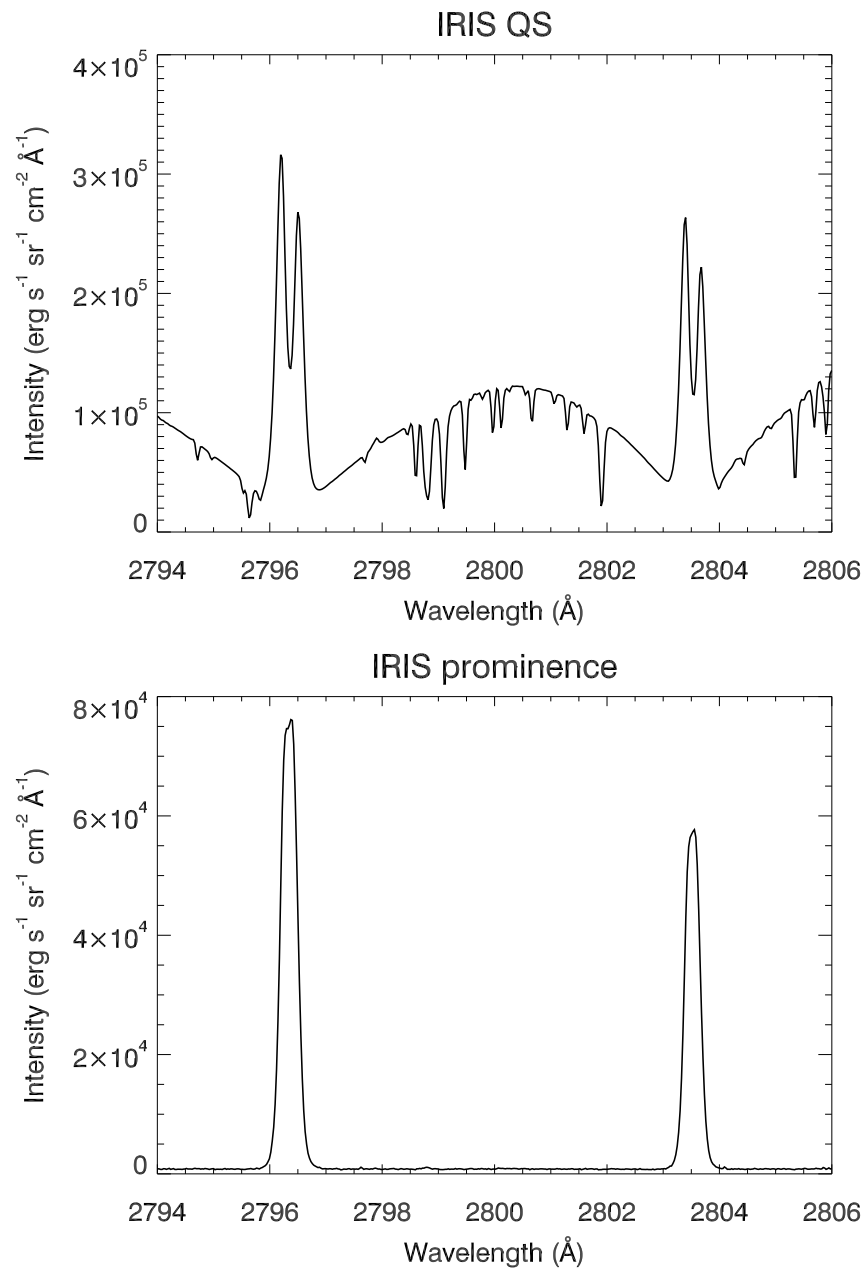


Figure 2.4: Averaged spectral profiles of the Mg II lines measured by *IRIS* for the quiet sun (*top*) and a prominence (*bottom*). Profiles are spatially averaged over the entire raster from which they were taken. QS profile is from 29 September 2013, prominence profile is from 15 July 2014. Mg II k is centred on 2796.35 Å, Mg II h is centred on 2803.53 Å.

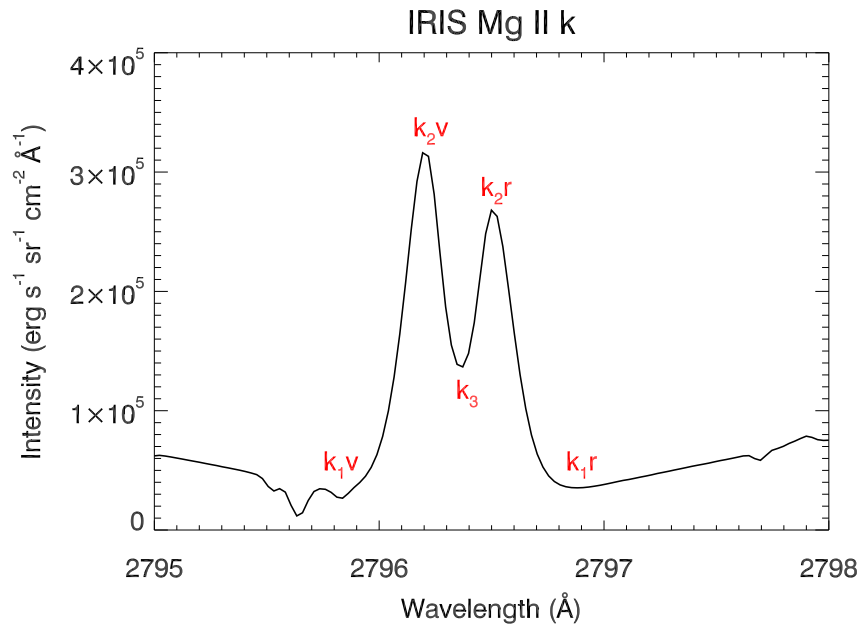


Figure 2.5: Example averaged spectral profile of the Mg II k line from *IRIS* for a quiet-sun region. Labelled in red are the k_3 (line centre), k_2 (emission peaks), and k_1 (wing absorption) regions, distinguished as ‘v’ and ‘r’ for blue and red sides of line centre respectively.

(the other triplet line, 2791.60 Å, is outside of the spectral range shown in Figure 2.4). The transitions responsible for these lines help populate the upper levels of the h and k lines, as seen in Figure 2.3, and they are now being investigated for their chromospheric diagnostic potential (Pereira et al. 2015).

The averaged prominence spectra in the Mg II lines is strikingly different to the chromospheric profiles. Prominences show the Mg II h and k lines strongly in emission, as can be seen in the lower panel of Figure 2.4, but their profiles are narrow, with little or no central reversal. The triplet lines are in emission in prominences, but they are extremely weak and not visible on the scale used in Figure 2.4. None of the other absorption lines seen in the QS spectrum are visible in the prominence spectrum. The prominence profile is also, naturally, missing the continuum emission seen in the wings of the h and k lines, from which the h_1 and k_1 regions are formed. Although prominence Mg II h and k profiles are generally narrow and single peaked, there are cases where these lines are reversed in prominences. Some aspects of these reversed prominence Mg II profiles are investigated throughout this thesis,

specifically in §3.4.2 and further in §4.3.

2.3.2 Mg II in the chromosphere and flares

Since the launch of *IRIS* a great deal of work has been done on the chromosphere and flares observed in Mg II. The diagnostic techniques used in these circumstances can be translated to analyse prominence observations, so it is worth mentioning some of these studies. In a series of papers ('THE FORMATION OF IRIS DIAGNOSTICS') from around the time of the *IRIS* launch, a detailed look at the Mg II lines in the chromosphere was presented in preparation for the upcoming observations (Leenaarts et al. 2013a,b; Pereira et al. 2013). The first paper in the series, Leenaarts et al. (2013a), outlines the atomic physics behind the Mg II h and k lines, which is essential for creating models for understanding observed plasma properties. A number of atmospheric models have been developed in order to model the chromosphere, e.g. *Multi3D* (Leenaarts & Carlsson 2009), *Bifrost* (Gudiksen et al. 2011), *RADYN* (Allred et al. 2015), and getting the atomic physics of the magnesium transitions correct is vitally important in accurately modelling those lines. This atomic physics is also important in prominence models (e.g. Paletou et al. 1993; Heinzel et al. 2014). The second paper of that series, Leenaarts et al. (2013b), concentrates on Mg II formation in the solar atmosphere, using results from numerical simulations to investigate the expected behaviour of the Mg II lines in the chromosphere in the context of *IRIS* observations. The third paper, Pereira et al. (2013), continues the theme of spectral diagnostics of the Mg II h and k lines in the chromosphere, outlining some of the physical parameters that can be derived from Mg II h and k observations, such as velocities of different parts of the chromosphere, velocity gradients, and chromospheric temperature. Some of these diagnostic techniques can be used to derive prominence characteristics, which is explored in Chapter 4.

Solar flares are huge releases of energy in the solar atmosphere (caused by reconnection in the magnetic field) with most of the flare energy being converted into emission in the optical and UV parts of the solar spectrum (Fletcher et al. 2011). Therefore the UV Mg II lines are greatly enhanced during flares, with the chromosphere being a region where a large amount of the flare energy is deposited. Prior to the launch of *IRIS* there had only been one reported observation of a solar flare in the Mg II lines (Lemaire et al. 1984). This was using the LPSP instrument on OSO-8,

and they note that during the flare the h and k lines are greatly enhanced, with the central reversal disappearing and the lines broadened. This is reflective of what has been found in more recent observations using *IRIS* (Kerr et al. 2015; Matthews et al. 2015; Liu et al. 2015b).

2.4 Instruments

Solar observations have been made using a huge number of instruments over many years, far too many to list here. This section will introduce the main instruments used during the analysis presented in this thesis. The majority of data used here is from the space-based *Hinode* (Kosugi et al. 2007) and *Interface Region Imaging Spectrograph* (*IRIS*, De Pontieu et al. 2014) satellites, with a portion of data coming from the French/Italian ground-based *Télescope Héliographique pour l'Etude du Magnétisme et des Instabilités Solaires* (THEMIS, López Ariste et al. 2000). The *Solar Dynamics Observatory* satellite (*SDO*, Pesnell et al. 2012) and its imager the Atmospheric Imaging Assembly (*AIA*, Lemen et al. 2012) is extensively used here, but mostly for context images. Other ground-based instruments are used for H- α context images – *Solar Magnetic Activity Research Telescope* (*SMART*) at the Hida Observatory, Kyoto, Japan and the *Meudon Solar Survey* telescope in Meudon, France. Outlined in the following sections are overviews of the main instruments and their relevant subsystems. This information is provided to give context to some of the observations presented later in this thesis. It is therefore not essential information in understanding the concepts at the core of this thesis, however it is useful to include in order to fully understand the relative capabilities of the instruments used. Data from all instruments are reduced and analysed using the *Interactive Data Language* (*IDL*) and its dedicated solar data analysis software suite *SolarSoft* (*SSW*, Freeland & Handy 1998).

2.4.1 *Hinode*

The *Hinode* satellite (Kosugi et al. 2007, meaning ‘sunrise’ in Japanese) is a JAXA spacecraft that was launched in 2006. It consists of three science instruments, designed and developed by teams in Japan, the United Kingdom and the United States of America. The instruments onboard *Hinode* are the *Extreme-ultraviolet Imaging Spectrometer* (*EIS*, Culhane et al. 2007), the *Solar Optical Telescope* (*SOT*, Suematsu

et al. 2008; Tsuneta et al. 2008), and the *X-Ray Telescope* (XRT, Golub et al. 2007). EIS, observing in the EUV at chromospheric and coronal plasma temperatures, and SOT, observing in visible wavebands at photospheric and chromospheric temperatures, are both extremely useful for prominence observations. Prominences are generally nowhere near active enough to emit strongly at X-ray frequencies, so the XRT instrument has not been used much in prominence analysis. One exception to this is in Heinzl et al. (2008), where XRT was used to help analyse volume blocking due to cool plasma in a prominence. The instruments are all designed to work together, each with different strengths that complement one another to help achieve the science goals of the mission, which are mostly to do with transport of energy from the photosphere through to the corona, and investigating photospheric magnetic fields (Kosugi et al. 2007). In this section only EIS and SOT will be outlined in detail, as XRT has not been used for any analysis in this thesis.

In 2008, two years after launch, *Hinode* suffered a problem with one of its downlink transmission systems, meaning it can no longer transmit full data loads (Shimizu 2009). A failure in the X-band system meant that the transmission path needed to be switched to *Hinode*'s S-band system, which has a slower downlink speed. The result of this is a reduction of the amount of bandwidth available for each downlink, so memory allocation for individual observations needed to be reduced. This is done in a number of ways, with smaller rasters and smaller/fewer spectral windows from EIS, lower cadence, data summing, and smaller FOV SOT images, and lower cadence XRT images, for example. Depending on the observing objectives of a campaign, a balance between the instruments can be achieved.

Hinode is in a Sun-synchronous orbit, with period of 98 minutes, meaning that the Sun is visible to *Hinode* continuously for nine months per year. For the remaining three months *Hinode* goes into eclipse behind the Earth, with affected data usually totalling around 30 minutes per day. *Hinode* also passes through the *South Atlantic Anomaly* (SAA), a place in the Earth's magnetosphere where the inner Van Allen Belt dips close to the surface. Those belts contain energetic particles that are trapped by the Earth's magnetic field, and they can interact with electronic components of the instruments creating a large number of erroneous pixel responses, making some data unusable. Passes over the SAA only last for a short time, however data that is affected by the SAA must be analysed carefully or not used at all.

2.4.1.1 Extreme-ultraviolet Imaging Spectrometer

The Extreme-ultraviolet Imaging Spectrometer, or EIS, is a slit (or slot) spectrometer designed to observe two spectral regions in the solar EUV spectrum – one from 170-210 Å and another from 250-290 Å. Unlike earlier instruments which observed in that spectral range that used grazing-incidence optics, EIS uses normal-incidence optics by using multi-layer coatings on both its primary mirror and grating to increase reflectivity (Culhane et al. 2007). Both the short waveband (SW, 170-210 Å) and long waveband (LW, 250-290 Å) spectra undergo the same optics until being detected by two separate but identical CCDs, each with pixel size of 1". Spectral resolution (FWHM) was measured as 0.047 Å in the SW and 0.055 Å in the LW prior to launch, but post-launch estimates suggest that these values could be higher now – 0.054 Å in the SW and 0.055 – 0.057 Å in the LW (Brown et al. 2008). A number of filters are used to remove stray light and isolate the SW and LW spectral ranges. Each waveband has an effective area (EA), which is peaked in wavelength. Due to this, certain lines that are at the extremes of the wavelength ranges are observed as being weaker than they would be normally relative to others, and lines near the peak of the EA are stronger. Lines near the peaks of the EAs generally have a very high SNR. The strongest lines observed in the SW and LW are Fe XII 195.119 Å and He II 256.32 Å respectively.

EIS has the option of two slit sizes, 1" and 2", and also two larger slots, 40" and 266", that can be used for observations. By passing the incoming light through the slit the light is collimated, and is then dispersed by the grating. The EIS slits have a maximum length of 512", however commonly much less of the slit length is used as the target usually only requires a portion of that size. Since the failure of the X-band transmitter it has become much more necessary to regularly reduce the amount of data recorded. Slit observations can be used in one of two ways: a *raster* study or a *sit-and-stare* study. Rasters are formed by taking consecutive exposures, offset from each other by a small amount (usually the width of the slit) in order to build up a larger field of view. Rastering allows EIS to scan across a region and build up an extended view of a source in the form of a raster map, extended in x and y directions, with a spectrum available at each pixel. Although the resulting FOV is small, EIS rasters provide powerful diagnostic potential. It is worth noting that each step in a raster is also temporally offset, so in a fast evolving region analysis of a raster must be done carefully. The sit-and-stare mode is done by simply keeping the slit position

fixed and taking one exposure after another. This allows the temporal evolution of the target to be studied, however for transient targets such as flares ensuring that the slit is covering the desired location at the correct time is challenging. Therefore many studies make use of both rasters and sit-and-stare options to ensure the best coverage of their target possible.

Exposure times for EIS are usually on the order of a few seconds, dependent on the target. Flares and active regions require shorter exposures, only $\sim 2 - 10$ seconds, whereas quieter targets such as off-limb regions or prominences require longer exposures, sometimes ~ 30 seconds or more.

2.4.1.2 Solar Optical Telescope

The Solar Optical Telescope (SOT) is the main instrument on board *Hinode*. It is a diffraction-limited Gregorian telescope, with a 50 cm primary mirror and three main science instruments. These are the *Broadband Filter Imager* (BFI), the *Narrowband Filter Imager* (NFI), and the *Spectro Polarimeter* (SP). The BFI and NFI share a common CCD, but are quite different in their observing capabilities. BFI has a full FOV of $218'' \times 109''$, and a number of filters available – CN (3883.0 \AA), Ca II H (3968.5 \AA), CH (4305.0 \AA) as well as three continuum filters in the blue (B, 4504.5 \AA), green (G, 5550.5 \AA) and red (R, 6684.0 \AA) parts of the spectrum. These filters mostly sample the photosphere, except for Ca II H, which is a chromospheric line and is also strongly in emission in prominences. This filter is therefore very useful for prominence observations. BFI observations are therefore the main SOT contribution to the work in this thesis. The NFI observes using filters containing lines from Mg I, Fe I, Na I and H I ($H-\alpha$) mostly for photospheric and some chromospheric diagnostics. SOT $H-\alpha$ can also be used for prominence observations (Schmieder et al. 2013). The SP measures two lines of Fe I to perform spectropolarimetry in the photosphere, to calculate the photospheric magnetic field. SOT also has a small ‘correlation tracking’ telescope, used for alignment purposes.

SOT observations cover a relatively small FOV, but the images are extremely high resolution. BFI has a maximum resolution of $0.054''$ per pixel, but it is normal to sum pixels 2×2 or 4×4 to reduce cadence and bandwidth usage. Even with 2×2 summing, which is regularly used for prominence observations, a resolution of $0.109''$ per pixel is extremely high, and is higher than that of most previous satellite imagers.

In early 2016 the filtergraph camera (that of the BFI and NFI) short circuited and

was turned off¹, rendering the two filtergraph imagers unusable. The other systems, SP and the correlation tracker, were not affected by the issue, but the SOT team were not able to save the filtergraph without risking the other instruments.

2.4.2 Interface Region Imaging Spectrograph

The *Interface Region Imaging Spectrograph* (*IRIS*, De Pontieu et al. 2014) is a NASA satellite, operated from the Lockheed Martin Solar and Astrophysics Laboratory in Palo Alto, California, U.S.A. Launched in 2013, it was designed to study the chromosphere and transition region between the chromosphere and the corona which is important in understanding the energy transport between the two regions. Many chromospheric and TR lines are also in emission in prominences, so they form good diagnostic probes for prominence study. *IRIS* is composed of two related instruments, a slit spectrograph (SG) and a slit-jaw imager (SJI) which provides a larger FOV around the slit for context. Its primary mirror is small compared to, say, SOT, employing a 19 cm Cassegrain design, but it is able to reach a relatively high spatial resolution, with a pixel size of 0.167'' and effective resolution of $\sim 0.35''$ (De Pontieu et al. 2014). The orbit of *IRIS* takes around 98 minutes, and as with *Hinode* it is Sun-synchronous so maintains a continuous view of the Sun for most of the year. For three months *IRIS* goes into eclipse behind the Earth for a part of each orbit, during which time it cannot make observations. Observations during this eclipse period require delicate planning to optimise the observing time available in between eclipses. Also similarly to *Hinode*, *IRIS* passes through the SAA, leading to increased numbers of energetic particles affecting the observations.

The *IRIS* spectrograph uses a slit which is 0.33'' wide and 175'' long. The slit can be rastered over a region, as described in §2.4.1.1 for *Hinode*/EIS, with the ability to perform rasters where the space between slit positions is larger than the slit width, creating a raster up to a maximum size of 130''. In all there are three options for step size: 'dense', where the step size of the raster matches the slit width (0.33''), 'sparse', with step size of 1'', and 'coarse', which has a 2'' step. Each raster can use the full slit length (175''), or less depending on the desired raster size. *IRIS* can also run sit-and-stare studies. In total there are 49 raster modes that *IRIS* can perform, shown in full in De Pontieu et al. (2014, table 12).

¹https://sot.lmsal.com/Operations_new.html#sot_status

Similarly to EIS, the *IRIS* spectrometer samples two spectral ranges using two CCDs, one in the near ultraviolet (NUV) and one in the far ultraviolet (FUV). The NUV channel has a passband from 2793 Å to 2835 Å which captures the Mg II h and k lines (§2.3.1), the Mg II triplet lines, and the surrounding continuum, along with several photospheric lines. Spectral resolution is 0.053 Å in the NUV. In the FUV the channel is split into two passbands, one from 1332 Å to 1358 Å (FUV 1) and another from 1389 Å to 1407 Å (FUV 2), both with spectral resolution of 0.026 Å. FUV 1 is focussed on the C II doublet at 1334.5 Å and 1335.7 Å, but also includes lines from O I and coronal lines of Fe XII and Fe XXI. FUV 2 contains lines formed at higher transition regions temperatures, primarily the Si IV lines at 1393.8 Å and 1402 Å, but also O IV lines at 1399.8 Å and 1401.2 Å. The Mg II h and k lines are strongly in emission in prominences, as discussed in §2.3.1, so are of great interest in this thesis. Lines from C II and Si IV are also in emission in prominences, however they are weaker and less well studied in that context.

The SJI is designed to give a context image around the slit. The FOV presented by the SJI is 175'' × 175'', with the slit position represented as a dark vertical line in the centre of the image. There are four options of filters for use with the SJI, with two isolating emission from NUV channels (4 Å bandpass) and two from FUV channels (55 Å bandpass). These filters are dominated by emission from certain lines and continuum – C II 1334 Å and 1335 Å, Si IV 1394 Å and 1403 Å, Mg II k 2796 Å, and Mg II far wing continuum at around 2830 Å.

IRIS frequently coordinates observations with *Hinode* (and other instruments) for joint scientific goals. The power of coordinated observing campaigns is in gaining as many views of the same region as possible, at as large a temperature range as possible and sampling lines formed under different conditions. This multi-instrument approach opens up new potentials for diagnostics that are not available from single instrument campaigns. This approach is used extensively in this thesis, with Chapters 3 and 4 largely using results from a coordinated prominence campaign in 2014.

2.4.3 THEMIS

The *Télescope Héliographique pour l'Etude du Magnétisme et des Instabilités Solaires* (THEMIS, López Ariste et al. 2000) is a French/Italian telescope at the El Teide

Observatory in Tenerife, Canary Islands. THEMIS is a spectropolarimeter, meaning that it measures the polarisation signals in the Stokes profiles of certain spectral lines that are sensitive to the magnetic field, and from those lines the magnetic field strength and orientation can be derived (§1.2.5). First light observations were made using THEMIS in 1998. The slit of THEMIS is 120'' long, and the slit width can be set manually, but usually is $\sim 0.5''$. The spatial resolution, however, is generally lower due largely to seeing effects – usually a resolution of $\sim 1''$ per pixel is expected. Similarly to *Hinode*/EIS and *IRIS*, THEMIS can raster over a region to build up an extended map of a solar feature. These rasters take some time, however, because of the nature of the observations – one raster can take up to one hour to complete. This is due to the requirement of repeating cycles of the Stokes parameter observations in order to increase signal-to-noise ratio, especially in above-limb observations.

THEMIS measures all four Stokes parameters (I , Q , U , V), taking measurements of $I \pm Q$, $I \pm U$, and $I \pm V$. Stokes Q and U are measures of the linear polarisation of the observed light, and V is the circular polarisation parameter. I is the intensity. Mostly He I lines are used for these calculations in prominences, with the D₃ (5875 Å) and 10830 Å lines commonly used, which are brightly in emission in prominences. H I lines, such as H- α , can also be used for on-disc filament field calculations – near the limb there are more problems from scattered light, so H- α polarimetry in prominences is more difficult to perform. In a prominence the most important consideration is the illumination of an emitting atom/ion by the radiation field from the solar surface below it, and the magnetic field that the atom/ion sits in. In the calculations of López Ariste & Casini (2002) the prominence is illuminated by a cone of radiation from below, and then scatters or re-emits the light into the observer's line of sight. The light from the surface is unpolarised, so any polarisation introduced will be because of the magnetic field in the prominence.

In 2015 THEMIS stopped making observations in order to install a new *adaptive optics* (AO) system (Gelly et al. 2016). The aim is for the project to be complete in 2017 and new observations to begin in early 2018 (Levens et al. 2016b). The AO system will greatly improve the potential spatial resolution of the telescope, even above the limb, mostly removing the limiting effects of atmospheric seeing. It is estimated that the upgraded resolution could be as high as 0.25'' at the correction centre, which is a large improvement on the current 1'' resolution. The new THEMIS will also have a higher throughput, so rasters will be able to be built faster with the

same SNR and polarimetric sensitivity.

2.4.4 Solar Dynamics Observatory

The *Solar Dynamics Observatory* (*SDO*, [Pesnell et al. 2012](#)) is a NASA satellite launched in 2010. *SDO* was designed as part of the NASA ‘Living With a Star’ program, aimed at further understanding the origins of space weather and its effects on Earth. It is comprised of three instruments, and is focussed on observing the Sun as a star. It has a full-disc UV/EUV imager, the *Atmospheric Imaging Assembly* (*AIA*, [Lemen et al. 2012](#)), an EUV Sun-as-a-star spectrometer, the *Extreme-ultraviolet Variability Experiment* (*EVE*, [Woods et al. 2012](#)), and the *Helioseismic and Magnetic Imager* (*HMI*, [Scherrer et al. 2012](#)), a full-disc photospheric magnetic field and visible-light continuum imager. *AIA* is the only instrument on *SDO* that is used in this thesis, as the other two do not lend themselves to prominence observations. *HMI* measures solar surface magnetic fields and photospheric Dopplergrams using the Fe I 6173 Å line, and unlike *THEMIS* it cannot measure prominence magnetic fields. This is due to the selected spectral line, which is formed in the photosphere and is not detectable in prominences. *EVE* is a spectrometer, however unlike *EIS* and *IRIS* it has no spatial resolution – it samples spectra from the Sun as a whole. Due to the observing nature of *EVE*, it is not useful for detailed prominence studies.

AIA is a UV/EUV full-disc imager (extending up to $+0.5R_{\odot}$), using four separate telescope systems to take images in ten wavebands with high temporal cadence, taking a set of images every 12s. *AIA* uses four CCDs that are 4096×4096 pixels in size. The spatial pixel size is $0.6''$, and the resulting spatial resolution is around $1.5''$. There are seven EUV bandpasses, two in the UV, and one white-light continuum bandpass (primarily for coalignment with other telescopes).

Most of the EUV filters of *AIA* (94 Å, 131 Å, 171 Å, 193 Å, 211 Å, and 335 Å) are sensitive to coronal temperature emission ($> 10^6$ K). The 304 Å filter, however, is dominated by emission from the He II 304 Å line, which is formed at chromospheric temperatures and is strongly in emission in prominences ([Labrosse & Gouttebroze 2004](#)). This means it is a good context image filter to complement prominence observations. Prominences are also visible as dark structures in some of the coronal filters, with prominence plasma absorbing and blocking emission from the background corona. This effect is largely caused by the presence of neutral hydrogen

and neutral/ionised helium in the prominence, which efficiently absorb wavelengths shorter than 912 \AA (H I), 504 \AA (He I), and 228 \AA (He II), which represent the heads of the relevant continua (Anzer & Heinzel 2005). Therefore for most of the AIA coronal channels these three species in a prominence will absorb part, or all, of the background coronal emission (the 335 \AA channel will be unaffected by He II continuum absorption). In fact, the dark structures seen in coronal channels generally match the H- α emission seen, due to the relationship between the optical thickness of the Lyman continuum below 912 \AA and that of the H- α line (Anzer & Heinzel 2005) – at 195 \AA $\tau_{195} = \tau_{\text{H-}\alpha}$, so the cool structure efficiently absorbs wavelengths at (and around) 195 \AA . Another reason for the reduction of intensity of coronal EUV wavelengths, also outlined in Anzer & Heinzel (2005), is due to *volume blocking*. This is where an extended region of cool plasma along the line of sight (which is not emitting in coronal lines) reduces the total emission of those lines along the l.o.s. by simply not contributing to that emission, as opposed to a l.o.s. through only coronal plasma.

AIA filters are naturally not monochromatic, so they contain emission from lines and continua formed at a range of temperatures. Because the EUV is a particularly busy part of the solar spectrum, this effect is unavoidable due to the width of the effective areas of the filters. However, this allows a ‘temperature response’ function to be constructed for each AIA filter (Boerner et al. 2012; Lemen et al. 2012) – the estimated filter response as a function of temperature. The result of this is that the EUV AIA filters can be used for DEM analysis (Hannah & Kontar 2012), especially in heating active regions or flares, meaning that AIA can provide more than just context images.

This chapter has outlined the concepts, analysis techniques, and instruments that are important for the research described in this thesis. Using these techniques a detailed spectral analysis of solar data can be made, revealing information about the plasma and magnetic field in prominences. The key to the work presented in the following chapters is the relationship between the observed spectral lines and the physical conditions of the plasma that emitted the photons which are detected. Plasma temperature structure, plasma motions and velocities, electron densities, and

magnetic field structure can all be derived from observed spectral line features. Using a combination of observations from *Hinode*, *IRIS*, *SDO*, and THEMIS, a picture of tornado-like prominences can be built. In order to answer the questions on whether these tornado structures are rotating or not, and on what the physical conditions are in tornadoes, spectral data must be used. Complemented by images and movies, the spectral data can be a powerful source of information.

Chapter 3

Plasma diagnostics of tornado-like prominences

With observations such as those by [Su et al. \(2012\)](#) reporting tornado-like motions in prominences by using time-distance diagrams from AIA, it became necessary to investigate the phenomenon further using spectral analysis. A logical first step is to investigate the line-of-sight velocity pattern of tornadoes – if they are a vertical, cylindrical (or conical) column rotating about a central axis one would expect them to have a very distinctive Doppler pattern. Rotating with a constant angular velocity would mean that, when viewed from the side, a tornado's velocity map would appear redshifted down one side of the column and blueshifted down the other, with zero Doppler shift in the middle. This anti-symmetrical pattern would be visible to slit spectrometers for tornadoes at the limb in lines where the optical thickness is 1 at the surface of the tornado. In September 2013 an observing campaign was run using the Extreme-ultraviolet Imaging Spectrometer (EIS) on the *Hinode* satellite to search for tornado-like prominences at the solar limb.

The campaign, designed by P. Gömöry (Astronomical Institute of the Slovak Academy of Sciences, Slovakia), consisted of two EIS observing modes and was repeated over the course of nine days in September 2013. On each day of the campaign a raster, a three-hour sit-and-stare and a second raster were taken using the 2'' slit of EIS. These studies were specially designed for observing tornadoes, with rasters named `eis_tornadoes_scan` and sit-and-stare studies named `eis_tornadoes_sns`. The rasters consisted of 50 slit positions, covering a spatial extent of 100'' in x , and the slit is 256'' long in the y direction. The sit-and-stare study used the same slit

length on one position, at the centre of the raster. These observations caught a tornado at the north-western limb of the Sun, on the 14 September 2013, and it is the data that is focused on in the first part of this analysis (§3.1). The results shown in the first part of this chapter are published in the peer-reviewed journal *Astronomy & Astrophysics* (Levens et al. 2015).

Further observing campaigns in 2014 also aimed to target tornado-like prominences, but this time using multiple instruments to do so. *Hinode* was again employed for these campaigns, along with the *IRIS* satellite and the ground-based observatory THEMIS. The campaigns, run in May and July 2014, observed a number of tornadoes with good spatial coverage from all three instruments. On the 15 July 2014 a prominence was observed which showed tornado-like motions in its legs. It is analysis of the data from this observation that constitutes the second part of this chapter (§3.3), which mainly focuses on plasma diagnostics from *IRIS* data. Further analysis of THEMIS and *Hinode* data from that day can be found in Chapter 4. Results from the second part of this chapter are published in *The Astrophysical Journal* (Levens et al. 2016a).

All analysis and figures presented in this chapter are original unless stated otherwise. Work done by co-authors of Levens et al. (2015) and Levens et al. (2016a) is clearly marked as such in this chapter, and any other research is original.

3.1 14 September 2013 – Observational overview

The EIS prominence observation on 14 September 2013 consists of two rasters, sandwiching a three-hour sit-and-stare study. A tornado-like prominence can be seen in the first raster and the sit-and-stare in this data set. By the second raster the tornado was no longer visible to EIS.

This data set was studied by Su et al. (2014), where they investigated line-of-sight velocities in coronal lines formed at temperatures from 1.5 – 2 MK. They found that there was a split, anti-symmetric Doppler pattern when looking at the tornado in both the raster and the sit-and-stare. From their study those authors concluded that the hot plasma observed indicates that the tornado is rotating around a central axis. They also showed non-thermal velocities across the structure, concluding that there was no clear structure, but that there could be small effects on the line width due to multiple threads. There is, however, much more that can be gained from a study

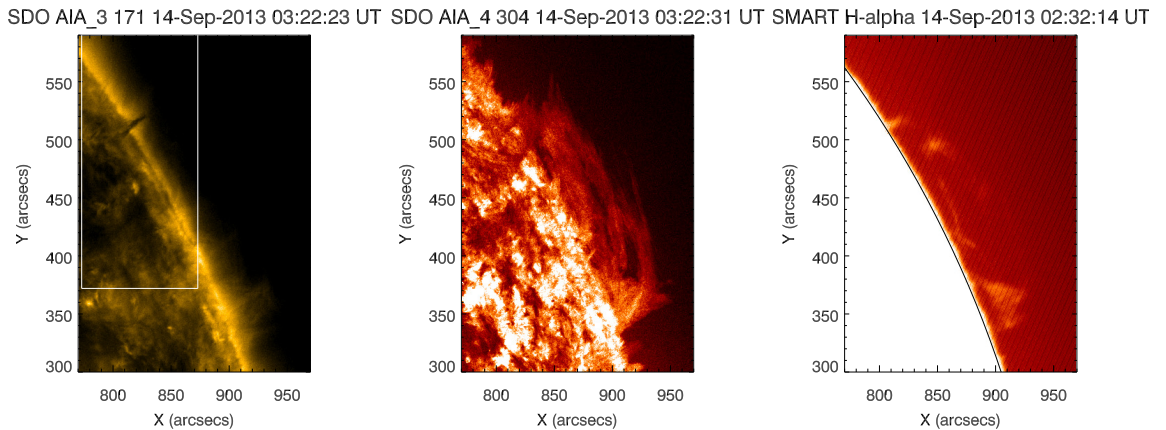


Figure 3.1: Images showing the tornado observed on 14 September 2013 by AIA 171 Å (*left*), AIA 304 Å (*middle*), and SMART at the Hida Observatory (*right*). White box in the left panel shows EIS pointing during its raster that day. This figure was used in [Levens et al. \(2015\)](#).

like this – electron densities, differential emission measures, as well as an extended plasma temperature range can all be investigated. Further analysis is required in order to fully understand the plasma properties of this tornado-like prominence.

3.1.1 Description of the event

The tornado observed on 14 September 2013 is relatively small, only around 20'' in height, and narrow at between 5–10'' in width. It is visible as a dark column in AIA coronal filters, most clearly in 171 Å (Figure 3.1, *left panel*) and 193 Å. It appears at the northern end of a more extended prominence which is seen in AIA 304 Å (Figure 3.1, *middle panel*). The tornado is also visible in emission in H- α , such as in the image from the *Solar Magnetic Activity Research Telescope* (SMART, Hida Observatory, Kyoto, Japan), and appears the same size as the dark structure in AIA (Figure 3.1, *right panel*). It appears darker in the AIA coronal channels than the surrounding corona due to emissivity blocking and absorption by the cool plasma ([Heinzel et al. 2008](#)). The column is mostly made of hydrogen (visible in the SMART image) and helium, and the absorption seen is due to the presence of H I, He I and He II. As described in §2.4.4, these species absorb coronal wavelengths below 912 Å, 504 Å, and 228 Å respectively ([Orrall & Schmahl 1976](#); [Labrosse et al. 2010](#)). Therefore

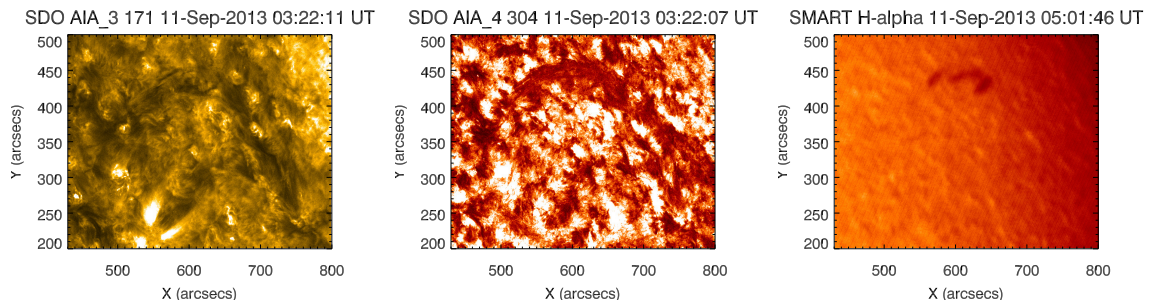


Figure 3.2: Observations on 11 September 2013 of the filament that would become the tornado-like prominence that was observed on 14 September 2013. *Left:* AIA 171 Å. *Middle:* AIA 304 Å. *Right:* SMART H- α . This figure was used in [Levens et al. \(2015\)](#).

nearly all background emission below these wavelengths is absorbed by the tornado, so any emission in AIA coronal channels or EIS EUV coronal lines is coming from in front of the tornado – the corona in front of the tornado and perhaps a ‘sheath’ of hot plasma at the top of the PCTR. The prominence could be seen for a number of days before it crossed the limb as a filament on the disc, as shown in Figure 3.2.

The EIS raster field of view is shown in white in the AIA 171 Å image (Figure 3.1, *left panel*). The tornado is seen at the centre of that field of view. Figure 3.3 shows the EIS 195.119 Å Fe XII raster alongside the corresponding AIA 193 Å with the same field of view. The EIS image is the result of Gaussian fitting of the Fe XII 195 Å doublet (see §3.1.3). Emission in the AIA 193 Å waveband is predominantly from Fe XII, so the emission seen is nearly identical to that of the EIS 195.119 Å line.

As well as being the strongest line observed by EIS, the Fe XII line at 195.119 Å is also the line that shows the tornado structure most clearly in this study. In that raster map the tornado is visible, but there is also some other structure visible above the limb, extending southwards from the top of the tornado, which is co-spatial with the main prominence body as seen in 304 Å and some faint emission visible in H- α .

3.1.2 Data reduction

All EIS data is acquired as level-0 data files, so must be calibrated to level-1 before it can be used for analysis. Calibration is done using the standard EIS SSW routine `eis_prep`, which removes hot/warm pixels, dark currents, and cosmic-ray hits, as

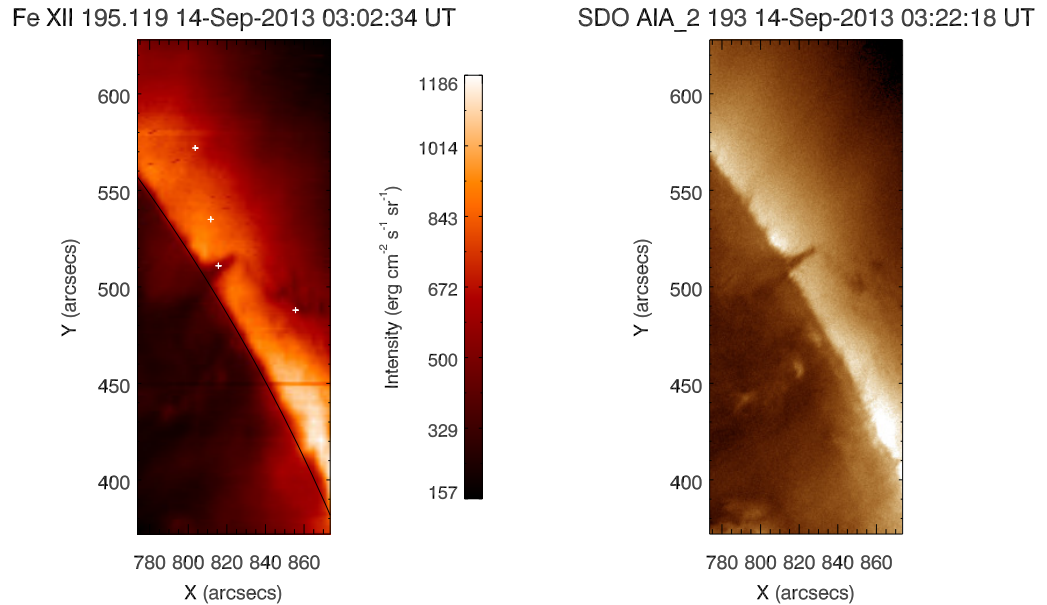


Figure 3.3: Intensity maps of the tornado observed on 14 September 2013. *Left:* EIS Fe XII 195.119 Å integrated line intensity from Gaussian fitting. White plus markers indicate points where DEMs are calculated in §3.2.4. *Right:* AIA 193 Å image. This figure was used in [Levens et al. \(2015\)](#).

well as performing absolute calibration of the data. Using CHIANTI v7.1 ([Dere et al. 1997](#); [Landi et al. 2013](#)) – the latest version of CHIANTI at the time that this analysis was carried out – spectral lines visible in the EIS spectral windows can be identified, and assuming a Gaussian fit to each they are fit using the `mpfit` SSW package ([Markwardt 2009](#)).

Wavelength calibration is done using the Fe VIII 185.213 Å line. This is a favoured spectral line for calibration as it is isolated, with no known blends, that is formed at a relatively low temperature, and does not generally display large Doppler velocities in quiet-sun regions. Averaging over 20 pixels in y the Fe VIII 185.213 Å spectrum for the quiet sun can be isolated, where binning the data removes pixel-to-pixel Doppler shifts. This corrects for orbital variations and solar rotation, but in order to investigate the tornado itself it is advantageous to take the zero velocity for the map as that at a central part of the tornado – in the frame of the tornado, and under the assumption of rotation, the centre of the column would have zero l.o.s. velocity.

Table 3.1: EIS spectral lines used in the analysis of the tornado on 14 September 2013. Ions are listed in order of wavelength, from short to long.

Ion	Wavelength (Å)	log T(K)	Blend
Fe x	184.537	6.1	Fe xi
Fe viii	185.213	5.7	–
Fe xi	188.216	6.2	Fe xii, Fe xi
Fe xi	188.299	6.2	Fe xii, Fe xi
Fe xi	192.627	6.2	–
Fe xi	192.814	6.2	O v, Ca xvii
O v	192.904	5.4	O v, Fe xi, Ca xvii
Fe xii	195.119	6.2	Fe xii
Fe xii	195.179	6.2	Fe xii
Fe ix	197.862	6.0	–
Fe xiii	202.044	6.3	–
He ii	256.320	4.9	S x, Fe x, Fe xiii, Fe xii
Si vii	275.361	5.8	–

Further intensity calibration of EIS data has become necessary in recent years due to the fact that the EIS detectors are decaying as a function of both time and wavelength (Del Zanna 2013; Warren et al. 2014) as opposed to simply as a function of time that was initially assumed. Two similar methods were outlined in those papers as a solution to this, and it is the more recent method of Warren et al. (2014) that is used here to correct the data. This method is simple to implement, where an SSW routine called `eis_recalibrate_intensity` calculates the calibration required on a given day for each wavelength, and applies it to the data at each pixel.

3.1.3 Spectral lines used for analysis

The studies `eis_tornadoes_scan` and `eis_tornadoes_sns` contained the same spectral window selection. Table 3.1 contains all the lines considered during the analysis of this event. Most lines are emitted by relatively hot plasma, compared to the cool plasma expected in prominence cores ($\log T \sim 4$). Any hotter plasma emission seen along the line of sight looking towards the tornado could be coming from a

combination of the foreground corona and the presence of a prominence-to-corona transition region (PCTR), as outlined in §1.2.

EIS observes a number of blended spectral lines, due to the finite spectral resolution of the instrument and because the EUV is a busy part of the solar spectrum. Using Gaussian fitting techniques outlined here and in §2.2.1 it is possible to resolve some of the blended lines. The following subsections detail specific de-blending procedures for each blend.

3.1.3.1 Fe x 184 Å blend

The Fe x line at 184.537 Å has a small contribution from an Fe xi line in its blue wing. Although it is weaker than the Fe x line, the Fe xi line, centred at 184.41 Å, is not negligible. A simple two-Gaussian fit is enough to remove the Fe xi component from the blend. This leaves the Fe x line, which is the only line from that ion in this study.

3.1.3.2 Fe xi 188 Å blend

The Fe xi doublet at 188.2 Å is partly resolvable. The two Fe xi lines that comprise it, at 188.219 Å and 188.299 Å, are the strongest lines in the blend, but there is also a small component of Fe xii in the blue wing. To fit this group the centroids of the two Fe xi lines are tied together – it is assumed that similar ion species are always moving with the same velocity, hence their Doppler shift will be the same. In some cases relative intensities can be tied for similar lines, but that cannot be done here because the 188.219 Å and 188.299 Å lines display density sensitivity (see §2.2.2). After the centroids of the Fe xi lines are tied, the group can be de-blended using three Gaussians. There is also an Fe ix line in this window, that is separate from the main blend, at 188.497 Å. This line is far enough from the blend that it can be fitted with a single Gaussian.

3.1.3.3 Fe xi and O v 192 Å blend

The blend at 192 Å is one of the most complicated blends seen by EIS. A number of authors have worked to de-blend these lines (Ko et al. 2009; Graham et al. 2013), mostly in flaring or active regions. Unlike in the quiet corona and prominence considered here, those regions have strong emission from a Ca xvii line, formed at $\log T = 6.8$. Those temperatures are commonly seen in flares, but in this raster

a minute contribution from plasma at that temperature would be expected, and therefore the Ca xvii line will contribute a negligible amount to the blend. Instead the Fe xi line at 192.814 Å becomes the dominant line in the blend, with significant contribution from O v lines, especially in the prominence.

There is another Fe xi line visible in this window at 192.627 Å, distinct from the blend. Being separate from the blend it is possible to fit this line with a single Gaussian, and it is always visible in this raster. It is therefore possible to tie the centroid of the blended Fe xi line to the centroid of this line, removing one unknown variable from the multi-Gaussian fit of the blend. The intensity ratio of these lines displays some density sensitivity (see §3.2.2.1), so the line intensities cannot be tied.

There are five O v lines in this blend, which are difficult to deal with. They are the only O v lines in the study so there is no way to tie parameters to lines external to the blend. Simplifying the lines in the blend is therefore necessary to achieve a good fit to the blend. These lines are handled here by making two assumptions about them – the first being that the five lines can be modelled by two Gaussians centred on the strongest lines (192.904 Å and 192.797 Å), and second that these Gaussians can be tied together in both centroid and in intensity values. Simplifying the O v lines in this way means that the blend can be fitted with three Gaussians (plus one outside the main group) instead of a potential seven. However, assuming a fixed intensity ratio between the two strongest O v lines is not entirely accurate as these lines do have a density sensitivity. The choice to take this step is justified by the fact that the density curve including all five lines, shown in Figure 3.4, shows a minimal density sensitivity in the range of densities expected in prominences. As outlined in §1.2.2 and Labrosse et al. (2010), the electron density calculated from O v would be around $\log n_e \sim 9.5$ for an active region prominence, and slightly lower for a quiescent prominence. Therefore a value of $I_{192.797} = 0.4I_{192.904}$ is taken for the intensity ratio for the lines.

Figure 3.5 shows an example of the resulting four-Gaussian fit to the 192 Å spectral window. The original spectrum is shown as a histogram, with error bars. The leftmost Gaussian, shown in orange, is the Fe xi 192.627 Å line. The fit for the 192.814 Å Fe xi line is plotted in green, and the two O v fits are shown in blue and purple. A thin blue line is plotted to represent the overall contribution from the O v lines. The overall fit to the line is shown as a solid black curve. This de-blending procedure is adequate for this analysis, and is the best possible using the

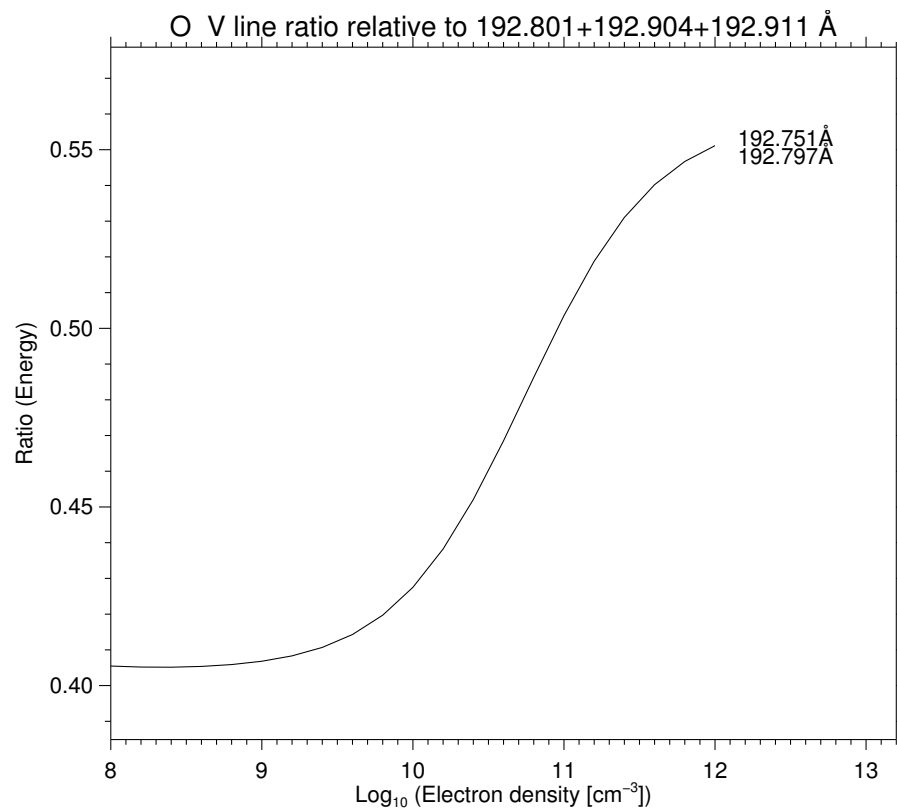


Figure 3.4: Density curve for the O v lines at 192 Å. Plotted is intensity ratio of the O v 192.797 Å/192.904 Å lines vs. electron density. Plot was made using CHIANTI v8.0.

lines available.

3.1.3.4 Fe xii 195 Å blend

The Fe xii line at 195.119 Å is the strongest line observed by EIS, due to the fact that it is inherently a strong line and it is located almost at the peak of the EIS short wavelength CCD response function (Culhane et al. 2007). The resulting high signal-to-noise ratio (SNR) means that it is an excellent line for use in analysis. There is contribution from another small Fe xii line at 195.179 Å, in the red wing of the dominant 195.119 Å line, that is non-negligible. To fit these lines a double Gaussian is used and, as with the Fe xi lines in §3.1.3.2, the centroid positions are tied together. Relative intensity values cannot be tied together as the 195.119 Å and 195.179 Å lines form a density-sensitive pair, as seen in Figure 3.6. Figure 3.7 shows the de-blending

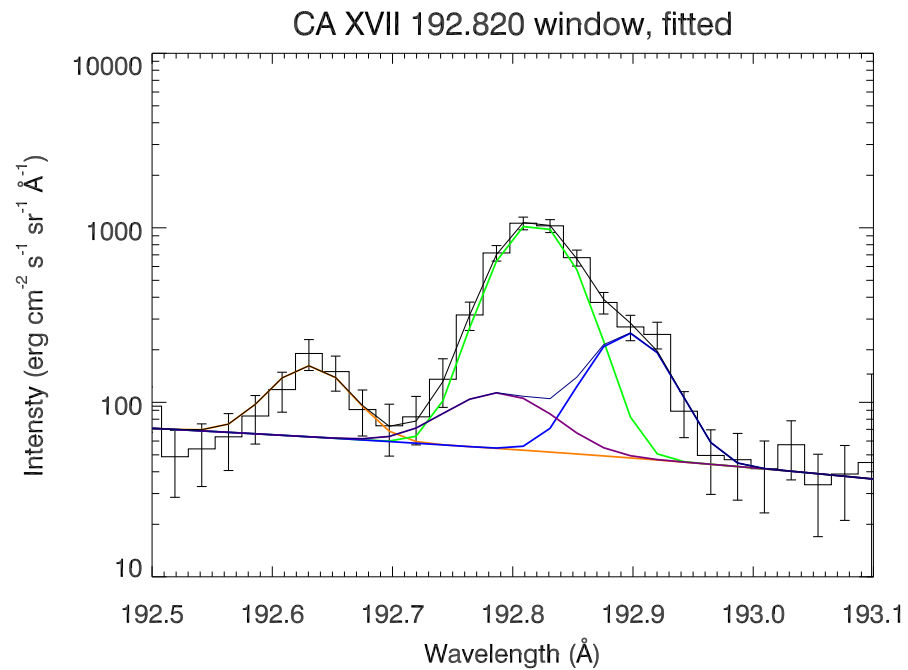


Figure 3.5: Fitted EIS 192 Å spectral window, showing the Gaussian fits to the blend. The original spectrum is shown as a histogram with error bars. Orange line is Fe XI 192.627 Å, green line is Fe XI 192.814 Å. Purple and blue lines show O V lines at 192.797 Å and 192.904 Å respectively. The thin, dark blue line shows overall contribution from O V, and the black line shows overall fit to the spectrum. This figure was used in [Levens et al. \(2015\)](#).

result for these lines. The dominant line in the blend, 195.119 Å, is shown in dark red, and the smaller 195.179 Å component is shown in magenta. A third line is visible at 195.4 Å, which is an unidentified line that is fitted in order to remove it from the background baseline of the two Fe XII lines.

3.1.3.5 He II 256 Å blend

The He II doublet at 256.32 Å are lines formed at the lowest plasma temperatures that EIS observes. He II emission at this wavelength is optically thick ([Labrosse & Gouttebroze 2001](#)), and prominences can generally be seen clearly in helium emission, mostly through scattered chromospheric light. When observed by EIS, however, the He II emission is complicated by its proximity to other lines which

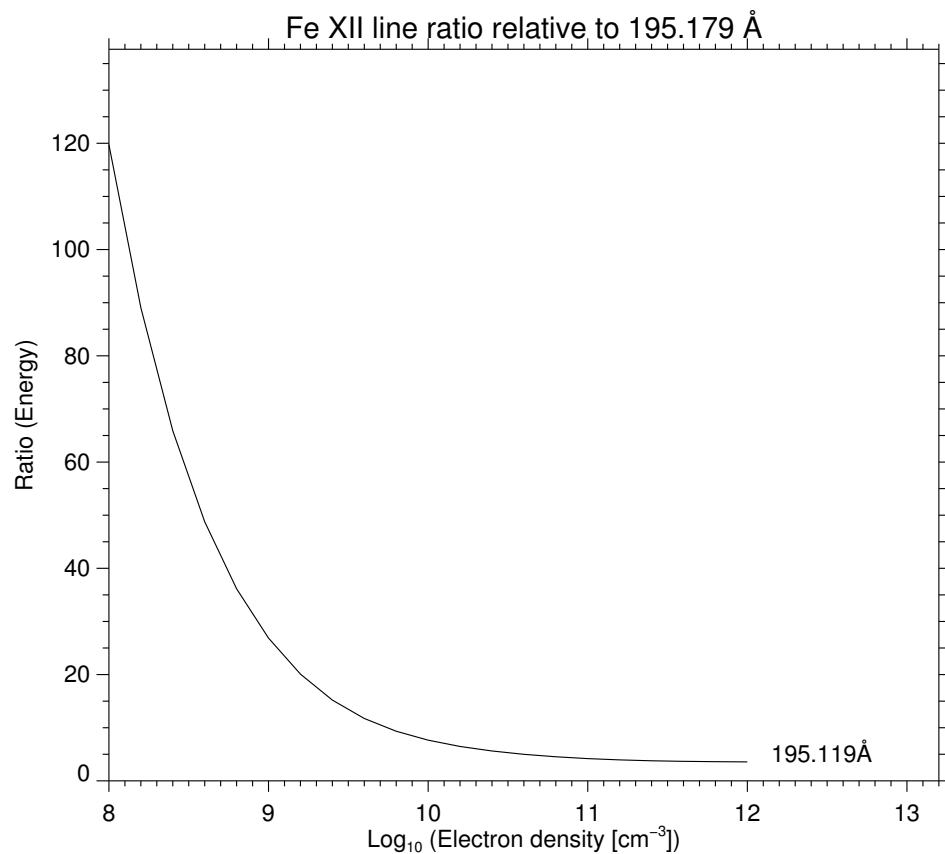


Figure 3.6: Intensity ratio of the Fe XII 195.119 Å/195.179 Å lines vs. electron density. Plot was made using CHIANTI v8.o.

are formed at much higher plasma temperatures ($\log T > 6$) – components of S x, Fe x, Fe XII, and Fe XIII are all close enough to contribute to the blend. These lines significantly complicate the analysis of this blend. Some progress can be made by noting that the He II lines are on the blue side of the blend and the hotter lines all appear on the red side of the blend. This way two Gaussians can be used to distinguish the cooler emission of He II from the hotter emission of all the other lines.

It must be noted, however, that this is a significant simplification and the resulting Gaussian fits cannot be regarded as accurate enough for detailed spectral analysis. The He II lines are optically thick, and nominally should have a non-Gaussian profile. For these reasons the He II line (and others in the 256 Å window) is largely absent from the detailed analysis performed here. It is still worthwhile considering this He II line, as it is one of the strongest lines observed by EIS, and one of the few that EIS observes that shows prominences in emission. Considerable work was done on

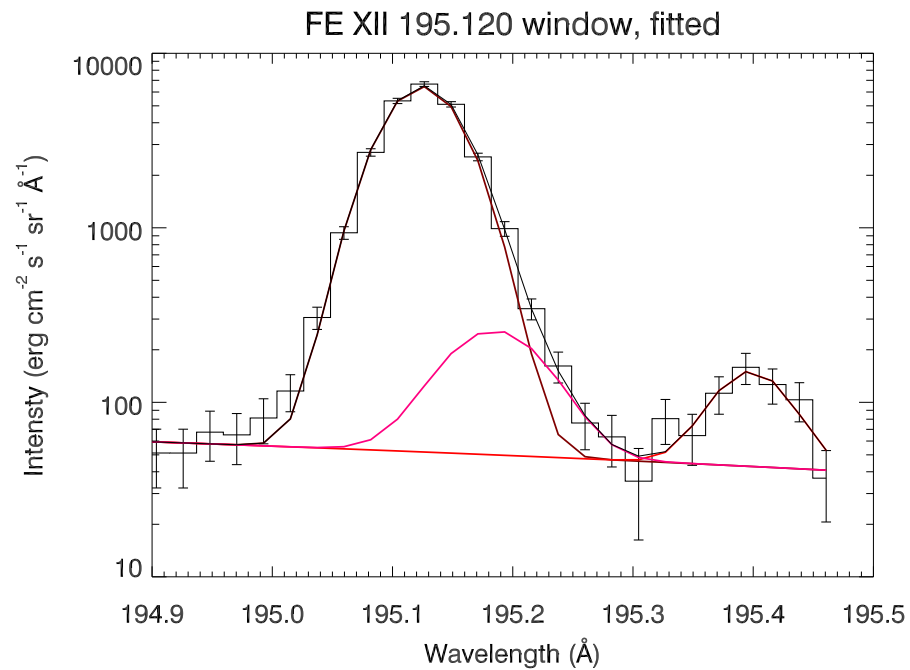


Figure 3.7: Result of the fitting of the EIS 195 Å spectral window. The original spectrum is shown as a histogram with error bars. Each fitted line is represented by a coloured Gaussian. Dark red and magenta Gaussians are the Fe XII 195.119 Å and 195.179 Å lines respectively. The red line shows an unidentified line at around 195.4 Å. Overall fit to the spectrum is shown as a black curve. This figure was used in [Levens et al. \(2015\)](#).

this blend by [Labrosse et al. \(2011\)](#) for a prominence observed in 2007. However in that paper they also recognise the limitations of the two-Gaussian de-blending approach.

3.2 Plasma diagnostics

Using the Gaussian parameters provided from the fitting of the EIS spectral lines, a number of plasma parameters can be probed. Some parameters can be taken directly from the Gaussian parameters, such as Doppler shifts, whereas others need more in-depth analysis, such as electron density diagnostics or DEM. The background for these techniques are outlined in §2.2.

3.2.1 Line-of-sight velocity measurements

Taking the centroid position of the Gaussian function fitted to a spectral line, it is possible to derive a Doppler velocity along the line-of-sight. This method is commonly used in spectral analysis, and it is the method used by [Su et al. \(2014\)](#) on this event to calculate line-of-sight velocities that suggest the tornado is rotating. In that analysis they studied Fe XII and Fe XIII lines, at 195.119 Å and 202.044 Å respectively, finding that the tornado has a split Doppler pattern across its width, consistent with what would be expected for a rotating column. The aim of the analysis presented here is to verify and extend that finding, considering other lines available from the raster.

The first step in this analysis is calculating the Doppler shifts themselves, which require a value for the non-shifted wavelength of the lines. As described in §3.1.2, absolute wavelength calibration is performed using the Fe VIII line, but further calibration on a line-by-line basis is done in order to put the observations in the reference frame of the tornado. This is done by selecting a pixel that is at the centre of the tornado structure in the 195.119 Å intensity map and specifying that it has zero Doppler shift in all lines. This step gives a value for zero velocity, under the assumption that the tornado is a column rotating about a central axis, allowing easy measurement of the redshifts and blueshifts on either side of the column that would be expected for such a structure.

With a zero wavelength, λ_0 , determined, the Doppler velocity, v_D , can be calculated using Equation 2.14 (page 45). By calculating this value at each pixel, for each line, maps of velocity can be constructed, giving a visual representation of the l.o.s. velocity in the region of the tornado. Figure 3.8 (*left panel*) shows one such velocity map for the Fe XII 195.119 Å line made using the raster at 03:04 UT on the 14 September 2013. The right panel of Figure 3.8 shows a zoom in of the tornado region, which is outlined as a purple bounding box in the left panel. These maps show the split, anti-symmetric Doppler pattern around the axis of the tornado, similarly to the analysis in [Su et al. \(2014\)](#). Extending this view to other ionised iron lines available in this study (Fe VIII – Fe XIII), emitted at a range of plasma temperatures, a number of things become notable. Figure 3.9 shows a close-up view of velocity maps of the tornado region in Fe VIII ($\log T \sim 5.7$, *top left*), Fe IX ($\log T \sim 6.0$, *top right*), Fe XI ($\log T \sim 6.2$, *bottom left*) and Fe XIII ($\log T \sim 6.3$, *bottom right*) lines. In

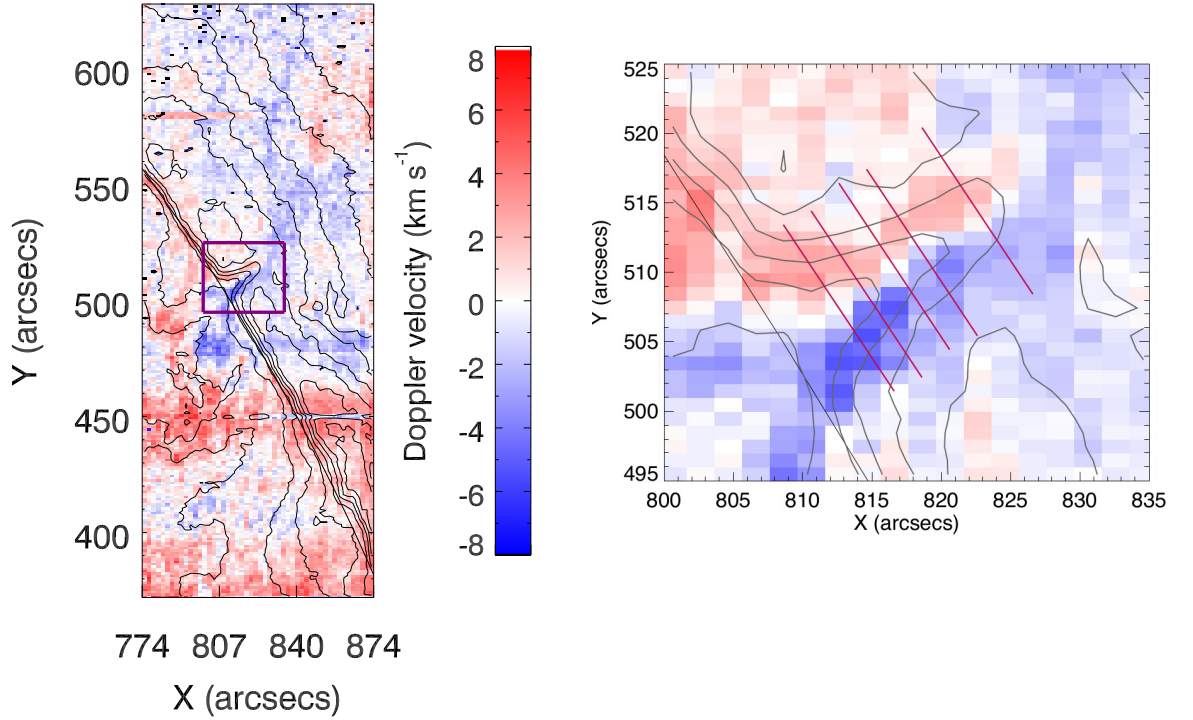


Figure 3.8: Doppler velocity maps of the Fe XII 195.119 Å line, calculated from the fitted Gaussian centroid value. Contours are from the 195.119 Å intensity image, to help identify the tornado. *Left:* Full EIS FOV. Purple bounding box shows FOV of the right panel. *Right:* Close up of the tornado region. Parallel lines show positions of cuts through tornado axis.

these maps the split Doppler pattern is visible in all but the lowest temperature line, Fe VIII 185.213 Å. All iron lines in this study formed above $\log T = 6.0$ show the characteristic Doppler pattern that has previously been presented as evidence for rotation.

Taking cuts mid-way up the tornado column (third cut, Figure 3.8 right panel) through the maps from iron lines formed at a plasma temperature $\log T \geq 6$, perpendicular to the long axis of the tornado column, the anti-symmetric Doppler pattern is evident. This is shown in Figure 3.10, where cuts through the velocity maps as seen in Fe IX 197.86 Å, Fe X 184.54 Å, Fe XI 188.21 Å and 192.63 Å, Fe XII 195.12 Å, and Fe XIII 202.04 Å lines are presented. Error bars are derived by propagating errors from the observed spectral intensities through the Gaussian fitting parameters to give an error on line centroid position. The pattern is clearly visible in all these

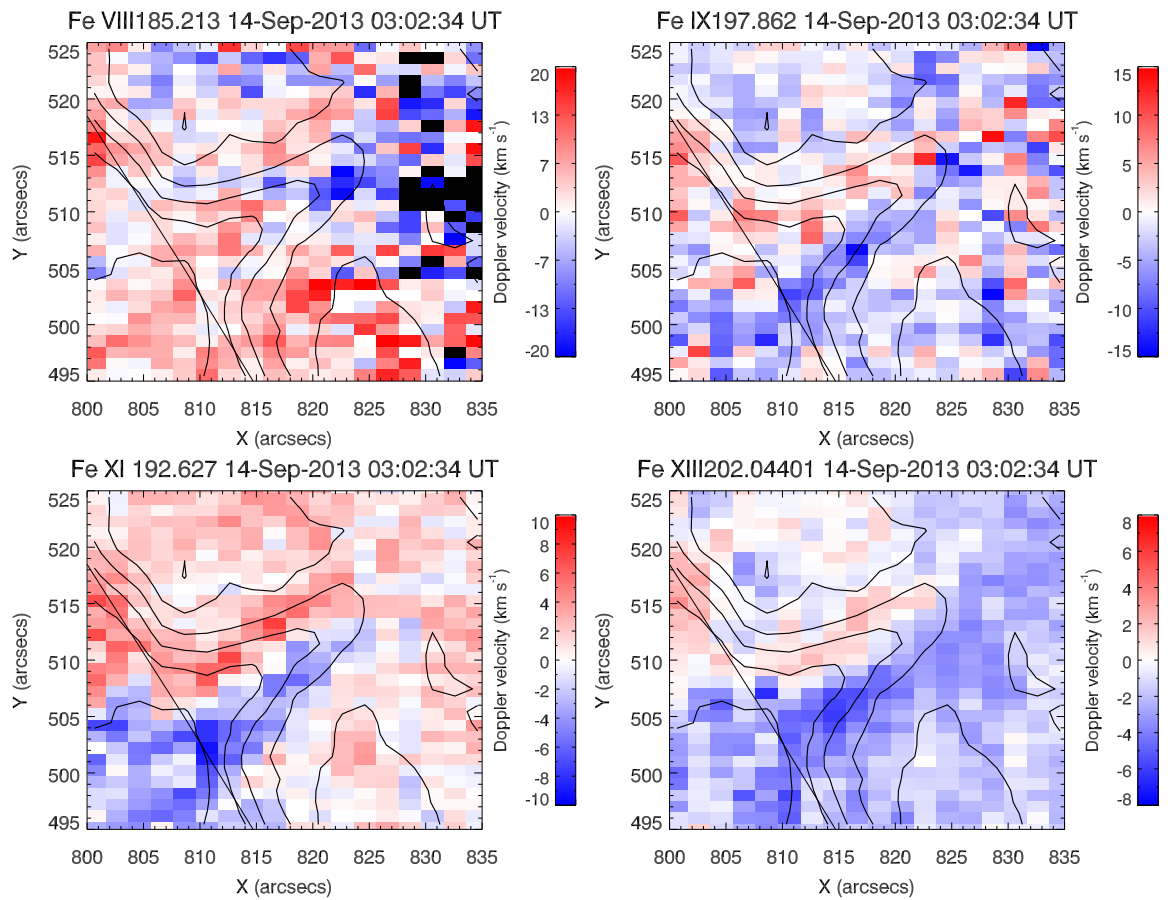


Figure 3.9: Doppler velocity maps of the tornado region for a number of ionised iron lines, formed at a range of plasma temperatures. Note different colour bar ranges for each plot. Colour bars are displayed to the right of the relevant plot. Contours are from the 195.119 \AA intensity image, to help identify the tornado. *Top left:* Fe VIII, $\log T = 5.7$. *Top right:* Fe IX, $\log T = 6.0$. *Bottom left:* Fe XI, $\log T = 6.2$. *Bottom right:* Fe XIII, $\log T = 6.3$.

lines, with the northern edge of the tornado (left half of Figure 3.10) redshifted and the southern edge (right half of Figure 3.10) blueshifted. The previously reported analysis in Su et al. (2014) evidence was only given for this pattern in the iron lines formed at $\log T > 6.2$, but here it has been possible to extend this pattern down to a plasma temperature of $\log T \simeq 6.0$. If this is taken as evidence for rotation, and the tornado is seen as a cool core with PCTR extending to high coronal temperatures, then that rotation would be expected to extend down through the temperature layers of the PCTR and into the core of the structure – this is the implied velocity structure

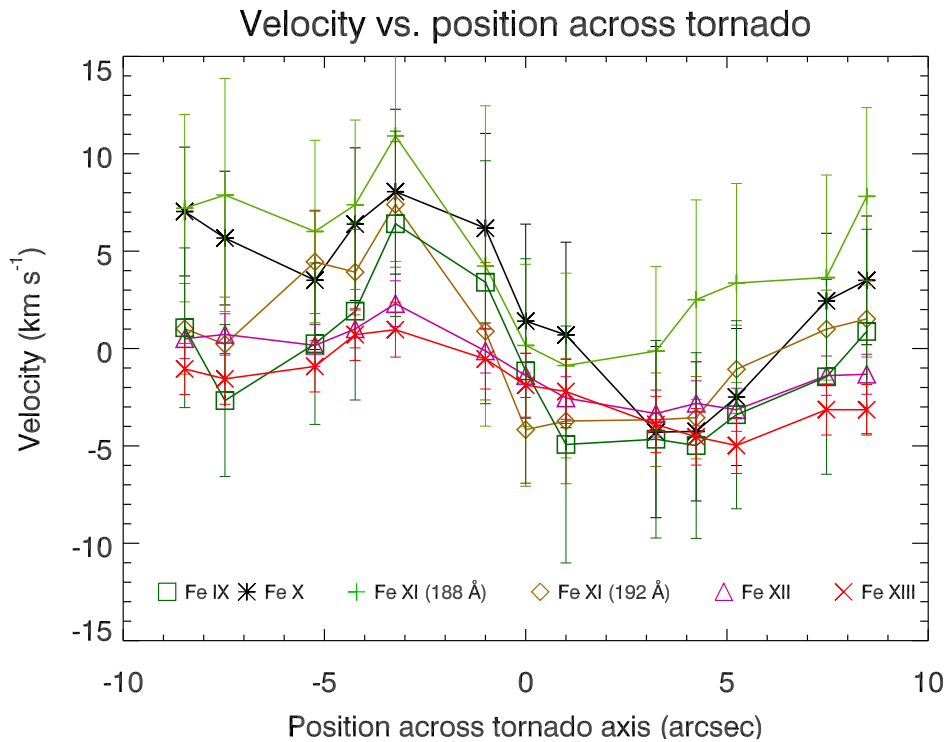


Figure 3.10: Line-of-sight velocities for Fe IX – Fe XIII lines for a cut through the tornado axis. The cut used here is the middle cut shown in Figure 3.8 (*right panel*). The tornado has a spatial extent of approximately $10''$ centred on the 0 of the x -axis. This figure was used in [Levens et al. \(2015\)](#).

by the observations of [Orozco Suárez et al. \(2012\)](#) and [Wedemeyer et al. \(2013a\)](#), where tornado-like Doppler patterns were found in lines formed at low plasma temperatures ($T \sim 10^4$ K).

The question then arises on what happens in this tornado at plasma temperatures lower than 1 MK. As can be seen in Figure 3.9, the Fe VIII line (formed at $\log T \sim 5.7$) does not echo the Doppler pattern seen at higher plasma temperatures. Other lines formed at lower plasma temperatures, such as the O V lines at 192 \AA and the Si VII line at 275 \AA , also show a lack of consistent Doppler pattern. There are a number of issues with analysing these lines in the prominence. As discussed in §3.1.3.3, the O V lines are heavily blended, so in order to de-blend them from other lines a number of assumptions must be made about them. To see any systematic line shifts the de-blending needs to be accurate, as expected line shifts will be small. Any uncertainty in the fitting of these lines, and the assumptions made to de-blend them,

could make any analysis of the Doppler velocities found unreliable. In the other lines there is a question of the signal-to-noise ratio above the limb – Fe VIII and Si VII emission is not expected to be strong in prominences, and it is clear from the spectra that these lines do not emit strongly in this prominence. Therefore any emission sampled in the tornado will be weak, and the fitted lines will not necessarily be far enough above the background for the derived l.o.s. velocity to be trustworthy.

A further effect that could be affecting this data and must be acknowledged is an instrumental one. It has been reported (Young et al. 2012, appendix B) that an artificial Doppler shift may be introduced by a tilted and elliptical point spread function (PSF), similar to that seen in *SOHO*/CDS data (Haugan 1999). It is suggested that this artificial Doppler shift would be found in regions where there is a large intensity gradient north-south along the EIS slit. The instrumental shift introduced by this effect is expected to be offset from the intensity maximum by around three to four pixels ($\sim 3 - 4''$)¹. With an increasing intensity gradient (dark to light) north to south along the slit, a blueshift would be introduced, whereas a decreasing intensity gradient (light to dark) north to south would introduce a redshift. In either case the expected artificial Doppler shift introduced is around 5 km s^{-1} (Young et al. 2012).

The potential implication of this artificial shift on the results shown here could be large. The velocity maps from the higher temperature lines where the split Doppler pattern is seen also correspond to lines where the absorption feature is seen most clearly against background coronal emission. However, the Fe IX and Fe X lines studied here have l.o.s. velocities in the tornado exceeding the expected 5 km s^{-1} from this effect. Also, notably, there is no specific intensity gradient quoted in the literature above which this effect is expected. Therefore it is difficult to assess whether the tornado data shown here is consistently being affected by this instrumental shift or not.

It is worth noting at this stage that there are other observations using different instruments that independently support the idea of rotational Doppler patterns in tornado-like prominence legs. As mentioned previously, Orozco Suárez et al. (2012) used the ground-based *Vacuum Tower Telescope* (VTT) to observe tornadoes, finding anti-symmetric Doppler shifts of around $\pm 20 \text{ km s}^{-1}$ on opposite sides of a tornado in the He I 10830 Å line. A similar pattern was found in an H- α observation of a

¹<http://solarb.mssl.ucl.ac.uk:8080/eiswiki/Wiki.jsp?page=Spatialoffsetofintensityandvelocityfeatures>

tornado by [Wedemeyer et al. \(2013a\)](#) using the ground-based *Swedish Solar Telescope* (SST), with redshifts of $10 - 30 \text{ km s}^{-1}$ observed on one side of the tornado column and blueshifts of $20 - 30 \text{ km s}^{-1}$ observed on the other. These results are, however, debated ([Panasenco et al. 2014](#)).

3.2.2 Density diagnostics

There are five density sensitive line pairs that are potentially useful for electron density diagnostics in this EIS study. As was alluded to in §3.1.3, there is one Fe XII pair that can be used, as well as three Fe XI pairs and a Fe IX pair. The Fe IX pair (188.497 \AA and 197.862 \AA) cannot be used as the density curve contains a local maximum, meaning that there is a non-unique density value for certain intensity ratios. Another potential diagnostic from O V is also ruled out due to the assumptions that had to be made to de-blend those lines, outlined in §3.1.3.3. The Fe XI and Fe XII lines considered here are all formed at plasma temperatures in the region of $\log T \sim 6.2$, so at the same temperatures that the split Doppler pattern is seen in.

3.2.2.1 Fe XI diagnostics

The three Fe XI diagnostics that are available all use the 192.627 \AA line as one of the diagnostic pair. The other Fe XI lines used are the 188.216 \AA , 188.299 \AA , and 192.814 \AA lines. Between these three lines there are no useful diagnostic pairs, so they each need to be compared to the 192.627 \AA line for diagnosis. Figure 3.11 shows a density map of the tornado region made using the $192.627 \text{ \AA}/192.814 \text{ \AA}$ ratio. This map shows a dip in density at the tornado location, with electron densities of around $\log n_e = 8.5 - 9$ recovered in the region of the tornado. Intensity contours of the Fe XII 195.119 \AA line are included to help identify the tornado. The density maps of the other two line pairs are identical, showing the same density dip at the tornado.

3.2.2.2 Fe XII diagnostic

The density map for the Fe XII line pair $195.119 \text{ \AA}/195.179 \text{ \AA}$ is shown in Figure 3.12. This map has intensity contours of the Fe XII 195.119 \AA line plotted to identify the tornado location, and cut locations used in Figure 3.13. As in the Fe XI maps (Figure 3.11) a small dip in density can be seen when looking towards the tornado. Figure 3.13 shows five parallel cuts through the tornado at different places in the

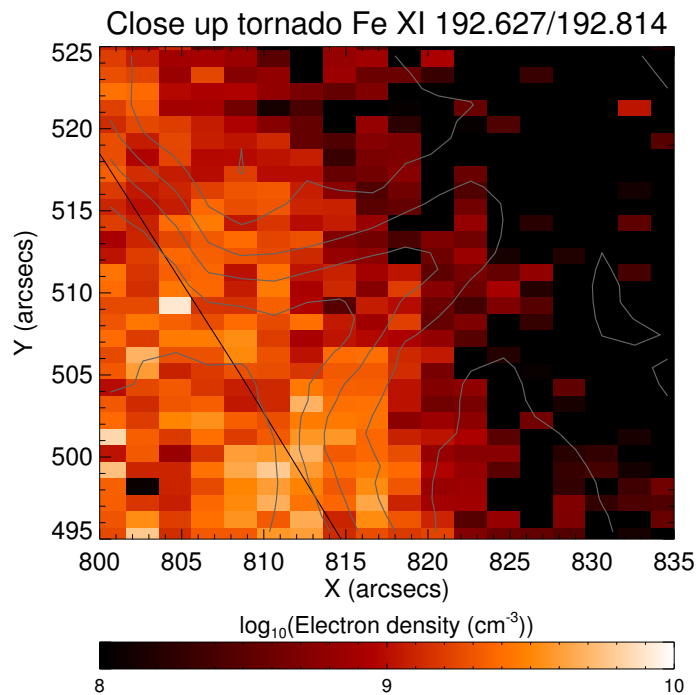


Figure 3.11: Electron density map for the ratio of Fe XI lines $192.627 \text{ \AA}/192.814 \text{ \AA}$. Contours are from the Fe XII 195.119 \AA intensity map. This figure was used in [Levens et al. \(2015\)](#).

density maps. These cuts, perpendicular to the tornado axis, show how the density changes across the width of the tornado. The dip in intensity can clearly be seen in Figure 3.13, especially in ‘cut 3’ (triangle markers, magenta line). This drop in density is around a factor of three, from around $\log n_e = 9$ to about $\log n_e = 8.5$. Other cuts also show a dip when looking at the centre of the tornado. The uppermost cut (‘cut 1’, plus markers, light green line) does not show any pattern, however this cut is at the top of the tornado and higher into the corona than the other cuts, so it is expected that the ambient coronal density will be lower here than at locations nearer the limb. The density values found here are consistent with previously reported values ([Labrosse et al. 2010](#)).

These observations raise questions about the origin of this density dip. As was discussed in §3.2.1, if the velocity pattern is coming from the tornado region, then it follows that the density pattern could also be coming from that region. The diagnostics used here are a measure of the electron density at a temperature of

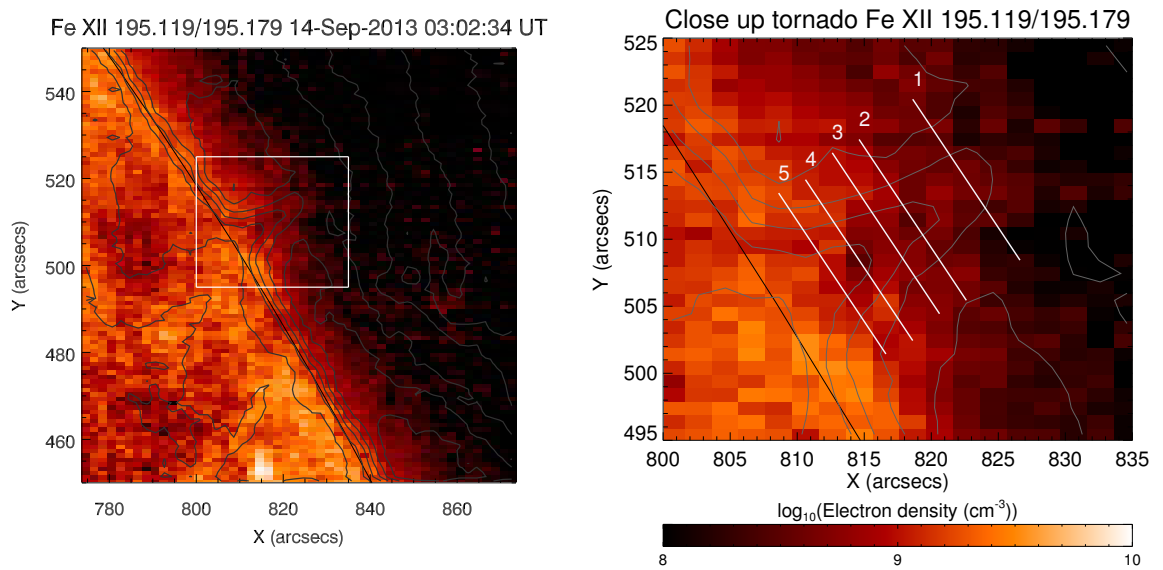


Figure 3.12: Electron density maps made using the Fe XII 195.119 Å/195.179 Å intensity ratio. Contours are from the Fe XII 195.119 Å intensity map. *Left:* Extended field of view showing more of the surrounding region. White bounding box is the field of view of the right panel. *Right:* Close up of the tornado region. Parallel white numbered lines indicate the positions of cuts through the tornado axis used in Figures 3.13 and 3.15. This figure was used in [Levens et al. \(2015\)](#).

$\log T = 6.2$, and the dip in density is visible in all available diagnostic pairs at that temperature. This suggests that the hot plasma that appears to be rotating is also less dense than the surrounding corona.

3.2.3 Non-thermal line widths

When emitted, spectral lines have a specific wavelength attributed to them. In an ideal case, each spectral line would be observed as a narrow δ -function of infinitely narrow width. Some natural broadening occurs, as described in §2.1. However, spectral lines are generally found to be further broadened when observed, and this broadening can be attributed to three main factors – instrumental, thermal, and non-thermal. Firstly the instrumental width, broadening caused by the optics of the telescope, generally has a measured value and can easily be removed from the measured profile width. Second is the thermal width, which is caused by thermal motions

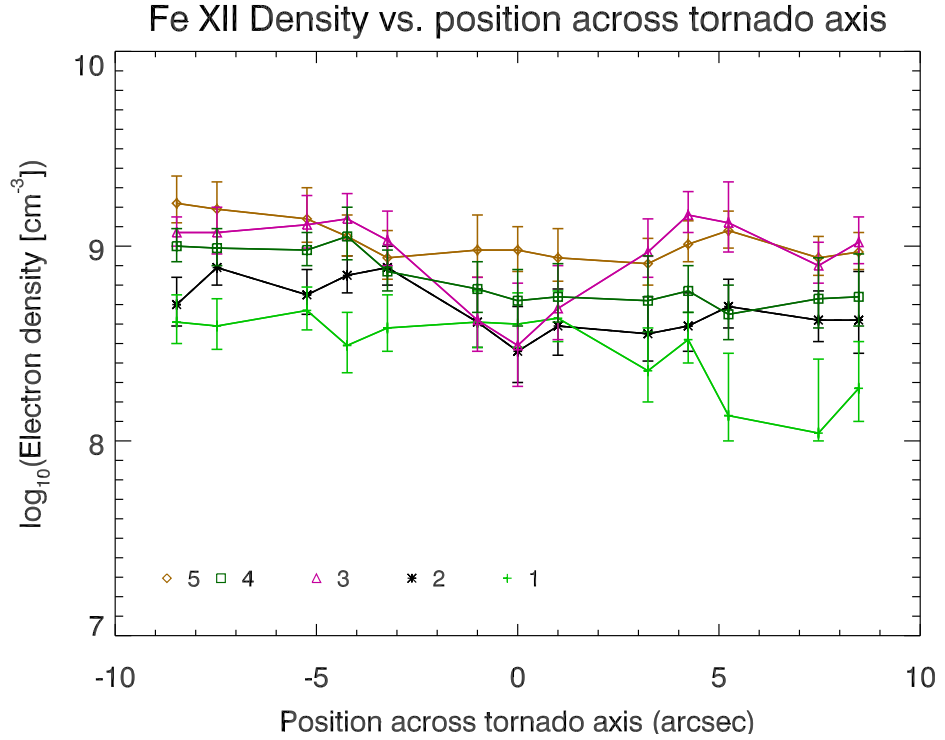


Figure 3.13: Electron density along five parallel cuts through the tornado at different distances from the solar limb. Cuts are numbered as in the right panel of Figure 3.12. The tornado has a spatial extent of approximately $10''$ centred on the 0 of the x -axis. This figure was used in [Levens et al. \(2015\)](#).

due to the ambient plasma temperature. The thermal width, $\Delta\lambda_{\text{th}}$, is characterised by Equation 2.16 (page 46). Any remaining line width is the non-thermal line width (NTLW), which could be caused by waves in the plasma, or motions caused directly by the magnetic pressure such as shifting or oscillating magnetic fields forcing the plasma to flow.

Assuming that each of the broadening mechanisms can be characterised by a Gaussian profile, the measured line width, $\Delta\lambda_{\text{meas}}$, can be split up into instrumental width, $\Delta\lambda_{\text{inst}}$, thermal width, $\Delta\lambda_{\text{th}}$, and non-thermal width, $\Delta\lambda_{\text{NT}}$, using Equation 3.1.

$$\Delta\lambda_{\text{meas}}^2 = \Delta\lambda_{\text{inst}}^2 + \Delta\lambda_{\text{th}}^2 + \Delta\lambda_{\text{NT}}^2 \quad (3.1)$$

The thermal width is calculated using Equation 2.16, which is around 0.014 \AA for the Fe XII 195.119 \AA line. The instrumental width of EIS was measured ([Brown et al. 2008](#)) prior to launch, and updated estimates have been made post-launch. For

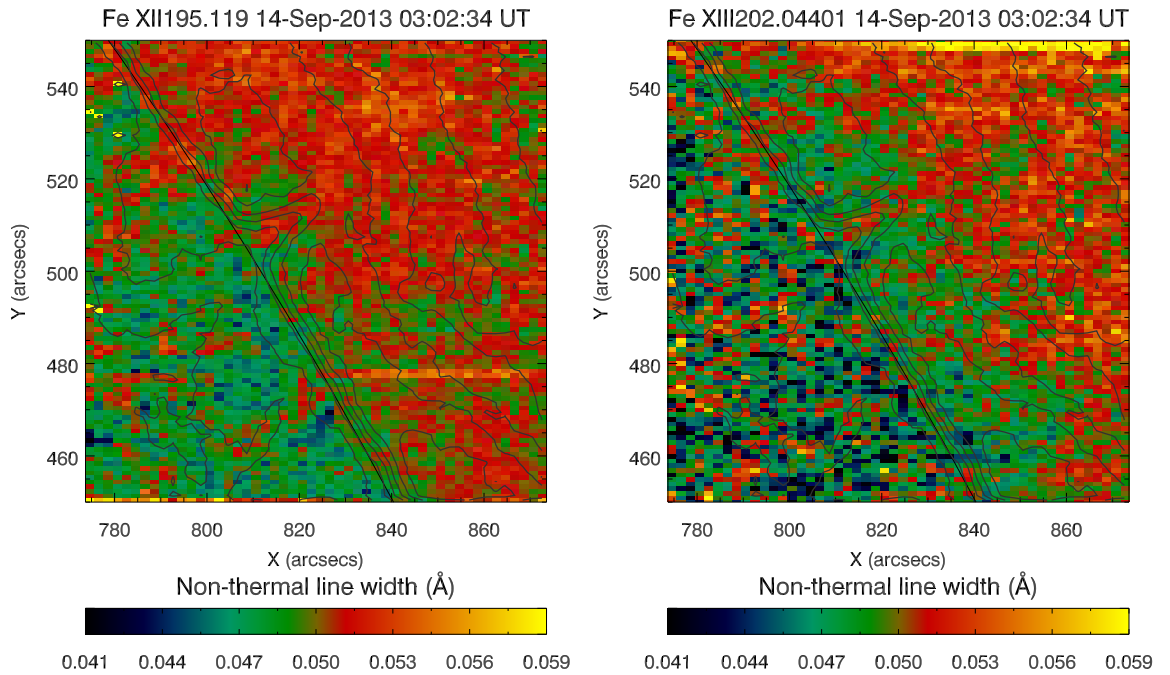


Figure 3.14: Non-thermal line width maps for the tornado region. Contours are from the Fe XII 195.119 Å intensity map. *Left:* Fe XII 195.119 Å. *Right:* Fe XIII 202.044 Å. This figure was used in [Levens et al. \(2015\)](#).

the short-wavelength CCD the pre-flight instrumental width was measured to be 0.047 Å, with post-launch updates measuring 0.054 Å – however this value assumes only thermal broadening mechanisms are important (no non-thermal components are regarded). The long-wavelength CCD was measured pre-flight to have instrumental widths of between 0.055 Å and 0.057 Å. More recent estimates indicated that those pre-flight measurements were accurate, returning an instrumental width of 0.055 Å. For the short-wavelength CCD the laboratory value is taken here for $\Delta\lambda_{\text{inst}}$ (0.047 Å), which gives an upper limit to NTLW values.

With both instrumental and thermal broadening removed from the measured line width, the remaining line width can be used to examine the non-thermal broadening. Figure 3.14 shows NTLW maps made using the Fe XII 195.119 Å and Fe XIII 202.044 Å lines. In both cases there are slightly broader profiles at the tornado compared to the corona immediately next to it, which can be seen more clearly in Figure 3.15, where cuts have been taken from the same place as in Figure 3.13. The corona next to the tornado has NTLW of around 0.049 Å, or $\sim 75 \text{ km s}^{-1}$ in units of non-thermal

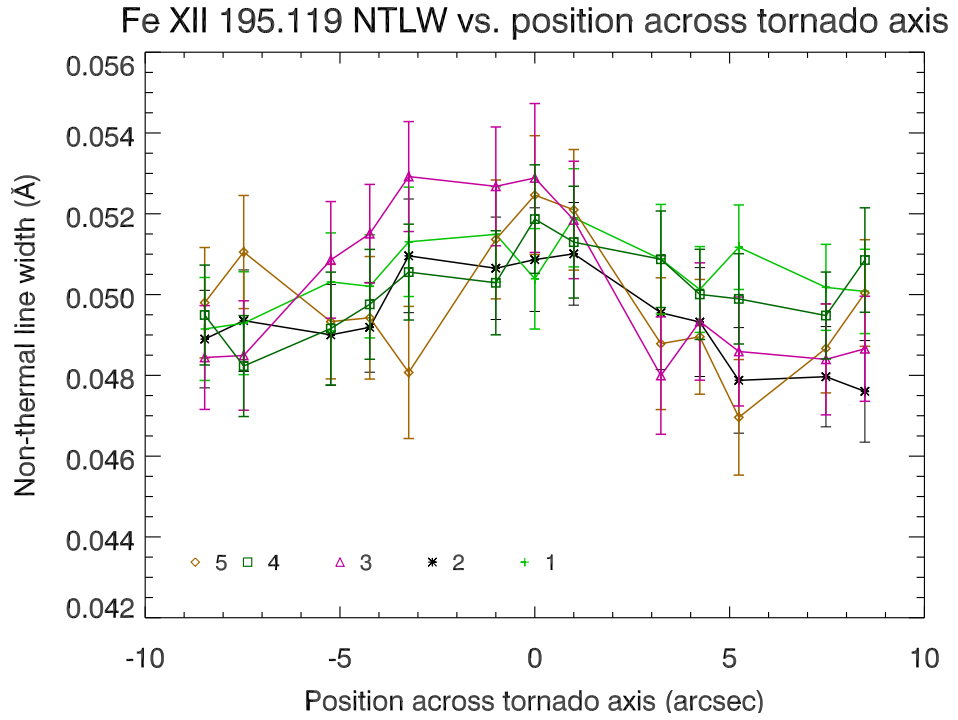


Figure 3.15: Non-thermal line widths of Fe XII 195.119 Å along five parallel cuts through the tornado axis, numbered as shown in the right panel of Figure 3.12. The tornado has a spatial extent of approximately 10'' centred on the 0 of the x -axis. This figure was used in [Levens et al. \(2015\)](#).

velocity, whereas the tornado has a maximum NTLW of around 0.053 Å, which is around 80 km s⁻¹. This suggests that there are additional broadening mechanisms in the tornado region. These values are higher than those found by [Su et al. \(2014\)](#), who reported values around 35 km s⁻¹ in the tornado. However, as noted earlier, the values for NTLW found here are an upper limit, due to the value of instrumental width used in this calculation. Also, despite suggesting that the broadening is local to the tornado, there are similar patterns of broader features at other locations above the limb, which can be seen in Figure 3.14. Therefore it cannot be ruled out that these broader profiles at the tornado are not directly related to the tornado itself.

If the non-thermal broadening is a real effect caused by the tornado then it must be explained by some physical mechanism. It is well reported that prominence magnetic fields are horizontal, but there is evidence that suggests that in some dynamic cases this horizontal field is combined with some 'turbulent' field component

(Schmieder et al. 2014). This additional ‘turbulent’ component could create non-thermal motions of the plasma and lead to non-thermal broadening of spectral lines. Another mechanism that could account for this broadening is the presence of Kelvin-Helmholtz instabilities at the boundary between the tornado and the surrounding corona (Zaqarashvili et al. 2015, for a rotating jet). The Kelvin-Helmholtz instability occurs when there is a shear flow between two plasmas of different densities, as would be expected at the boundary between the tornado and the surrounding corona. This is supported by the fact that the density diagnostics shown in §3.2.2 show a lower density at the tornado than in the corona. Kelvin-Helmholtz instabilities have been discussed in relation to the boundaries of observed Rayleigh-Taylor instabilities in quiescent prominences before, as outlined in Berger (2014).

3.2.4 Differential emission measure

Differential emission measure (DEM) is a method for identifying the temperature structure along the line of sight. In this analysis four locations are investigated in the EIS raster – the tornado, the main prominence body, and two locations in the corona at similar distances from the limb as the tornado and prominence locations. This analysis makes use of a regularised inversion code, from Hannah & Kontar (2012) (see §2.2.3), that can be used for a range of EIS spectral lines. The direct output of this code is the emission measure distribution (EMD), which is related to the DEM as outlined in §2.2.4, and the DEM itself. Using this method the regularised DEM can be calculated at points across the raster. The inputs to this code are the intensities from the Gaussian fits employed here to characterise each line, along with contribution functions calculated using CHIANTI v7.1 (Dere et al. 1997; Landi et al. 2013). Here an assumption must be made about the abundances – CHIANTI has several abundance files available for analysis, but not one dedicated to prominences. Photospheric abundances are assumed while calculating the DEM for pixels in the tornado and prominence body, whereas coronal abundances are used for pixels in the corona.

DEMs have been calculated in a number of prominences using data from a number of different instruments (Schmahl & Orrall 1986; Wiik et al. 1993; Parenti & Vial 2007; Parenti et al. 2012), but none previously have used EIS data. No DEMs of tornado-like prominences have previously been reported.

Table 3.2: List of spectral lines from EIS used for DEM analysis on 14 September 2013.

Ion	λ_0 (Å)	$\log T$ (K)
O v	192.904	5.4
Fe viii	185.213	5.7
Si vii	275.361	5.8
Fe ix	197.862	6.0
Fe x	184.537	6.1
Fe xi	188.216	6.2
Fe xi	188.299	6.2
Fe xi	192.814	6.2
Fe xii	195.119	6.2

Table 3.2 lists the EIS lines used in this DEM analysis. Due to the nature of the study, the full spectral range of EIS was not available. Therefore only nine reduced spectral windows are available, limiting the number of spectral lines available. Some of the available lines also had to be omitted when calculating DEMs, for a number of reasons. Firstly, the He ii 256 Å line (the lowest temperature line in the study) is ignored due to the fact that it is optically thick, as well as the difficulties in separating it from its blend (as described in §3.1.3.5). The hottest line in the raster, Fe xiii 202.044 Å, is also omitted as the contribution function for this line is sensitive to densities at densities below $\log n_e = 10$ (Graham 2014). Therefore there are nine lines useful for this DEM analysis, as shown in Table 3.2. It should be noted that O v, Si vii and Fe viii lines are used in this analysis, despite previous statements about the low signal in these lines above the limb. Despite being weak, there is still signal in these lines above the limb. Although the fitting may not be accurate enough for e.g. detailed l.o.s. velocity studies, the intensity from the fits is deemed to be reliable.

For this DEM analysis errors on line intensity values are taken to be 22% as opposed to the errors derived directly from line fitting. This is considerably higher than the directly derived errors, but due to a combination of uncertainties from the EIS response function and the CCD response between long-wavelength and short-wavelength CCDs (Lang et al. 2006) the larger percentage error is assumed for this analysis. The uncertainty is the standard uncertainty in the radiometric calibration of

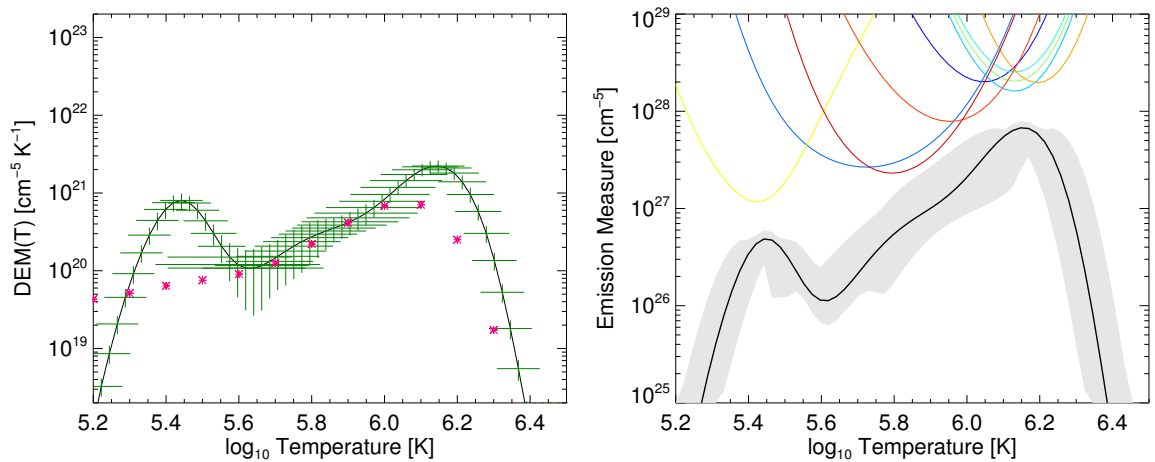


Figure 3.16: Result of DEM inversion code for a pixel in the tornado. Photospheric abundances were assumed for these plots. *Left:* DEM(T) curve (black), with green ‘error bars’ indicating confidence regions for the DEM fit. Magenta asterisks are the DEM result for a quiescent prominence from Parenti & Vial (2007). *Right:* Emission measure distribution curve (black) for the same region as the left panel. Grey shaded region indicates confidence region for this EMD. Coloured curves are the constraint curves for each of the lines used in the DEM calculation. This figure was used in Levens et al. (2015).

the instrument, and was measured pre-flight. Therefore it must be assumed that this is a lower limit for the calibration uncertainty, as it may have changed post-launch.

The positions in the raster where the DEMs are sampled are shown in the left panel of Figure 3.3. Figure 3.16 shows DEM (*left panel*) and EMD (*right panel*) plots for the tornado of 14 September 2013, and Figure 3.17 shows corresponding DEM and EMD for a point in the prominence body. These sets of plots show that different solutions are recovered for the tornado and the main prominence body. Both show a primary peak at coronal temperatures, around $\log T = 6.2$, and a range of emission extending downward in temperature, and a second smaller peak at around $\log T = 5.4$. The primary peak in the tornado DEM (Figure 3.16) reaches DEM(T) values of $2 \times 10^{21} \text{ cm}^{-5} \text{ K}^{-1}$, with the secondary peak reaching DEM(T) = $8 \times 10^{20} \text{ cm}^{-5} \text{ K}^{-1}$. In the prominence body DEM (Figure 3.17), the primary peak is around a factor of < 2 lower than the tornado DEM value. At lower plasma temperatures, around $\log T = 5.4$, the tornado shows more emission, by a

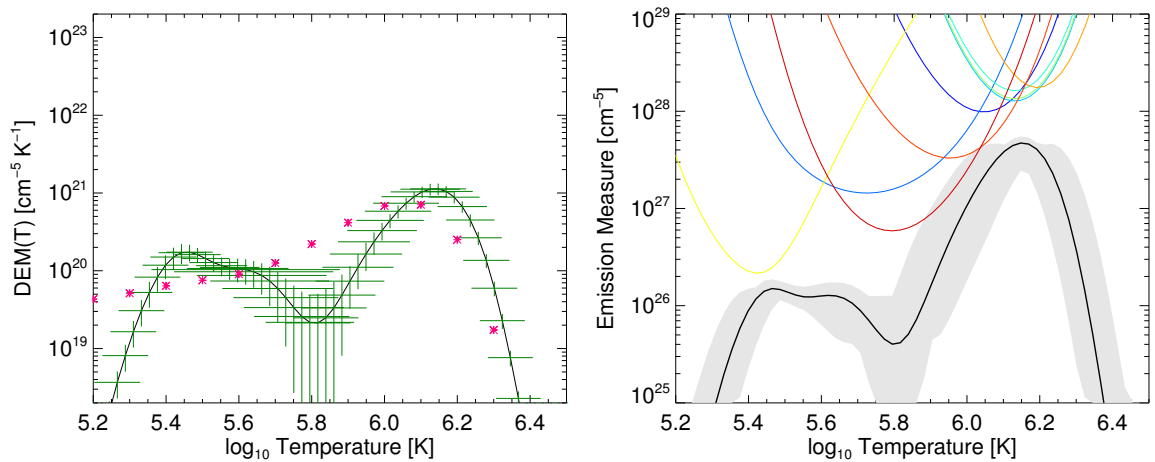


Figure 3.17: Same as Figure 3.16 for a pixel in the prominence body. This figure was used in [Levens et al. \(2015\)](#).

factor of 4–5, than the rest of the prominence. This suggests that there is more cool material along the line of sight intersecting the tornado, which is supported by the appearance of the tornado when viewed in coronal lines. The blocking of background emission from those lines is caused primarily by the presence of lower temperature hydrogen and helium species. The gradients between $\log T = 5.65$ and $\log T = 6.10$ for the tornado and $\log T = 5.88$ and $\log T = 6.10$ for the prominence body are found to be $2.6^{+0.7}_{-0.5}$ and $6.4^{+4.3}_{-1.7}$ respectively.

Figures 3.18 and 3.19 show DEM and EMD plots for two points in the corona, one (Figure 3.18) at a similar distance from the limb as the tornado pixel and the other at a similar distance (Figure 3.19) from the limb as the prominence body pixel.

These coronal DEMs both show two distinct peaks, with a main peak at around $\log T = 6.1$ – 6.2 , and a smaller, less-well constrained peak at around $\log T = 5.4$. In both coronal cases the DEM and EMD is lower at all temperatures than those from the respective tornado and prominence-body plots, but especially so at lower temperatures. This is a clear indication that there is more low temperature plasma in the prominence/tornado, as is expected. However this also indicates that not all emission at coronal temperatures is coming from the foreground corona – there is additional emission at these temperatures in the tornado and prominence body too. This result reinforces that the l.o.s. velocity measurements, non-thermal line widths, and electron densities measured in iron lines at the tornado could be caused

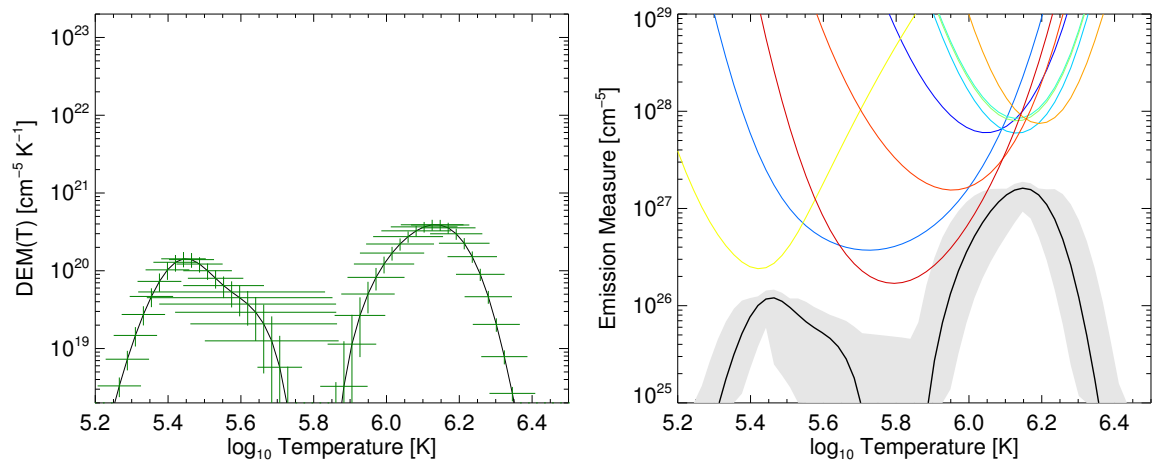


Figure 3.18: Same as Figure 3.16 for a pixel in the corona at a similar distance from the solar limb as the tornado pixel. This figure was used in [Levens et al. \(2015\)](#).

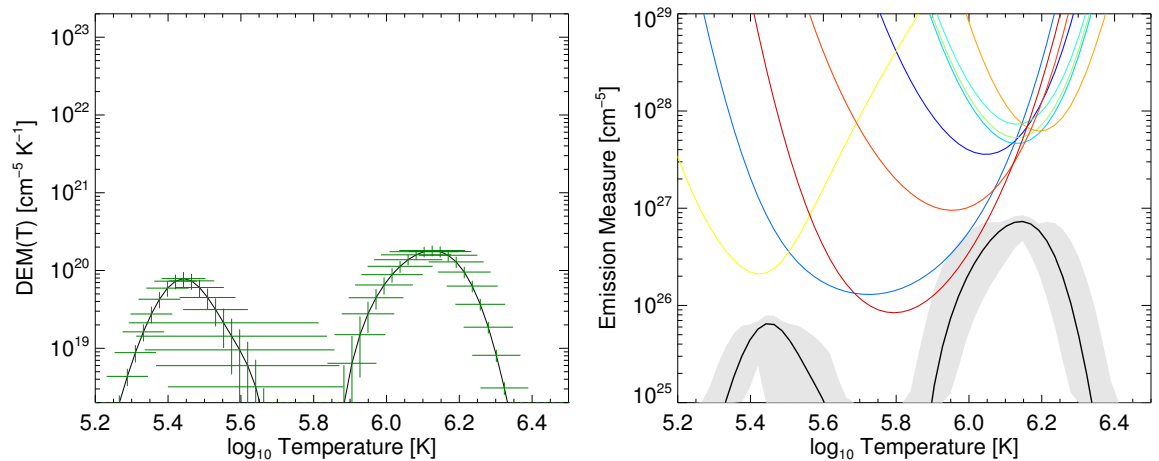


Figure 3.19: Same as Figure 3.16 for a pixel in the corona at the same distance from the solar limb as the prominence body pixel. This figure was used in [Levens et al. \(2015\)](#).

by the tornado itself, but it must be noted that part of the emission from pixels in the tornado is probably from foreground corona.

EMD plots are shown in the right-hand panels of Figures 3.16, 3.17, 3.18, and 3.19. The coloured curves in these plots show the constraint curves used during the calculation of the DEM. Each of these curves corresponds to a different spectral line

used for the DEM, peaking at the line's formation temperature. The spectral lines used here are shown in Table 3.2. Despite being a limited number of lines, there is still a good temperature range available. However, having more lines at low temperatures would have helped with the constraint, especially for the prominence/tornado pixels, as prominences mostly consist of plasma that is below $\log T = 6$.

Figures 3.16 and 3.17 also show the DEM of Parenti & Vial (2007), plotted as asterisks, which was for a quiescent prominence. That DEM was made using data from a large prominence, with a number of spectral lines observed by *SOHO*/SUMER. Parenti & Vial (2007) found a high-temperature peak at around $\log T = 6$. The lines used in that analysis were generally formed at lower temperatures than those used here, and they sampled regions in a much larger prominence – the prominence shown here is much smaller, so sampling emission nearer the limb means that there is more hot plasma along the line of sight. Parenti & Vial also used an older version of CHIANTI for calculating abundances (v4.2 as opposed to v7.1 used here). The newer versions have updated iron ionisation equilibria (Landi et al. 2013), so there could be differences in ion fractions at higher temperatures. The largest factor in the differences seen, though, is the choice of lines available from the respective studies. Here EIS lines are sampled down to $\log T = 5.4$, and below that temperature there are no constraints for the DEM, so a sharp drop-off is seen. This is not the case in Parenti & Vial (2007), where the DEM continues decreasing steadily to lower plasma temperatures (before increasing again as $\log T$ approaches photospheric temperatures). The sharp drop-off seen in the DEMs presented here cannot be associated with any real effect, and is simply due to the selection of lines available in the data set. Notably, however, in the temperature range $\log T = 5.6$ – 6.0 the slope of the tornado DEM presented here (Figure 3.16) matches closely that of the Parenti & Vial DEM.

Up to now this chapter has primarily focussed on observations from one instrument, *Hinode*/EIS, finding that there are intriguing results regarding tornado-like prominences. The characteristic anti-symmetrical Doppler pattern is found in all lines formed at plasma temperatures above 1 MK, but results from lower plasma temperatures are inconclusive. It is found that the electron density is marginally

lower in the tornado than in the surrounding corona at $\log T = 6.2$, and that there appears to be some additional line broadening mechanism along the line of sight of the tornado. From the DEM analysis it is shown that the tornado is most similar in temperature structure to the rest of the prominence. These results leave a number of unanswered questions, however, especially regarding the nature of the low temperature plasma in tornadoes. Luckily there are many other solar telescopes that are capable of observing tornado-like prominences, which could potentially provide a wealth of new information. The remainder of this chapter details the analysis of a coordinated observation of two tornado-like prominence legs observed in a quiescent prominence on the 15 July 2014.

3.3 15 July 2014 – Coordinated observations

Studying plasma parameters from *Hinode*/EIS can provide a large amount of information about tornado-like structures in prominences, but having coordinated observations of tornadoes can provide much more. To further investigate the nature of tornadoes it is logical to use multiple instruments in order to gain different perspectives of them. In 2014 a coordinated campaign was designed to study both the magnetic field and the plasma in tornado-like prominences. Using a combination of ground-based and space-based instruments, many spectral lines at UV, EUV, and visible wavelengths could be probed. The instruments involved in the campaign included UV and EUV spectrometers and imagers on board the *IRIS* and *Hinode* satellites, as well as the *Télescope Héliographique pour l'Etude du Magnétisme et des Instabilités Solaires* (THEMIS, López Ariste et al. 2000), which is capable of measuring magnetic fields in prominences (see §2.4.3). Other ground-based telescopes observed during the campaign, mostly giving H- α observations, such as the Meudon Solar Tower and Meudon Solar Survey. This campaign ran for two weeks in May and two weeks in July 2014 (as well as further observations in 2015 and 2016), and a number of tornado-like prominences were observed during that time. This work concentrates on the tornadoes observed on 15 July 2014, where two tornadoes were observed at the north-west limb.

On the 15 July 2014 a prominence with tornado-like legs was observed over the course of the day. *IRIS*, *Hinode* (SOT and EIS) and THEMIS made observations of the prominence (outlined in the following sections), along with AIA and Meudon Solar

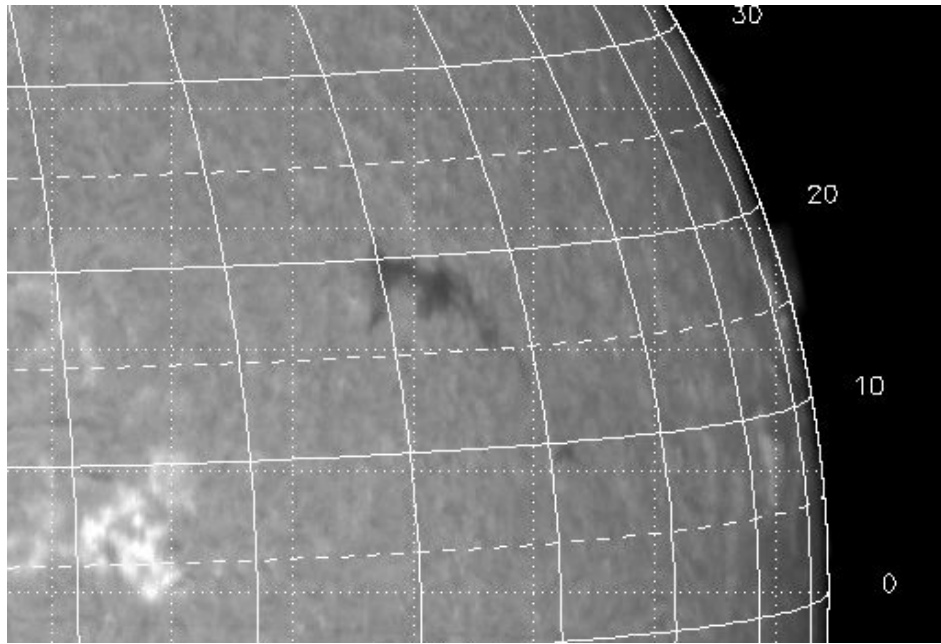


Figure 3.20: Filament observed on 11 July 2014 in H- α using the Meudon Solar Survey instrument. This filament would eventually become the prominence observed on 15 July 2014. This figure is from [Levens et al. \(2016a, figure 1\)](#) and was made by B. Schmieder.

Survey full disc scans. The prominence could be seen as a filament in H- α on disc for a number of days beforehand (Figure 3.20). The orientation of the prominence on disc was mostly east-west, with barbs visible to the east side of the prominence spine. These barbs are what are identified as ‘tornadoes’ as they reach the limb. On 15 July 2014 the prominence is visible in H- α above the west solar limb (Figure 3.21), where the two prominence legs are visible as bright columns.

3.3.1 SDO AIA observations

The data set on this day was chosen as it shows a good spatial coverage of the tornadoes with all the instruments. Figure 3.22 shows the fields of view of the instruments on the 15 July 2014, overlaid on the AIA 171 Å image from 11 UT. In the AIA 171 Å image the tornadoes are visible as dark structures above the solar limb, where the cool plasma composing the tornadoes is absorbing coronal emission from behind them. These dark columns line up with the bright structures seen in

Spectroheliograph 6563 15-Jul-2014 09:40:17 UT

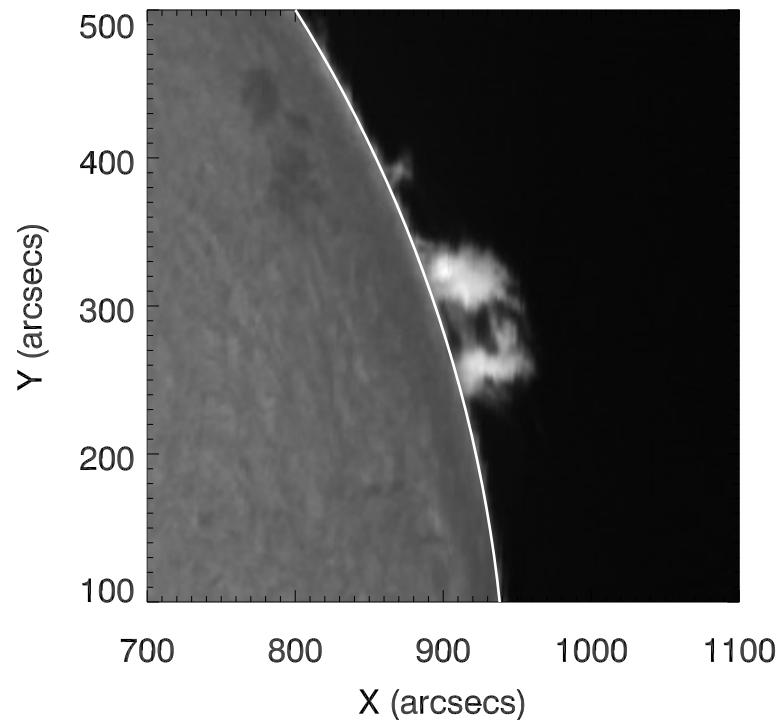


Figure 3.21: H- α observation of the prominence on 15 July 2014 from the Meudon Solar Survey instrument. Solar limb is shown in white.

H- α images (Figure 3.21). This is similar to how the tornado of 14 Sept 2013 appears above the limb in AIA and H- α images from that day.

In the 304 Å images from AIA, which are dominated by emission from He II lines at 303.78 Å, the prominence appears as a more extended feature (shown in Figure 3.23, *left panel*). Horizontal, thread-like structure can be seen in the 304 Å images which shows clearly the full extent of the prominence plasma, but the tornado-like legs of the prominence are not obviously visible. The He II 304 Å lines are optically thick, and prominence emission in these lines is mostly scattered light from the solar surface (Labrosse & Gouttebroze 2001). As such, the light seen in these images comes from the frontmost parts of the prominence, as all other light along the line of sight is scattered or absorbed by the plasma in front of it. It is noted, however, that the northern tornado can be identified as a darker part of the prominence. This is probably due to the contribution of other lines in the AIA filter, which are formed

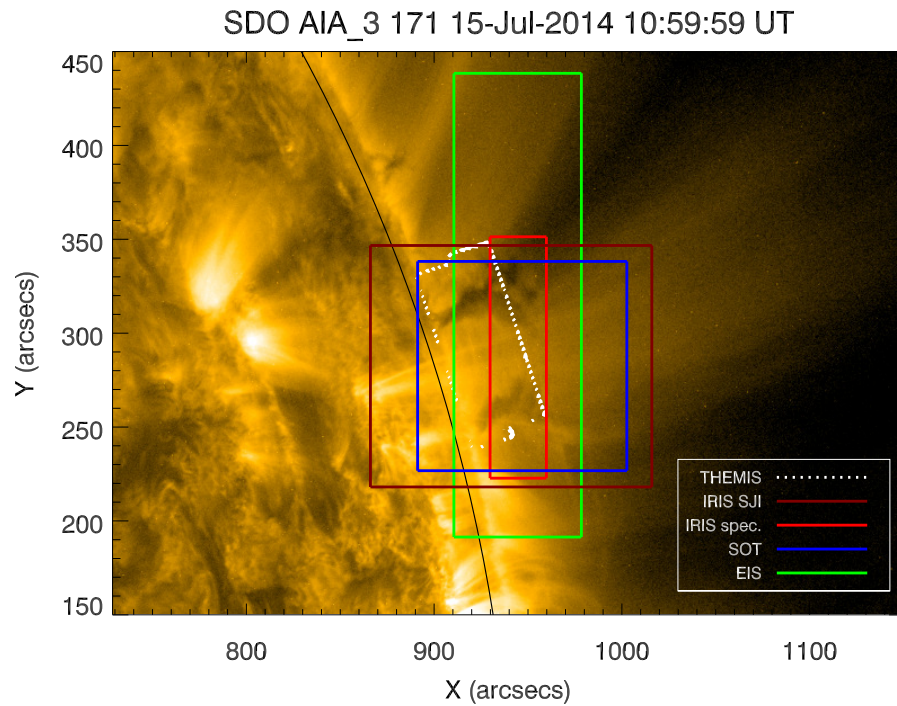


Figure 3.22: AIA 171 Å observation from 15 July 2014. Coloured boxes indicate the fields of view of the other instruments. This figure was used in [Levens et al. \(2017\)](#).

at higher plasma temperatures, such as the Si xI line at 303.3 Å ([Dere et al. 1997](#); [Landi et al. 2013](#)).

The AIA 193 Å filter of AIA predominantly shows emission from the Fe xII line at 193.5 Å. The prominence on 15 July 2014 observed in the 193 Å filter is shown in the right panel of [Figure 3.23](#). In that filter the northern tornado is visible, as in the 171 Å filter, but the view of the southern tornado is mostly blocked by hot coronal emission from plasma in the foreground. Therefore it is hard to claim that any emission from the southern tornado location at temperatures over 1.5×10^6 K (formation temperature of Fe xII) is actually from the tornado and not from the foreground corona.

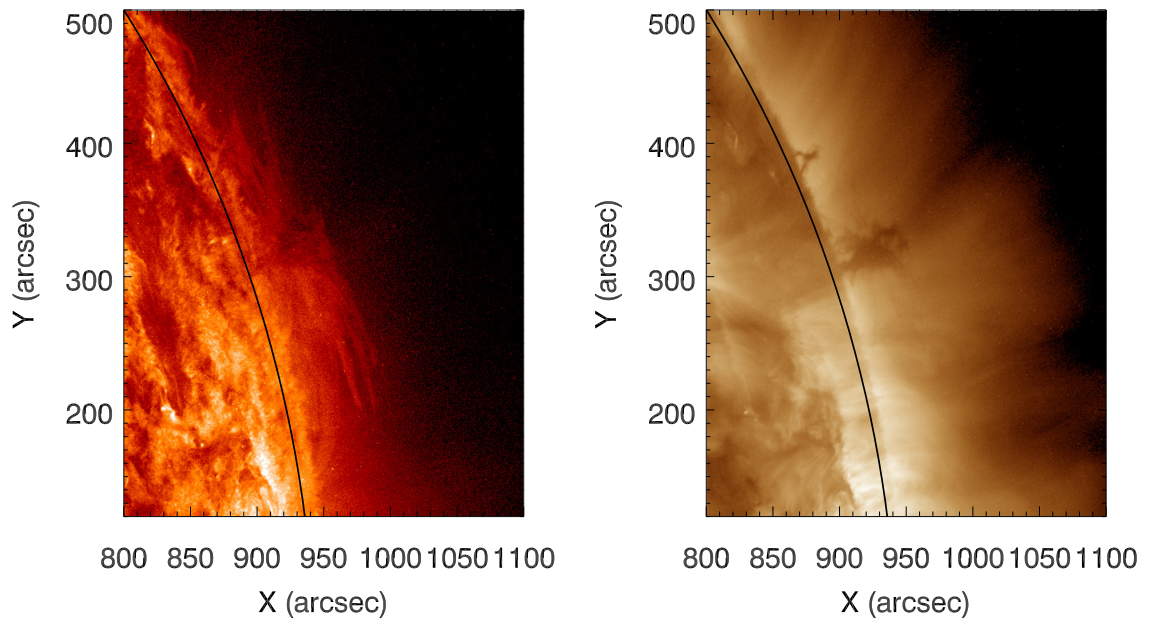


Figure 3.23: AIA images of the prominence on 15 July 2014. Limb position is shown in black. *Left:* 304 Å. *Right:* 193 Å.

3.3.2 IRIS observations

IRIS performed 16-step, coarse rasters between 08:00 UT and 11:00 UT on 15 July 2014. Each raster took 86.4 s to complete, with an exposure time of 4 s per slit position and a step cadence of 5.4 s. The step size for coarse rasters by *IRIS* is 2'' and the spatial scale is 0.167'' per pixel. The *IRIS* spectrograph has two wavelength ranges in the far-ultraviolet (FUV, 1331–1358 Å and 1390–1407 Å), with spectral resolution of 27 mÅ, and one in the near-ultraviolet (NUV, 2782–2834 Å), with spectral resolution of 55 mÅ (De Pontieu et al. 2014). Observations can use only parts of these spectral ranges, with only the lines of interest selected for the study provided in the data set. The observation on 15 July 2014 used the ‘Medium Linelist’ of *IRIS*², which includes the C II lines around 1335 Å, the Si IV lines at 1394 Å and 1403 Å, and the Mg II k and h lines at 2796 Å and 2803 Å respectively, all of which are visible in prominences. The slit-jaw imager of *IRIS* took images using two filters in C II (1330 Å) and Mg II (2796 Å), with a cadence of 11 s. The pointing on 15 July 2014 was (940'', 284''), with FOVs of 30'' × 119'' for the raster and 119'' × 119'' for

²https://www.lmsal.com/iris_science/doc?cmd=dcur&proj_num=IS0301&file_type=pdf

the SJI. The FOVs of the raster and SJI are shown in Figure 3.22 as a bright red box and a dark red box respectively. *IRIS* data is calibrated and used at level 2, where dark current subtraction, flat field correction, and geometrical correction are each accounted for (De Pontieu et al. 2014).

After calibration, the *IRIS* spectral intensities have been converted from data number (DN) into physical units of $\text{erg s}^{-1} \text{sr}^{-1} \text{cm}^{-2} \text{\AA}^{-1}$ (herein cgs \AA^{-1}). It is occasionally useful, however, to consider these intensities in terms of $\text{erg s}^{-1} \text{sr}^{-1} \text{cm}^{-2} \text{Hz}^{-1}$ (herein cgs Hz^{-1}). This conversion is made simply by using Equation 3.2, where I_ν and I_λ are the intensities in cgs Hz^{-1} and cgs \AA^{-1} respectively.

$$I_\nu = I_\lambda \frac{\lambda_0^2}{c} \quad (3.2)$$

The wavelength of the line centre is λ_0 and c is the speed of light.

From Equation 3.2 the intensity as a function of frequency can be calculated. For the h and k lines of Mg II the line-centre wavelengths are $\lambda_{0,k} = 2796.35 \text{ \AA}$ for k and $\lambda_{0,h} = 2803.53 \text{ \AA}$ for h (from CHIANTI v8.0). In terms of Ångstroms, the speed of light $c = 2.99 \times 10^{18} \text{ \AA s}^{-1}$. Therefore there are two conversion factors (at the line centres) between cgs \AA^{-1} and cgs Hz^{-1} :

$$\text{k} : I_\nu = 2.615 \times 10^{-12} I_\lambda$$

$$\text{h} : I_\nu = 2.629 \times 10^{-12} I_\lambda$$

These values are very close, and rounding we end up with one factor of $I_\nu = 2.6 \times 10^{-12} I_\lambda$ that can be applied everywhere for the Mg II h and k lines.

3.3.3 Hinode SOT observations

The *Hinode* Solar Optical Telescope observed with the broadband filtergraph (BFI) using the Ca II H filter, which is centred on that line at 3968.5 \AA . Images were taken with a 30 s cadence from 10:21 UT until 11:06 UT, which overlaps temporally with the last part of the *IRIS* observations. The SOT images are the highest spatial resolution images obtained of the prominence on 15 July 2014, with a pixel size of $0.109''$. The field of view of SOT was $112'' \times 112''$ and is shown as a blue box in Figure 3.22.

3.3.4 *Hinode* EIS observations

The Extreme-ultraviolet Imaging Spectrometer made two rasters and two short sit-and-stare studies on 15 July 2014. The first raster, at 08:17 UT, had a large section of the data missing due to an eclipse of the satellite, so here the second raster, beginning at 10:34 UT, is the only one studied. Using the 2'' slit, EIS ran a 35-step raster using the full 248'' length of the slit and a 50 s exposure per slit position. Therefore the raster covered a 70'' × 248'' region, shown as a green box in Figure 3.22, with the full raster taking around 30 minutes to complete. The EIS study used here is named `madj_qs`, which splits the EIS CCDs into eleven wavelength channels containing a number of spectral lines from around 8×10^5 K to over 2×10^6 K. The main spectral lines in this study are presented in Table 3.3. Each spectral line listed in Table 3.3 was fitted with a Gaussian in order to characterise them for analysis, but also to de-blend lines that are close enough to appear blended as described in §3.1.3.

3.4 Plasma parameters

Having multi-instrument observations of two tornado-like prominence legs provides very powerful diagnostic tools for studying the plasma in these structures. The combination of spectra and images covering several hours allows both plane-of-sky and line-of-sight motions to be studied over time.

3.4.1 AIA time-distance analysis

Several authors have used time-distance analysis of AIA images to identify potential tornado-like motions in prominences (Su et al. 2012, 2014; Mghebrishvili et al. 2015), as described in §1.3. In the time-distance method a cut is taken through an image and those points are plotted as a function of time, which enables plasma motions to be identified and plane-of-sky velocities to be calculated. For tornado-like prominences cuts are generally taken parallel to the solar limb, i.e. through the ‘axis’ of the tornado. This was done in Su et al. (2012), where they found sinusoidal motions which they interpreted as rotational motion of the plasma around a vertical tornado axis, displaying rotation speeds of 6 – 8 km s⁻¹. A similar analysis was done in Mghebrishvili et al. (2015), where they estimated a rotational velocity of ~ 6 km s⁻¹. This result is in the range of values commonly found in tornadoes ($\sim 5 - 10$ km s⁻¹).

Table 3.3: List of the main spectral lines in the EIS `madj_qs` study used to study the tornado on 15 July 2014.

Window	Ion	λ (Å)	$\log T$ (K)	Note
1	O VI	183.397	5.5	Other lines in raster (also fitted): O VI, 2 Fe XI, Fe X
	Fe VIII	185.213	5.7	
2	Fe XII	186.241	6.2	
	Fe VIII	186.599	5.7	
	Fe XII	186.854	6.2	
3	Fe XI	188.216	6.2	Blend
	Fe XI	188.299	6.2	
4	O V	192.797	5.4	Blended with: 5 O V and Fe XI
	Fe XI	192.814	6.2	
5	Fe XII	195.119	6.2	Blend
	Fe XII	195.179	6.2	
6	Fe XIII	202.044	6.3	
7	Fe XIII	203.772	6.3	Blended with: 3 Fe XIII lines and 2 O V
	Fe XIII	203.796	6.3	
	O V	203.822	5.4	
8	He II	256.320	4.9	Blended with: Fe XII, S XIII
9	Si VII	274.184	5.8	
	Fe XIV	274.204	6.3	
10	Si VII	275.361	5.8	Weak line
11	Fe XV	284.163	6.4	Hottest line in study

[Panasenco et al. \(2014\)](#) argue against the inference of rotational motions in this type of analysis, stating that the observed motion could be explained by counter-streaming or oscillation. If prominence legs show sinusoidal/oscillatory motions, and they have a column or funnel shape in AIA images, then they are identified as tornadoes in this thesis, as described in §1.3.

The time-distance method is applied to the tornadoes seen on the 15 July 2014.

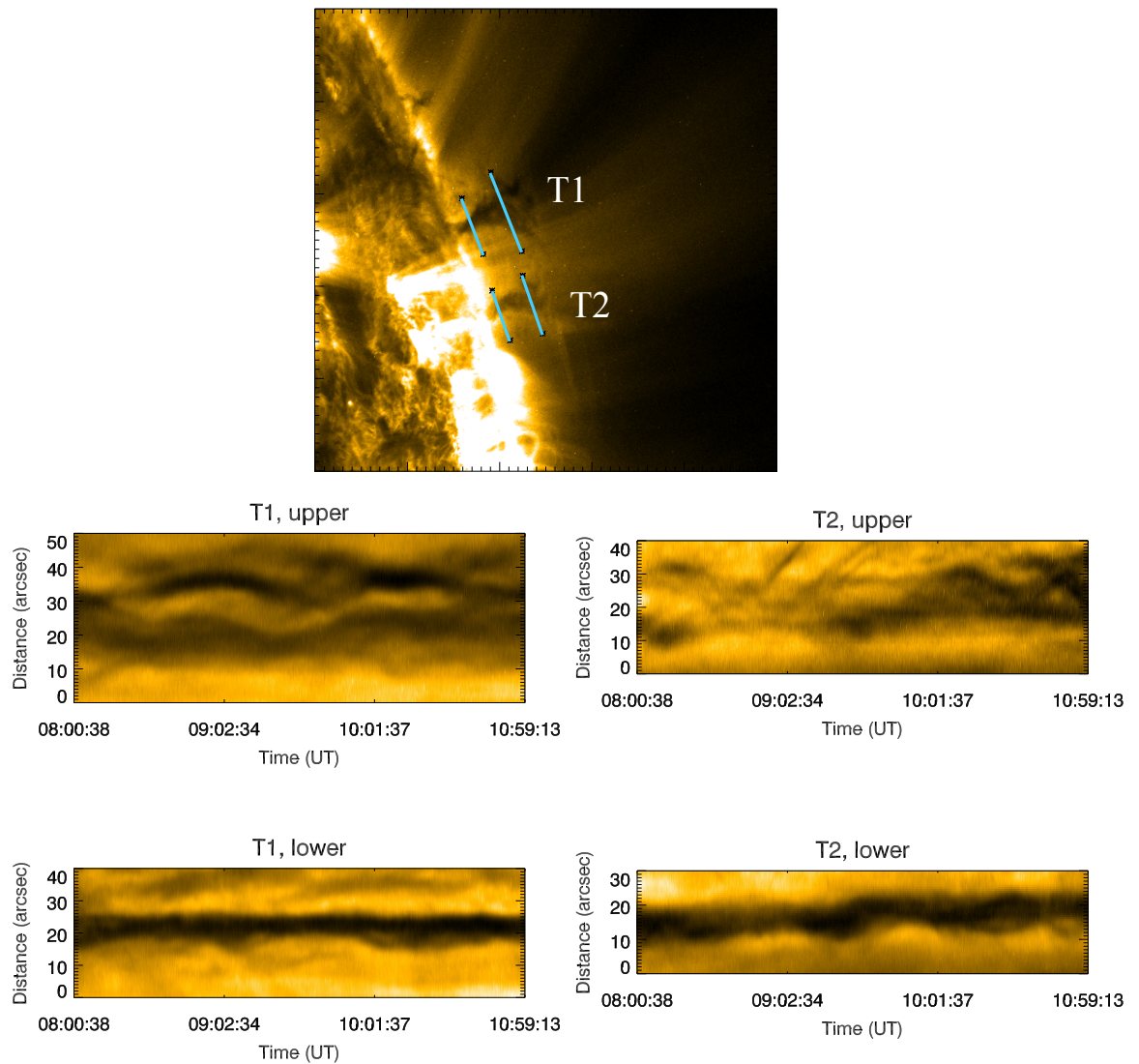


Figure 3.24: Time-distance diagrams for the tornadoes on 15 July 2014 using the AIA 171 Å filter. ‘T1’ is the northern tornado, ‘T2’ is the southern tornado. *Top:* Context image from 11:00 UT with the cut locations shown in blue. Cuts are taken at two heights in each tornado. *Bottom:* Corresponding time-distance diagrams for the four cuts. This figure was used in [Levens et al. \(2016a\)](#).

Figure 3.24 shows the cuts taken through the tornado columns in the AIA 171 Å filter and the associated time-distance plot for each. In this figure the tornadoes are identified as ‘T1’ and ‘T2’ for the northern and southern tornado respectively. Two cuts are taken through each tornado column (shown in Figure 3.24, *top panel*), parallel to the limb, at heights of $\sim 10''$ and $\sim 35''$ above the solar limb. The resulting

time-distance plots are shown as the bottom four panels of Figure 3.24. Only a small amount of oscillation can be seen in the lower cuts, and there is not enough contrast in the AIA images to measure them accurately. In the upper cuts, however, the sinusoidal pattern is clearer. From the panel titled ‘T1, upper’ an estimate of the period of oscillation (in the plane of sky) can be made of around 1.25 hours, with an amplitude of $10''$. Then, assuming rotation around a central axis and using the equation $v = 2\pi r/T$ where v is the velocity, r is the amplitude of the displacement, and T is the period, a velocity of 10 km s^{-1} is recovered. This is of the same order as Su et al. (2012) and Mghebrishvili et al. (2015). However, as stated in Panasenco et al. (2014) these motions cannot be taken as proof of rotation, as due to projection effects they are indistinguishable from oscillations.

3.4.2 IRIS spectral analysis

The Mg II h and k lines, at 2803.50 \AA and 2796.35 \AA respectively, are the brightest spectral lines visible in prominences by the IRIS satellite. Other lines are visible, such as the Si IV lines and the C II lines, but are very weak with a low signal-to-noise ratio. This is caused by the relatively short exposure time of the IRIS study used here (4 s), however the problem can be remedied somewhat by averaging spectral profiles along each slit position over time. Unfortunately in doing so any small-scale temporal evolution of the prominence is lost. Averaging over an hour of data results in the plots in Figure 3.25, which show intensity as a function of position along slit for the Mg II k, Si IV 1393.78 \AA , and C II 1335.71 \AA lines. Notably the Mg II intensities are much higher, and the curve is smoother, due to the higher signal-to-noise ratio in that line. The Si IV and C II profiles are much more noisy and have relatively lower intensities.

The intensity profile in Mg II k does not show any sign of the tornado-like columns that are seen in H- α , AIA and SOT images. The same is true of the C II profile, and in both cases a more extended emission profile is seen. In Si IV, however, the two columns are clearly visible, bright in emission. The difference can be accounted for by considering the optical thickness of the lines in question – Mg II is optically thick in prominences (Heinzel et al. 2014), and C II are known to be optically thick under chromospheric conditions (Rathore & Carlsson 2015) but have not been studied in prominences. Si IV is optically thinner, so more emission along the l.o.s. is seen in

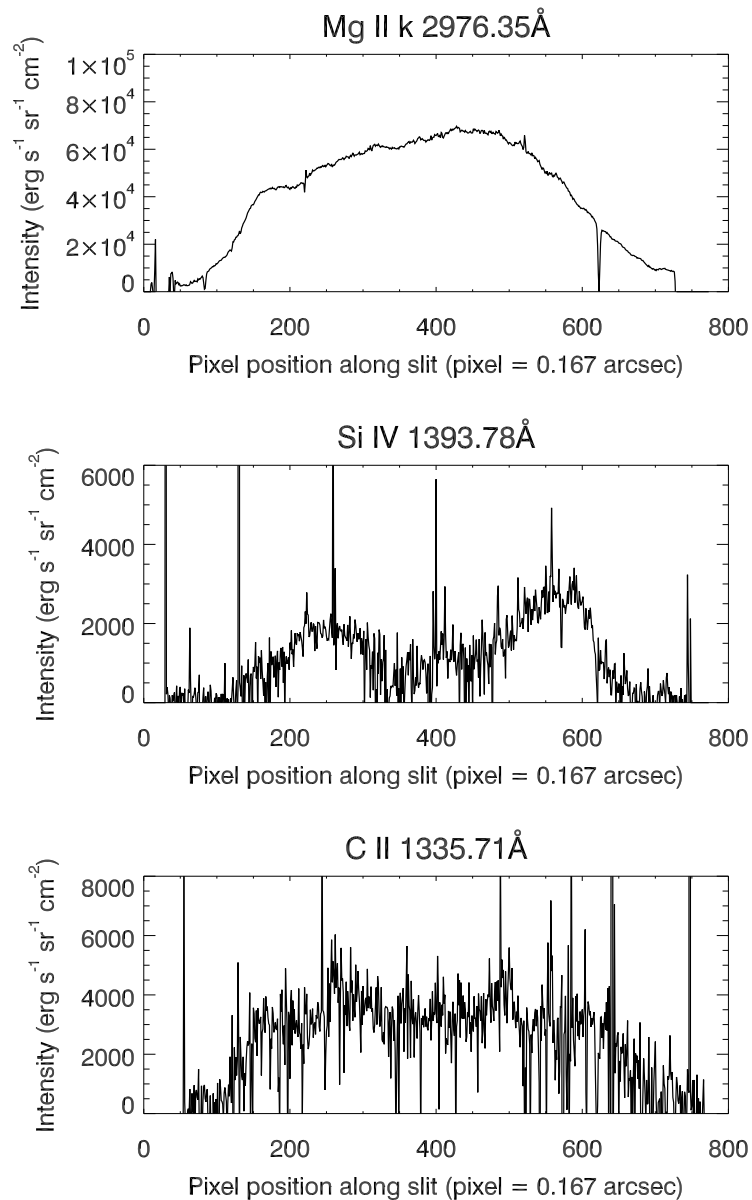


Figure 3.25: Integrated intensity against position along slit for three *IRIS* lines. *Top:* Mg II k 2796.35 Å. *Middle:* Si IV 1393.78 Å. *Bottom:* C II 1335.71 Å. Each profile is averaged over one hour of data for the third *IRIS* slit position. In these plots pixel 0 is the bottom of the slit, to the south. Sudden drops in intensity around pixels 90 and 620 are due to the fiducial lines on the *IRIS* CCD (most clearly seen in Mg II). This figure was used in [Levens et al. \(2016a\)](#).

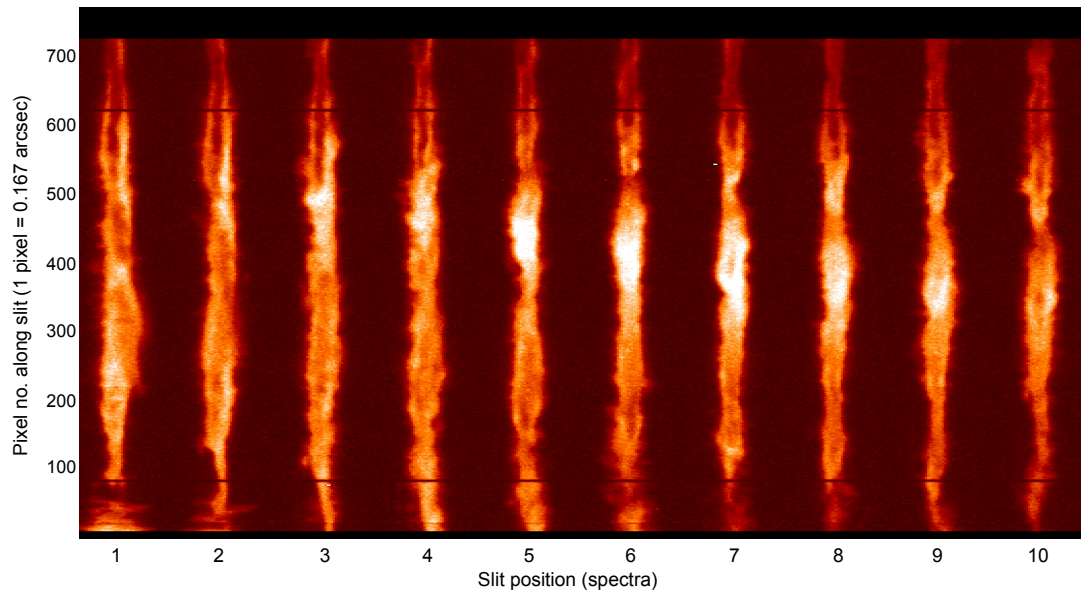


Figure 3.26: Examples of Mg II k spectra from the *IRIS* raster at 10:21 UT. The first ten slit positions of the raster are shown here, with the left-most spectra being closest to the limb. This figure shows y position along slit as a function of wavelength for each of the slit positions, covering the entire y extent of the raster. Dark horizontal lines near the top and bottom of each slit position are due to the fiducial lines on the *IRIS* CCD. Broad profiles at the bottom of the first two slit positions are due to spicules at the limb. This figure was used in [Levens et al. \(2016a\)](#).

the densest parts of the prominence, i.e. the prominence legs.

Turning attention to the spectral profiles of the Mg II lines, a number of things are notable. Throughout the prominence on 15 July 2014 there are a mix of reversed and non-reversed profiles, evident from the spectra shown in Figure 3.26. In this figure the spectral profile of Mg II k is shown for the entire slit for the first ten positions in the raster. Figure 3.26 also indicates that there are not any large Doppler shifts in this prominence, suggesting that the overall plasma velocity along the l.o.s. is not high. Figure 3.27 shows Mg II k (black line) and h (grey line) profiles at three points in the prominence. The top panel of Figure 3.27 shows typical reversed profiles. These are contrary to previous prominence observations with *IRIS* ([Schmieder et al. 2014](#); [Liu et al. 2015a](#); [Vial et al. 2016](#)) where mostly single-peaked profiles are reported. Single-peaked profiles are common in this prominence, as in the middle panel of Figure 3.27, however a large portion of the profiles have a central reversal. There

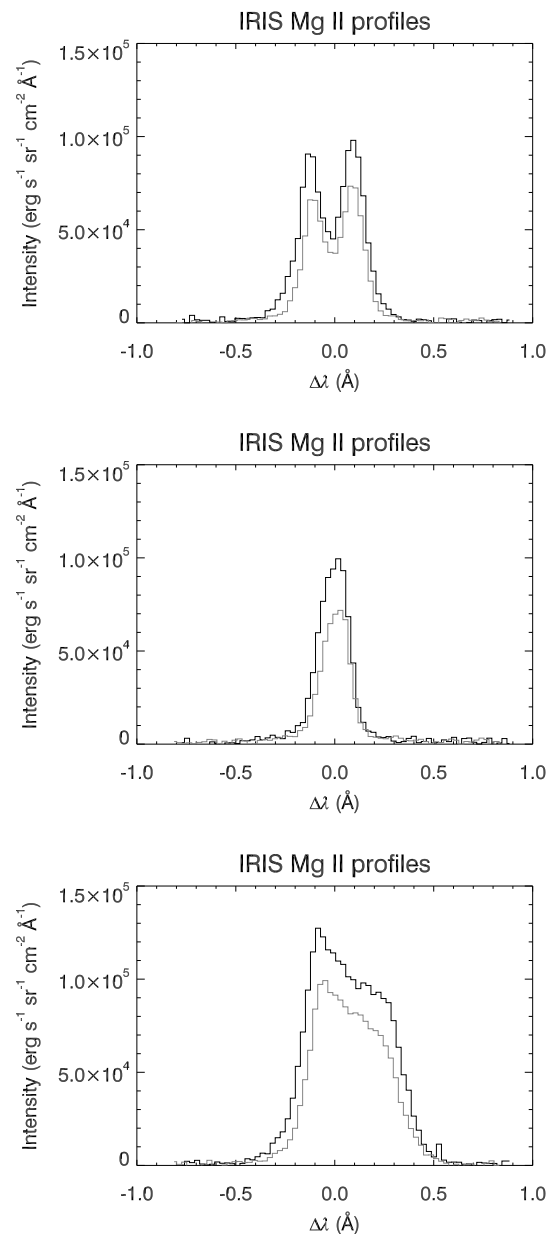


Figure 3.27: Examples of Mg II k (black curves) and h (grey curves) line profiles from the prominence on 15 July 2014. They are all taken from the raster starting at 10:21 UT. *Top:* Reversed profiles. *Middle:* Single-peaked profiles. *Bottom:* Complex profiles. This figure was used in [Levens et al. \(2017\)](#).

are also other profiles which do not fit into either category, as in the bottom panel of Figure 3.27. These are referred to here as ‘complex’ profiles. Complex profiles could have no clear central reversal, a broad, flat line core, have several intensity

peaks, or they may have one peak which is away from the line centre (at a distance of $> 0.04 \text{ \AA}$).

The formation of these ‘complex’ profiles has two possible explanations. The first is as in [Schmieder et al. \(2014\)](#) where the complex, broadened profiles are created by viewing a number of threads with different line-of-sight velocity components. This creates profiles made up of several narrow Gaussian profiles, which blend together when viewed by *IRIS*. In [Schmieder et al. \(2014\)](#) they found flows of up to 80 km s^{-1} in a quiescent prominence by using multiple Gaussian fits. The second explanation is that the observed profiles are a reversed profile with one of the peaks missing. This could be due to multiple optically thick threads along the line of sight with different velocity components. Asymmetries in Lyman line profiles in prominences were explained using this model by [Gunár et al. \(2008\)](#), and the model was also used by [Labrosse & Rodger \(2016\)](#) for helium line profiles in prominences. [Gunár et al. \(2008\)](#) show that a combination of a number of reversed profiles with different l.o.s. velocities can create emergent profiles with one peak missing. It follows that the same could be true for Mg II, assuming a multi-thread model – an optical thickness difference across the h and k line profiles, and differences in where each part of the lines are formed in the prominence, could create such an effect. The observed ‘complex’ profiles would then be explained by ‘stationary’ line wings and k_2 peaks, resulting from integrating along a line of sight crossing several threads, and a shifted k_3 core caused by motion of the front-most thread. Emission from one of the k_2 peaks is then absorbed by the optically thick k_3 part of the line, reducing the emission of that peak. Deciding which of these scenarios is more likely depends on the Doppler velocities of the plasma, and also the optical thickness of the plasma. Both of these parameters can be estimated from *IRIS* Mg II data.

Studying the profiles more carefully in the tornadoes a few parameters can be extracted, which are listed in Table 3.4. Typical integrated intensities, I_{int} , are around $4 \times 10^4 \text{ erg s}^{-1} \text{ sr}^{-1} \text{ cm}^{-2}$ for k and around $3 \times 10^4 \text{ erg s}^{-1} \text{ sr}^{-1} \text{ cm}^{-2}$ for h in this prominence. A first measure of the ratio of intensities of the k and h lines (I_k/I_h , referred to as k/h here) is also presented in Table 3.4. This ratio is discussed further in §4.3.2. Notably, upon first inspection, it appears that in the tornado locations the Mg II profiles are primarily reversed, whereas there is much more variation elsewhere in the prominence. The peak intensity to core intensity ratio, I_p/I_0 , gives the level of reversal of these lines, which is important to consider when comparing to models

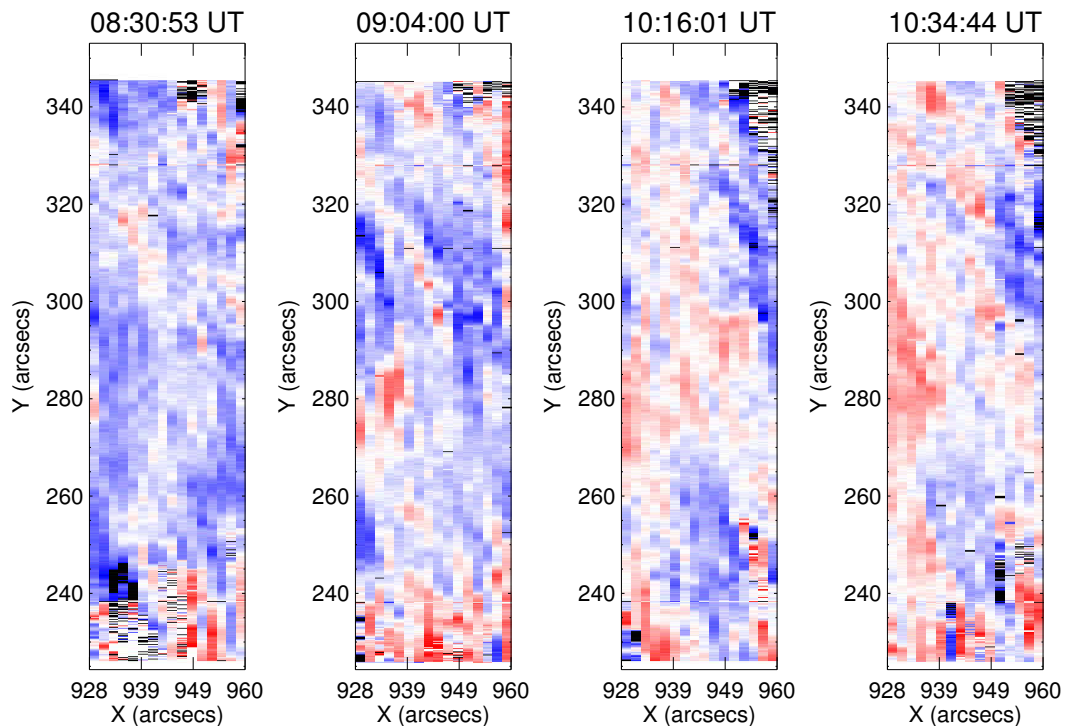


Figure 3.28: Line-of-sight velocity maps at four times from the *IRIS* study on 15 July 2014 using the Mg II k line. Velocities are calculated using a single Gaussian assumption on that line. Limits for the velocity in these plots are $\pm 10 \text{ km s}^{-1}$. This figure was used in [Levens et al. \(2016a\)](#).

(see §3.4.4). FWHM values stated in Table 3.4 are estimated from a single Gaussian simplification, but give a good indication of the overall width of these lines. The FWHM is found to be around $0.3 - 0.4 \text{ \AA}$.

3.4.3 Doppler shifts

To investigate whether or not tornado-like Doppler patterns are seen in the Mg II lines it is necessary to characterise the line-of-sight velocity. Unlike most of the EUV lines observed by *Hinode*/EIS, the Mg II lines are not Gaussian in shape and may display complex profiles (as discussed in §3.4.2). It is therefore more challenging

to calculate the Doppler shift in these lines. As was mentioned in §3.4.2 there do not appear to be any profiles with large Doppler shifts from a first inspection of the spectra in Figure 3.26, so it is considered here that these profiles are not made up of multiple narrow Gaussians. In order to get an idea of the overall line shift a single Gaussian is fitted to the Mg II profiles. This is a vast simplification, but it works as a good ‘first estimate’ of the centroid position of these lines, and with the range of profiles displayed in this prominence (Figure 3.27) it is useful to have a method to quickly estimate line-of-sight Doppler velocities. The centroid given by the Gaussian fit is then compared to the nominal centroid of the line, given by CHIANTI (Dere et al. 1997; Landi et al. 2013).

Figure 3.28 shows velocity maps of the rasters at four times during the *IRIS* study, created using the Gaussian approximation. These show relatively small l.o.s. velocities, on the order of $\pm 5 \text{ km s}^{-1}$. The velocity pattern does not show any signature of tornado-like rotation in Mg II, instead the velocity pattern appears to follow loop-like structure in between the tornadoes. Time-distance plots can also be constructed from the *IRIS* data by using one slit position in each raster, shown for intensity and velocity in Figure 3.29 (left and right panel respectively). In these plots there is no consistent red-blue asymmetry down the axis of the tornadoes as was seen in EIS data from the 14 September 2013 (§3.2.1). Instead there appears to be slow evolution between blueshifts and redshifts everywhere, perhaps indicating oscillations. However it must be remembered that these velocities were calculated using a single Gaussian. Calculating centroid positions from the first moment of the profiles returns similar results for the calculated Doppler shift, and examples of l.o.s. velocity values at several points in the two tornadoes are given in Table 3.4.

3.4.4 Gas pressure and optical thickness

In order to estimate the gas pressure and optical thickness of the plasma some prominence model must be invoked. A grid of models was calculated by Heinzel et al. (2014) for Mg II emission in a 1D isothermal isobaric prominence slab suspended in the solar atmosphere, and their results are presented in a table where observable parameters, such as the reversal level of the Mg II k and h lines, were presented alongside the corresponding model parameters – temperature, gas pressure, slab thickness, and optical thickness. Reversal level, or ratio of k_2 peak intensity to k_3

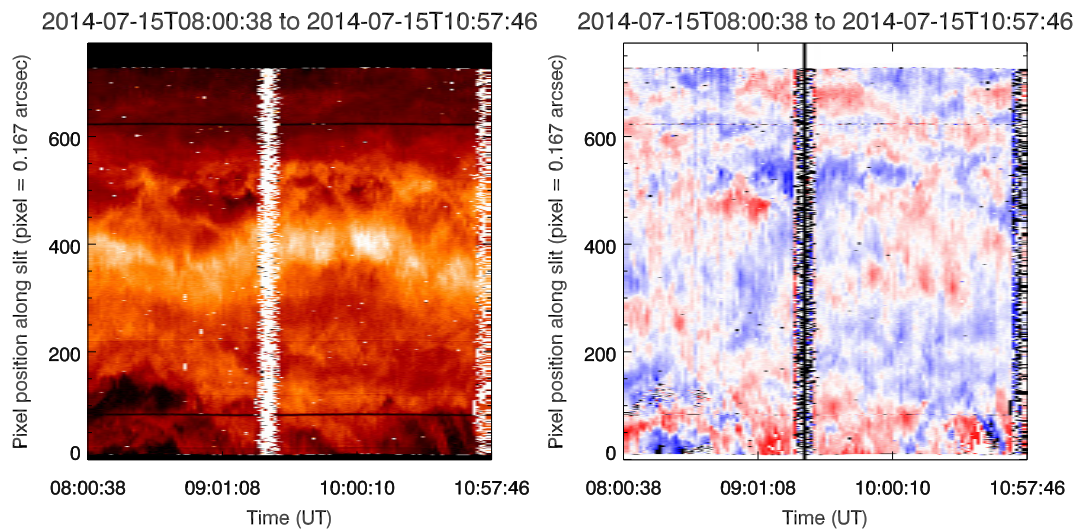


Figure 3.29: Time-distance plots of Mg II k peak intensity (*left*) and l.o.s. velocity (*right*) for the prominence on 15 July 2014. These were made using the central slit position of the *IRIS* raster. South Atlantic Anomaly passes are visible as noisy vertical strips in the middle and the end of each panel. This figure was used in [Levens et al. \(2016a\)](#).

reversal minimum intensity (referred to here as the k_2/k_3 ratio), is the ratio of the peak intensity of the line to the intensity at the line core for a reversed line. For Mg II k profiles in this prominence reversal levels of between 1.1 and 2.6 are found in T₁, with values in T₂ being lower, in some cases non-reversed. Comparing these high reversal values to the table in [Heinzel et al. \(2014\)](#) indicates high pressures, reaching 0.5 dyne cm^{-2} , and for expected prominence temperatures (6000 K) and slab thicknesses (1000 km) the optical thickness could be 820. Lower reversal levels of around 1.2 or 1.3 could indicate lower pressure ($\sim 0.1 \text{ dyne cm}^{-2}$) and optical thicknesses of around 140, or at higher temperatures (8000 K) optical thickness could be around 100. Non-reversed profiles are indicative of low gas pressures ($\sim 0.01 \text{ dyne cm}^{-2}$) and lower optical thickness. These cases, however, do not indicate that the plasma is optically thin – [Heinzel et al. \(2015\)](#) investigate a case where narrow single-peaked profiles in a prominence can be caused by the addition of a prominence-corona transition region (PCTR) into the 1D isothermal isobaric models. High optical thicknesses such as are found here indicate that the emission that is seen in this prominence is only coming from the front-most layers, nearest the observer.

Table 3.4: Line parameters measured for the *IRIS* Mg II k and h lines at points ‘N’ (north), ‘C’ (centre), and ‘S’ (south) in the tornadoes. Peak intensity, I_p , has units $\times 10^{-7}$ erg s $^{-1}$ sr $^{-1}$ cm $^{-2}$ Hz $^{-1}$, and integrated intensity, I_{int} , has units $\times 10^4$ erg s $^{-1}$ sr $^{-1}$ cm $^{-2}$. FWHM is in Å. For reversed profiles, I_p/I_0 (or k_2/k_3) is defined as the ratio of the peak intensity to the intensity at the reversal minimum, ‘nr’ indicates non-reversed. Also shown here are values of line-of-sight velocity, v_{los} with units in km s $^{-1}$, as derived from a single Gaussian fit to the Mg II k line.

Mg II k	Slit	0			8			15		
		N	C	S	N	C	S	N	C	S
T1	I_p	2.00	4.15	4.15	2.32	2.84	3.25	0.58	1.08	2.01
	I_p/I_0	2.41	2.63	1.89	1.70	1.95	1.25	1.72	1.17	1.62
	I_{int}	2.22	4.48	5.13	2.80	3.62	4.01	0.43	1.36	2.81
	FWHM	0.31	0.33	0.31	0.30	0.29	0.30	0.08	0.31	0.35
	k/h	1.39	1.37	1.41	1.37	1.39	1.35	1.16	1.75	1.37
	v_{los}	-1.19	0.88	1.57	-1.70	-3.53	-0.09	-7.65	0.17	-4.58
T2	I_p	3.74	4.18	3.77	3.87	3.83	2.97	2.91	2.72	2.66
	I_p/I_0	1.29	1.36	nr	1.21	1.23	nr	nr	1.33	1.25
	I_{int}	6.33	5.28	4.56	4.39	4.32	2.40	4.06	3.86	3.54
	FWHM	0.39	0.30	0.28	0.30	0.27	0.25	0.33	0.33	0.30
	k/h	1.39	1.41	1.39	1.45	1.37	1.49	1.33	1.25	1.30
	v_{los}	2.28	-1.61	-2.68	-1.57	-4.04	-1.23	-2.10	0.87	-2.46
Mg II h	Slit	0			8			15		
		N	C	S	N	C	S	N	C	S
T1	I_p	1.46	3.63	2.98	1.78	2.28	2.70	0.50	0.70	1.40
	I_p/I_0	2.42	3.21	1.68	1.40	1.26	1.64	n/a	1.29	1.63
	I_{int}	1.60	3.27	3.63	2.04	2.61	2.97	0.37	0.77	2.06
	FWHM	0.35	0.30	0.30	0.26	0.28	0.25	0.41	0.35	0.33
T2	I_p	2.92	3.11	3.20	2.89	2.89	2.44	2.41	2.22	2.63
	I_p/I_0	1.07	1.21	1.12	1.33	1.42	nr	1.19	1.32	1.57
	I_{int}	4.57	3.76	3.30	3.05	3.17	1.61	3.05	3.09	2.74
	FWHM	0.34	0.24	0.23	0.24	0.28	0.24	0.30	0.29	0.27

It is also true, however, that the optical thickness varies over the line profile, with the most optically thick part being at the line core, and becoming more optically thin towards the line wings. Therefore emission seen in the wings of the Mg II lines is an integration along more of the line of sight than at the core. Figure 3.30 shows Mg II raster images made using only parts of the Mg II k spectral line. Reversal of profiles is an indication of high optical thickness, and central reversals are seen for many optically thick spectral lines – lines from H I, He I, and He II amongst others. However, not all optically thick lines show reversal, the Ca II H and K lines generally do not show reversal in prominences but are optically thick (Paletou et al. 1993; Gouttebroze et al. 1997) and it has been shown here and by others (Schmieder et al. 2014; Vial et al. 2016) that Mg II lines are not always reversed.

3.5 Conclusion

This chapter has been concerned with investigating plasma diagnostics in tornado-like prominences observed on 14 September 2013 and 15 July 2014. Using spectral data from the EIS instrument on the *Hinode* satellite and the *IRIS* satellite it has been possible to quantify many physical characteristics of solar tornadoes. The results from the analysis of these data sets are published in Levens et al. (2015) and Levens et al. (2016a).

The first data set dedicated to the study of tornado-like prominences is from 14 September 2013, and consists of a study from *Hinode*/EIS. These data were used by Su et al. (2014), where they studied line-of-sight velocities and non-thermal velocities in the Fe XII 195.119 Å and Fe XIII 202.044 Å lines, formed at $\log T = 6.2$ and $\log T = 6.3$ respectively. From that analysis those authors concluded that the tornado was a rotating structure. However, they only concentrated on two coronal temperature lines in that analysis, while there are a number of other spectral lines available in the EIS study. The Su et al. analysis also only concentrated on one plasma aspect (plasma velocity), but there are other questions left open that can be investigated with the same EIS study – what are the other plasma characteristics of the tornado (density, temperature structure)? Is the rotation visible at lower plasma temperatures? Those are the questions that were aimed to be answered in this analysis. Firstly spectral lines from EIS are fitted with Gaussian functions, allowing access to Gaussian parameters (intensity, centroid and line width), and

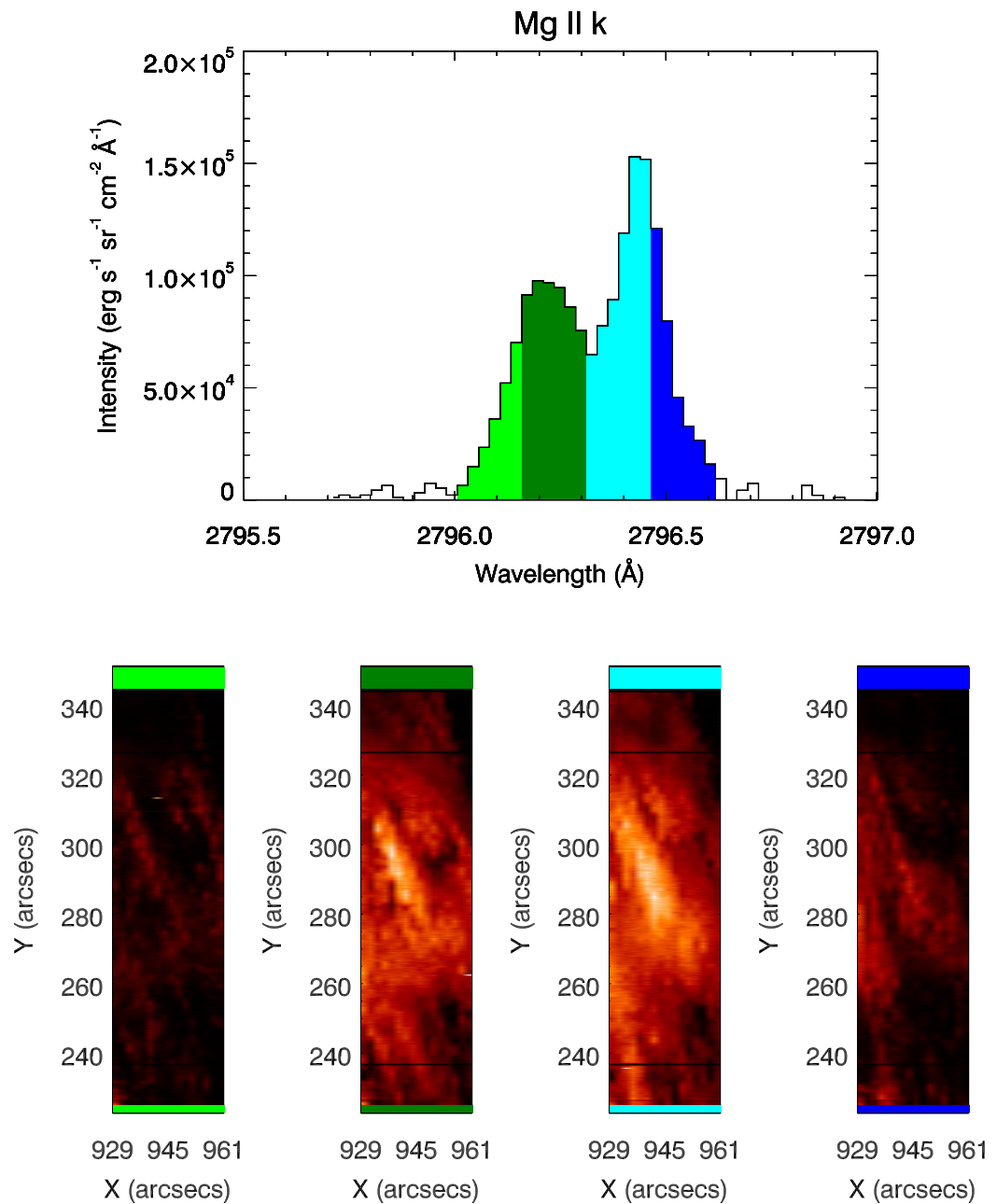


Figure 3.30: Raster maps made using integrations of different parts of the Mg II k line. *Top:* Example Mg II spectrum showing four regions over the line that are integrated to give the maps. Light green and dark blue sections show wings of the line, dark green and cyan sections show line core regions. *Bottom:* Raster maps corresponding to the regions shown in the top panel.

velocities can be calculated directly from the derived centroid values. This is done for lines formed at plasma temperatures from $\log T = 5.7 - 6.3$, extending the view of the tornado presented by [Su et al. \(2014\)](#). From that analysis it is found that the split-Doppler pattern, indicative of rotation, is visible in all lines formed above $\log T = 6$. Below that temperature the pattern is not visible, however the lines at temperatures lower than this suffer from low signal levels above the solar limb, or are parts of large blends of spectral lines, meaning their centroid values cannot be recovered accurately enough for detailed velocity analysis. Therefore from this study alone no definitive conclusions can be drawn about the plasma velocity below $\log T = 6$. Previous studies ([Orozco Suárez et al. 2012](#); [Wedemeyer et al. 2013a](#)) have reported tornado-like Doppler velocities in prominence legs in lines formed at lower temperatures, with $T \sim 6000$ K (He I 10830 Å and H- α lines). Unfortunately Doppler velocities for lines formed at those plasma temperatures were not available for the tornado on 14 September 2013.

Further analysis is presented on the plasma conditions in the tornado. Electron densities can be calculated using known density-sensitive line ratios from CHIANTI (v7.1, [Dere et al. 1997](#); [Landi et al. 2013](#)). The only density sensitive lines that can be used from this data set are formed at $\log T = 6.2$ – one Fe XII ratio and three Fe XI ratios. In all cases it is found that the electron density at this temperature is lower along a line of sight intersecting the tornado than in the nearby corona. This points towards a scenario where there is a ‘sheath’ of hot plasma surrounding the tornado that has a lower density than the corona, possibly made of lower density threads. Non-thermal line widths have also been investigated, finding that there is some additional broadening at the tornado. This effect could be caused by a different magnetic field structure in the tornado to the surrounding corona – a ‘turbulent’ magnetic field component ([Schmieder et al. 2014](#)) could cause non-thermal broadening. Alternatively, the presence of Kelvin-Helmholtz instabilities at the tornado boundary could also cause line broadening ([Zaqarashvili et al. 2015](#)).

Finally, for the 14 September 2013 data set, differential emission measures (DEMs) are presented for the first time in a tornado-like structure, along with complementary DEMs from the corona and the main prominence body. This is also the first representation of prominence DEMs using EIS data. Nine spectral lines, with formation temperatures ranging from $\log T = 5.4 - 6.2$, are used to constrain the DEM curve. It is found in these DEMs that the tornado and prominence body have more emission

at lower plasma temperatures than the corona at similar distances from the solar limb, as expected. However, it is also found that there is more emission at higher temperatures in the tornado and prominence than the surrounding corona too. This result supports the statement that the velocity, density and NTLW measurements could be coming from the tornado itself, however it must be noted that such differences could arise from hot loops in the foreground of the tornado/prominence that are not present in the line of sight of the coronal DEMs.

Further questions arise from these results regarding the lower temperature plasma and the magnetic field – is the lower temperature plasma ($\log T < 6$) behaving the same way as the hot plasma observed by EIS? What is the magnetic field structure? A coordinated observing campaign, run in 2014, aimed to answer these questions. The *Hinode* and *IRIS* satellites were used along with ground based spectropolarimeter THEMIS (magnetic field results are presented in Chapter 4). The first results from that campaign are reported here. Primarily using the Mg II h and k lines observed by *IRIS*, a tornado observation from 15 July 2014 has been studied. A first estimate of the line Doppler shifts is done with a Gaussian approximation for the Mg II k line, which indicates that overall line shifts in this prominence are low, on the order of $\pm 5 \text{ km s}^{-1}$. No evidence for rotation is found in the *IRIS* observations from 15 July 2014. Other diagnostics available from these lines mostly come from comparisons to prominence models, such as the 1D Mg II model of [Heinzel et al. \(2014\)](#). Comparing observed line profiles to models allows an estimate of physical parameters to be made, with gas pressure and optical thickness coming directly from model parameters. The reversal of the Mg II k line (k_2/k_3 ratio) is sensitive to the model parameters, so this ratio is one of the best for comparing to the model of [Heinzel et al. \(2014\)](#). Line reversals observed in the 15 July 2014 prominence suggest high optical thickness, up to 820, and high pressure, around 0.5 dyne cm^{-2} , in regions with the most reversed profiles, with regions of lower reversal indicating optical thickness near 100 for lower pressures ($\sim 0.1 \text{ dyne cm}^{-2}$). This is the first report of a quiescent prominence with such large reversal levels – previous prominences observed with *IRIS* mostly show non-reversed Mg II profiles ([Schmieder et al. 2014](#); [Vial et al. 2016](#)).

The complexity of the observed Mg II h and k line profiles from *IRIS* cannot be fully explained by the simple models of [Heinzel et al. \(2014\)](#). Having an extended grid of isothermal isobaric models would give a bigger range of models to compare to, and the ability to directly compare observations to models with a prominence-corona

transition region (PCTR) would allow for a more accurate description of the observed prominence. These updated models are explored in detail in [Chapter 5](#).

Chapter 4

Relationship between magnetic field and plasma in tornadoes

Chapter 3 describes plasma diagnostics of prominences with tornado-like characteristics. It has been shown that the UV and EUV parts of the solar spectrum contain lines which allow powerful diagnostics for studying the plasma in prominences, and comparing to radiative transfer models allows an estimate of the physical conditions of the plasma to be made. However, studying the plasma only tells half the story of prominences. Prominences are magnetic structures, and the magnetic field plays an important role in prominence dynamics (Mackay et al. 2010). It is therefore essential to study the magnetic field in tornado-like prominences in order to properly interpret their observed characteristics.

To understand how the plasma and magnetic field are linked it is first important to have accurate measurements of the magnetic field itself. During the coordinated campaign in 2014 (outlined in §3.3) THEMIS (López Ariste et al. 2000) was used to observe tornadoes in the He I D₃ line, which is sensitive to polarisation in the ways described in §2.4.3. From these profiles the magnetic field strength and orientation can be derived (described in §4.1). Further to these magnetic field measurements, this chapter goes on to investigate whether or not there are any significant, measurable links between the plasma parameters from *IRIS* and *Hinode* observations and the magnetic field from THEMIS (§4.2). In order to properly investigate this a robust spatial co-alignment must first be performed on all data sets, before a pixel-by-pixel analysis can take place (§4.2.1). Scatter plots are presented for plasma and line parameters versus magnetic field parameters in order to ascertain whether or not

there are any links between them (§4.3, 4.4).

The research presented in this chapter is published in [Levens et al. \(2016a\)](#) and [Levens et al. \(2017\)](#). As with Chapter 3, all analysis and figures in this chapter are original unless stated otherwise. Contributions from co-authors of [Levens et al. \(2016a\)](#) and [Levens et al. \(2017\)](#) are marked as such.

4.1 THEMIS observations

The THEMIS spectrograph, with the MulTi Raies (MTR) instrument ([López Ariste et al. 2000](#)), usually performs prominence observations by scanning its slit parallel to the limb, starting at a pointing near the limb. The observations on 15 July 2014 consisted of two rasters, starting at 14:41 UT and 16:55 UT, at two heights above the solar limb. Figure 4.1 shows raw intensity images of the two rasters, before any further data reduction is done. Raster ‘t035’ (14:41 UT, Figure 4.1 *bottom panel*) is near the limb, with raster ‘t037’ (16:55 UT, Figure 4.1 *top panel*) starting from a position at the same height above the limb as the top of t035. For an unknown reason the first raster (t035) stopped after 11 steps. The second raster (t037) started at the same height above the limb as the first raster ended and covered the same number of steps. Each raster contains 11 slit positions, with each step separated by 2'', covering a height of 22'' in each raster. The THEMIS slit is 120'' long, with each pixel along the slit 0.23'' in size, and a grid with three 15.5'' wide windows is used, parallel to the slit, to measure the full polarisation of the four Stokes parameters (I , Q , U and V) observable in the He I D₃ line. These windows are separated by 17''. Images are taken by displacing the grid to two successive positions, and the difference in window size and separation results in dark vertical strips in the images, as seen in Figure 4.1.

Data from THEMIS must be reduced further in order to measure the Stokes profiles, and this is done using the DeepStokes procedure ([López Ariste et al. 2009](#)). These profiles are then passed to an inversion code (based on Principal Component Analysis, see [López Ariste & Casini 2002](#); [Casini et al. 2003](#)) which takes the Stokes profiles from each pixel and compares them to a database of over 90000 model profiles. The models in the database are based on polarisation effects on an atom in the solar atmosphere by (unpolarised) radiation from the photosphere and the presence of a magnetic field around the atom. These models take into account both

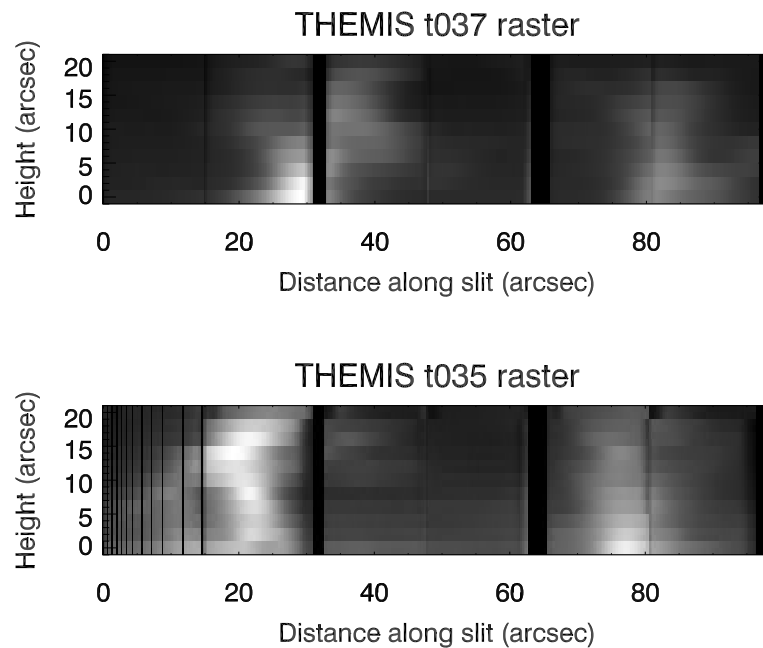


Figure 4.1: Two THEMIS rasters obtained in the afternoon of 15 July 2014. Vertical axis is height above limb from first slit position in the raster. *Top:* Raster t037, from 16:55 UT. *Bottom:* Raster t035, from 14:41 UT.

Hanle and Zeeman effects, both of which affect the polarisation of the He I D₃ line (López Ariste & Casini 2002). The polarisation profile for each point in the database is then a result of the effect of the magnetic field on scattered photospheric light. Observed profiles are compared to all models in the database, and the most similar model is taken as the magnetic field vector for each pixel, with error bars being constructed by the number of candidate models that are similar enough to the chosen one. This data reduction was performed by Arturo López Ariste, and is presented for analysis after reduction.

4.1.1 Magnetic field

The technique described above provides magnetic field strength and orientation for each pixel in the raster. Maps of each of these parameters can be made (Casini et al. 2003), providing a visual representation of the structure of the magnetic field throughout the prominence. Figure 4.2 shows maps of magnetic field strength (*top*

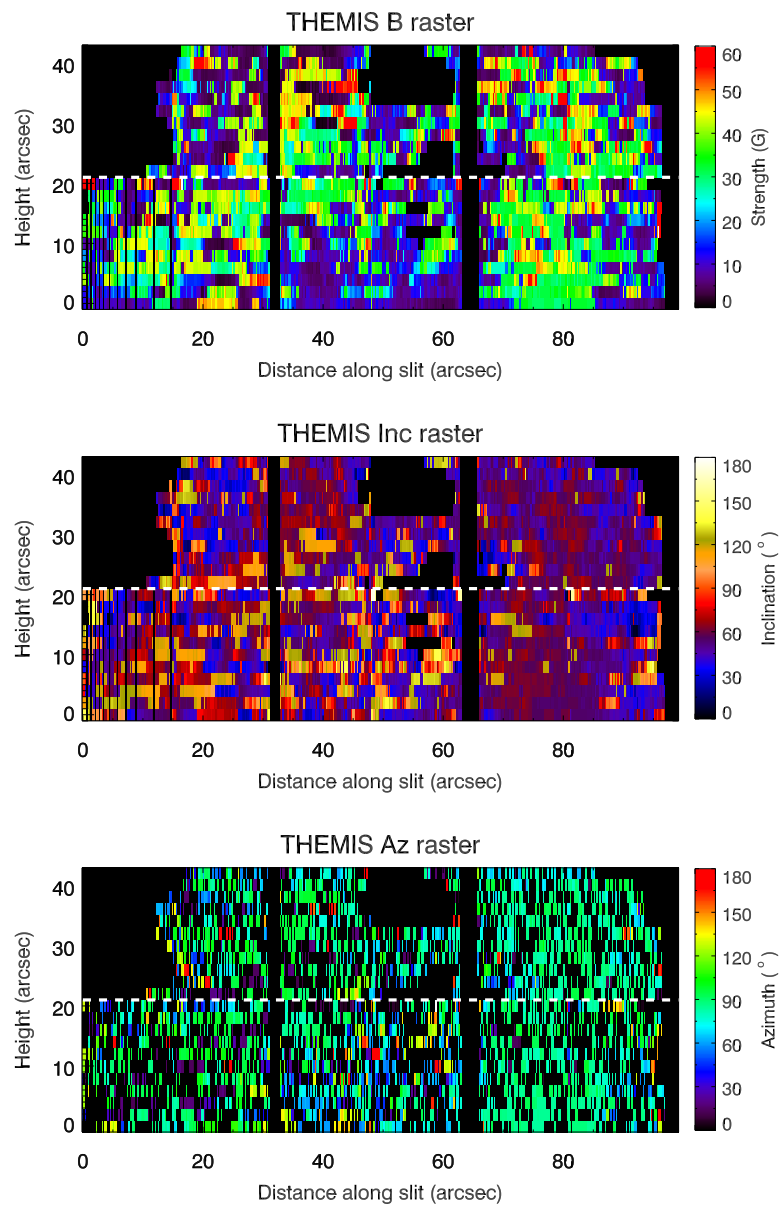


Figure 4.2: THEMIS rasters from 15 July 2014 showing magnetic field strength (*top*), inclination with respect to the local vertical (*middle*), and azimuth with respect to the line of sight (*bottom*). Images are composed of the two rasters from the day, with the white dashed line showing the separation between the two. Vertical axis is height above limb from the first slit position in the first raster.

panel), inclination with respect to the local vertical (*middle panel*), and azimuth with respect to the line of sight (*bottom panel*) for the prominence on 15 July 2014. Each

image is a combination of t035 (bottom) and t037 (top) rasters, separated by a white dashed line. From these images and (Figure 4.1) it can be seen that the brightest parts of the prominence (the two tornado-like columns) have field strengths ranging from about 10 G to around 60 G in places. The field inclination takes a range of values, but is generally around 90° (horizontal, or parallel to the solar surface). The azimuth generally takes values ranging from around 60° to 100° , although there are many noisy pixels, with discrepancies in the data. For further analysis the THEMIS data was provided in a binned $1'' \times 1''$ format. Square pixels make analysis of multiple arrays more straightforward, and the binning helps to ‘smooth’ any pixel-to-pixel inconsistencies.

The main result of [Levens et al. \(2016a\)](#) regarding the magnetic field is that in tornado-like prominences the field is predominantly horizontal. This result is clear from figure 7 of that paper, shown here as Figure 4.3, where a histogram of inclinations is presented for all points in the prominence on 15 July 2014. The blue histogram is for points where the error on the inclination is $< 10^\circ$, i.e. the magnetic field is recovered successfully. These points are clustered around a magnetic field inclination of 90° – the black curve shows a Gaussian with FWHM of 10° centred on 90° , which fits the blue data well. The red curve, on the other hand, shows points where the error is larger ($> 30^\circ$) and the magnetic field is less well described by the model from the database. Two distinct peaks are formed by these points, one at between 30° and 60° , and another between 120° and 150° . These peaks are interpreted as being due to an unresolved ‘turbulent’ magnetic field, superimposed on a horizontal field in one pixel ([Schmieder et al. 2014](#); [Levens et al. 2016a](#)) – this ‘turbulence’ could simply be the integration of two or more magnetic field components along the line of sight. The database does not include solutions that have such magnetic field structures (all solutions have only one magnetic field orientation per pixel), so the code finds a larger range of candidate models for the fit, resulting in larger error bars. [Levens et al. \(2016b\)](#) show similar analysis for another tornado prominence on 23 May 2014, wherein the same results are obtained. Therefore the 15 July 2014 prominence is not an isolated case, and the result of horizontal magnetic fields in tornadoes is robust.

The important result here is that the magnetic field is horizontal. This result notably casts doubt on the vertical or twisted magnetic field orientation in these tornadoes suggested by [Su et al. \(2014\)](#). A twisted field model was explored by [Luna](#)

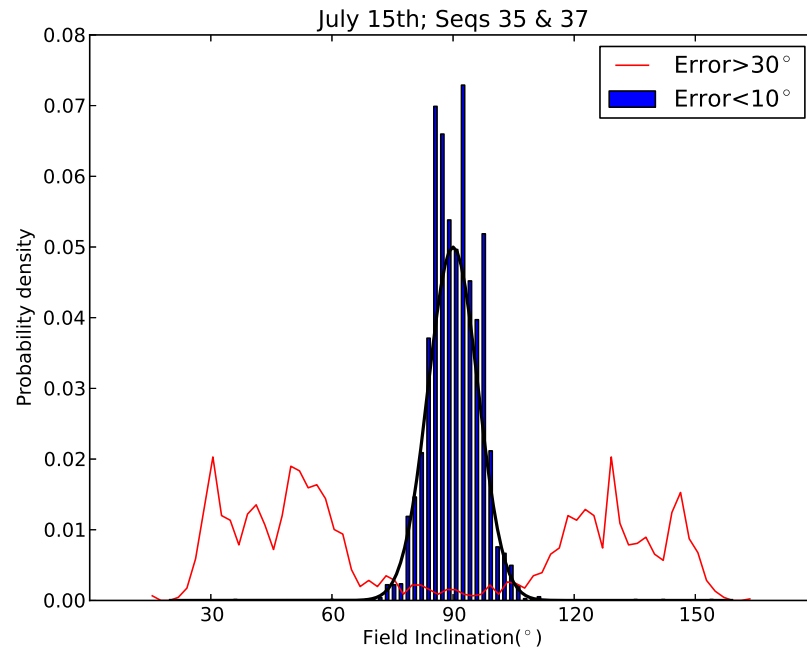


Figure 4.3: Histogram of magnetic field inclination for the prominence of 15 July 2014. Blue histogram shows points where error on the inclination is $< 10^\circ$, with the black line showing a Gaussian with FWHM of 10° . Red line indicates points where error is $> 30^\circ$. This figure is from [Levens et al. \(2016a, figure 7\)](#) and was made by A. López Ariste.

[et al. \(2015\)](#), however that model requires the field to become more and more vertical towards the central axis of the tornado. This is not supported by the observations, as that would result in a full mix of l.o.s. azimuth values where in the THEMIS observations they are mostly clustered around 70° .

Horizontal magnetic fields in tornadoes points towards the standard prominence magnetic field models (see [Mackay et al. 2010](#)), with cool plasma being supported in ‘dips’ in the magnetic field ([Aulanier & Demoulin 1998](#)). This configuration for tornadoes is discussed in [Schmieder et al. \(2017b\)](#), where it is described that a dipped field, caused by parasitic polarities on the solar surface and filled with plasma, could cause apparent tornado-like motions due to oscillations of the magnetic field. Another model that could explain the observed plasma motions is that of *large amplitude longitudinal oscillations* (LALOs, [Luna et al. 2016](#)). As with the scenario outlined by [Schmieder et al. \(2017b\)](#), LALOs rely on a dipped magnetic field but

with counter-streaming plasma oscillating within the dips. Viewed in projection, the oscillating plasma could create tornado-like motions on the plane of the sky.

4.2 Comparing magnetic field and plasma parameters

In Chapter 3 and [Levens et al. \(2016a\)](#) plasma properties of tornado-like prominences were investigated, and §4.1.1 introduces observations of the magnetic field in tornadoes. The question remains, however, on how the observed magnetic field and the plasma are related, and whether or not there is any measurable link between them. To address this question it is necessary to perform a robust co-alignment of all the relevant data sets. It is then possible to explore the statistical relationship between the magnetic field and plasma/line parameters on a pixel-by-pixel basis.

The aim of this work is to study the magnetic field parameters – field strength, inclination and azimuth as measured by THEMIS – and compare them to plasma parameters and line parameters derived from spectral lines observed by *IRIS* and *Hinode*/EIS. The question of whether the conditions in the tornadoes matches that of the rest of the prominence also remains open. As discussed in Chapter 3 there appear to be some differences in the Mg II lines when comparing pixels looking at the tornadoes to those from the rest of the prominence, but it is more informative to consider a statistical approach to this analysis. The comparison between points in the tornadoes and points elsewhere in the prominence or corona will be discussed throughout the following sections. The work presented in the remainder of this chapter has recently been published in the journal *Astronomy & Astrophysics* ([Levens et al. 2017](#)).

4.2.1 Co-aligning data sets

The first step in a statistical analysis on a pixel-by-pixel basis is to ensure that data sets from different instruments are well aligned. A 2D cross-correlation method is used to perform the alignment, which makes use of a *Mean Absolute Difference* (MAD) algorithm. As the name suggests, the MAD technique considers the mean of the absolute difference between points in two arrays (or in this case, images). By finding the minimum value of this quantity across all points in the two arrays being compared, the position where the difference between them is smallest can be found.

Table 4.1: Summary of instruments and observations from 15 July 2014 which are used for co-alignment.

Instrument	Type	Resolution	λ (Å)	Dominant ion	Time (UT)
<i>SDO/AIA</i>	imager	0.6×0.6''	304	He II	continuous
<i>SDO/AIA</i>	imager	0.6×0.6''	193	Fe XII	continuous
<i>IRIS SJI</i>	imager	0.17×0.17''	2796	Mg II	08 – 11
<i>IRIS spec.</i>	raster	2×0.17''	2796	Mg II	08 – 11
<i>Hinode/SOT</i>	imager	0.11×0.11''	3968	Ca II	10:21 – 11:06
<i>Hinode/EIS</i>	raster	2×1''	195	Fe XII	10:34
THEMIS	raster	1×1''	5875	He I	14:41 & 16:55

This is then the position where the two arrays are most similar. The SSW routine `get_correl_offsets`, which employs the MAD algorithm, is used to calculate the $x - y$ pixel offsets between two images. For this method to work effectively similar images need to be used, so it is necessary to carefully consider which correlations should be made. The data from each instrument used here also has different spatial resolutions, so it is necessary to degrade the higher resolution data to match the resolution of the lower resolution data. This degradation is done using the SSW routine `coreg_map`.

There are five instruments that are to be used for this correlation; *SDO/AIA*, *IRIS* (SJI and spectrograph), *Hinode/SOT*, *Hinode/EIS*, and THEMIS. A summary of each instrument's observations on the 15 July 2014, including a summary of spatial resolutions, is displayed in Table 4.1. The aim is to investigate correlations between the data from *IRIS* (raster), *Hinode/EIS*, and THEMIS, but other instruments are required in order to perform the co-alignment.

It is also important to note the differences in times of observation, especially between THEMIS and the space-based instruments – the satellites finished observing at ~ 11 UT, whereas THEMIS only observed in the afternoon. Therefore any co-alignment will not be temporally absolute, however the prominence does not evolve much over the course of the day, therefore it is not expected that the conditions in the prominence would change significantly between observations. It can then be assumed that the data obtained in the afternoon by THEMIS is not significantly different to what it would have been had THEMIS observed in the morning, though

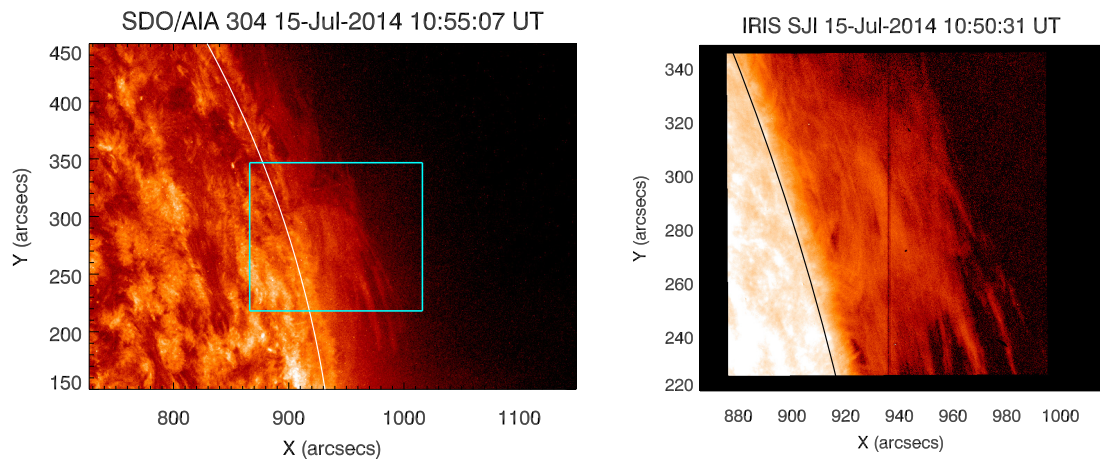


Figure 4.4: *Left:* AIA 304 Å image from 10:55 UT on 15 July 2014. Blue bounding box is the FOV of the *IRIS* SJI. Solar limb position is shown in white. *Right:* *IRIS* SJI from 10:50 UT on 15 July 2014. Solar limb position is shown in black. Vertical dark strip is the position of the *IRIS* slit at this time.

it is important to keep in mind that this temporal discrepancy exists.

4.2.1.1 *IRIS* with SDO AIA

AIA images in the 304 Å and 193 Å passbands are taken as the base for the co-alignment of these data sets. All other data sets will eventually be brought into alignment with the AIA images from 11:00 UT (for 304 Å) and 10:34 UT (for 193 Å). For aligning *IRIS* slit-jaw images it is noted that the prominence appears as an extended structure with horizontal, thread-like structures in both the SJI and in the 304 Å channel from AIA. This can be seen in Figure 4.4, which shows the AIA 304 Å filter (*left panel*) and the *IRIS* Mg II SJI (*right panel*) on 15 July 2014. The similarity is due to the fact that the dominant emission in both filters – He II in AIA and Mg II h and k in *IRIS* – comes from lines which are extremely optically thick, with $\tau_{MgIIh} \sim \tau_{HeII304}$ (Levens et al. 2016a).

The *IRIS* SJI selected for the co-alignment was taken at 10:50 UT. *IRIS* passed through the SAA at the end of its observing time, so the data from 10:50 UT to 11:00 UT was deemed unusable. Data from the end of the observing time of the satellites is used in order to minimise the temporal difference between those data and the data from THEMIS.

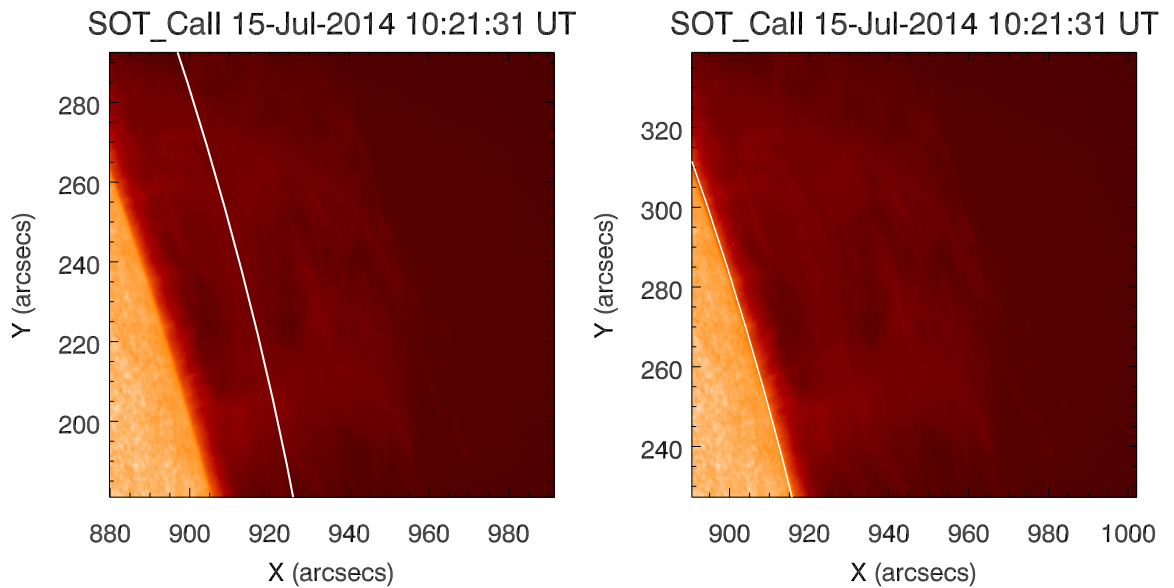


Figure 4.5: SOT Ca II image from 15 July 2014 at 10:21 UT, the start of the SOT observations on that day. *Left:* Image made using the pointing in the SOT FITS header. *Right:* Image from after co-alignment with the *IRIS* SJI. Plotted in white is the limb position, according to each pointing.

Using the cross-correlation routines described above, the two data sets are brought into alignment with each other. It is found that an offset of $x = 0.81''$ and $y = -1.65''$ should be applied to the *IRIS* SJI to align it with the AIA 304 Å image.

4.2.1.2 *Hinode* SOT with *IRIS*

Although spectral information cannot be gained from *Hinode*/SOT, it is still important that it is aligned with the rest of the data as it is an SOT image that is used to align the THEMIS data (described in §4.2.1.3). The Ca II H and K lines are optically thick resonance lines (Gouttebroze et al. 1997), but notably they are not as optically thick as the Mg II h and k lines. This is clear when comparing images of the prominence of 15 July 2014 in Mg II from *IRIS* and Ca II from SOT – in magnesium we see the horizontal structure only, whereas in calcium it is possible to distinguish the brighter prominence legs more clearly. This is an optical thickness effect. In magnesium we are only looking at the frontmost layers of plasma due to its high optical thickness, whereas in calcium we can see slightly further into the structure,

and the denser parts of the prominence (the legs) appear brighter. It is worth noting, however, that the horizontal thread-like structure is still very much visible in Ca II, therefore it is possible to co-align the SOT images with those from *IRIS* or AIA. The *IRIS* images are chosen for this cross-correlation as they are higher resolution than those from AIA (Table 4.1), resulting in the least degradation of the SOT data.

Before the SOT images could be aligned with the *IRIS* SJI it was necessary to manually shift the SOT pointing, after a ‘by eye’ consideration of the limb position in the images, by $x = 11''$ and $y = 44''$. This manual shift is to bring the SOT image closer to its true pointing and to minimise the chance of `get_correl_offsets` reaching the iteration limit – if the procedure fails to reach an acceptable correlation within the iteration limit the resulting co-alignment is not correct. Figure 4.5 (left panel) shows the SOT map made using the pointing information from the *Hinode* header, with limb position according to that pointing plotted in white. The true position of the limb can clearly be seen in Figure 4.5 (left panel), and it is a long way from the plotted limb position. This is due to known errors with the *Hinode* pointing, where even upon calibration the pointing for SOT images is not absolute¹.

Once the manual offset is applied, the cross-correlation routine can be run on the SOT images. An overall offset of $x = 11.22''$ and $y = 45.64''$ is applied to SOT images, bringing them in line with the *IRIS* and therefore AIA images. Figure 4.5 (right panel) shows the SOT image with plotted limb position after this correction is included in the pointing.

4.2.1.3 THEMIS with *Hinode* SOT

Aligning THEMIS data with the other instruments is more complex than for the other data sets, due to the way that THEMIS makes observations. To observe prominences the THEMIS slit is orientated parallel to the solar limb at a position angle (PA) which is measured anti-clockwise from solar north. THEMIS then scans from a position near the limb, with each step in its raster observing a higher altitude than the previous (see §4.1). Therefore there is no traditional ‘pointing’ for THEMIS rasters. It is necessary to ensure that the map is correctly orientated before any co-alignment can be done.

To begin with, the THEMIS rasters are orientated so that the slit is along the x -axis of the image, as in Figure 4.1, meaning that the solar limb is parallel to the

¹<https://hesperia.gsfc.nasa.gov/ssw/hinode/sot/doc/guide/SAGv3.3.pdf>, Appendix C

x -axis. The two THEMIS rasters (taken at 14:41 UT and 16:55 UT) from the 15 July 2014 are spliced together, as they have a known offset in height above the limb – t037 was started at the same place that t035 stopped. A small offset in x is introduced (a 5 pixel shift) between the two rasters in order that the brightest parts of the two columns are aligned. Herein these two spliced rasters are considered as one image. To correctly orientate this image it must be rotated by 360° minus the PA at which the prominence was observed, which here was $PA = 288^\circ$. Therefore the map is rotated clockwise by 72° . To properly achieve this rotation the spliced rasters are placed within a larger array of $121'' \times 120''$ with highly negative values elsewhere – this avoids issues at the edges of the image when rotating a map. The size of this array is chosen such that the centre of the original map(s) remains the centre of the new image in both x and y , and that there is enough room to accommodate the rotated map. A pixel binning is performed when rotating a map in order to maintain square pixels. Using the technique outlined here the pixels at the edge of the rasters are averaged with highly-negative value pixels outside of the FOV, so can easily be identified and removed. Due to the fact that there is no pointing information in the THEMIS headers this rotated map is, by default, centred on $(0'', 0'')$ in solar coordinates. The THEMIS map is then manually shifted to be centred on $(936'', 292'')$ before co-alignment. This rotated THEMIS map is shown in Figure 4.6, where intensity (*top left*), magnetic field strength (*top right*), inclination (*bottom left*), and azimuth (*bottom right*) maps are presented.

The magnetic field strength map shown in Figure 4.6 raises some questions regarding the appearance of the magnetic field. In this map the high magnetic field strength regions (up to 60 G) mostly appear clumped together, into small spots with spatial scales of only a few arcseconds in size. It can then change over a few arcseconds to values around an order of magnitude smaller. In most cases these are artefacts of individual pixels where the profiles are poorly inverted and there are large inversion errors (A. López Ariste, *private communication*), which are extended in all directions when the maps are interpolated and rotated. There are, however, places in this map where the strong magnetic field regions are more extended, such as the region around $(930'', 320'')$. This region shows more consistently high field strengths, and it is found that profiles from these pixels are well inverted (A. López Ariste, *private communication*). Field strengths on this order have been found before using this method (Casini et al. 2003), but they have not been fully explored.

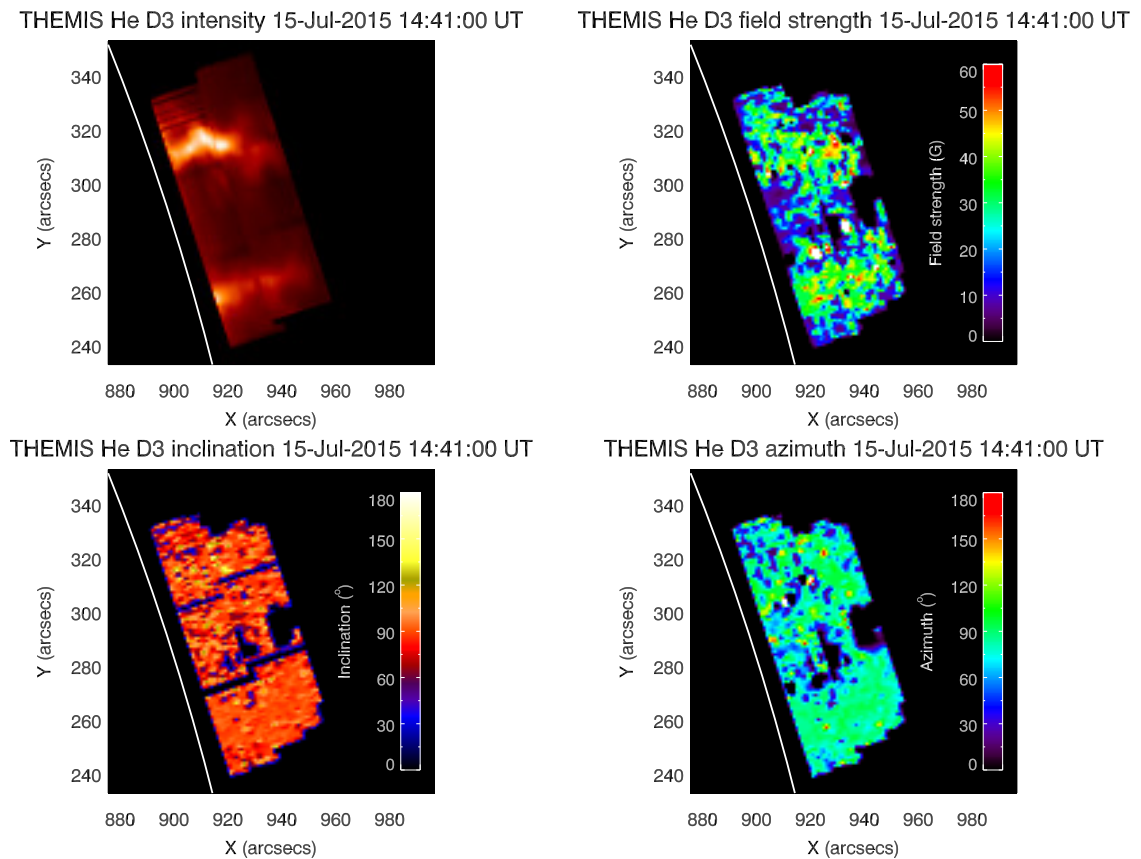


Figure 4.6: THEMIS intensity and magnetic field maps from 15 July 2014. These images are made from a composite of the two rasters from that day, which have been rotated and aligned to the SOT image. Solar limb position is shown in white. *Top left:* He I D₃ intensity. *Top right:* Magnetic field strength. *Bottom left:* Magnetic field inclination. *Bottom right:* Magnetic field azimuth.

The question then arises about what instrument to co-align the THEMIS image with. The He I D₃ line is mostly optically thin (Labrosse & Gouttebroze 2004), which can be seen brightly in emission in prominences, and in this data set the two tornado columns can be clearly seen (Figure 4.6). Considering again the Ca II emission from SOT, which is formed at a similar temperature to He I D₃, gives a potential image to align the THEMIS map with. As was mentioned in §4.2.1.2, the tornado columns are visible in Ca II, which becomes more obvious when a threshold is applied to the SOT image, as shown in Figure 4.7. Only the brightest parts of the prominence remain visible, which coincide with the two tornadoes with some thread-like structure between them, similar to the He I D₃ view of the prominence. Figure 4.7 also has

Hinode SOT threshold 15-Jul-2014 10:21:31 UT

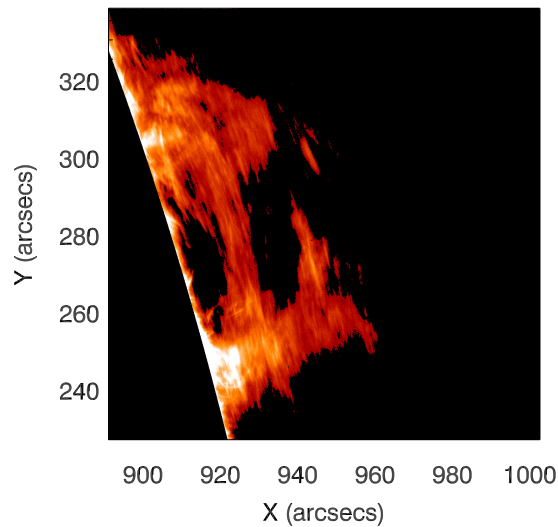


Figure 4.7: SOT Ca II image with disc mask and threshold applied to show only brightest parts of the prominence.

the bright disc masked (photospheric disc + $6''$). This is done to make the SOT image as similar to the THEMIS image as possible, which increases the chance of the cross-correlation procedure arriving at a result. It is this thresholded and masked image that is used to align the THEMIS map.

The offsets for the THEMIS image, further to the manual shift, is found to be $x = 0.91''$ and $y = 0.61''$, meaning that the centre of the THEMIS image is ($936.91''$, $292.61''$). This transformation and shift is then applied to the arrays containing all of the THEMIS parameters of interest – magnetic field strength, inclination and azimuth.

4.2.1.4 *Hinode* EIS with SDO AIA

The EIS instrument has two CCDs, which have a known pointing offset between them of around $2''$ in x and $17''$ in y (Young et al. 2009; Graham et al. 2015). The offset for a specific wavelength observed by EIS can be resolved using the SSW routine `eis_ccd_offset`, relative to the He II 256 \AA line. This is done to the EIS data before performing co-alignment with the other instruments.

There is then the question of which data to align the EIS raster with, and which

corresponding EIS line to use. An obvious choice might be the AIA 304 Å passband and the EIS 256 Å line, both of which are dominated by He II resonance line emission in prominences. However, there is a non-negligible amount of emission from hotter lines in both the 304 Å passband of AIA and the 256 Å blend as observed by EIS. Therefore using this pairing for the co-alignment is not ideal, and a better solution is required. As noted previously, tornadoes are visible as silhouettes in coronal emission lines and there is another pairing of lines that can be used – the 193 Å passband from AIA and the 195 Å line from EIS. The dominant emission in both cases is from Fe XII, and the prominence looks similar in both cases. The 195 Å line observed by EIS is described in Chapter 3 (§3.1.3.4), and the same technique for de-blending is used here. The 193 Å passband of AIA is dominated by emission from the Fe XII 193.51 Å line in the quiet corona. These lines are formed by the same ion under the same conditions, so the resulting images are very similar, seen in Figure 4.8.

Figure 4.8 shows the AIA 193 Å image (*left panel*) and the two EIS 195 Å raster maps (*middle and right panels*) for the 15 July 2014 at 10:34 UT. The left and middle images of Figure 4.8 are used for co-aligning these data sets, and an offset of $x = 4.08''$ and $y = 18.24''$ needs to be applied to the EIS rasters to bring them in line with AIA.

With all data sets spatially co-aligned it is possible to study the parameters from each on a pixel-by-pixel basis. Figure 4.9 shows a composite image showing the resulting co-alignment of AIA 304 Å, *IRIS* Mg II SJI, SOT Ca II and EIS 256 Å images, with contours from THEMIS indicating the locations of the tornadoes. This composite image shows how structures in the prominence are spatially related in emission from different wavebands. An estimate of the overall uncertainty on the spatial co-alignment of the images is 2'', the spatial resolution of the lowest resolution data used.

4.3 Correlation between THEMIS and *IRIS* data

Using line ratios and parameters calculated from the Mg II h and k lines it is possible to study some properties of the plasma that is observed by *IRIS*. To investigate

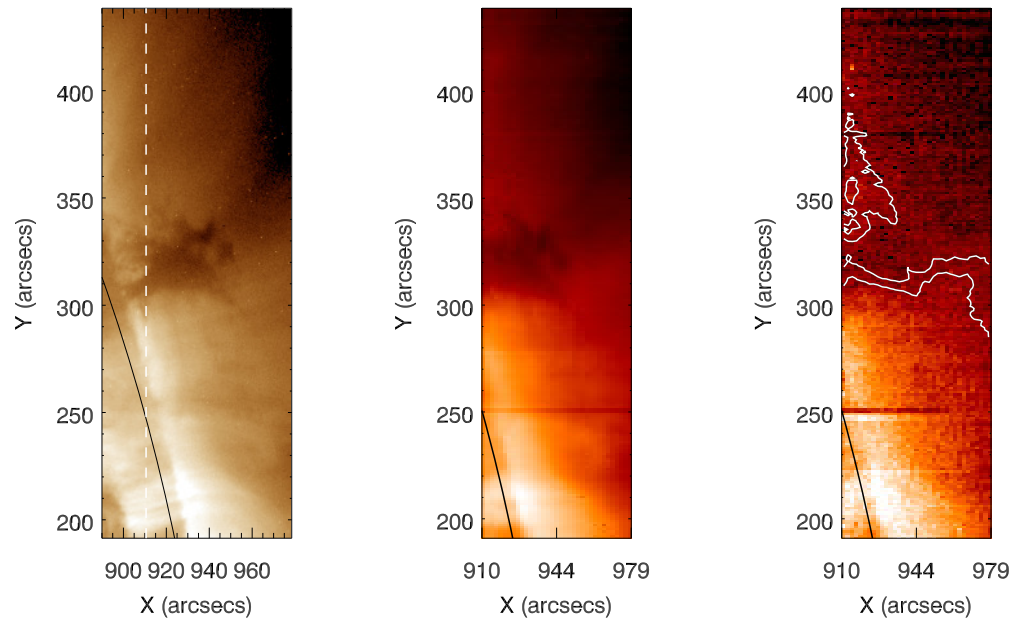


Figure 4.8: Maps from 10:34 UT on 15 July 2014: *Left:* SDO/AIA 193 Å. *Middle:* Hinode/EIS 195.119 Å. *Right:* Hinode/EIS 195.179 Å with contours of 195.119 Å. The white vertical dashed line in the AIA image shows the edge of the EIS field of view. The solar limb is shown in black. The dark horizontal feature in the EIS maps at around $y = 250''$ is an artifact from the EIS detector. This figure was used in [Levens et al. \(2017\)](#).

whether or not there is any link between these parameters and the magnetic field parameters from THEMIS it is instructive to construct scatter plots to look for correlations. In order to do this, however, it is first necessary to calculate the area of overlap between the *IRIS* raster and the THEMIS rasters. With the two data sets aligned, this can be done simply by calculating the limits of the rasters and where they overlap – Figure 4.10 (*left panel*) shows the overlap area with x - y range identical to those of the THEMIS map. This image is used as a mask, and from this the relevant *IRIS* raster pixels and spectra can be identified and compared with the magnetic field parameters at the same point. Due to the difference in spatial resolution between the two instruments it is necessary to average the *IRIS* spectra in the y direction – binning by 6 pixels in y is used to achieve the $1''$ resolution of the THEMIS data.

It is also interesting to consider points in the tornadoes versus points outside of them. As was noted, the tornado columns appear bright in the He I D₃ emission,

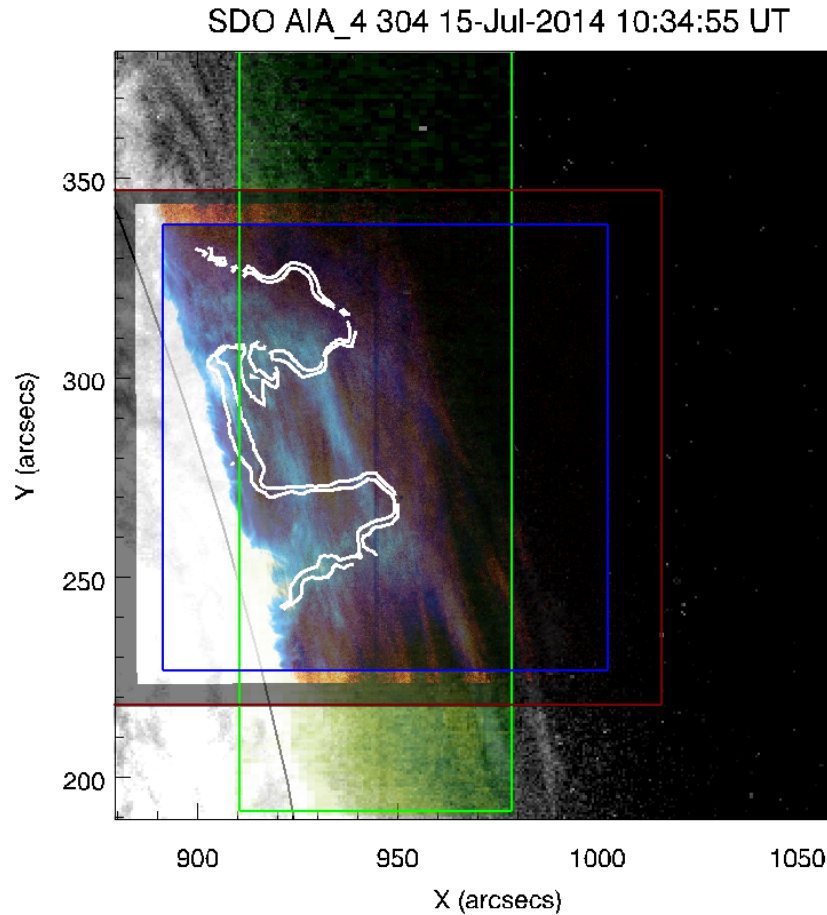


Figure 4.9: Composite plot showing co-alignment of data sets for optically thick channels on 15 July 2014. Images are: AIA 304 Å (greyscale), EIS 256 Å (green), *IRIS* Mg II SJI (red), and SOT Ca II (blue). White contours show positions of the tornadoes from THEMIS intensity image. This figure was used in [Levens et al. \(2017\)](#).

so are easily identified. Figure 4.10 shows masks of the tornadoes (*middle panel*) and points outside of them (*right panel*), which are in the rest of the prominence – the entirety of the overlapped area covered by the THEMIS raster is filled with prominence emission in the *IRIS* raster. It is worth noting, however, that there is only a partial overlap between these two data sets, so only the top of the northern tornado and just over half of the southern tornado (as seen by THEMIS) are visible in the *IRIS* raster.

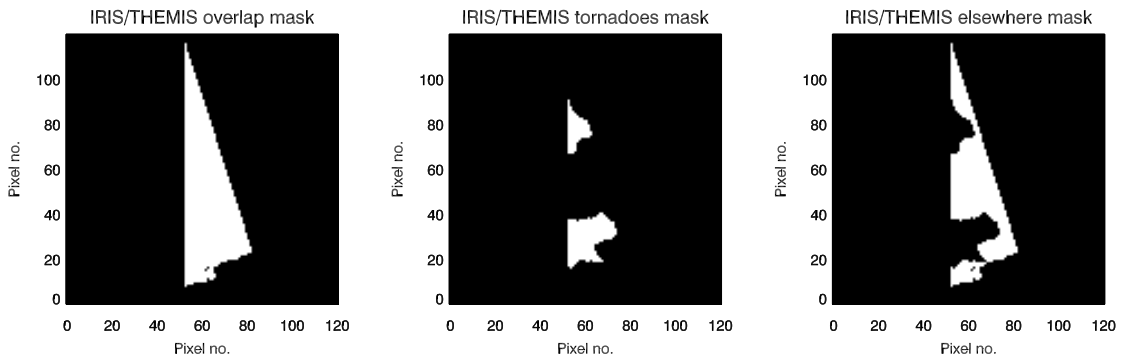


Figure 4.10: Masks showing the overlapped area between *IRIS* and THEMIS rasters for data sets on 15 July 2014. White areas indicate overlap. *Left:* Full overlap area. *Middle:* Mask for tornadoes. *Right:* Mask for rest of prominence. This figure was used in [Levens et al. \(2017\)](#).

Table 4.2: Previously observed Mg II line parameters in prominences by authors using *IRIS* – [Schmieder et al. \(2014\)](#); [Harra et al. \(2014\)](#); [Liu et al. \(2015a\)](#); [Levens et al. \(2016a\)](#); [Vial et al. \(2016\)](#). Here ‘nr’ means non-reversed for the k line.

Author (year)	prominence type	k_2/k_3 ratio	k/h ratio	l.o.s. velocity (km s ⁻¹)	FWHM (Å)
Schmieder et al. (2014)	quiescent (+ flows)	nr	~ 1.5	± 15 (→ 75)	~ 0.15
Harra et al. (2014)	eruption	nr	1.5 – 1.9	± 20	0.1 – 0.4
Liu et al. (2015a)	eruption	nr	1 – 1.8	± 100	not given
Levens et al. (2016a)	quiescent (+ tornado)	nr – 2.6	1.2 – 1.7	± 10	0.24 – 0.41
Vial et al. (2016)	polar crown	nr	1.4 – 1.5	~ -9	0.12 – 0.16

4.3.1 Mg II k_2/k_3 ratio

The Mg II k_2/k_3 ratio is a measure of the level of reversal of the k line (equivalently h_2/h_3 for the h line), which can be used to compare observations to models of the

Mg II lines in prominences, as was done in §3.4. Previous authors have generally found the Mg II h and k lines to be non-reversed (see Table 4.2), but in this prominence there is a mix of reversed and non-reversed profiles. These reversed profiles were explored somewhat in Chapter 3, but the question here is whether the level of reversal of the Mg II lines is spatially related to the magnetic field parameters. To try to answer this question the k_2/k_3 ratio is plotted against the magnetic field strength, inclination, and azimuth (Figure 4.11). Here the k_2 value is taken to be the intensity of the higher peak (k_{2v} or k_{2r}), and the k_3 intensity is the value of the intensity at the minimum between the two peaks. These plots are split into two groups: those defined as being ‘tornado’ pixels, and those defined as ‘rest-of-prominence’ pixels by the masks described above and in Figure 4.10. Points are also separated into those that are ‘reversed’ (red asterisks), ‘complex’ (blue diamonds), and ‘single peaked’ (green triangles). Single-peaked profiles are arbitrarily assigned a k_2/k_3 ratio of 0.5 in Figure 4.11 to distinguish them. The profiles found in this prominence are discussed in §3.3.2.

Figure 4.11 does not provide any convincing evidence that there is a link between the Mg II k reversal level and the magnetic field parameters. However, comparing the distribution of values from each instrument for points inside and outside the tornadoes shows some interesting differences between the two. Figure 4.12 shows histograms of the magnetic field parameters in the tornadoes (blue lines) and elsewhere in the prominence (orange dashed lines). The top left panel of Figure 4.12 shows the distribution of magnetic field strengths, from which it is clear that the magnetic field is generally stronger inside the tornadoes than outside of them. The tornadoes have a mean field strength of around 30 G, whereas the rest of the prominence has a mean of around 20 G. Table 4.3 (page 152) contains moments and standard deviations of the distributions for the magnetic field parameters from THEMIS, as well as for parameters from IRIS and EIS. Along with the mean and variance (first and second moments), higher order moments (third and fourth moments) are given for each distribution. The third moment, the *skewness*, gives an indication of how asymmetric a distribution is, with a symmetric distribution having a skewness of zero. The fourth moment, the *kurtosis*, is a measure of how Gaussian a distribution is – a kurtosis of 3 is a perfect Gaussian, with departures from that number giving an indication of deviation from a normal distribution.

The inclination of the magnetic field does not provide any new information

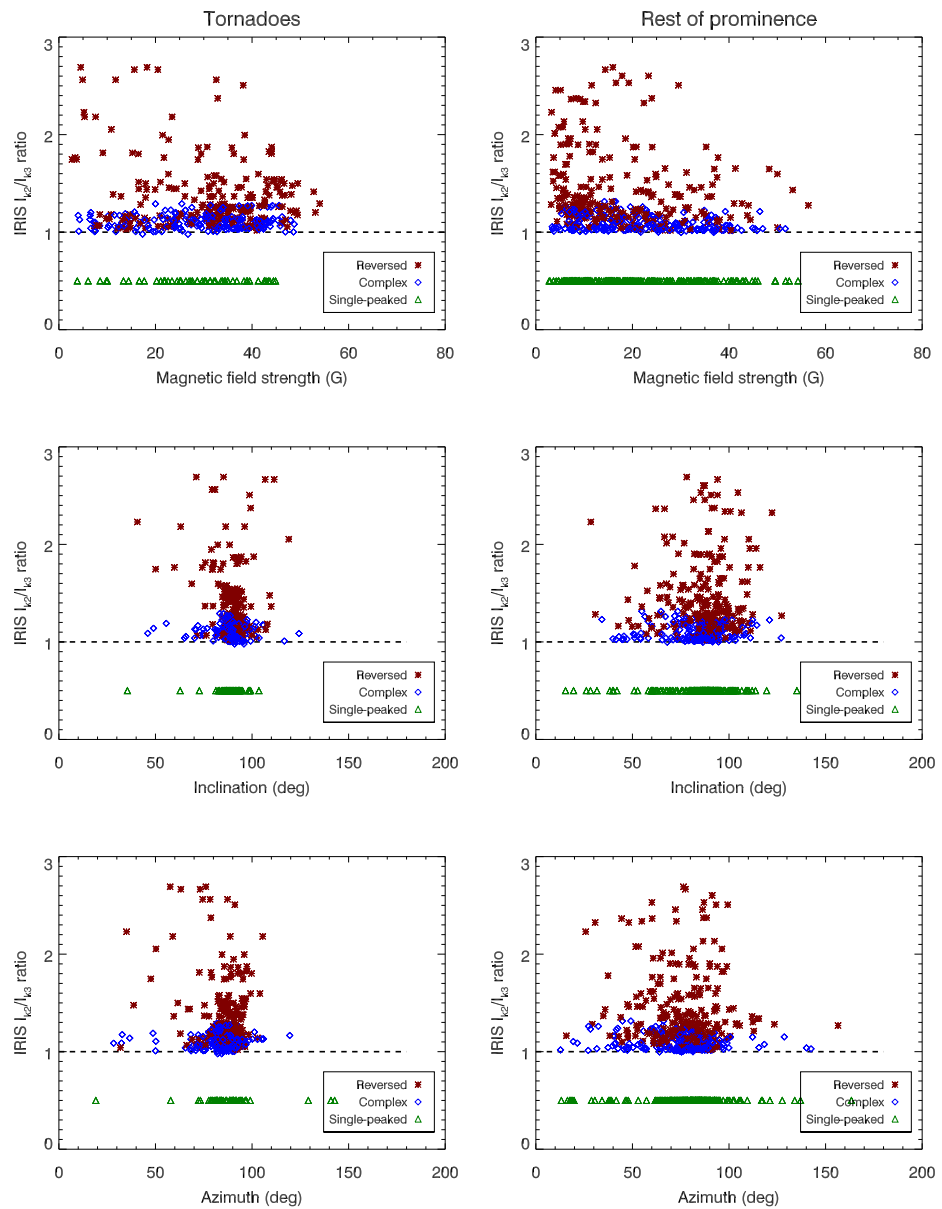


Figure 4.11: Plots of Mg II k_2/k_3 ratio vs. magnetic field parameters. Left column is points in the tornadoes, right column is points in the rest of the prominence. Red points are where the Mg II k line is reversed. Green triangles are points that are single peaked and narrow (manually placed at a ratio of 0.5 to distinguish them from the rest of the points). Blue diamonds are points where the profiles are ‘complex’. Black dashed line represents the cutoff for reversed profiles, with a ratio of 1 corresponding to a non-reversed profile. This figure was used in [Levens et al. \(2017\)](#).

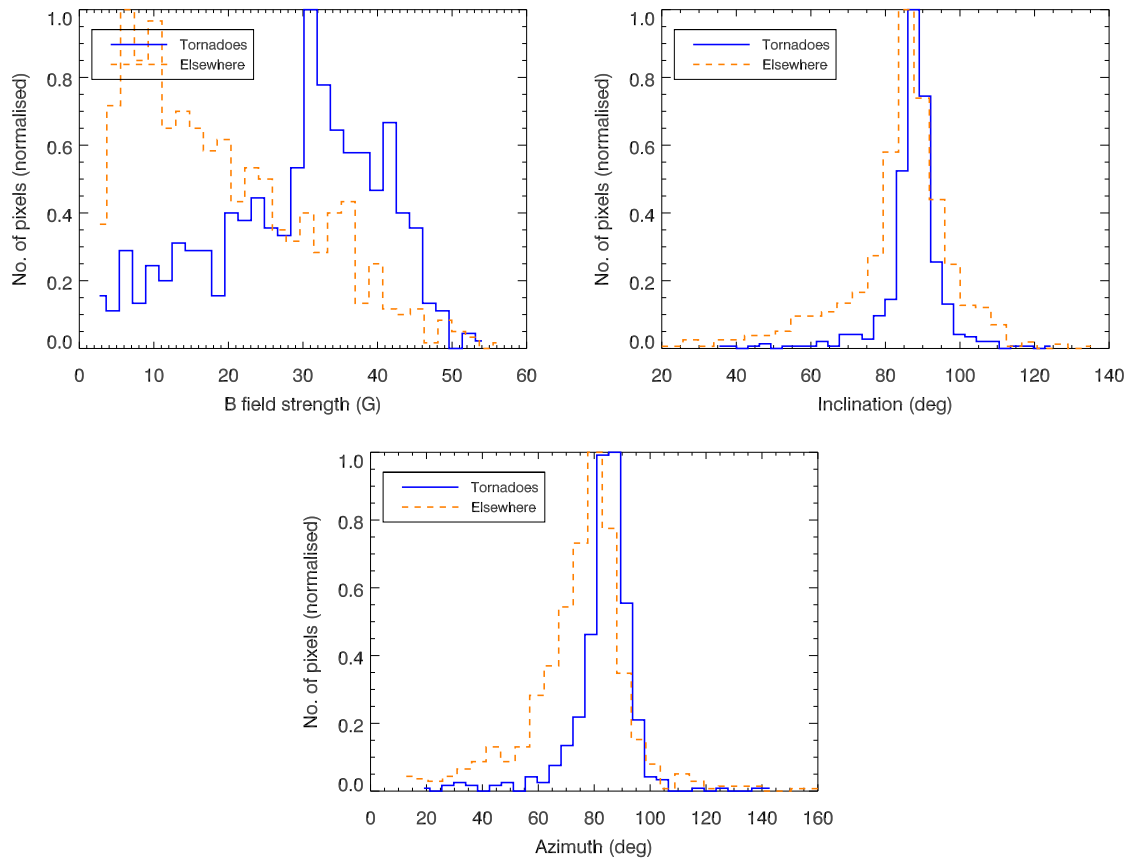


Figure 4.12: Normalised histograms of magnetic field parameters from THEMIS for points in the tornadoes (blue lines) and in the rest of the prominence (orange dashed lines). *Top left:* Magnetic field strength. *Top right:* Inclination with respect to the local vertical. *Bottom:* Azimuth with respect to the line of sight. This figure was used in [Levens et al. \(2017\)](#).

(Figure 4.11, *middle panels*). Most of the points are clustered around an inclination of 90° , or horizontal, which is consistent with values found previously in tornadoes ([Levens et al. 2016a,b](#)) and prominences in general (e.g. [Schmieder et al. 2014](#); [López Ariste 2015](#)).

In the plots of k_2/k_3 ratio vs. l.o.s. azimuth (Figure 4.11, *bottom panels*), a similar pattern can be seen to the inclination case. Most points are clustered around a mean value of 85° in the tornadoes and 77° elsewhere. This can be seen more clearly in the histograms (Figure 4.12, *bottom panel*).

Figure 4.13 shows histograms of the spread of values of the Mg II parameters

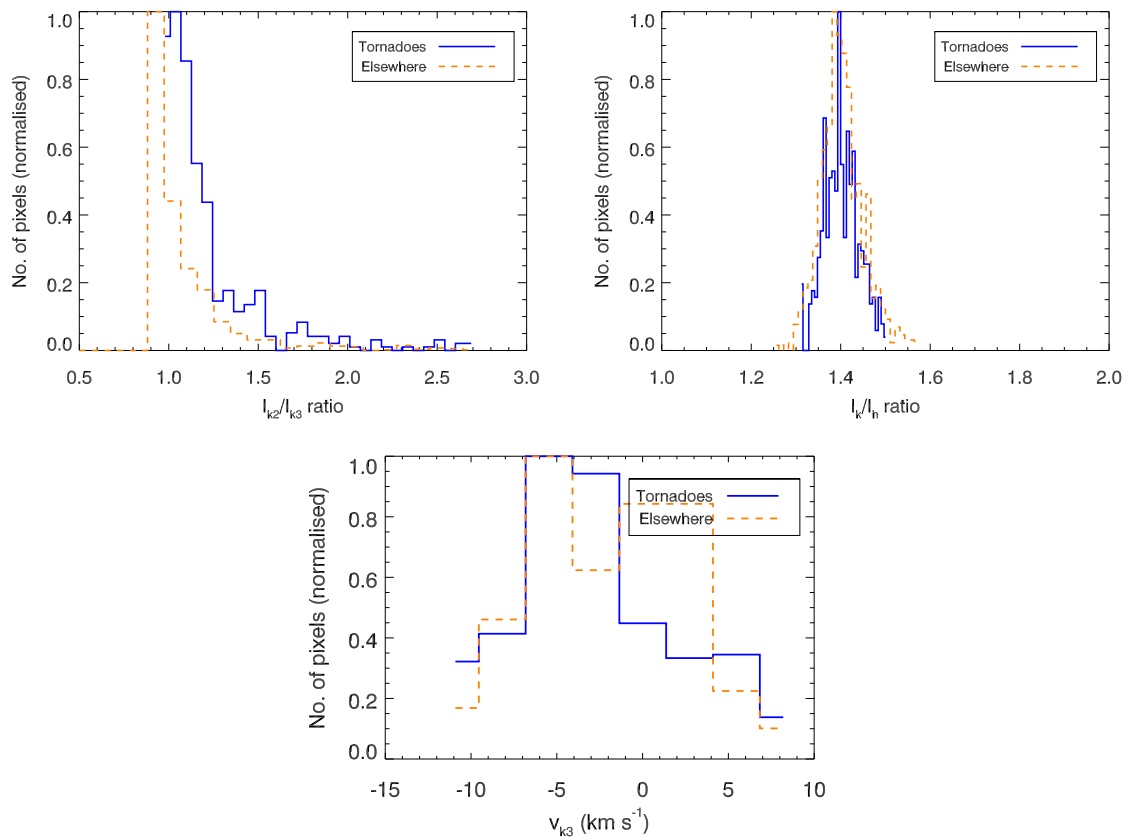


Figure 4.13: Normalised histograms of Mg II parameters from *IRIS* for points in the tornadoes case (blue lines) and the rest-of-prominence case (orange dashed lines). *Top left:* k_2/k_3 ratio. *Top right:* k/h ratio. *Bottom:* k_3 Doppler shift. This figure was used in [Levens et al. \(2017\)](#).

considered here. The top left panel shows distributions of the k_2/k_3 ratio. Taking moments of this distribution (Table 4.3) reveals that the mean reversal level in the tornadoes is 1.23, whereas in the rest of the prominence it is 1.14, with a standard deviation of 0.3 in both cases. This higher value in the tornadoes indicates that there is relatively more reversal in tornado points than non-tornado points, and it is also notable that there are more points extending to higher reversal levels in the tornadoes. This statistical approach confirms the results of §3.4 in that the reversal, and hence gas pressure and optical thickness, is higher in the tornadoes.

4.3.2 Mg II k/h ratio

The ratio of intensities of the k and h lines of magnesium, called the k/h ratio here, can give information on the formation of these lines. In the chromosphere, where the Mg II lines are normally collisionally excited, the k/h ratio is expected to be 2 (Leenaarts et al. 2013a; Kerr et al. 2015) and the plasma would be optically thin. Values lower than this suggest that scattering occurs in the emitting region, i.e. an increase in optical thickness to the point where the plasma is no longer optically thin. Table 4.2 shows values for k/h ratios, along with several other Mg II parameters, found previously in prominences by several authors (Schmieder et al. 2014; Liu et al. 2015a; Vial et al. 2016; Harra et al. 2014), as well as the results from §3.4 and Levens et al. (2016a). All previous studies of prominences with *IRIS* have found k/h ratios of lower than 2, suggesting that Mg II emission in prominences is mostly optically thick.

Figure 4.14 shows the k/h ratio of the Mg II lines against the magnetic field parameters from THEMIS, with symbols and colours having the same meaning as in Figure 4.11. As with the k_2/k_3 ratio, there is no obvious correlations when considering the k/h ratio vs. magnetic field parameters. Once again it is clear that the magnetic field strength is generally stronger in the tornadoes than elsewhere in the prominence, and the inclination and azimuth values are clustered around a mean, with moments of the distributions in Table 4.3. There is a small spread of values of k/h ratio, as can be seen in Figure 4.13 (*top right panel*). The mean k/h ratio, for both tornadoes and rest-of-prominence pixels, is 1.41, with a standard deviation of 0.05. This is similar to values found previously (Table 4.2), and is important to note in the context of the prominence modelling that is discussed in Chapter 5.

4.3.3 Mg II k_3 Doppler shift

The third Mg II parameter that is considered here against the magnetic field parameters is the k_3 Doppler shift. The most optically thick part of the Mg II k line is the line core, where the k_3 reversal is found (if the line is reversed). Observing a prominence in the emission near line centre means observing only the frontmost layer(s) of material. Any emission coming from material behind that is almost all re-absorbed or scattered out of the line of sight at line centre wavelengths. It then stands to reason that any change in the position of the k_3 feature with respect to the

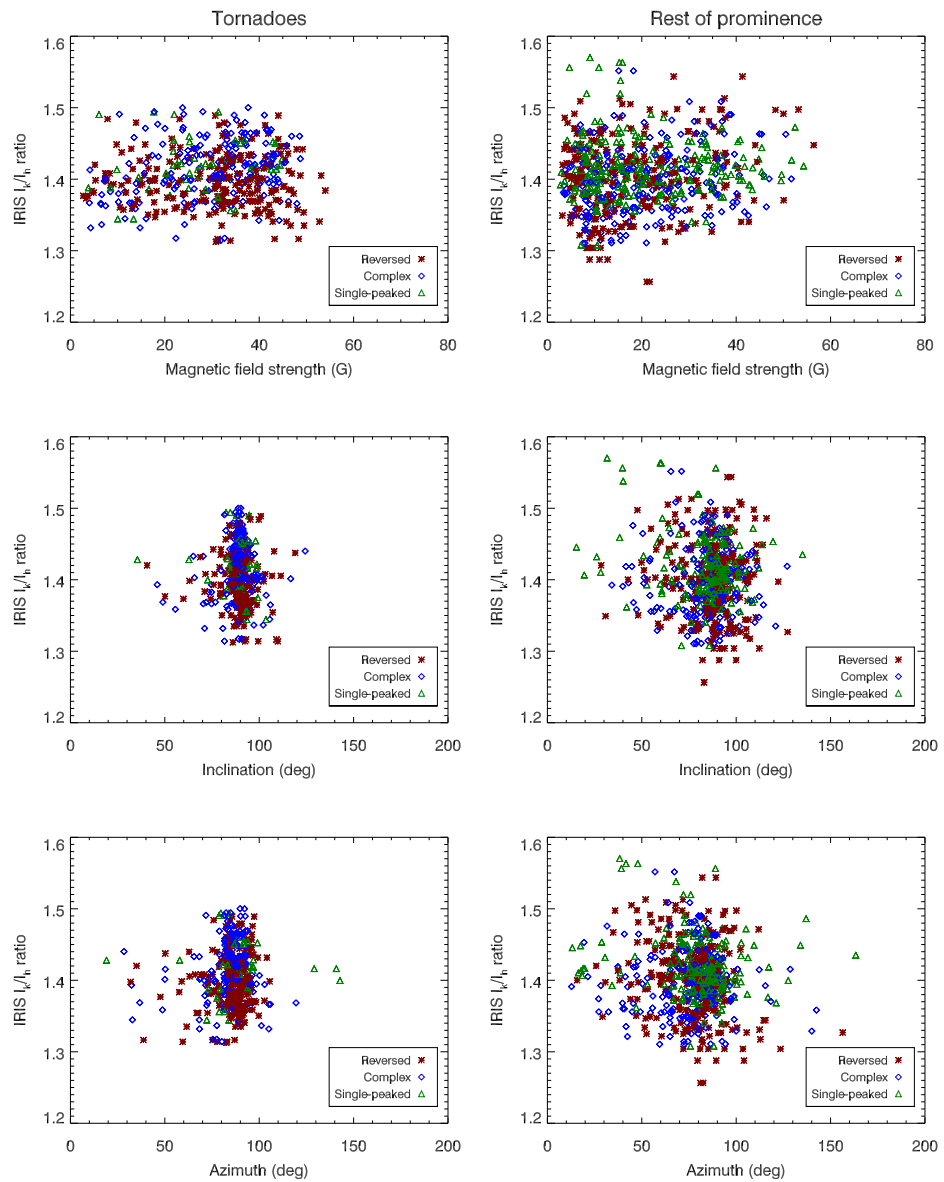


Figure 4.14: Plots of Mg II k/h ratio vs. magnetic field parameters. Left column is points in the tornadoes, right column is points in the rest of the prominence. Red asterisks are points where the Mg II k line is reversed. Green triangles are points that are single peaked and narrow. Blue diamonds are points where the profiles are ‘complex’. This figure was used in [Levens et al. \(2017\)](#).

nominal line centre will be due to motion along the line of sight of the frontmost parts of the prominence. The question here is: does the magnetic field strength, and hence magnetic pressure, affect the plasma velocity in a measurable way? For a

prominence with number density of $\sim 10^{19}$, as in [Heinzel et al. \(2008\)](#), the plasma β is around 3×10^{-4} . This is the low plasma β scenario and the plasma is magnetically dominated, as described in §1.2.5, so it would be expected that the magnetic force is causing the plasma motions seen.

Figure 4.15 shows the Mg II k_3 Doppler shift vs. magnetic field parameters. Here the k_3 position is taken to be the position of the minimum between the two peaks, which can only take discrete values due to the fact that *IRIS* has a specific spectral resolution (55 mÅ in the NUV). To increase the accuracy of the position of k_3 would require the reversal profile to be fitted with some function, for example a Gaussian, but this would require some physical interpretation of the function chosen. To assume a Gaussian profile would be assuming a lot about the absorption profile, and hence the absorption process, which would not necessarily be true. This approach is therefore not adopted here.

The top panels of Figure 4.15 show the k_3 Doppler shift vs. magnetic field strength. In the tornadoes it is notable that there is a larger range of Doppler velocities at higher field strengths, whereas at lower field strengths the Doppler velocity is much closer to zero. The opposite is true, however, in the rest-of-prominence case. This could be due to differences in plasma β between the tornadoes and the rest of the prominence. The Doppler velocity is always below around 10 km s^{-1} , however, which is similar to values found previously for non-eruptive prominences (Table 4.2). The plots of k_3 Doppler shift vs. inclination and azimuth do not reveal any correlations.

Figure 4.13 (*bottom panel*) shows the k_3 Doppler shift distribution in the tornadoes (blue) and the rest of the prominence (orange dashed). The Doppler shift in the tornadoes is peaked at around -5 km s^{-1} , whereas there is a more even spread of values in the rest of the prominence. No values in either case exceed $\pm 11 \text{ km s}^{-1}$.

4.4 Correlation between THEMIS and EIS data

Chapter 3 and [Levens et al. \(2015\)](#) contained extensive analysis of plasma parameters derived from *Hinode*/EIS observations. The same method of line identification and de-blending is used for this data set as previously, although the study used is different to that used in Chapter 3 and [Levens et al. \(2015\)](#). The EIS observation on 15 July 2014 is detailed in §3.3.4. For this analysis only the electron density is considered

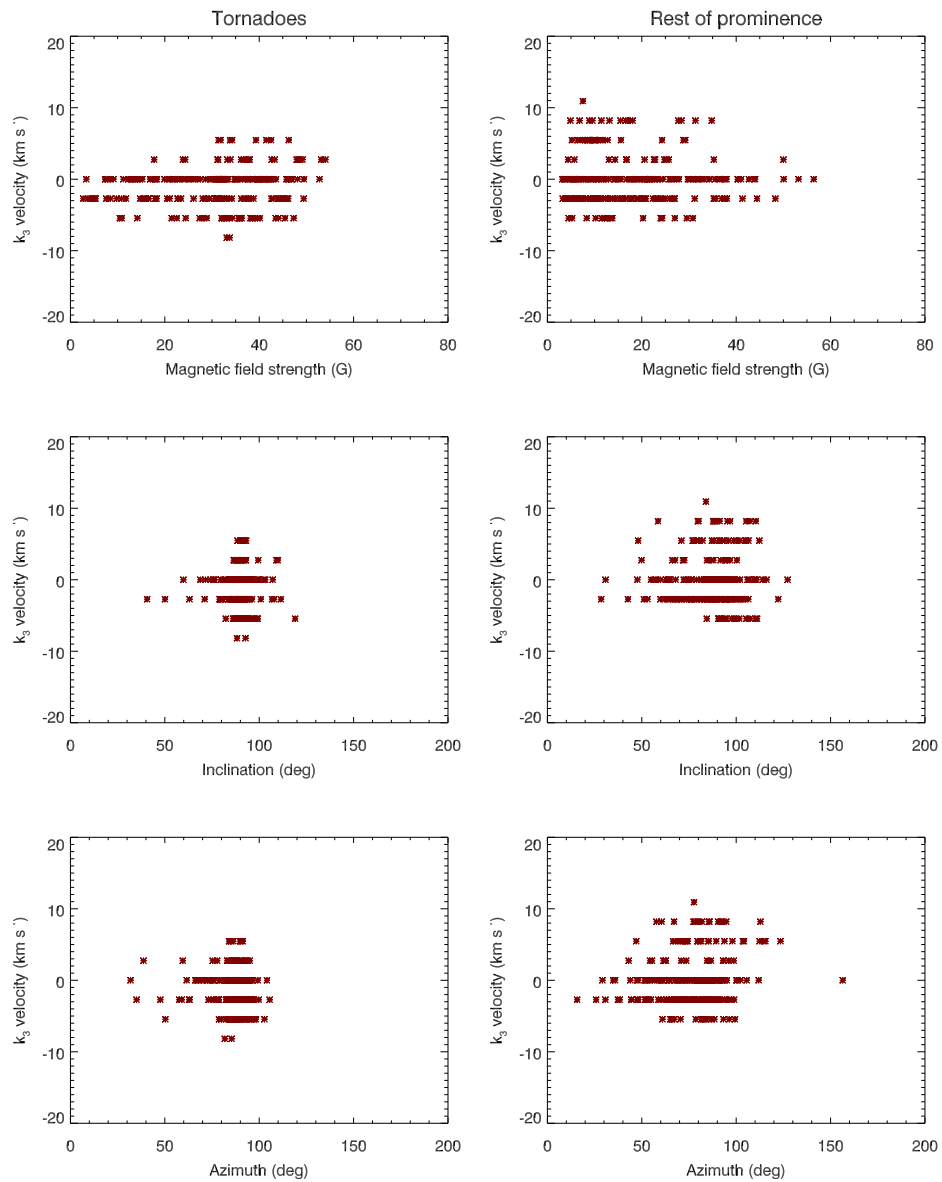


Figure 4.15: Plots of Mg II k_3 velocity vs. magnetic field parameters. Left column is points in the tornadoes, right column is points in the rest of the prominence. Points are all taken from pixels where the Mg II k line is reversed. This figure was used in [Levens et al. \(2017\)](#).

against the magnetic field parameters from THEMIS.

The EIS study used here contains lines formed at a range of temperatures, however very few of them have density-sensitive line pairs. The Fe XII lines at 195.119 \AA and 195.179 \AA are used for this analysis, and are de-blended using the two Gaussian

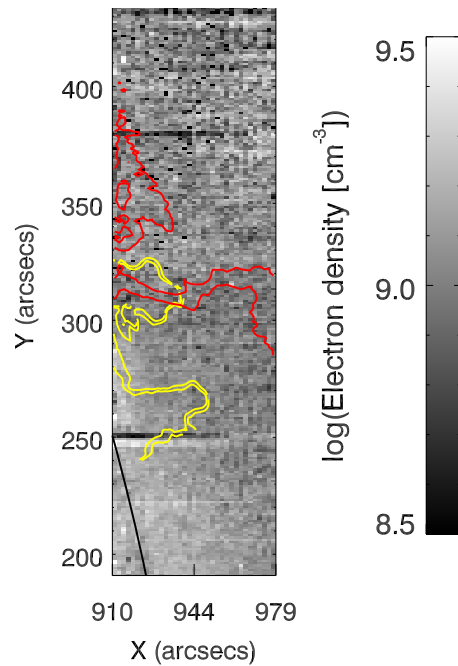


Figure 4.16: Density map of the prominence on 15 July 2014 made using the density sensitive Fe xii line ratio 195.119/195.179. Yellow contours show positions of the tornadoes as seen by THEMIS, red contours are from the EIS 195.119 Å intensity map. This figure was used in [Levens et al. \(2017\)](#).

technique described in §3.1.3. Figure 4.8 (*middle and right panels*) shows the resulting raster maps made using the de-blended lines, with the middle panel showing 195.119 Å and the right panel showing 195.179 Å with contours from the 195.119 Å image. Using atomic data from CHIANTI v7.1, as in §3.2.2, the electron density can be calculated at each pixel, and a density map can be formed (Figure 4.16). It is important to remember that the densities calculated here are done so for a specific temperature, which is the formation temperature of the lines used (Fe xii $\sim 1.5 \times 10^6$ K).

The overlap region between EIS and THEMIS data sets is, naturally, different to the overlap between *IRIS* and THEMIS shown in Figure 4.10, so new masks are required for the analysis. These new masks are shown in Figure 4.17. For this correlation the ‘tornado’ pixels are only taken to be those in the northern tornado. The southern tornado is barely visible in the Fe xii lines considered here (seen in Figure 4.8) due to bright foreground coronal emission, so it is false to claim that

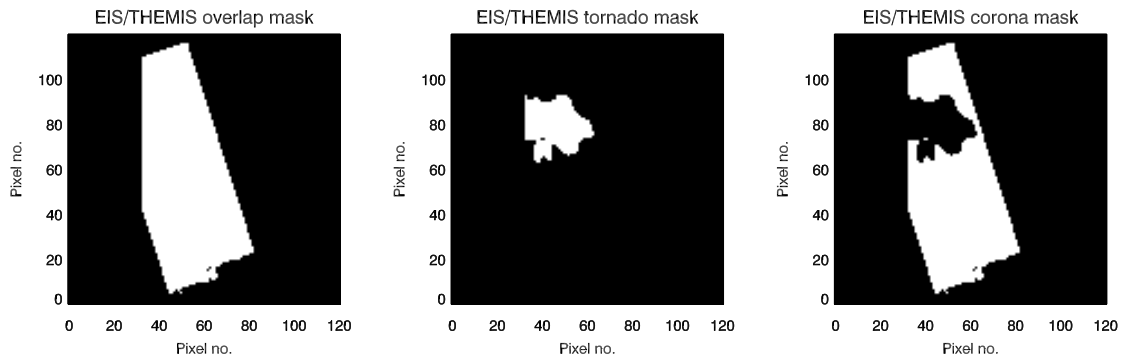


Figure 4.17: Masks showing the overlapped area between EIS and THEMIS rasters for data sets on 15 July 2014. White areas indicate overlap. *Left:* Full overlap area. *Middle:* Mask for tornado. *Right:* Mask for surrounding corona. This figure was used in [Levens et al. \(2017\)](#).

emission along that line of sight is coming from the tornado. It is also noted that the emission seen outside of the tornado region is not coming from the rest of the prominence, as it is in Mg II, but rather from the surrounding corona.

Correlation plots of electron density versus magnetic field parameters are shown in Figure 4.18. From these plots there are no clear correlations between the magnetic field parameters and the electron density at $\sim 1.5 \times 10^6$ K. These plots show a relatively small scatter in values for density, ranging from around electron densities of $\log n_e = 8.5$ to $\log n_e = 9.5$. Figure 4.19 shows histograms of the electron density in the tornado (blue line) and surrounding corona (orange dashed line). Taking moments of these distributions reveal mean values of electron density of $\log n_e = 8.98 \pm 0.14$ and $\log n_e = 9.06 \pm 0.14$ in the tornado and surrounding corona respectively (n_e in cm^{-3}). The values of electron density found in this prominence (and surrounding corona) are comparable to values found in Chapter 3 and [Levens et al. \(2015\)](#).

4.5 Correlation between *IRIS* and EIS data

It is also worth comparing the Mg II parameters from *IRIS* to the electron density from EIS to check for correlations. The bounds of the *IRIS* raster lie entirely within the EIS raster, so the overlap region is defined by the *IRIS* field of view. The *IRIS* data is binned to match the spatial resolution of EIS. Points are divided into those in the

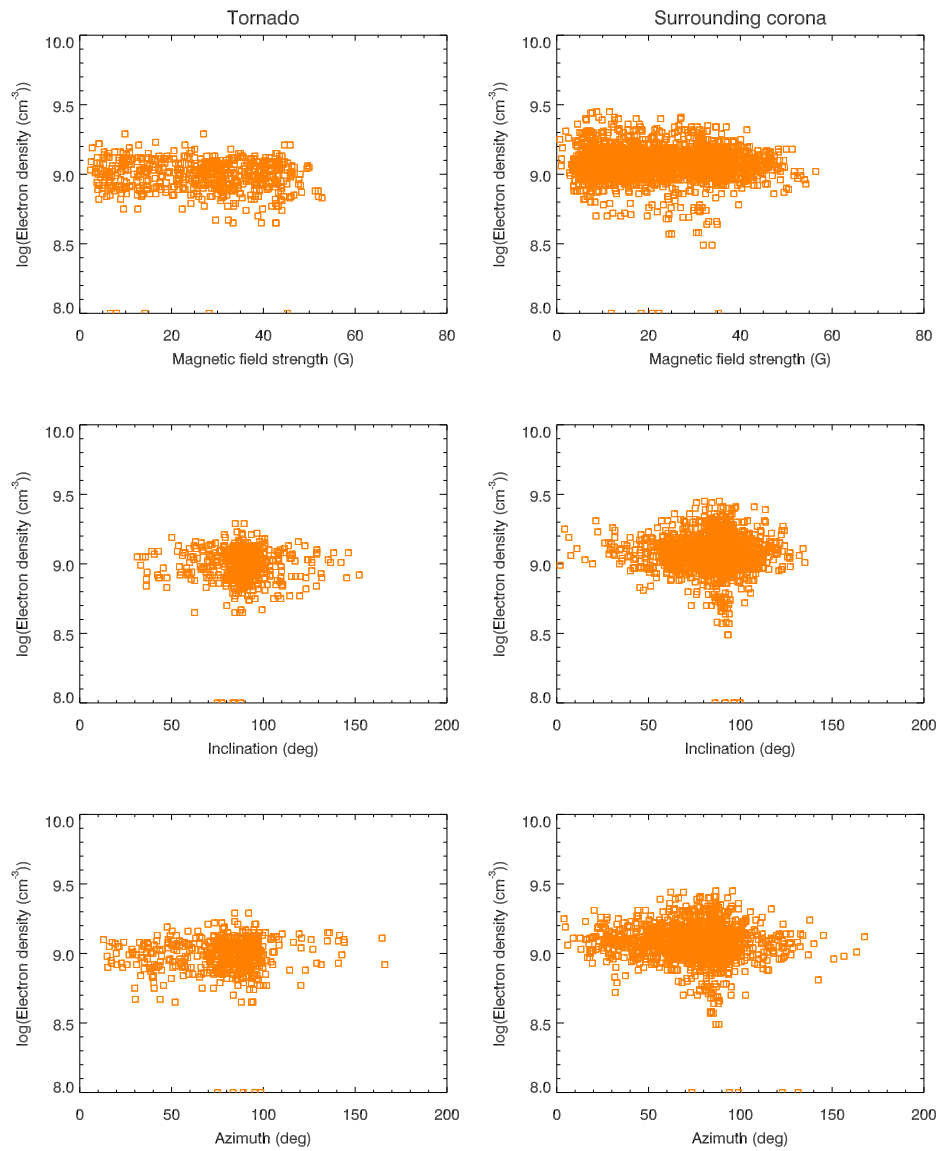


Figure 4.18: Plots of electron density vs. magnetic field parameters. Left column is points in the tornadoes, right column is points in the surrounding corona. This figure was used in [Levens et al. \(2017\)](#).

northern tornado and those outside of it. This is done using the THEMIS intensity map, as before, however notably this region excludes the highest altitude parts of the tornado in the *IRIS* raster.

Figure 4.20 shows plots of electron density versus $\text{Mg II } k_2/k_3$ ratio (*top left panel*), k/h ratio (*top right panel*), and k_3 Doppler shift (*bottom panel*). There appear to

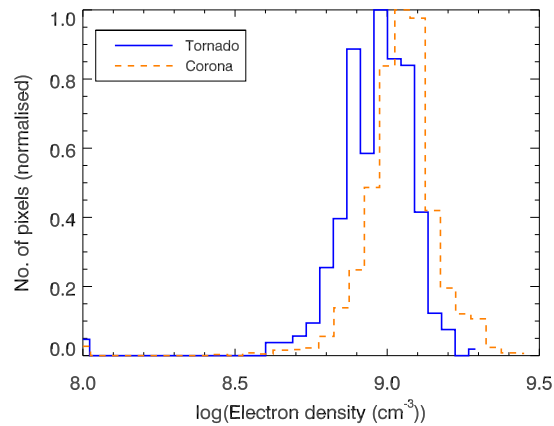


Figure 4.19: Histograms of electron density for points in the northern tornado (blue line) and in the surrounding corona (orange dashed line). This figure was used in [Levens et al. \(2017\)](#).

be no meaningful correlations between the electron densities and parameters from the *IRIS* data. The lines used in this comparison are formed under very different circumstances – The Fe xii lines are optically thin and formed at a plasma temperature of around 1.5×10^6 K, whereas the Mg ii lines are optically thick and formed at temperatures around 10^4 K. These differences alone could explain why there are no correlations seen in these plots.

4.6 Conclusion

This chapter has been concerned with the magnetic field in tornado-like prominences and investigating whether or not there are any correlations between parameters measured in (or derived from) prominence data obtained by *IRIS*, *Hinode*, and THEMIS during a coordinated observing campaign on 15 July 2014. The analysis presented here represents the first detailed study of the magnetic field in a tornado-like prominence. Magnetic fields in prominences can be derived using the Stokes parameters (I , Q , U , and V) which have been measured in tornado-like prominences using the THEMIS spectropolarimeter. For the prominence observed on 15 July 2014 magnetic field strengths of up to 60 G are found in places, however on average the field strength is lower, around 30 G. The field orientation is given by the inclination (with respect to the local vertical) and azimuth (with respect to the line of sight).

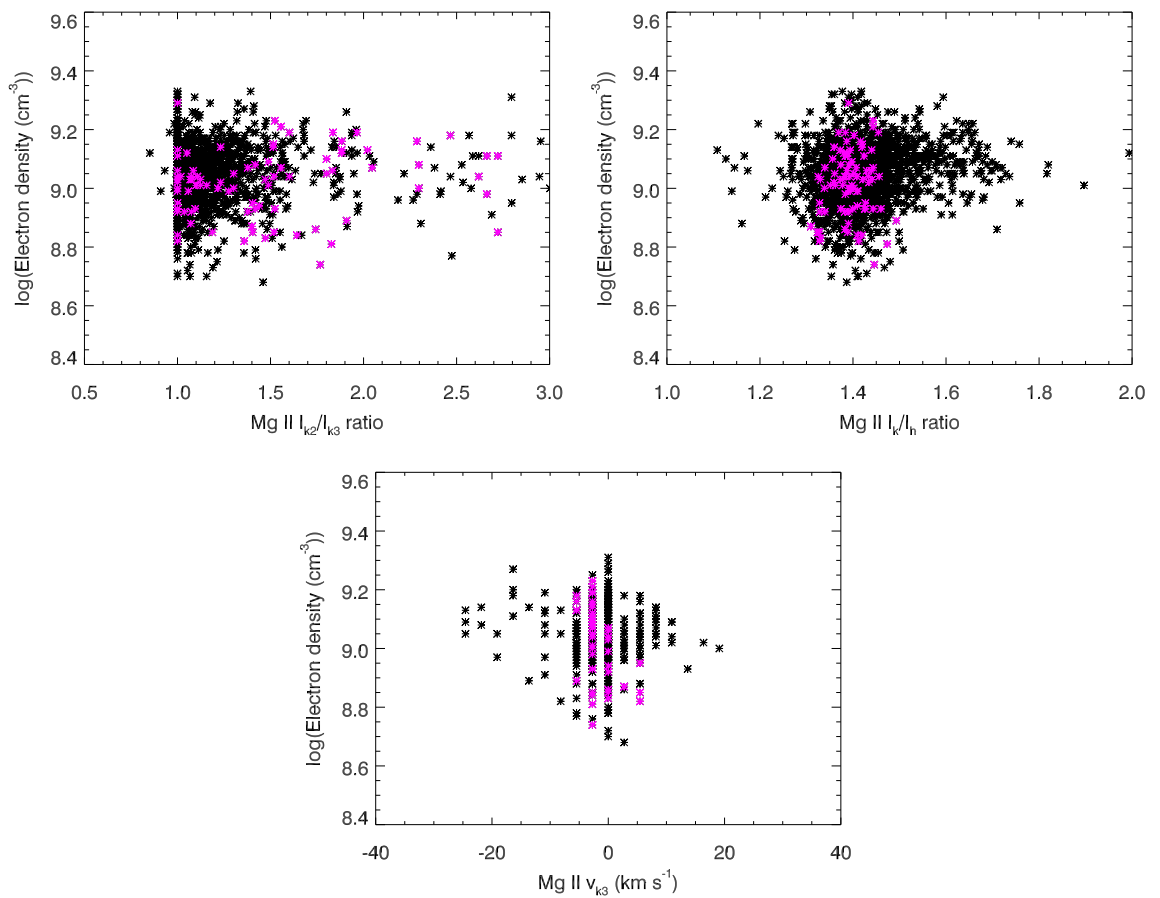


Figure 4.20: Electron density from EIS vs. Mg II parameters from *IRIS*. Density vs. *Top left*: Mg II k_2/k_3 ratio, *Top right*: Mg II k/h ratio, *Bottom*: k_3 Doppler shift. Magenta points are points in the northern tornado. Black points are from the rest of the overlapped region. This figure was used in [Levens et al. \(2017\)](#).

Inclinations of around 90° are found everywhere in the tornadoes, indicating a horizontal magnetic field, and the azimuth is found to be between around 60° and 100° . This is contrary to the vertical or twisted magnetic structures that have been suggested for tornadoes in prominences ([Su et al. 2014](#); [Luna et al. 2015](#)). It appears that tornadoes are in fact horizontal magnetic structures, with plasma being suspended in dips in the magnetic field, as per previous models of prominences ([Aulanier & Demoulin 1998](#); [Heinzl & Anzer 1999](#)). The ‘tornado’ motions seen in AIA movies are then a projection effect where the oscillations of plasma are happening in the legs, or barbs, of the prominence.

Table 4.3: Moments of the distributions of parameters from THEMIS, *IRIS* and EIS for points in the tornadoes and elsewhere in the prominence. In the ‘Param.’ column, ‘B’ is the magnetic field strength, ‘Inc.’ is the field inclination and ‘Az.’ is the field azimuth. For *IRIS*, ‘ k_2/k_3 ’ is the reversal level, ‘k/h’ is the k to h line ratio and ‘ v_{k3} ’ is the Doppler shift of the k_3 position. For EIS, ‘ n_e ’ is the electron density. The first four moments are shown for each distribution (mean, variance, skewness and kurtosis), along with the standard deviation, $\sigma = \sqrt{\text{variance}}$.

Instrument	Param.	Tornado?	Mean	Variance	Skewness	Kurtosis	σ
THEMIS	B	yes	30.0	131.2	-0.5	-0.6	11.5
	Inc.	yes	89.0	70.7	-1.7	10.4	8.4
	Az.	yes	85.4	139.5	-1.5	9.2	11.8
	B	no	19.8	136.4	0.7	-0.4	11.7
	Inc.	no	85.7	224.1	-1.2	3.1	15.0
	Az.	no	77.1	343.4	-0.4	2.7	18.5
<i>IRIS</i>	k_2/k_3	yes	1.23	0.09	2.47	7.05	0.30
	k/h	yes	1.41	0.00	0.13	-0.33	0.04
	v_{k3}	yes	0.00	20.8	0.13	0.27	4.56
	k_2/k_3	no	1.14	0.07	2.37	10.50	0.27
	k/h	no	1.41	0.00	0.43	0.60	0.05
	v_{k3}	no	0.72	15.61	0.07	-0.03	3.95
<i>Hinode</i> /EIS	$\log n_e$	yes	8.98	0.02	-2.97	18.69	0.14
	$\log n_e$	no	9.06	0.02	-2.75	19.93	0.14

Despite the fact that it does not seem that tornadoes are rotating structures, it is still important to understand the dynamic motions seen, and how the magnetic field is related to the plasma. Plasma parameters derived from space-based observatories *IRIS* and *Hinode* have been used in conjunction with magnetic field measurements from the ground-based spectropolarimeter THEMIS. A detailed statistical analysis of magnetic field data and plasma parameters will help to constrain physical prominence models. It is also important to try to understand the link between the magnetic field and the plasma in prominences, as the two are inherently linked. The data set on 15 July 2014 was chosen for this analysis as it has a relatively good spatial coverage of the prominence, which was identified as having tornado-like structures

in it. However, the THEMIS rasters taken were obtained a few hours after the data from the satellites, so there is no temporal overlap.

It is necessary to perform co-alignment on data sets before correlations between parameters can be explored on a pixel-by-pixel basis. This co-alignment is done using a 2D cross correlation method where similar images from each data set are compared and brought into alignment. AIA images are used as a base, with *IRIS* Mg II being aligned directly with AIA 304 Å, SOT Ca II being aligned with *IRIS* Mg II SJI and THEMIS data being aligned with SOT images. EIS data is aligned using the AIA 193 Å filter. When considering the accuracy of the spatial co-alignment performed here it is important to also remember the temporal differences between the satellite data (from the morning) and the THEMIS magnetic field data (from the afternoon). A co-temporal alignment would be preferable for analysis of this type, but due to practical difficulties of performing a coordinated observing campaign such as this one the ideal case is difficult to achieve.

No correlations are found between the magnetic field (strength, inclination and azimuth) from THEMIS and Mg II parameters (k_2/k_3 ratio, k/h ratio and k_3 Doppler shift) from *IRIS*, nor between magnetic field parameters and the electron density calculated from EIS data. There are also no correlations found between Mg II parameters and the electron density. This fact further highlights the limitations of this study. Several factors are worth considering when comparing data from different instruments – formation temperature of the observed emission, optical thickness of the lines observed, and relative co-alignment of observations (both temporally and spatially). Perhaps most important are the line formation temperature and optical thickness. Sampling emission from lines formed at, e.g., chromospheric and coronal temperatures is sampling different regions of the solar atmosphere. The plasma in each case is under different conditions, so comparing the two is probing different parts of the structure along the line of sight. The optical thickness is also important to consider. He I D₃ and Mg II h and k lines are all seen in emission in prominences and formed at similar plasma temperatures, but due to differences in the optical thickness of the lines comparing emission from them is challenging. Emission from He I D₃ is mostly optically thin, meaning that the observed emission is an integration of all (or most) of the emitting plasma along the l.o.s., whereas the Mg II resonance lines are extremely optically thick, so emission seen in them will largely be formed at the emitting region nearest to the observer. Turning to the reconstruction of the

magnetic field from spectropolarimetry, the signal observed with THEMIS in He I D_3 is therefore an integration through the entire emitting region, meaning that the derived magnetic field is also an integrated magnetic field. Therefore this measured field does not necessarily reflect the magnetic field conditions in the region that the Mg II emission is from. Spatial and temporal alignment of data is also an issue for any coordinated campaign. Solving the spatial offsets between data sets can be done, as shown in this analysis, to a reasonable degree of certainty, however errors still arise from these techniques. The temporal offsets are more difficult to deal with, but in the 15 July 2014 observation the quiescent prominence structure is expected to be stable for a number of days, so an offset of a few hours is deemed to be of minor significance. For a more dynamic prominence (eruptive, or with fast flows) such a temporal offset could be more of a problem.

Despite the lack of correlations found, this data set is still extremely useful for characterising many physical parameters about the magnetic field and plasma in tornado-like prominences. The magnetic field is generally found to be stronger in the tornadoes (~ 30 G) than in the rest of the prominence (~ 20 G). The field inclination is horizontal everywhere, as in previous cases (Schmieder et al. 2014; Levens et al. 2016a,b), and the l.o.s. azimuth has a mean value of 85° in the tornadoes and 77° elsewhere.

The level of reversal in the Mg II k line is found to vary from non-reversed to a k_2/k_3 ratio of 2.8. Parts of the prominence with a high reversal level ($k_2/k_3 > 2$) suggests a high optical thickness at these locations, which was discussed in Chapter 3. Taking moments of the distributions of reversal level gives means of 1.23 and 1.14 in the tornadoes and rest of prominence respectively, which suggests that there is generally more reversal in the tornadoes than the rest of the prominence. The k/h ratio is measured to have a distribution of values between 1.3 and 1.5, with a mean value of 1.41 in both tornado and rest-of-prominence cases, which is a similar value to those found previously in prominences (Schmieder et al. 2014; Harra et al. 2014; Liu et al. 2015a; Levens et al. 2016a; Vial et al. 2016). This ratio is again indicative of optically thick emission of Mg II in prominences, as for collisionally excited, optically thin emission a k/h ratio of 2 would be expected (Leenaarts et al. 2013a), assuming the same formation mechanism for these lines in prominences as in the chromosphere. The position of the k_3 feature can be used to infer a Doppler velocity for the frontmost layers of the prominence plasma. These Doppler shifts are

found to be between $\pm 10 \text{ km s}^{-1}$ everywhere. This is a similar shift to those found previously, and is similar to the overall shift of the profiles found in Chapter 3.

The electron density can be calculated from the Fe XII $195.119 \text{ \AA}/195.179 \text{ \AA}$ intensity ratio and comparing this to the density curve for the ratio computed using CHIANTI. This reveals, for plasma at temperatures of $\sim 1.5 \text{ MK}$, that electron densities are mostly between $\log n_e = 8.5$ and $\log n_e = 9.5$. Mean electron densities are found to be $\log n_e = 8.98$ in the tornadoes and $\log n_e = 9.06$ in the surrounding corona. These values are similar to those found in Chapter 3 and [Levens et al. \(2015\)](#) for the tornado observed on 14 September 2013.

The coordinated observations presented here represent the first multi-instrument coordinated campaign dedicated to investigating tornado-like prominences. They also present the first set of dedicated investigations into tornado magnetic fields. However, as has been noted, there are a number of limitations of this study, so it would be beneficial to investigate further with new campaigns including other instruments. The *Chromospheric Lyman-Alpha SpectroPolarimeter* telescope (CLASP, [Kano et al. 2012](#); [Kobayashi et al. 2012](#)) was a sounding rocket experiment that allows for spectropolarimetric measurements of the H I Lyman- α line, which would provide both plasma and magnetic parameters for prominences and tornadoes. Combining CLASP observations with THEMIS would provide a much clearer picture of the magnetic field and its relation to the cool plasma in prominences. Further studies using the *IRIS* satellite would also be beneficial. The *IRIS* study used here utilised a short exposure time, concentrating on the strong Mg II lines, but this was to the detriment of other *IRIS* lines that are in emission in prominences. It would be worthwhile exploring the Si IV and C II lines with *IRIS*, as these weaker transition region lines have not yet been fully utilised in the prominence context. Increasing exposure times to 15 s or 30 s would help combat the lower signal in these lines, returning a much clearer picture of how the prominence looks at those wavelengths. This would also help with the development of prominence models using those lines.

Chapter 5

Modelling of Mg II lines in prominences

With observations of the Mg II h and k lines in prominences such as those presented in Chapters 3 and 4, it is necessary to have detailed models which can deal with the full physics of the prominence conditions. These models must be equipped to handle the full radiative transfer and statistical equilibrium calculations required to accurately simulate the emission from prominences. Many models have been constructed in the past to deal with optically thick emission in prominences (e.g. Hirayama 1963; Heasley et al. 1974; Heinzel et al. 1987; Gouttebroze et al. 1993; Paletou et al. 1993; Gouttebroze et al. 1997; Labrosse & Gouttebroze 2001; Heinzel et al. 2001; Gunár et al. 2007; Heinzel et al. 2014), one of which, Gouttebroze et al. (1993), is outlined in detail in §5.2. In order to build a model such as these, it is first necessary to understand the processes that are relevant in computing the emergent line profiles.

This chapter introduces the physics behind these radiative transfer prominence models, and work that has gone into developing codes to calculate the emission of Mg II in prominences. This work is an extension to the code developed by Gouttebroze et al. (1993, herein GHV), called PROM, which in its simplest form is a 1D isothermal isobaric hydrogen prominence model. The 1D code was expanded to compute calcium profiles (Gouttebroze et al. 1997; Gouttebroze & Heinzel 2002), helium profiles (Labrosse & Gouttebroze 2001), and to include a prominence-corona transition region (PCTR, Labrosse & Gouttebroze 2004), as well as 2D cylindrical versions (Gouttebroze 2004, 2005, 2006) and multi-threaded models (Labrosse &

Rodger 2016) which allow for fine-structure modelling. Work has also been done recently using the Ondřejov code (similar to PROM) to calculate magnesium profiles in prominences (HVA, Heinzel et al. 2014, 2015), including isothermal isobaric models and PCTR models. However, those papers present a limited grid of models that cannot fully explain the range of observed profiles that have been found in Chapters 3 and 4. The Ondřejov code was also used to build 2D multi-thread models of hydrogen lines which have been used to investigate fine-scale thread dynamics in prominences (Gunár et al. 2007, 2008, 2012). The aim of the work presented in this chapter is therefore to build a more extensive grid of Mg II models, based on the PROM code, that can be used freely to try to account for the complexity of the observed line profiles – the asymmetries of profiles cannot be explained by the HVA grid of models. This work is done on the basic PROM code, however it has the scope to act as the base for more complex models (e.g. 2D models, multi-threaded models).

Starting from the set of PROM codes for Ca II (Gouttebroze et al. 1997), which has a similar atomic layout to Mg II, the work outlined here begins by attempting to recreate the grid of 27 1D isothermal isobaric models presented by Heinzel et al. (2014). Using the Heinzel et al. results as a baseline allows a consistent model to be constructed, which will then act as the base for more complex models. An extended grid of models is the natural first step, outlined in §5.5.2, and the effects of including a PCTR in these models is described in §5.6. These give scope for investigating 2D and multi-thread Mg II models in the future.

The codes for the modelling of Mg II that are used in this chapter are based on the provided PROM codes, which are written in the programming language FORTRAN. The Mg II codes that have been developed here were adapted from the Ca II codes because of the similarity between the atomic models of Mg II and Ca II. Atomic data for Mg II has been gathered from sources that are clearly stated in the relevant sections, and following the structure of the Ca II codes a new part has been implemented to calculate Mg II spectra in prominences. The equations for radiative transfer and statistical equilibrium presented here have been adapted from Labrosse et al. (2010), Hubeny & Mihalas (2014), and Heinzel (2015).

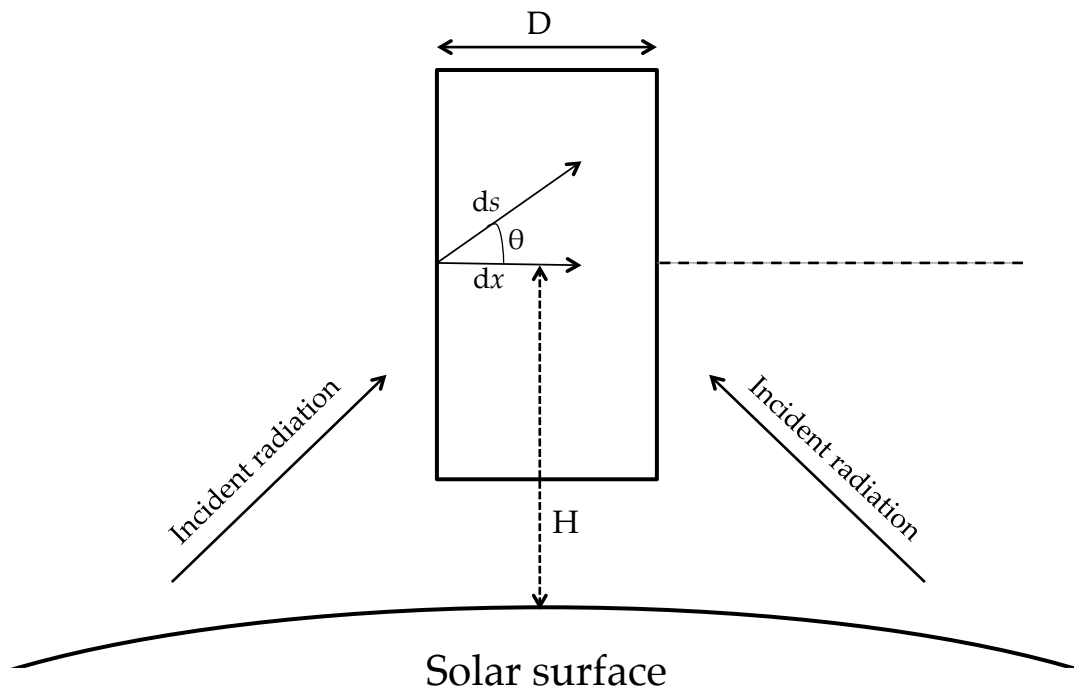


Figure 5.1: Geometry of a vertical prominence slab above the solar surface, viewed above the limb, used in solving the 1D radiative transfer equations. The line of sight perpendicular to the prominence slab is shown by a long-dashed line. The slab is illuminated from below by the incident radiation. The prominence is at height H above the surface, and has thickness D . dx indicates line of sight parallel to the solar surface, with ds being an arbitrary line of sight at angle θ with respect to the local horizontal.

5.1 Radiative transfer in prominences

An important aspect of the physics and energy balance of solar prominences is the *radiative transfer* that affects the emitted radiation. Radiative transfer deals with the transport of photons and their interaction with other particles. This is required to account for the changes to the emergent line profiles due to absorption, re-emission, and scattering effects within the prominence itself. These processes are especially important in optically thick plasmas, such as prominences, where there is a cool, dense plasma above the solar surface that is being irradiated from below.

The equation of radiative transfer, Equation 5.1, calculates how the specific

intensity at frequency ν , I_ν , measured along path ds , is altered by emission and absorption processes. Considering a simple 1D slab model for the prominence, illustrated in Figure 5.1, the radiative transfer can be calculated in a simple way.

$$\frac{dI_\nu}{ds} = -\chi_\nu I_\nu + \eta_\nu \quad (5.1)$$

This equation indicates that the observed line intensity along the line of sight is a balance between absorption processes, with *absorption coefficient* χ_ν , and emission processes, with *emission coefficient* η_ν . If x is taken to be the direction through the prominence parallel to the solar surface, it can be related to an arbitrary line of sight s at angle θ by Equation 5.2 (see Figure 5.1). The parameter μ is defined as the cosine of the viewing angle.

$$\frac{dx}{ds} = \cos \theta = \mu \quad (5.2)$$

Optical depth, τ_ν , is then defined by the absorption coefficient at depth x into the slab (Equation 5.3).

$$\tau_\nu(x) = \int_{x_0}^x -\chi_\nu dx' \quad (5.3)$$

In the limits for the integral, x_0 is at the surface of the slab, where the optical thickness is zero, and usually $x_0 = 0$. τ_ν then increases towards the interior of the slab, at x . Therefore the change in τ_ν , $d\tau_\nu$, along element dx is given by Equation 5.4.

$$d\tau_\nu = -\chi_\nu dx \quad (5.4)$$

The *source function*, S_ν , is defined as the ratio of emission and absorption coefficients (Equation 5.5).

$$S_\nu \equiv \frac{\eta_\nu}{\chi_\nu} \quad (5.5)$$

Dividing Equation 5.1 by χ_ν , then substituting Equations 5.2, 5.4, and 5.5 in turn leaves Equation 5.6. This is the radiative transfer equation for a 1D plane-parallel slab.

$$\frac{dI_\nu}{d\tau_\nu} \mu = I_\nu - S_\nu \quad (5.6)$$

In the case of LTE the source function is equal to the *Planck function*, B_ν (Equation 5.7).

$$B_\nu = \frac{2h\nu^3}{c^2} \frac{1}{e^{\frac{h\nu}{kT}} - 1} \quad (5.7)$$

However, prominences cannot be considered to be in LTE due to relatively low densities and the importance of irradiation from the Sun (Hirayama 1963). Therefore

calculating the source function requires a full, non-LTE treatment which usually requires that it is solved numerically.

Calculating the source function requires consideration of the absorption (ϕ_ν) and emission (ψ_ν for spontaneous emission, κ_ν for stimulated emission) profiles of the plasma. The absorption profile takes the form of a Voigt profile, a convolution of a Gaussian and a Lorentzian profile, and under the approximation of *complete redistribution* in frequency (CRD) the emission profile is the same as the absorption profile ($\phi_\nu = \psi_\nu$). CRD assumes that the absorbed energy is evenly redistributed across all frequencies upon re-emission. In *partial redistribution* (PRD) this is not the case, and the scattered photon is more likely to emerge at a smaller range of frequencies, centred around the frequency of the incoming photon. In the extreme case, *coherent scattering* occurs when photons absorbed at a frequency will be re-emitted at exactly the same frequency.

Considering the *Einstein coefficients* for emission and absorption – A_{ji} for spontaneous emission, B_{ji} for stimulated emission, and B_{ij} for absorption – the absorption coefficient can be written as in Equation 5.8, which corrects the absorption for stimulated emission effects.

$$\chi_\nu = n_i B_{ij} \frac{h\nu_{ij}}{4\pi} \phi_\nu - n_j B_{ji} \frac{h\nu_{ij}}{4\pi} \kappa_\nu \quad (5.8)$$

Similarly, the emission coefficient is given by Equation 5.9.

$$\eta_\nu = n_j A_{ji} \frac{h\nu_{ij}}{4\pi} \psi_\nu \quad (5.9)$$

In these equations, ν_{ij} is the frequency of the photon emitted or absorbed by the transition of an electron between levels i and j , related to the energy difference between the levels, $E_{ij} = h\nu_{ij}$. Level populations are given by n_i and n_j for their respective levels. Substituting in Equation 5.5 for χ_ν and η_ν gives Equation 5.10.

$$S_\nu = \frac{n_j A_{ji} \psi_\nu}{n_i B_{ij} \phi_\nu - n_j B_{ji} \kappa_\nu} \quad (5.10)$$

In general the profiles of ϕ_ν and κ_ν are equal, therefore Equation 5.10 can be approximated to Equation 5.11.

$$S_\nu \simeq \frac{n_j A_{ji}}{(n_i B_{ij} - n_j B_{ji})} \frac{\psi_\nu}{\phi_\nu} \quad (5.11)$$

Under CRD approximations, $\frac{\psi_\nu}{\phi_\nu} = 1$ so the source function is simply related to the level populations and the Einstein coefficients (Equation 5.12).

$$S_\nu \simeq \frac{n_j A_{ji}}{n_i B_{ij} - n_j B_{ji}} \quad (5.12)$$

In most optically thick resonance lines, however, the CRD approximation does not hold. CRD tends to over-estimate the line wing emission in resonance lines such as the Mg II h and k lines (e.g. Milkey & Mihalas 1974). Paletou et al. (1993) showed there are significant differences between CRD and PRD considerations for Ly- α line profiles, however the effects on their calculated Ca II profiles was minimal. Therefore it is necessary to employ PRD in most cases – the PROM treatment of Ca II uses PRD for the resonance lines (Gouttebroze et al. 1997).

The intensity emergent from a prominence slab can then be calculated. At the slab surface $\tau_\nu = 0$, so the emergent intensity at angle θ is given by Equation 5.13.

$$I(0, \theta) = I_0(\tau_\nu, \theta) e^{-\frac{\tau_\nu}{\mu}} + \int_0^{\tau_\nu} S_\nu(t) e^{-\frac{t}{\mu}} \frac{dt}{\mu} \quad (5.13)$$

$I_0(\tau_\nu, \theta)$ is the incident radiation on the opposite side of the slab. Assuming that the source function, S_ν is constant, and expanding the integral, leaves Equation 5.14.

$$I(0, \theta) = I_0(\tau_\nu, \theta) e^{-\frac{\tau_\nu}{\mu}} + S_\nu(1 - e^{-\frac{\tau_\nu}{\mu}}) \quad (5.14)$$

There are two limiting cases for Equation 5.14, where $\tau_\nu \ll 1$ and $\tau_\nu \gg 1$ – optically thin and optically thick, respectively. When $\tau_\nu \ll 1$, $(1 - e^{-\frac{\tau_\nu}{\mu}}) \simeq \frac{\tau_\nu}{\mu}$, and when $\tau_\nu \gg 1$, $(1 - e^{-\frac{\tau_\nu}{\mu}}) \simeq 1$. In a prominence viewed above the limb the background intensity $I_0 = 0$, and for a line of sight perpendicular to the prominence slab the viewing angle $\theta = 0$, i.e. $\mu = 1$. Therefore, the intensity from Equation 5.14 becomes Equation 5.15.

$$I(0) = S_\nu(1 - e^{-\tau_\nu}) \quad (5.15)$$

In an optically thin slab this becomes Equation 5.16, whilst in an optically thick slab it is Equation 5.17.

$$I(0) \simeq S_\nu \tau_\nu \quad (5.16)$$

$$I(0) \simeq S_\nu \quad (5.17)$$

In reality, however, the prominence is illuminated from the solar surface, not from behind, so I_0 will be altered by this, and non-zero. This will have an effect on the emergent intensity, as seen in Equation 5.14.

5.1.1 Statistical equilibrium

The source function under non-LTE conditions varies from the Planck function, and is not explicitly known, so must be calculated numerically by solving the radiative transfer equation (Labrosse et al. 2010). In order to calculate it, a consideration of the level populations and the radiation field must be made. The equations required to calculate the level populations are the equations of statistical equilibrium, Equation 5.18.

$$\frac{dn_i}{dt} = \sum_{j \neq i} n_j (R_{ji} + C_{ji}) - n_i \sum_{j \neq i} (R_{ij} + C_{ij}) \quad (5.18)$$

The level populations are given by n_i and n_j . C_{ij} and C_{ji} are the collisional rates, which are proportional to the electron density. Radiative rates, R_{ij} and R_{ji} , depend on the Einstein coefficients and the mean intensity as in Equations 5.19-5.22, resulting in a net radiative rate, R_{ij}^{net} , shown in Equation 5.23.

$$R_{ij} = B_{ij} \bar{J}_{ij} \quad (5.19)$$

$$R_{ji}(\text{spont}) = A_{ji} \quad (5.20)$$

$$R_{ji}(\text{stim}) = B_{ji} \bar{J}_{ij} \quad (5.21)$$

$$R_{ji} = R_{ji}(\text{spont}) + R_{ji}(\text{stim}) \quad (5.22)$$

$$R_{ij}^{\text{net}} = n_j R_{ji} - n_i R_{ij} = n_j A_{ji} - (n_i B_{ij} - n_j B_{ji}) \bar{J}_{ij} \quad (5.23)$$

The integrated mean intensity, weighted by the absorption profile ϕ_ν , is \bar{J}_{ij} , given by Equation 5.24. The quantity J_ν is the mean intensity at frequency ν .

$$\bar{J}_{ij} = \int_0^\infty J_\nu \phi_\nu d\nu \quad (5.24)$$

The left-hand side of the equation of statistical equilibrium (Equation 5.18) can be split into the local temporal change of n_i and the divergence of the flux of atoms or ions in state i by Equation 5.25.

$$\frac{dn_i}{dt} = \frac{\partial n_i}{\partial t} + \frac{\partial n_i V}{\partial x} \quad (5.25)$$

V is the macroscopic velocity of the plasma. In all cases considered here $V = 0$. It is also important to consider the equations for gas pressure, P_g (Equation 5.26), and charge conservation (Equation 5.27).

$$P_g = N k_B T \quad (5.26)$$

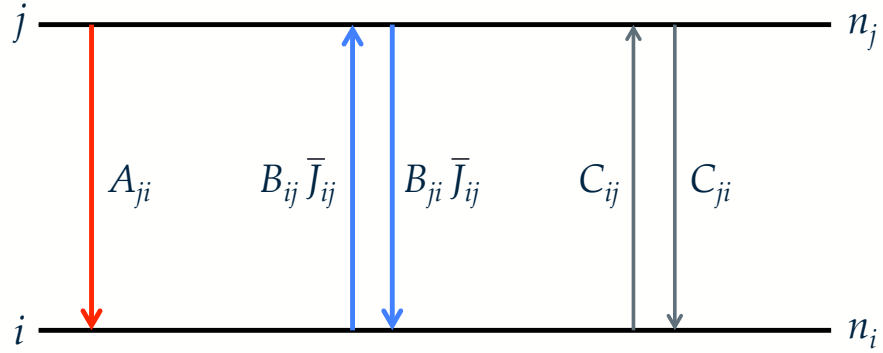


Figure 5.2: Two-level atom diagram showing atomic transitions between states i and j . Transitions from spontaneous emission (red), absorption and stimulated emission (blue), and collisional excitation/de-excitation (grey) are shown.

$$\sum_k N_k Z_k = n_e \quad (5.27)$$

N is the total particle number density, k_B is the Boltzmann constant, and T is temperature. For an atom in ionisation stage k , N_k is the total number density of atoms in that stage, and $N = \sum N_k + n_e$. The ionisation degree of species k is Z_k .

It is convenient to consider transitions in a two-level atom for most atomic transitions, shown in Figure 5.2, because in that case the equation of statistical equilibrium simplifies to Equation 5.28 (Heinzl 2015). This states that the transitions from state i to state j are balanced by the transitions from state j to state i .

$$n_i B_{ij} \bar{J}_{ij} + n_i C_{ij} = n_j A_{ji} + n_j B_{ji} \bar{J}_{ij} + n_j C_{ji} \quad (5.28)$$

From here the source function (Equation 5.12) can be reduced to Equation 5.29.

$$S_\nu = (1 - \epsilon) \bar{J} + \epsilon B_\nu \quad (5.29)$$

For a typical resonance line in the UV, the parameter ϵ can be approximated as Equation 5.30.

$$\epsilon = \frac{C_{ji}}{C_{ji} + A_{ji}} \quad (5.30)$$

This gives an indication of the likelihood of photon destruction. At high densities, collisional processes dominate and $\epsilon \approx 1$. This allows for LTE conditions in the

plasma. However, if densities are low (such as in a prominence) ϵ becomes very small and non-LTE conditions must be considered. In calculating transitions in a multi-level atom/ion it is possible to use an ‘equivalent two-level atom’ (e.g. [Gouttebroze et al. 1993](#)), where each transition is treated as a two-level system, but the source function is modified due to the populations of the other levels.

5.2 The PROM prominence models

The 1D prominence models of [Gouttebroze et al. \(1993\)](#), built using the PROM codes, were aimed at improving on previous works by [Heasley et al. \(1974\)](#); [Heasley & Mihalas \(1976\)](#); [Heasley & Milkey \(1976, 1978, 1983\)](#) – all of which built on the original code ([Heasley et al. 1974](#)) – which calculated emission of hydrogen, helium and calcium lines in a simple prominence slab model. [Gouttebroze et al.](#) aimed to improve on those codes with updated incident radiation and atomic physics, as well as an extended set of models, and it is this PROM code that forms the base of the magnesium code that is developed here. They used a 20-level plus continuum hydrogen atom and presented detailed line profiles for three Lyman lines (Ly- α , Ly- β , Ly- γ), five Balmer lines (H- α , H- β , H- γ , H- δ , H- ϵ), and one Paschen line (P- α), as well as calculating intensities at the heads of the Lyman and Balmer continua. By varying different physical parameters – gas pressure, slab thickness, and temperature – a grid of models was constructed that consisted of 140 individual models. Gas pressures of 0.01, 0.02, 0.05, 0.1, 0.2, 0.5, and 1 dyne cm⁻² were used, along with slab thicknesses of 200, 500, 1000, 2000, 5000, and 10000 km, and temperatures of 6000, 8000, and 10000 K to create the grid of models. They also used two ‘extreme’ temperature cases of 4300 and 15000 K at a fixed 5000 km slab thickness for the seven pressures. Other model parameters that can be altered in these models are the *microturbulent velocity* – simulating unresolved motions in the plasma, causing additional line broadening – which is set at 5 km s⁻¹, and the prominence height above the surface, H , which is set at 10000 km.

An important aspect of these models is the incident radiation on the slab, which is essential in calculating the emergent profile from a prominence. The strength of the incident radiation will help determine the level populations in the prominence, and therefore the intensities of the emergent line profiles. For the hydrogen calculations, [Gouttebroze et al.](#) used OSO-6 and OSO-8 disc observations for the incident lines

and continuum. In each resonance line a detailed frequency-dependent incident profile must be supplied to the code (a frequency-dependent profile is not required for other lines as in these cases the effects of resonant scattering of incident radiation are minimal), and each element that is included in the code must have the relevant incident profiles for each transition considered. The non-resonant lines can use a single representative intensity value for the incident radiation. The radiation field within the prominence slab is critical in calculating the excitation, ionisation, and electron density of the plasma, as well as the line profiles. These are important in then calculating the ionisation and level populations of other elements, so the hydrogen spectrum must be calculated in each case. The PROM code was updated by [Gouttebroze & Labrosse \(2000\)](#) to include updated incident radiation from *SOHO/SUMER*, centre-to-limb variations for the incident profile, and to present a more refined, user-friendly version of the code.

[Gouttebroze et al. \(1997\)](#) added to the PROM codes to include transitions of ionised calcium, specifically interested in the H and K and infrared triplet lines of Ca II. This model atom was relatively simple, with five levels in Ca II and only one each in Ca I and Ca III to handle ionisation and recombination between each ionisation stage. However, it was found that this simplified model is enough to reproduce reasonable Ca II H and K line profiles. Further work on Ca II was done by [Gouttebroze & Heinzel \(2002\)](#), where they compared calcium intensities to the hydrogen intensities from [Gouttebroze et al. \(1993\)](#). They presented line ratios between the Ca II 8542 Å triplet line and H- β for a large range of models, finding correlations in many cases, concluding that the observed 8542 Å line intensities should be closely related to the H- β line intensities for a large range of models, and that this can act as a diagnostic tool when comparing to observations.

The PROM code was expanded to include helium transitions by [Labrosse & Gouttebroze \(2001\)](#), where a detailed atomic model of helium is used to calculate lines of He I and He II. Due to the complexity of the atomic structure of neutral/ionised helium, and its close relation to the hydrogen radiation field, a much more detailed approach was needed to that of calcium. A total of 29 neutral helium levels are considered in the [Labrosse & Gouttebroze](#) models, and a simplified four-level system is used for the singly ionised helium transitions and one level representing doubly ionised helium. Through this, [Labrosse & Gouttebroze](#) were able to investigate in detail the effect of each plasma parameter on the emergent line profiles, as well as the

relationship between calculated intensities of He I and He II lines. In a further paper, [Labrosse & Gouttebroze \(2004\)](#) studied the He I triplet lines (primarily 10830 Å and D₃), investigating integrated intensities and their relations. This paper also marked the introduction of PCTR models to the PROM code, using pressure and temperature gradients outlined by [Anzer & Heinzel \(1999\)](#), finding that the inclusion of a PCTR has large effects on the observed line ratios, especially at higher temperatures. They conclude that it is best to include a PCTR in order to compare computed line profiles to observations.

Further work on the PROM codes went on to investigate the effects of cylindrical thread geometries ([Gouttebroze 2004, 2005, 2006](#)) and multi-thread models ([Labrosse & Rodger 2016](#)), which are important for investigating the effects of prominence fine structure on the observed line profiles.

5.3 The model Mg II atom

The atomic structure of singly-ionised magnesium is similar to that of singly-ionised calcium. The allowed radiative transitions of Mg II and Ca II both result in two strong resonance lines and three weaker triplet lines. The Mg II h and k resonance lines share the Mg II ground state as their lower level, and originate from the ²P excited states of Mg II (see [Figure 2.3](#), page 53). Other important lines to consider are the three UV triplet lines, which are formed from transitions between the ²D states and the ²P states, so these transitions are important in populating the h and k upper levels. In many regards the atomic structure of Mg II is comparable to that of Ca II, so here the calcium model of [Gouttebroze et al. \(1997\)](#) is used as a basis for this magnesium model. In the model outlined here, ionisation between Mg I states and the Mg II ground level are not considered. The effect of Mg I on the h and k lines is discussed in detail in [Leenaarts et al. \(2013a\)](#), where they find that the inclusion of Mg I transitions does not affect the h and k line cores at all in the chromosphere. Therefore it is not necessary to include Mg I for the calculation of Mg II transitions in a prominence.

In [Heinzel et al. \(2014\)](#) a five-level plus continuum magnesium atom is used. This is less than the eleven-level plus continuum atom used in chromospheric models by [Leenaarts et al. \(2013a\)](#), however the simplified five-level Mg II atom is sufficient to describe the h and k lines because the other, higher order subordinate lines do

not significantly affect the source functions of the h and k lines (Milkey & Mihalas 1974). This is also the approach taken in this work, with a five-level plus continuum Mg II atom being employed, shown in Figure 2.3. These levels allow five possible bound-bound transitions and five emission lines: the h and k lines (2803.53 Å and 2796.35 Å respectively), shown as red transitions in Figure 2.3, and three triplet lines (2791.60 Å, 2798.75 Å, and 2798.82 Å), shown as grey transitions in Figure 2.3. There are also bound-free, continuous radiative transitions from each of the Mg II levels (yellow transitions Figure 2.3), which result in absorption edges at 824.62 Å, 1168.25 Å, 1169.50 Å, 2008.94 Å, and 2008.97 Å.

Atomic energy levels for Mg II are here taken from RH¹ (Uitenbroek 2001; Pereira & Uitenbroek 2015) – an open-source stellar atmosphere radiative transfer code, regularly used to compute solar atmospheric spectra – which contains atom files for a large number of atoms and ions, including ionised magnesium. Although the RH code is not used here the atomic files that it uses are a convenient source of relevant atomic data, which are collected from a number of other sources. Ionisation energies, photoionisation cross sections, line oscillator strengths, bound-bound collisions and collisional ionisation data are all provided in the RH atom file. These each have their own origins, with photoionisation cross sections and oscillator strengths from *TopBase* (Cunto et al. 1993), bound-bound collisions from Sigut & Pradhan (1995), and collisional ionisation from Allen (1964). Heinzl et al. (2014) use parameters from a code called PANDORA (Avrett & Loeser 1992) for many of these parameters, but the RH values are used here instead. The abundance of magnesium is taken from Vial (1982b), which has a fixed value of 3.5×10^{-5} . Einstein coefficients for all five Mg II lines are taken from CHIANTI v8.0 (Dere et al. 1997; Del Zanna et al. 2015), which uses atomic data from Liang et al. (2009) for Mg II.

There are two additional line broadening effects to consider for the Mg II h and k lines beyond the natural, thermal, and collisional broadening of the lines: Stark broadening and Van der Waals broadening. Stark broadening, Γ_{elec} given by Equation 5.31, is an effect of the electric fields in the plasma, causing a split in the atomic levels of an atom – it is the electric equivalent to the Zeeman effect caused by magnetic fields. Van der Waals broadening, Γ_{vdW} given by Equation 5.32, is caused by collisions in the plasma, with collisional broadening becoming an important factor

¹Energy levels in RH are from the National Institute of Standards and Technology (NIST) <https://www.nist.gov/pml/atomic-spectra-database>

in the PRD case (Milkey & Mihalas 1974).

$$\Gamma_{\text{elec}} = \Gamma_{QS} N_e \quad (5.31)$$

$$\Gamma_{\text{vdW}} = \Gamma_{VW} T^{0.3} N_H \quad (5.32)$$

The Stark and Van der Waals coefficients used here, Γ_{QS} and Γ_{VW} respectively, are taken from Milkey & Mihalas (1974). These take the values $\Gamma_{QS} = 4.8 \times 10^{-7}$ and $\Gamma_{VW} = 6.6 \times 10^{-10}$. As suggested in Milkey & Mihalas (1974), the value for Γ_{VW} has been increased by a factor of 10 compared to the quoted value ($\Gamma_{VW} = 6.6 \times 10^{-11}$), as their method is said to underestimate the Van der Waals coefficient by that much. In Equations 5.31 and 5.32, N_e is electron number density, T is temperature, and N_H is the hydrogen number density.

Partial redistribution is used for the Mg II resonance lines – as was mentioned earlier, CRD is not appropriate for the calculation of the Mg II h and k line profiles. In this work a constant microturbulent velocity of $v_T = 5 \text{ km s}^{-1}$ is taken, and a height above the limb $H = 10000 \text{ km}$. Table 5.1 shows a comparison between the atomic parameters used here and in Heinzl et al. (2014), and their sources. §5.5.1 outlines the comparison between the resulting outputs of the HVA code and those calculated here.

5.4 Incident radiation

An important aspect of the model is the incident radiation on the prominence slab. In this work the incident Mg II profiles are taken from *IRIS* observations, and will be the first prominence radiative transfer code to use *IRIS* for this – previous Mg II codes have used OSO-8 (Paletou et al. 1993) and RASOLBA (Heinzl et al. 2014) observations for the incident profiles. *IRIS* regularly makes observations of the quiet sun at (or near) disc centre with high spectral, spatial and temporal resolution. The study used must contain all five Mg II lines of interest, in order to have both the resonance lines and the subordinate lines.

An observation from 29 September 2013 is used here for the incident profiles, which consisted of one large coarse raster centred on solar coordinate $(-1'', 5'')$. This raster is a coarse raster, meaning there are $2''$ between slit positions, with a total of 64 steps creating a full field of view of $127'' \times 120''$. The raster includes a full CCD

Table 5.1: Comparison between the atomic and prominence parameters used in HVA and those used here. References — (1) Avrett & Loeser (1992), (2) Cunto et al. (1993), (3) Sigut & Pradhan (1995), (4) Allen (1964), (5) Dere et al. (1997); Del Zanna et al. (2015), (6) Vial (1982b), (7) Staath & Lemaire (1995), (8) Milkey & Mihalas (1974). Parameters marked with n/a were not specified in Heinzl et al. (2014).

Parameter	HVA (source)	Here (source)
Mg II levels	5	5
Continuum	Mg II–Mg III	Mg II–Mg III
Ionisation energy	PANDORA (1)	RH
Photoionisation cross-section	PANDORA (1)	TopBase/RH (2)
Oscillator strength	PANDORA (1)	TopBase/RH (2)
Bound-bound collisions	(3)	RH (3)
Collisional ionisation	PANDORA (1)	RH (4)
Einstein coefficients	n/a	CHIANTI (5)
Mg abundance	3.5×10^{-5} (6)	3.5×10^{-5} (6)
Incident profile	RASOLBA (7)	<i>IRIS</i>
Line centre k/h ratio	1.25	1.20
Stark broadening	(8)	(8)
Van der Waals broadening	n/a	(8)
v_T	5km s ⁻¹	5km s ⁻¹
H	10000 km	10000 km
PRD/CRD (h and k lines)	PRD	PRD

readout, meaning that the entire spectral range of *IRIS* is available. Data is calibrated as in §3.3.2.

After calibration, the Mg II spectra are averaged spatially over the entire spatial extent of the raster. The specific intensities of the calibrated data are also multiplied by the factor 2.6×10^{-12} , as described in §3.3.2, to convert from cgs Å⁻¹ to cgs Hz⁻¹. The spatially averaged NUV spectrum around the Mg II lines is shown in Figure 5.3, with positions of the five Mg II lines marked with dashed lines. From left to right, the lines are 2791.60 Å (subordinate), 2796.35 Å (k), 2798.75 Å (subordinate), 2798.82 Å (subordinate), and 2803.53 Å (h).

The code requires half profile inputs for each line, which are assumed to be

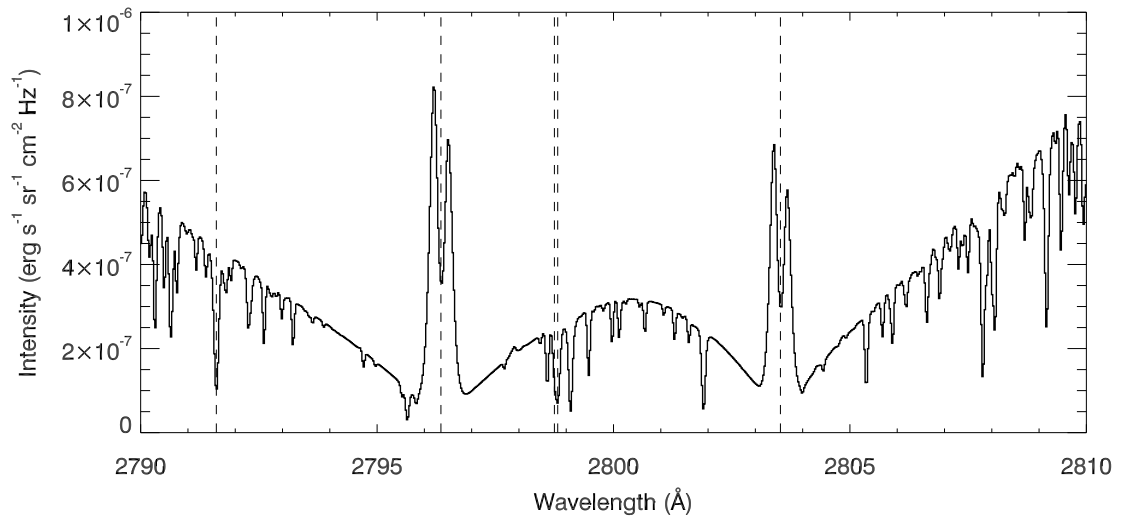


Figure 5.3: Averaged Sun-centre spectrum from 29 September 2013, used in the calculation of incident profiles in the Mg II updates to the PROM code. Dashed lines indicate locations of the five Mg II lines of interest. From left to right: 2791.60 Å, 2796.35 Å (k), 2798.75 Å, 2798.82 Å, and 2803.53 Å (h).

symmetrical about the line core. For the h and k lines the profiles are taken from line centre out to 3 Å in both directions, limited by the shape of the continuum between h and k. As can be seen in Figure 5.3 the red and blue peaks of the h and k lines are not symmetrical, with the blue peak larger in both cases. To deal with this asymmetry the half profiles are formed by averaging the blue and red sides of the line together. In the wings of these lines there are a number of absorption lines which are not needed in the calculation of the emergent Mg II h and k profiles. To help deal with these, smoothing is applied to the wings after averaging the profiles beyond the k_1 and h_1 positions. Figure 5.4 shows the original red-side (red line) and blue-side (green line) profiles, with the blue side mirrored about the line centroid, and the resulting averaged half profile (black histogram) for the Mg II h (*upper panel*) and k (*lower panel*) lines. The black histogram also has the wing profile smoothed to reduce the depth of the absorption lines visible. Notably some of the deepest absorption lines are still visible, so a linear interpolation is performed in those spectral regions, at the far wings of the profiles, in order to remove the remaining absorption. The final incident half profiles for the h and k lines are shown in Figure 5.5.

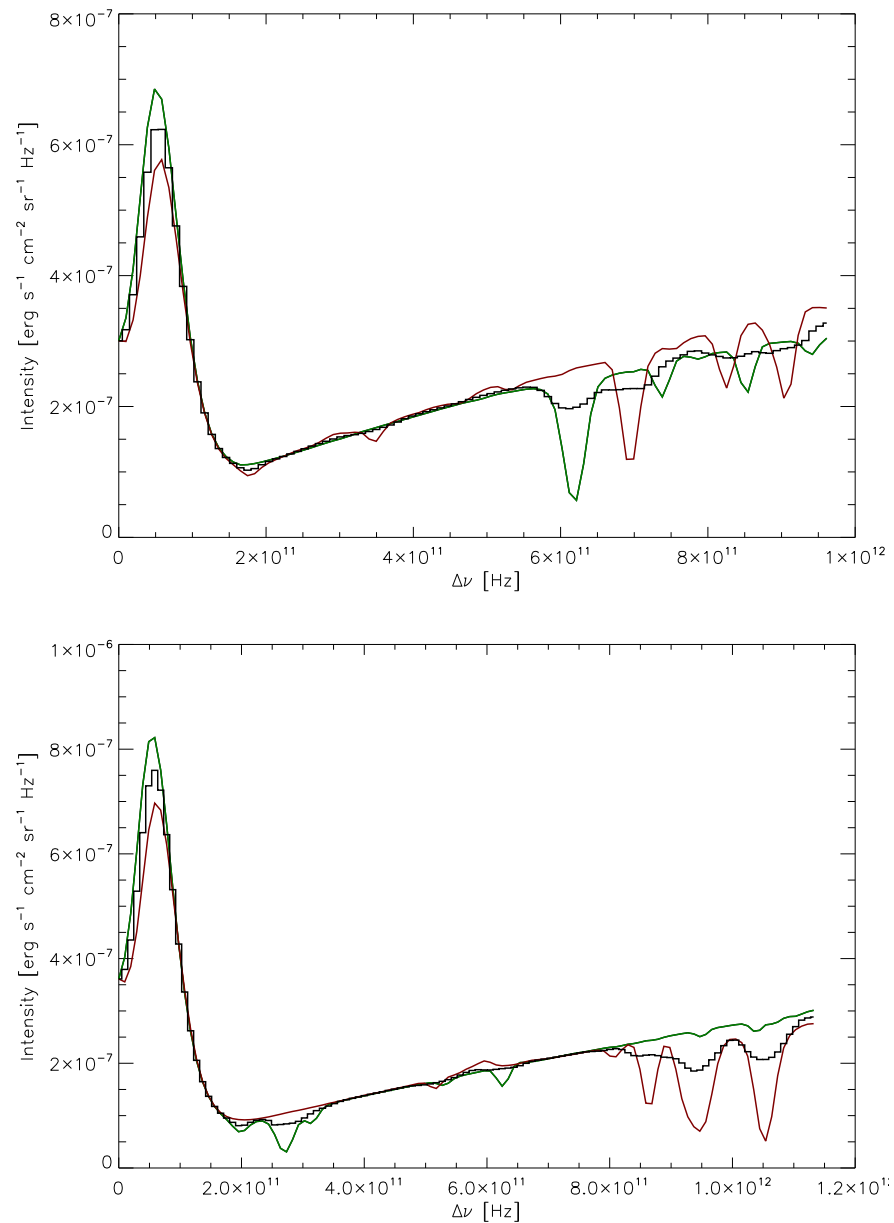


Figure 5.4: Half line profiles for the h and k lines of Mg II. The red profiles show the red side of line centroid, while green profiles show (mirrored) blue side of line centroid. The black histogram is the averaged profile between the red and blue profiles, additionally with smoothed line wings beyond the h_1 and k_1 positions. *Top:* Mg II h profile. *Bottom:* Mg II k profile.

A detailed line profile for the subordinate lines is not required due to the fact that the incident radiation does not play a large role in the emergent profile. An

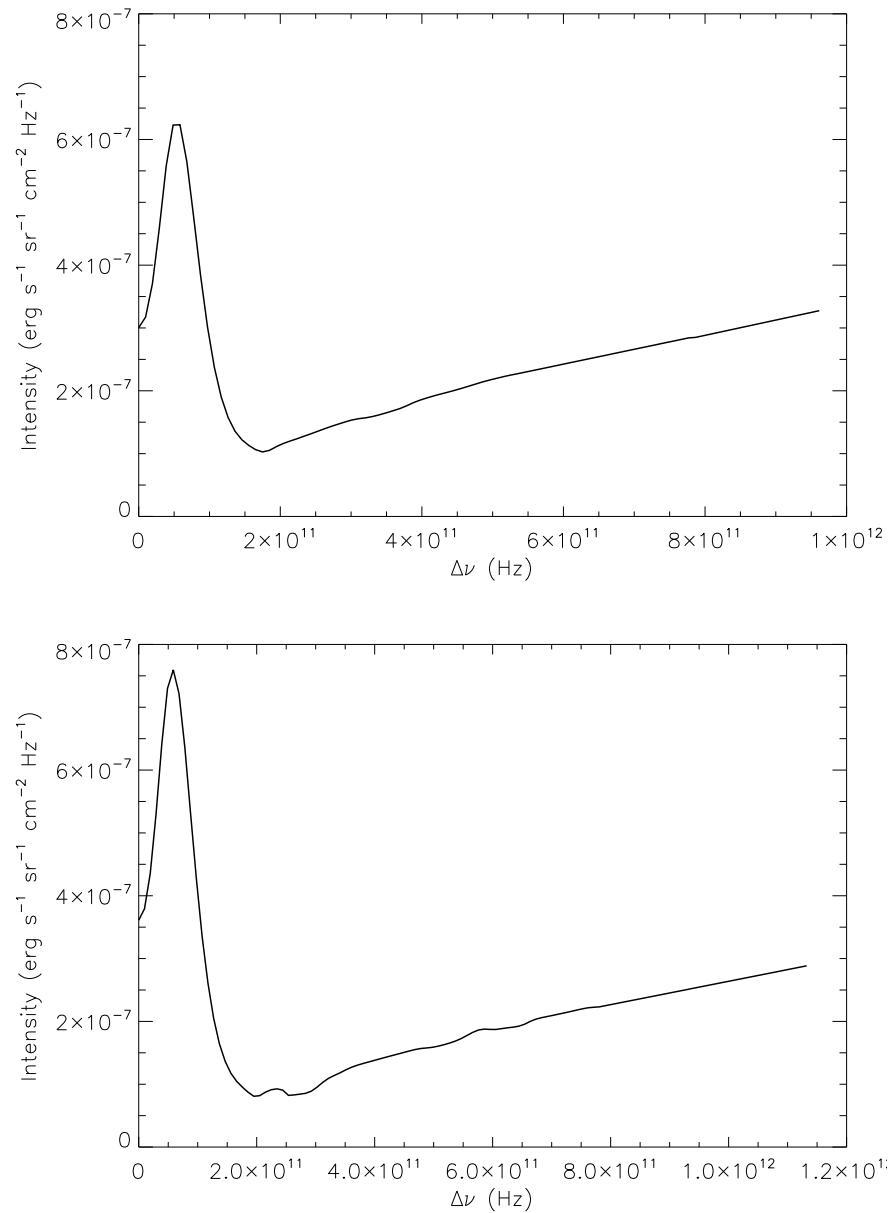


Figure 5.5: Half line profiles for Mg II h and k lines. Line cores ($\Delta\nu \sim 0 - 2 \times 10^{11}$ Hz) are the average of the blue and red sides of the profile only. Above $\Delta\nu \sim 2 \times 10^{11}$ Hz profiles are averaged and smoothed. Absorption lines in the far wings are removed by interpolating between points in the continuum. *Top:* Mg II h profile. *Bottom:* Mg II k profile.

approximation is therefore made that they can be described by a single representative intensity value at the centroid position of each line. This intensity value is taken as

the value of the continuum at the line centroid positions – 4.35×10^{-7} cgs Hz⁻¹ for 2791.60 Å, 2.49×10^{-7} cgs Hz⁻¹ for 2798.75 Å, and 2.54×10^{-7} cgs Hz⁻¹ for 2798.82 Å.

5.5 Isothermal isobaric models

As has been mentioned, this work has primarily been done on a 1D isothermal, isobaric prominence slab model. This basic geometry acts as a base for more complex models, such as ones with a PCTR (§5.6). A basic isothermal isobaric model can, however, also act as a reference for observations. The code outputs the optical thickness, τ , for each allowed transition, as well as emergent line profiles and integrated line intensities. This allows for a comparison between observables, such as the line profile characteristics, and the prominence physical parameters, such as temperature, gas pressure, optical thickness, and slab width.

5.5.1 The HVA grid of models

The grid of models presented in [Heinzel et al. \(2014\)](#) contained a total of 27 individual isothermal isobaric models. Gas pressures of 0.01, 0.1 and 0.5 dyne cm⁻², slab thicknesses of 200, 1000, and 5000 km, and temperatures of 6000, 8000, and 10000 K were used in the isothermal isobaric case. They present line profiles of the Mg II k line for each model, as well as a table outlining the results for both h and k lines. The table presents the integrated intensities of the lines, along with reversal levels and calculated line core optical thicknesses. It is this table that is used in §3.4.4 to compare observations to models in order to estimate plasma parameters.

For the incident radiation, they use quiet sun line profiles from the RASOLBA balloon ([Staath & Lemaire 1995](#)), giving a k/h line centre intensity ratio of 1.25. In the subordinate lines they take the intensity at the centroid position of each line to be representative of the line intensity itself. These models maintain a 5 km s⁻¹ microturbulent velocity and a prominence height of 10000 km.

The HVA model results range from non-reversed profiles, with low optical thicknesses ($\tau \sim 0.5$ to 1), up to large line reversals in the thickest, highest temperature slabs. In these cases the optical thickness can reach over 1000. They also investigate the effects of PRD vs. CRD in the Mg II h and k lines, confirming that PRD is the correct redistribution function to use, especially in the case of high gas pressures.

Another aspect explored in [Heinzel et al. \(2014\)](#), although briefly, is the inclusion of a PCTR into the prominence slab. They find that the inclusion of a PCTR slightly enhances the emission in the k line core.

Further analysis in [Heinzel et al. \(2015\)](#), in comparison to the *IRIS* observations of [Schmieder et al. \(2014\)](#), revealed the importance of including a PCTR in the calculations of Mg II h and k line profiles. In that paper they also investigated 2D isothermal isobaric models, however that alone could not explain the observed profiles. These updates could account for many of the line profiles found in the observations of [Schmieder et al. \(2014\)](#), but there are still many line profiles described in Chapters 3 and 4 that cannot be accounted for even under those conditions. This creates the requirement for an updated set of models, which can account for the complexity of the observed Mg II h and k profiles. An extended grid of 1D models, PCTR models, and eventually a multi-thread model, should help to simulate the complex profiles described in §3.4.2.

The first step in extending the HVA grid is to replicate that grid of models using the updated PROM code. This enables a direct comparison to be made between the outputs of this code and the HVA code, allowing confirmation of the new code's integrity given the differences in atomic data and incident radiation used. Table 5.2 shows the HVA grid and their calculated integrated line intensities, I_{peak}/I_0 ratio value (reversal level), and optical thickness. In Table 5.3 the HVA grid of models is recreated, using the same temperature, gas pressure, and slab thickness values, but instead calculated with the updated PROM code. This table has been arranged in the same way as the table in [Heinzel et al. \(2014\)](#), Table 5.2, for convenience of comparison.

Figures 5.6, 5.7, and 5.8 show the emergent Mg II h (*left panels*) and k (*right panels*) line profiles for all 27 models. Each plot shows profiles for a different slab thickness – 200 km (Figure 5.6), 1000 km (Figure 5.7), and 5000 km (Figure 5.8). In these plots the colours indicate different gas pressures, red profiles are for $0.01 \text{ dyne cm}^{-2}$, green profiles are for 0.1 dyne cm^{-2} , and blue profiles are for 0.5 dyne cm^{-2} . Temperatures are indicated by shades of colour, with 6000 K being the darkest, 8000 K being intermediate, and 10000 K being the lightest shade.

These emergent profiles show that the line intensities and reversal levels generally increase with both pressure and temperature, and also that the h and k lines respond to $T/P/D$ changes in very similar ways. For all models (apart from the highest $T/P/D$

Table 5.2: Table 2 from [Heinzel et al. \(2014\)](#) for their grid of 27 models. Temperatures of 6000, 8000, and 10000 K, pressures of 0.01, 0.1, and 0.5 dyne cm⁻², and slab thicknesses of 200, 1000, and 5000 km are used to create this grid. For each model there are three output parameters given for the h and k lines: integrated intensity (top row), reversal level (middle row), and optical thickness (bottom row). ‘+n’ indicates ‘×10ⁿ’.

Mg line	h	k	h	k	h	k	
p [dyne cm ⁻²]	0.01	0.01	0.1	0.1	0.5	0.5	
$T = 6000$ K	0.37+4 nr 0.10+1	0.72+4 nr 0.20+1	0.11+5 1.04 0.14+2	0.16+5 1.08 0.28+2	0.17+5 1.30 0.80+2	0.24+5 1.43 0.16+3	$D = 200$ km
$T = 8000$ K	0.28+4 nr 0.70+0	0.59+4 nr 0.14+1	0.11+5 1.02 0.90+1	0.16+5 1.08 0.18+2	0.25+5 1.60 0.55+2	0.41+5 2.11 0.11+3	$D = 200$ km
$T = 10000$ K	0.23+4 nr 0.50+0	0.49+4 nr 0.10+1	0.11+5 1.01 0.65+1	0.17+5 1.07 0.13+2	0.46+5 1.66 0.32+2	0.84+5 2.30 0.64+2	$D = 200$ km
$T = 6000$ K	0.85+4 nr 0.50+1	0.13+5 1.02 0.10+2	0.16+5 1.22 0.70+2	0.22+5 1.31 0.14+3	0.25+5 1.89 0.41+3	0.36+5 2.22 0.82+3	$D = 1000$ km
$T = 8000$ K	0.77+4 nr 0.34+1	0.12+5 nr 0.68+1	0.17+5 1.26 0.46+2	0.26+5 1.48 0.92+2	0.76+5 4.14 0.25+3	0.12+6 5.79 0.50+3	$D = 1000$ km
$T = 10000$ K	0.69+4 nr 0.25+1	0.11+5 nr 0.50+1	0.20+5 1.31 0.30+2	0.33+5 1.62 0.60+2	0.19+6 4.15 0.15+3	0.32+6 5.87 0.30+3	$D = 1000$ km
$T = 6000$ K	0.13+5 1.08 0.25+2	0.18+5 1.13 0.50+2	0.22+5 1.62 0.36+3	0.30+5 1.77 0.72+3	0.40+5 3.20 0.21+4	0.58+5 3.55 0.42+4	$D = 5000$ km
$T = 8000$ K	0.12+5 1.05 0.17+2	0.17+5 1.11 0.34+2	0.33+5 2.42 0.23+3	0.51+5 3.17 0.46+3	0.28+6 11.47 0.12+4	0.39+6 14.30 0.24+4	$D = 5000$ km
$T = 10000$ K	0.12+5 1.04 0.13+2	0.17+5 1.09 0.26+2	0.52+5 2.82 0.14+3	0.89+5 3.96 0.28+3	0.75+6 10.38 0.70+3	0.11+7 13.79 0.14+4	$D = 5000$ km

model) k line centre intensities are in the range $10^{-7} - 10^{-6}$ erg s⁻¹ sr⁻¹ cm⁻² Hz⁻¹. Intensities of the h line are always lower than those of the k line. The lowest P/D profiles show little dependence on temperature, and the lines are all unreversed which indicates that the source function is nearly the same everywhere in the slab.

Table 5.3: HVA grid of 27 models using the modified PROM code. Rows are as in Table 5.2. Pressure, P , is in dyne cm^{-2} . The first column is temperature, and last column is slab thickness.

Mg II line	h	k	h	k	h	k	
P	0.01	0.01	0.1	0.1	0.5	0.5	
6000 K	0.35 + 04	0.65 + 04	0.11 + 05	0.15 + 05	0.17 + 05	0.22 + 05	200 km
	nr	nr	1.05	1.11	1.28	1.38	
	0.97 + 00	0.19 + 01	0.14 + 02	0.27 + 02	0.79 + 02	0.16 + 03	
8000 K	0.27 + 04	0.53 + 04	0.11 + 05	0.16 + 05	0.23 + 05	0.35 + 05	200 km
	nr	nr	1.03	1.09	1.50	1.89	
	0.66 + 00	0.13 + 01	0.92 + 01	0.18 + 02	0.52 + 02	0.10 + 03	
10000 K	0.21 + 04	0.43 + 04	0.11 + 05	0.16 + 05	0.40 + 05	0.71 + 05	200 km
	nr	nr	1.01	1.07	1.55	2.10	
	0.47 + 00	0.94 + 00	0.64 + 01	0.13 + 02	0.31 + 02	0.61 + 02	
6000 K	0.85 + 04	0.12 + 05	0.16 + 05	0.21 + 05	0.23 + 05	0.30 + 05	1000 km
	nr	1.03	1.23	1.30	1.63	1.84	
	0.50 + 01	0.99 + 01	0.69 + 02	0.14 + 03	0.41 + 03	0.82 + 03	
8000 K	0.75 + 04	0.11 + 05	0.17 + 05	0.24 + 05	0.61 + 05	0.97 + 05	1000 km
	nr	1.01	1.26	1.43	3.37	4.65	
	0.33 + 01	0.66 + 01	0.46 + 02	0.91 + 02	0.25 + 03	0.49 + 03	
10000 K	0.66 + 04	0.11 + 05	0.19 + 05	0.29 + 05	0.14 + 06	0.25 + 06	1000 km
	nr	nr	1.27	1.54	3.40	4.87	
	0.24 + 01	0.47 + 01	0.30 + 02	0.59 + 02	0.14 + 03	0.28 + 03	
6000 K	0.13 + 05	0.17 + 05	0.21 + 05	0.27 + 05	0.31 + 05	0.44 + 05	5000 km
	1.11	1.16	1.48	1.62	2.21	2.53	
	0.26 + 02	0.51 + 02	0.37 + 03	0.73 + 03	0.21 + 04	0.42 + 04	
8000 K	0.12 + 05	0.17 + 05	0.29 + 05	0.42 + 05	0.21 + 06	0.30 + 06	5000 km
	1.08	1.13	2.03	2.63	8.62	11.03	
	0.17 + 02	0.34 + 02	0.22 + 03	0.45 + 03	0.11 + 04	0.23 + 04	
10000 K	0.12 + 05	0.16 + 05	0.41 + 05	0.70 + 05	0.48 + 06	0.79 + 06	5000 km
	1.05	1.11	2.34	3.33	7.76	10.37	
	0.12 + 01	0.24 + 02	0.14 + 03	0.28 + 03	0.63 + 03	0.13 + 04	

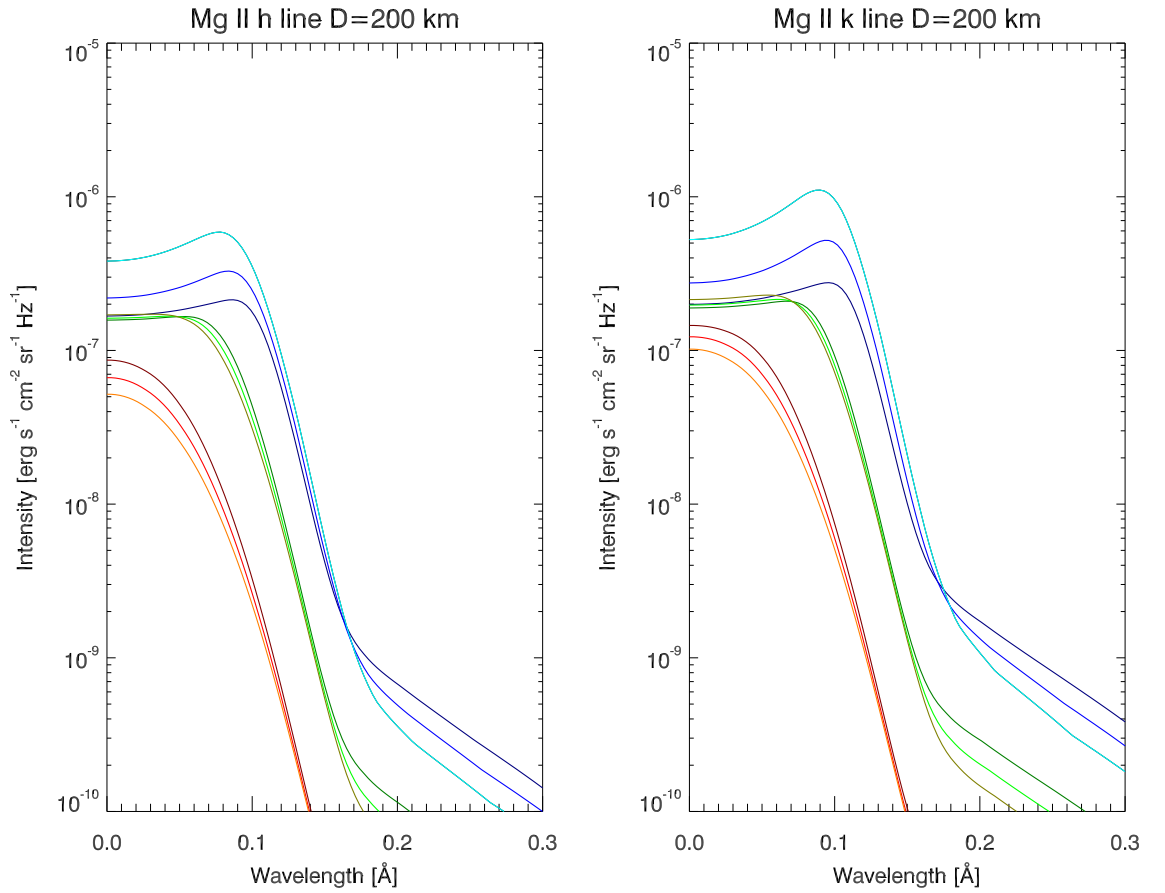


Figure 5.6: Emergent half line profiles of the Mg II lines for a 200 km thick prominence slab, viewed along a line of sight perpendicular to the slab surface. *Left:* Mg II h. *Right:* Mg II k. Red profiles are for a gas pressure of $0.01 \text{ dyne cm}^{-2}$, green profiles are for 0.1 dyne cm^{-2} , and blue profiles are for 0.5 dyne cm^{-2} . Temperatures are from dark to light: 6000 K, 8000 K, and 10000 K. Profiles are symmetrical about the line centre.

At higher pressures and slab thicknesses the line-centre source function decreases towards the edge of the slab with respect to the slab centre, so the resulting line profiles are reversed. For high P models, especially at 1000 km and 5000 km, some sudden changes in the slope can be seen in the line wings. This can be attributed to the frequency grid over which the profiles are calculated, which is more sparse in the line wings. It is therefore an artifact of the code and is not a real effect of the prominence conditions. Comparing to Table 5.3, line centre optical thickness varies

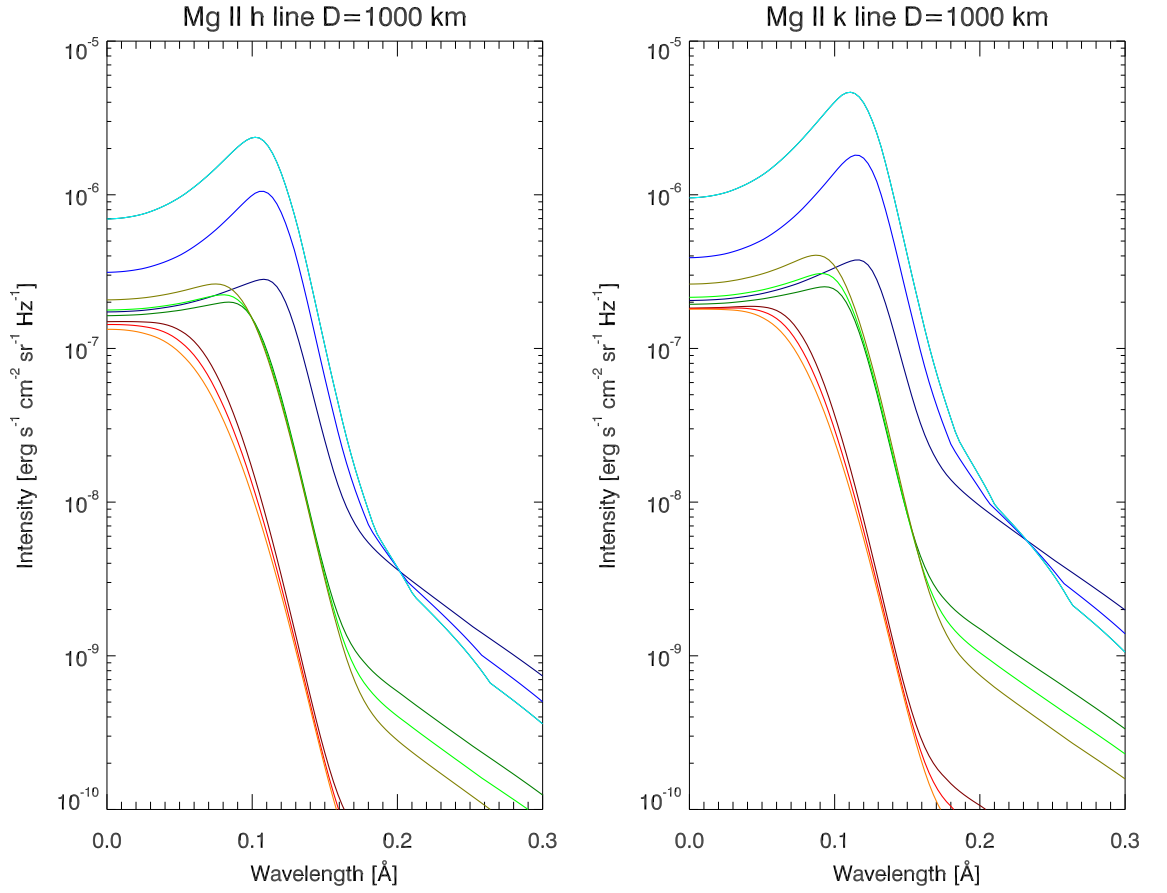


Figure 5.7: Same as Figure 5.6 but for a 1000 km thick prominence slab.

from near 1, for low $T/P/D$ models, to as high as $\sim 10^4$.

The new grid of models differs slightly from those of HVA, as can be seen by comparing Table 5.3 with Table 5.2. At low $T/P/D$ there is not a significant difference between the results here and the HVA results, however at higher $T/P/D$ the results begin to diverge. This can be seen more clearly by plotting the *relative difference* for each model (Equation 5.33), using integrated intensities I_L (Levens) for the results found here and I_H for the HVA results.

$$\text{Relative difference} = \frac{|I_L - I_H|}{I_H} \quad (5.33)$$

Plotting this parameter against gas pressure, for each temperature and slab thickness, gives the plots shown in Figure 5.9 for h (*left panel*) and k (*right panel*) lines. As can be seen, variations of up to 35% are seen for some models in the h line, for high T , P , and D models, but for some lower $T/P/D$ models the relative difference is

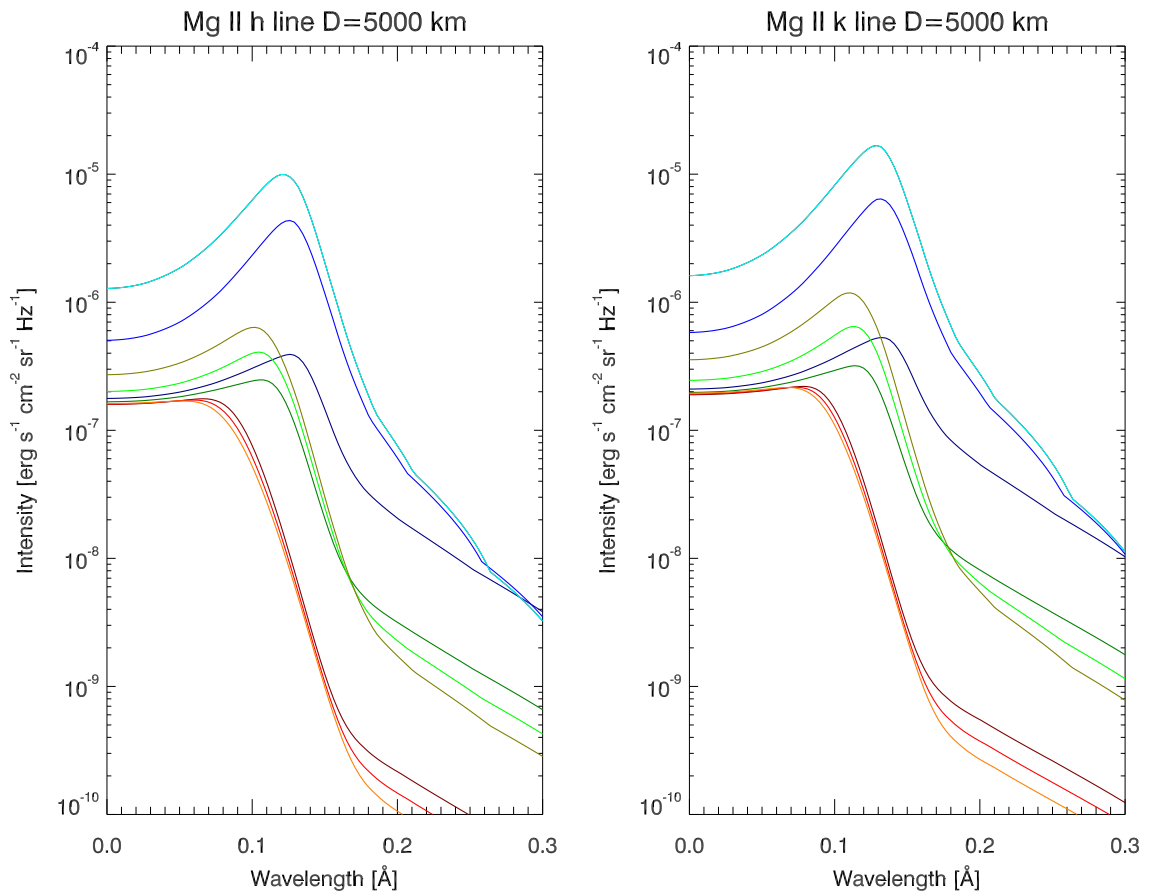


Figure 5.8: Same as Figure 5.6 but for a 5000 km thick prominence slab.

near zero. Variations for the k line are generally lower, below 30%, but the lowest relative differences are higher than those for h. The reason for these variations is not clear at this stage, but are probably due to differences in the atomic physics used in constructing the model atom. Considering the resultant optical thickness instead of the integrated intensities, comparing Tables 5.2 and 5.3, reveals that the differences between HVA and here are much smaller. In many cases the optical thickness from the updated PROM code is identical to those from HVA, and all models are within 10% of the HVA values.

Although there are some differences between the HVA grid of results and those found here, the overall trends in integrated intensity are found to be similar, and the optical thicknesses are in good agreement. It is therefore possible to extend the grid of isothermal isobaric models to include a larger range of temperatures, pressures

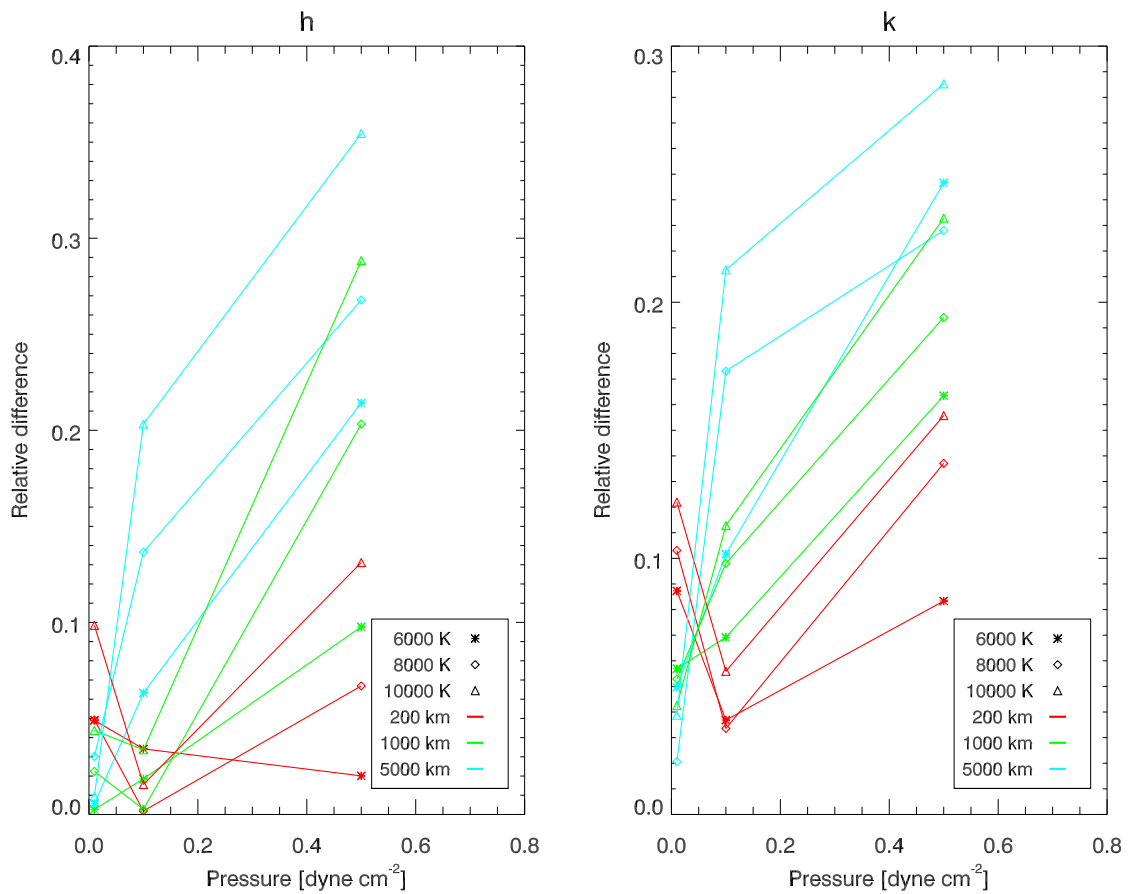


Figure 5.9: Plots of relative difference versus gas pressure for the range of temperatures and slab thicknesses defined in the 27 HVA models. *Left:* Mg II h. *Right:* Mg II k.

and slab thicknesses.

5.5.2 Extended grid of models

With the basic grid of 27 1D HVA models computed using the updated PROM code, a natural first step is to expand that grid to include more gas pressures, temperatures, and slab thicknesses. For this a total of 252 models are considered, with model parameters being shown in Table 5.4. Nine temperatures between 6000 K and 40000 K are considered here, as the Mg II lines are stated to form at chromospheric temperatures of ~ 30000 K in CHIANTI v8.0 (Dere et al. 1997; Del Zanna et al. 2015), where the atomic data comes from Sigut & Pradhan (1995). The figure of 30000 K for

Table 5.4: Model parameters for the grid of 1D isothermal isobaric Mg II models. T denotes temperature, P is gas pressure, and D is slab thickness. v_T and H are microturbulent velocity and prominence height above the solar surface, respectively.

Parameter	Unit	Value
T	K	6000, 8000, 10000, 15000, 20000, 25000, 30000, 35000, 40000
P	dyne cm ⁻²	0.01, 0.02, 0.05, 0.1, 0.2, 0.5, 1
D	km	200, 500, 1000, 2000
v_T	km s ⁻¹	5
H	km	10000

the formation of Mg II lines comes from calculations considering purely collisional excitation (Sigut & Pradhan 1995), and does not take into account radiative excitation, which is important in prominences. Radiative effects can have a large effect on the population of the h and k levels, and the formation of those lines, meaning that they can form at lower plasma temperatures of around 10000 K (Leenaarts et al. 2013a,b). The range of possible gas pressures is expanded compared to HVA, with seven gas pressures of between 0.01 and 1 dyne cm⁻² being considered in this grid. Slab thicknesses of 200, 500, 1000, and 2000 km are considered. For these isothermal isobaric models the turbulent velocity and prominence height are again kept constant at $v_T = 5$ km s⁻¹ and $H = 10000$ km respectively.

Figure 5.10 shows relationships between observable parameters for h vs. k for all 252 models. The plots of h against k integrated intensities show an almost perfect power-law relationship, with a power law index of 1.02, as may be expected from the ratio of oscillator strengths of the h and k lines, however there is a small ‘bump’ at around $I_{\text{int}}(k) = 10^4$ erg s⁻¹ sr⁻¹ cm⁻². This departure from linearity can be explained by considering the optical thickness of the lines. Figure 5.11 presents the h (*left panel*) and k (*right panel*) integrated intensities versus the optical thickness of the line for all 252 isothermal isobaric models. The ‘bump’ in Figure 5.10 corresponds to the intensity where the h and k lines become optically thick, and the models with the highest optical thickness can be found to have an integrated intensity around

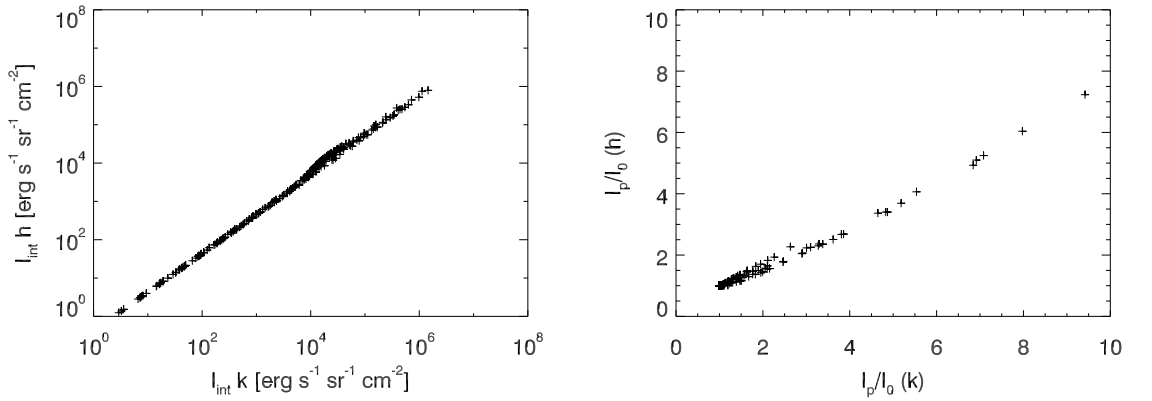


Figure 5.10: Correlations between observable properties of the Mg II h and k lines. Points are for each of the 252 isothermal isobaric models. *Left:* Correlation between integrated intensities of the Mg II h and k lines. Power law index is 1.02. *Right:* Correlation between Mg II h and k reversal level.

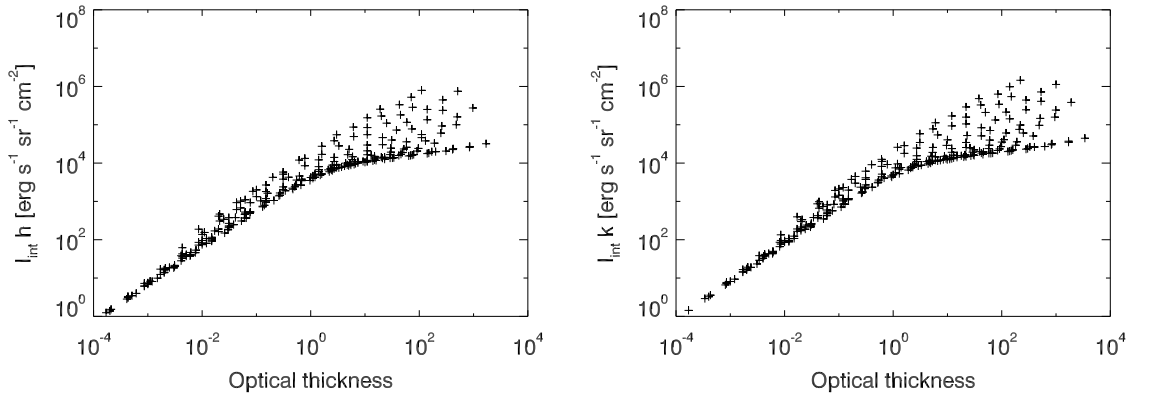


Figure 5.11: Plots of integrated intensity against optical thickness for the Mg II resonance lines, for all of the 252 isothermal isobaric models. *Left:* Mg II h. *Right:* Mg II k.

$10^4 \text{ erg s}^{-1} \text{ sr}^{-1} \text{ cm}^{-2}$ in both lines. A small number of models deviate from this value, having higher intensities for optically thick models, creating a scatter of points in Figure 5.11. These mostly continue the (approximate) power law seen at lower optical thicknesses and integrated intensities. Importantly, as shown in Figure 5.12, optical thicknesses higher than around 10 are where the h and k lines begin to become reversed. A reversal at line centre results in a reduction of integrated intensity

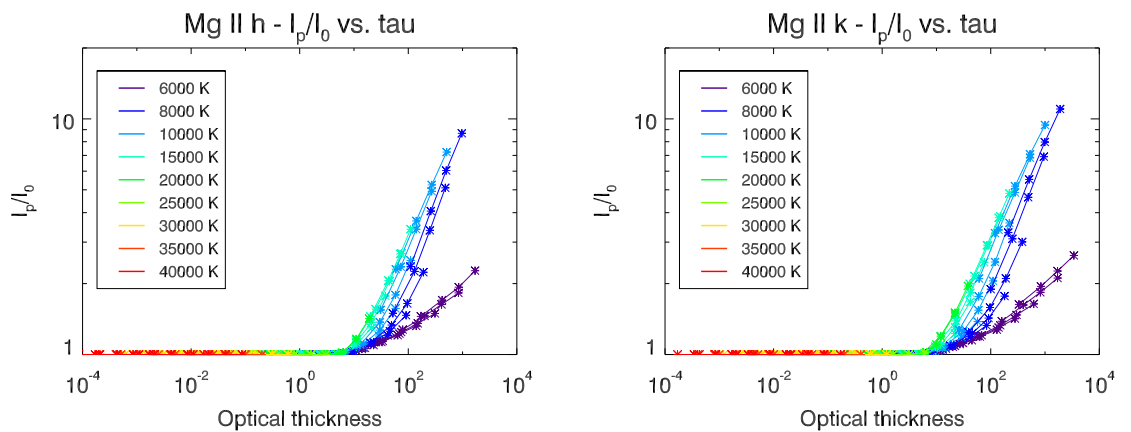


Figure 5.12: Reversal level against optical thickness for all 252 isothermal isobaric models. Colours indicates temperature. *Left:* Mg II h. *Right:* Mg II k.

compared to an equivalent non-reversed profile, which accounts for the flattening of the plots in Figure 5.11. Differences in the optical thickness for the h and k lines means there will be different possible relative h and k intensity values depending on the model. This, then, causes the small departure from power-law linearity seen in Figure 5.10.

The right-hand plot of Figure 5.10 shows the correlation between line reversal of the h and k lines. In this there is a roughly linear relationship between h line reversal and k line reversal. Most points are clustered at lower reversal values ($\sim 1 - 2$), with relatively few models showing high reversal in either line.

Some of the 252 models in this grid are overlapped with the 27 HVA models, which was discussed in §5.5.1. This grid, however, extends the temperature coverage well beyond that of HVA. Figure 5.13 shows the emergent Mg II k profiles for each of the models, with each panel showing all P and D combinations for a single temperature. Notably, lower temperature models (≤ 20000 K) show a mix of reversed and non-reversed profiles, whereas higher temperature models (> 20000 K) do not show any line reversals. It is therefore worth exploring these high-temperature models in more detail to gauge their viability. Figure 5.14 shows the emergent half h and k profiles for models with $T \geq 15000$ K at one slab thickness, $D = 1000$ km, and two gas pressures, $P = 0.1$ dyne cm^{-2} (solid lines) and $P = 0.5$ dyne cm^{-2} (dashed lines). Each temperature is given a different colour to distinguish them. The profiles are reversed for the 15000 K models, becoming flat-topped at 20000 K, and are not

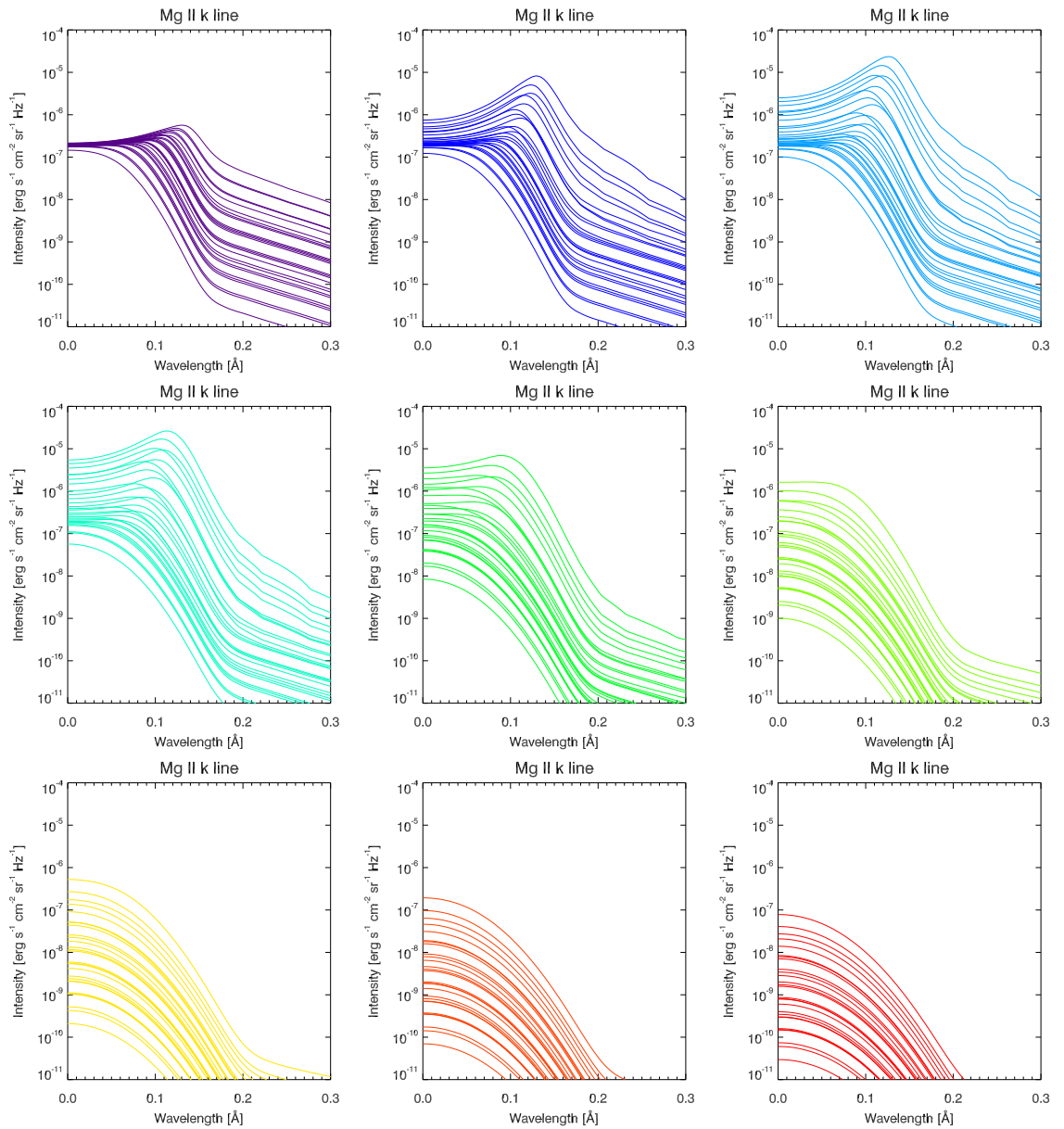


Figure 5.13: Emergent half-line Mg II k profiles for the grid of 252 isothermal isobaric models. Each panel/colour represents a different temperature: 6000 K (purple), 8000 K (dark blue), 10000 K (light blue), 15000 K (teal), 20000 K (green), 25000 K (lime green), 30000 K (yellow), 35000 K (orange), and 40000 K (red). Intensities generally increase for higher pressure and slab thickness.

reversed above 25000 K – this can already be seen in Figure 5.12 where all high temperature models do not show central reversals. Also, as the temperature increases

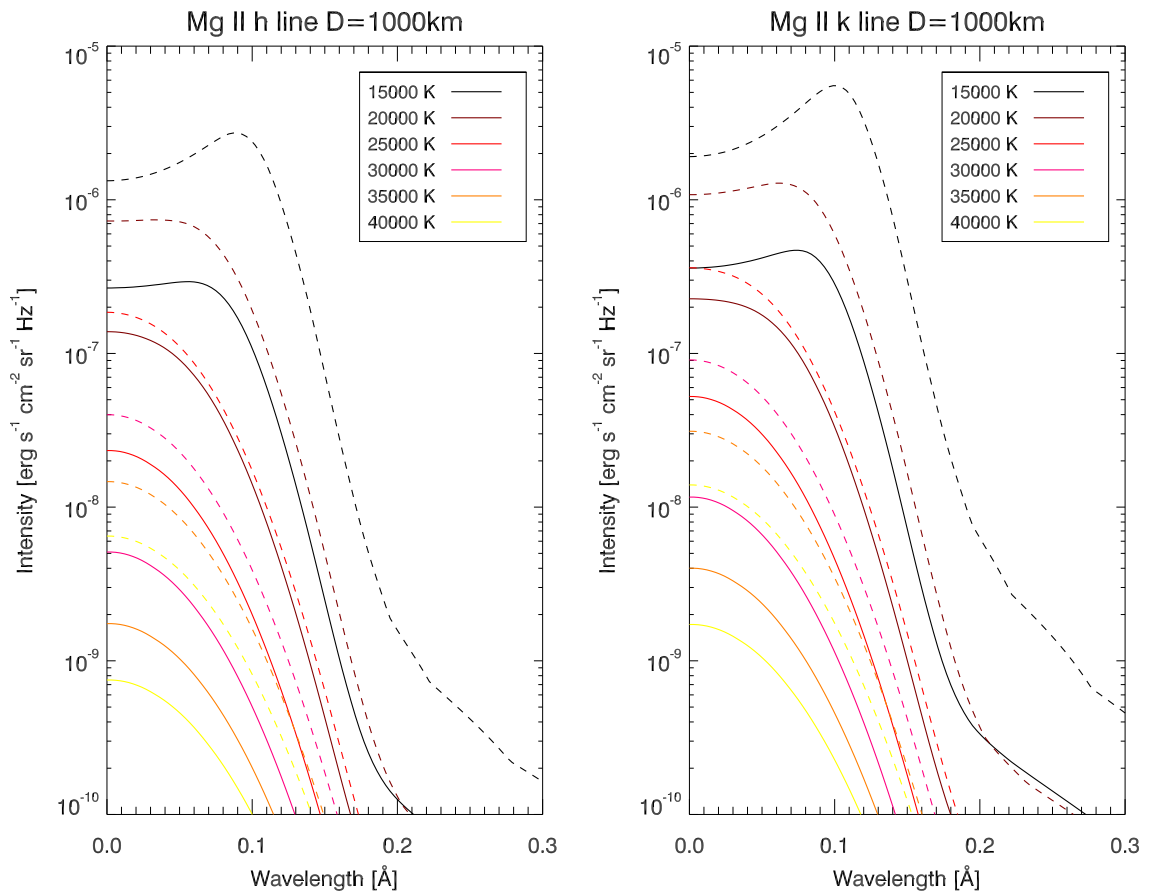


Figure 5.14: Half-line emergent profiles for the Mg II h (*left*) and k (*right*) lines from models with $T \geq 15000$ K. All profiles are from models with $D = 1000$ km. Profiles for two pressures are shown, with $P = 0.1$ dyne cm^{-2} (solid lines) and $P = 0.5$ dyne cm^{-2} (dashed lines). Temperatures are: 15000 K (black), 20000 K (maroon), 25000 K (red), 30000 K (pink), 35000 K (orange), and 40000 K (yellow).

the line intensity decreases. This can be seen for line centre intensity in Figure 5.14, and also for the integrated line intensity which is plotted as a function of temperature in Figure 5.15. Figure 5.15 only shows plots for models with $D = 1000$ km, but includes all pressures which are indicated by the colour gradient. These plots mostly have peaks at a temperature of around 10000 – 15000 K for higher pressure models, around the formation temperature of Mg II (Leenaarts et al. 2013a,b). In these cases the peak occurs where collisional processes would be expected to begin to dominate over radiative ones. At low pressures the emission seen will mostly be the result of

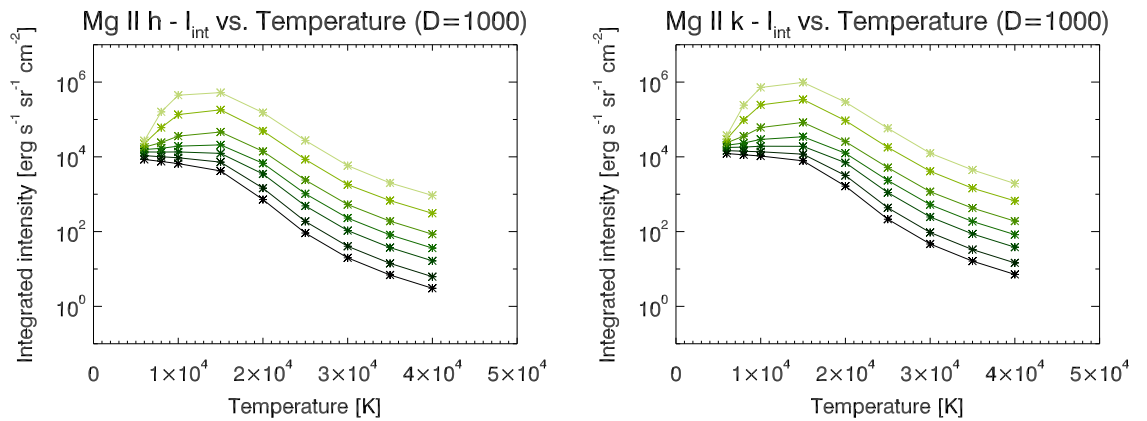


Figure 5.15: Plots of integrated intensity against temperature for models with $D = 1000$ km. Colour indicates pressures of, from dark to light, 0.01, 0.02, 0.05, 0.1, 0.2, 0.5, and 1 dyne cm^{-2} . *Left:* Mg II h. *Right:* Mg II k.

scattering of light from the solar disc, causing radiative excitation of the Mg II ion. As the pressure increases the collisional processes become more important so the line intensity generally increases with respect to lower pressure models. Above 15000 K a larger proportion of Mg II is ionised to Mg III so there is relatively less Mg II in the relevant energy levels for the h and k transitions, and so the intensity drops off as temperature increases.

Figure 5.16 shows plots of integrated intensity against gas pressure (*top*) and slab thickness (*bottom*) for the Mg II h (*left panels*) and k (*right panels*) lines. The top panels are shown for one slab thickness ($D = 1000$ km) and the bottom panels are shown for one gas pressure ($P = 0.1$ dyne cm^{-2}). Temperatures are represented by the colours, with low temperatures having darker colours and high temperatures having lighter colours. Gas pressure and slab thickness both increase with integrated intensity for the h and k lines. The temperature structure seen in Figure 5.15 (peaked around 10000 – 15000 K) can also be identified in these plots.

The results shown here indicate that the formation temperature of the Mg II lines estimated from purely collisional excitation, 30000 K (Sigut & Pradhan 1995; Dere et al. 1997; Del Zanna et al. 2015), is an overestimation. This is as was found for the chromosphere (Leenaarts et al. 2013a,b), where the importance of radiative excitation means that photons of Mg II h and k are created much more frequently at lower temperatures, around 10000 K. The effects of ionisation from Mg II to Mg III at

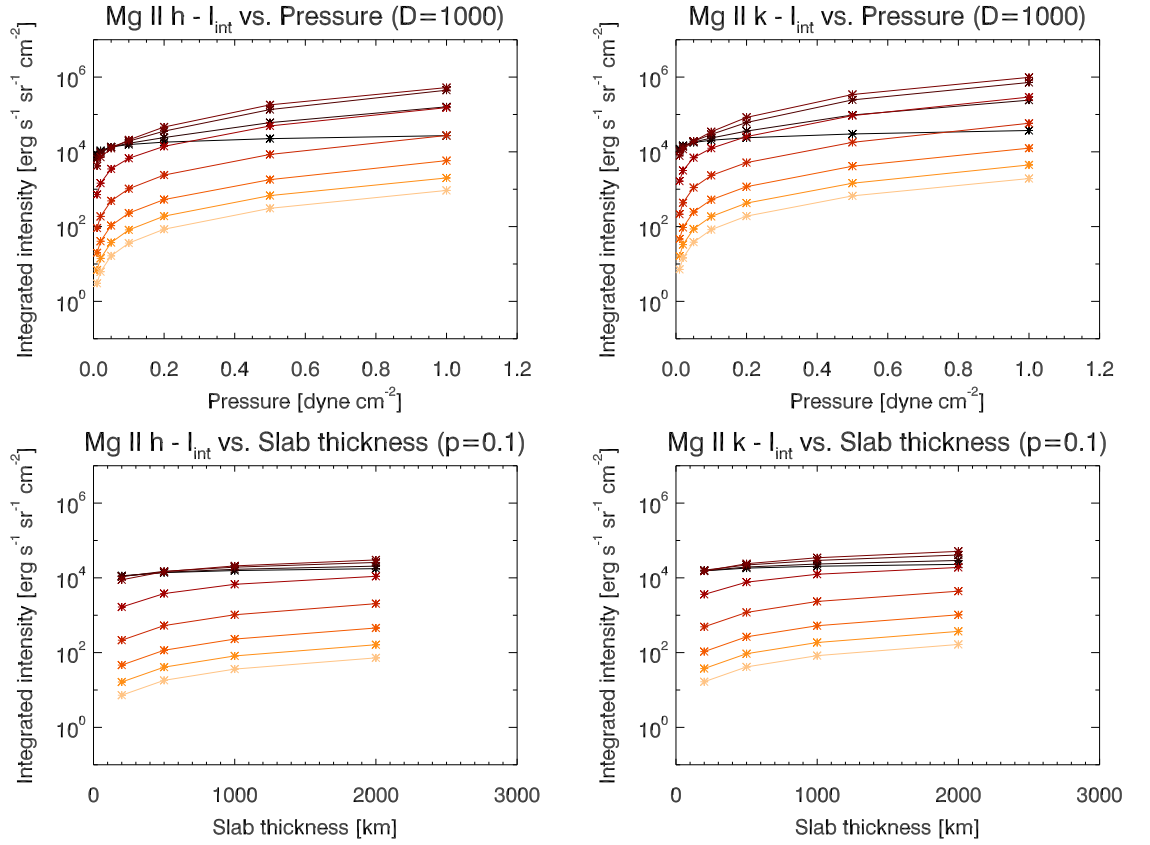


Figure 5.16: Plots of integrated intensity against gas pressure (*top*) and slab thickness (*bottom*). Pressure plots are for models with $D = 1000$ km, slab thickness plots are for models with $P = 0.1$ dyne cm^{-2} . In all cases colour indicates temperature, with lighter colours indicating higher temperatures. *Left:* Mg II h. *Right:* Mg II k.

30000 K are also considerable, with the population of the Mg II ground level being reduced to the stage that the plasma becomes optically thin at h and k wavelengths, and no central reversals are seen.

This grid of 252 models provides a large extension to the 27 models presented by [Heinzel et al. \(2014\)](#). However, models with higher temperatures (≥ 20000 K) present non-reversed profiles with extremely low peak intensity values, below 10^{-7} cgs Hz^{-1} and as low as 5×10^{-11} cgs Hz^{-1} for some of the highest temperature slabs. They also show no central reversal above 20000 K. This is contrary to observations, where central reversals are observed, and for non-reversed profiles line-centre intensities of more than 10^{-7} cgs Hz^{-1} are recovered (see Table 3.4 in §3.4.4, page 115). It is therefore inappropriate to consider models with extremely high temperatures in

comparison to observations, but it appears to be reasonable to consider models with temperatures up to ~ 20000 K.

5.6 PCTR models

The Mg II lines are formed at plasma temperatures around $10000 - 15000$ K, but an isothermal model with that temperature does not best describe the prominence – it is known from the hydrogen emission that there is much lower temperature plasma in the prominence too. Therefore it is more sensible to consider models that have a PCTR, a transition region between the cool, dense core and the hot, tenuous corona. The PCTR models here follow the temperature and pressure gradients described by [Anzer & Heinzel \(1999\)](#), and are dependent on the total column mass of the prominence, M . Equations 5.34 and 5.35 show the equations describing the pressure, $P(m)$, and temperature, $T(m)$, respectively, as a function of column mass m across the PCTR.

$$P(m) = 4P_c \frac{m}{M} \left(1 - \frac{m}{M}\right) + P_0 \quad (5.34)$$

$$T(m) = T_{\text{cen}} + (T_{\text{tr}} - T_{\text{cen}}) \left(1 - 4 \frac{m}{M} \left(1 - \frac{m}{M}\right)\right)^\gamma \quad (5.35)$$

The pressure at the outer edge of the PCTR is P_0 , while at the centre of the slab is $P_{\text{cen}} = P_c + P_0$. The central temperature is T_{cen} , and the temperature at the outer edge of the PCTR is T_{tr} . γ is a free parameter that dictates the size of the PCTR, and $\gamma \geq 2$. When γ is small, the PCTR is thick, and when γ is large, the PCTR is thin.

For the PCTR models considered here, the T and P values listed in Table 5.4 are taken to be the range of central pressure and temperatures, P_{cen} and T_{cen} respectively. The PCTR models do not require the input of a slab thickness, instead it needs a column mass for each model in the grid. For this the result of the isothermal isobaric models are used, as they provide a column mass as an output. Each combination of $T/P/D$ has an associated column mass, which can be entered directly to the PCTR input. These column mass values generally range from around 1×10^{-7} g cm $^{-2}$ to around 1×10^{-3} g cm $^{-2}$. T_{tr} is set with a value of 1×10^5 K, with P_0 taking a value of 0.01 dyne cm $^{-2}$. The parameter γ is varied, with three values for γ of 2, 5, and 10. Microturbulent velocity is kept at a constant 5 km s $^{-1}$ and prominence height is again 10000 km. A summary of the parameters used in the PCTR models is presented in Table 5.5. In total there are $252 \times 3 = 756$ possible unique PCTR models.

Table 5.5: Parameters used in the grid of models with a PCTR for Mg II. T_{cen} is central temperature, T_{tr} is temperature at the edge of the slab, P_{cen} is the pressure at the centre of the slab, P_0 is pressure at the edge of the slab, M is column mass, γ controls PCTR size, v_T is microturbulent velocity, and H is height above solar surface.

Parameter	Unit	Value
T_{cen}	K	6000, 8000, 10000, 15000, 20000, 25000, 30000, 35000, 40000
T_{tr}	K	100000
P_{cen}	dyne cm ⁻²	0.01, 0.02, 0.05, 0.1, 0.2, 0.5, 1
P_0	dyne cm ⁻²	0.01
M	g cm ⁻²	$1 \times 10^{-7} - 1 \times 10^{-3}$
γ		2, 5, 10
v_T	km s ⁻¹	5
H	km	10000

The resulting PCTR models can be compared to the isothermal isobaric models. Figure 5.17 replicates Figure 5.10 for models with a PCTR, but for each of the three γ values. As can be seen, the three left-hand panels follow the same trend as seen in the isothermal isobaric case, with the same power-law relationship between the h and k integrated intensities. The power-law indices for the three cases are 1.02 ($\gamma = 2$), 1.02 ($\gamma = 5$), and 1.01 ($\gamma = 10$). They also all show the ‘bump’ at around $10^4 \text{ erg s}^{-1} \text{ sr}^{-1} \text{ cm}^{-2}$, which can be explained in the same way as for the isothermal isobaric case. The right-hand panels, showing reversal of h versus reversal of k, have a slightly different spread of values to the isothermal isobaric models, however. The approximately linear trend is the same, but there are no models with higher (> 4) reversal levels in either line for any γ . This indicates that the inclusion of a PCTR inhibits the creation of extremely deep central reversals in the line profiles – the presence of a PCTR near the surface of the slab changes the source function in the slab due to the larger effect of collisional excitation.

Figure 5.18 shows plots of h and k integrated intensity against optical thickness

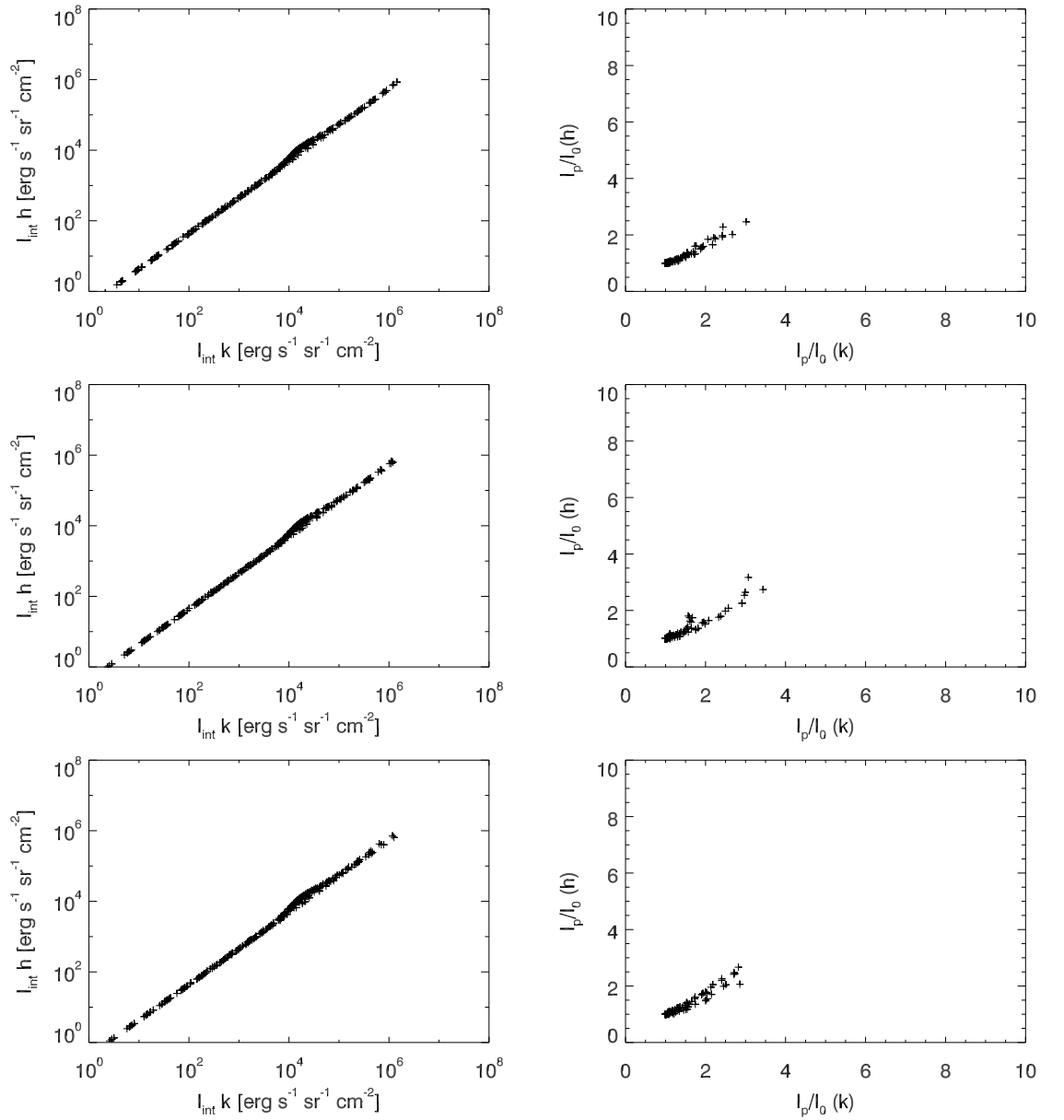


Figure 5.17: Correlations between observable parameters of the Mg II h and k lines: integrated intensities (*left*), and reversal level (*right*). Points are for each of the PCTR models. Axis scales are the same as in Figure 5.10. *Top:* $\gamma = 2$. *Middle:* $\gamma = 5$. *Bottom:* $\gamma = 10$.

for each of the three γ values. The optical thickness for the PCTR models is similar to that of the isothermal isobaric ones, but at high optical thicknesses there are some variations. In the PCTR models the higher optical thickness values are only

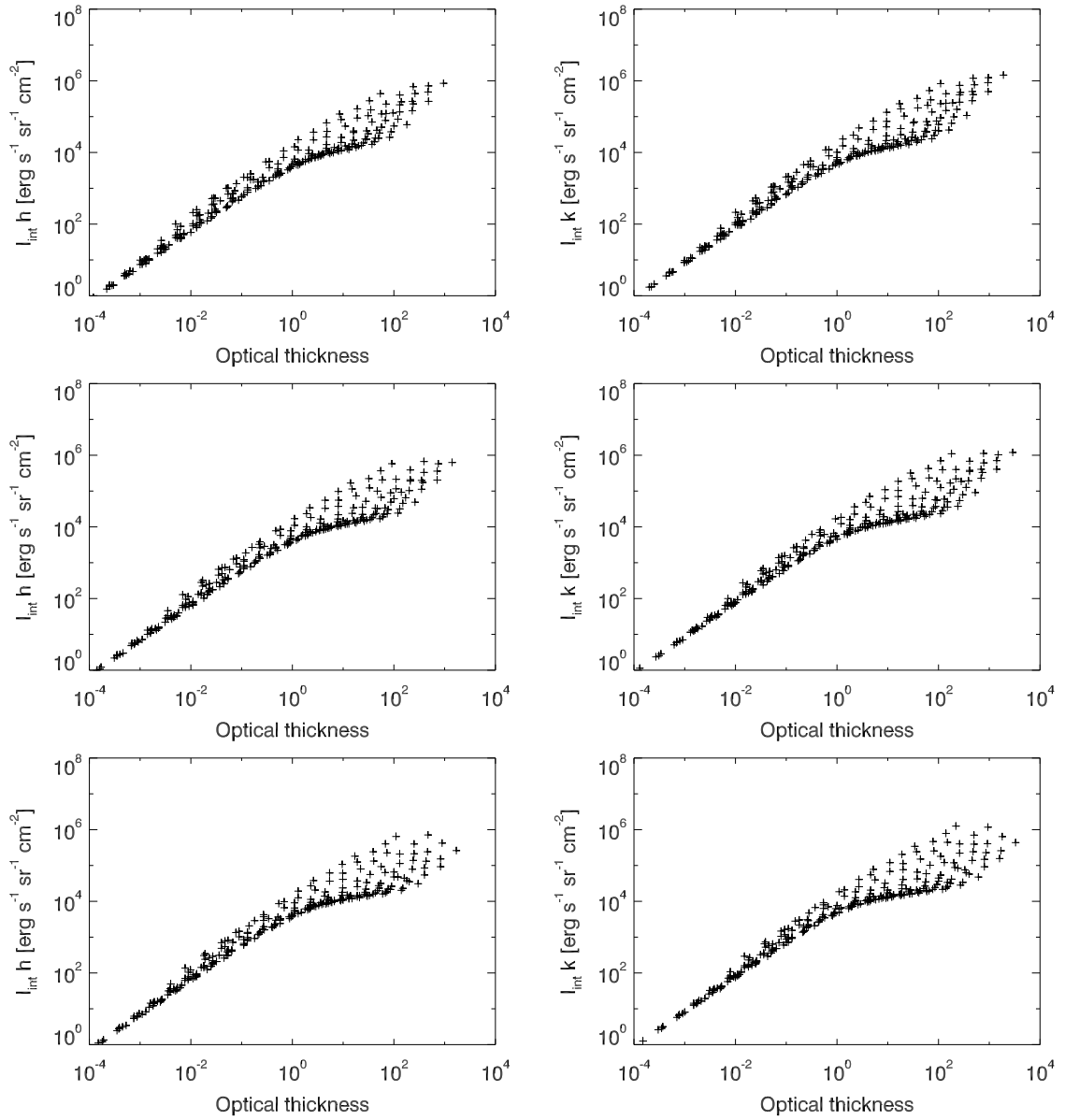


Figure 5.18: Plots of integrated intensity against optical thickness for the Mg II h (left panels) and k (right panels) lines for models with a PCTR. Top: $\gamma = 2$. Middle: $\gamma = 5$. Bottom: $\gamma = 10$.

found at higher integrated intensities – the relation is more linear and there is less ‘flattening’ of the scatter plots at $\sim 10^4 \text{ erg s}^{-1} \text{ sr}^{-1} \text{ cm}^{-2}$. This has an effect on the resulting line profiles, as can be seen in Figure 5.19. These profiles are only shown for $\gamma = 2$. Comparing these plots to the equivalent for the isothermal isobaric models (Figure 5.13), there are some notable differences, especially at lower

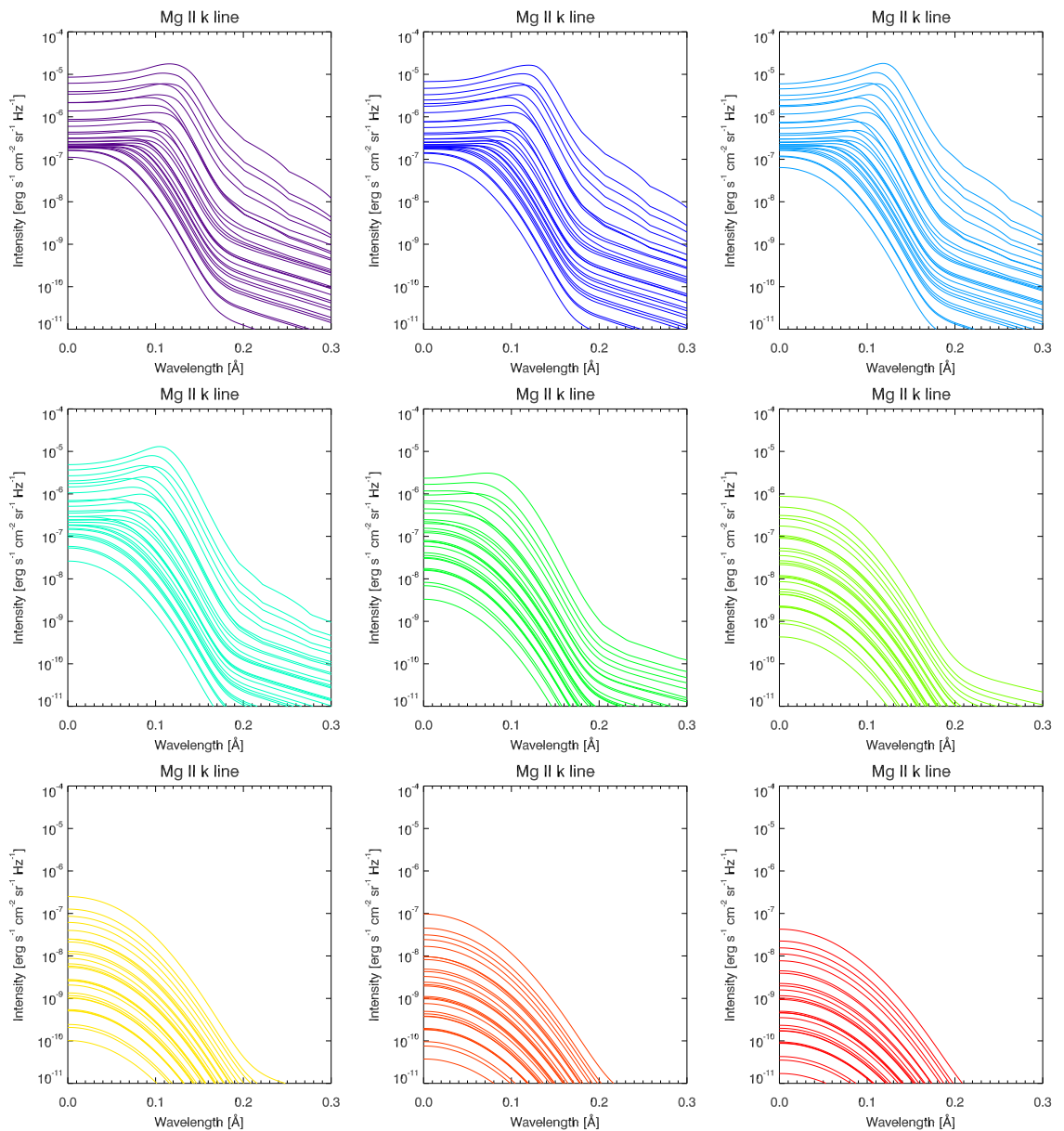


Figure 5.19: Emergent half-line Mg II k profiles for the PCTR models where $\gamma = 2$. Each panel/colour represents a different slab-centre temperature: 6000 K (purple), 8000 K (dark blue), 10000 K (light blue), 15000 K (teal), 20000 K (green), 25000 K (lime green), 30000 K (yellow), 35000 K (orange), and 40000 K (red). Intensities generally increase for higher pressure and slab thickness.

temperatures. Line centre intensities for models with low central temperature ($T_{\text{cen}} = 6000, 8000, 10000$ K) have a much larger spread of values for the PCTR

models than the isothermal models. This is caused by the fact that there is plasma with much higher temperatures than the stated core temperature in the slab, due to the presence of the PCTR. The parameter γ controls the size of the PCTR, with the size of γ inversely proportional to the size of the PCTR, so for $\gamma = 2$ the PCTR is relatively large. This means that there will be more high temperature plasma nearer the slab centre. As γ becomes larger the PCTR becomes smaller, and the solutions for high γ should converge to the isothermal case (Labrosse & Gouttebroze 2004). As a consequence, the central reversals seen in the h and k profiles should become deeper as γ increases. The effects of this are not seen, however, for the three values of γ considered here, as seen in the right panels of Figure 5.17.

5.7 Results from modelling

With the grids for both isothermal isobaric and PCTR models calculated, comparisons can be made – both between model parameters and between models and observations. Of course, these comparisons depend on having observable line features that can be measured by instruments such as *IRIS*. Using spectrometers, detailed line profiles of the Mg II lines are obtainable, meaning that line features (such as central reversals, line intensities, etc.) can be measured in prominences with a high spectral resolution. This section aims to explore whether any of these observables are related to the prominence parameters (temperature, gas pressure, slab thickness, optical thickness) in such a way that can be directly inferred.

5.7.1 Correlations

A natural question arises about how the observables from line profiles relate to the physical parameters of the prominence. To answer this, correlation plots can be made of observable characteristics, such as k/h intensity ratio or k (or h) line reversal level (also referred to generally as I_p/I_0 and specifically for h and k as h_2/h_3 and k_2/k_3 respectively), versus model parameters T , P , D , and τ .

The k/h ratio is defined as the ratio of integrated intensities of the Mg II k and h lines. It is one of the simplest parameters to calculate from observations, so understanding how it is related to the physical parameters of the plasma could potentially be very powerful for analysis. Figure 5.20 shows the k/h ratio against

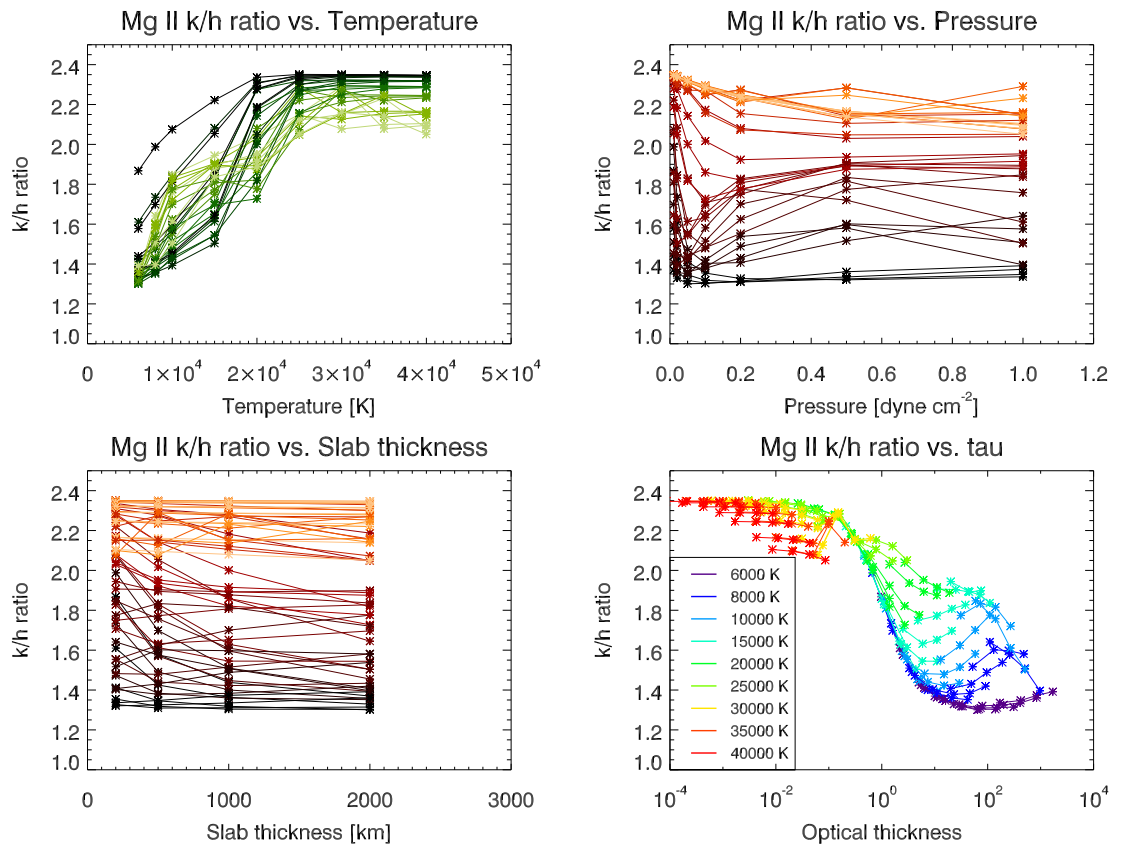


Figure 5.20: Plots of the Mg II k/h ratio against physical parameters for the isothermal isobaric models. *Top left:* k/h vs. T , colour scale indicates pressure. *Top right:* k/h vs. P , colour scale indicates temperature. *Bottom left:* k/h vs. D , colour scale indicates temperature. *Bottom right:* k/h vs. τ_h , colours indicate temperature.

temperature (*top left panel*), pressure (*top right panel*), slab thickness (*bottom left panel*), and optical thickness (*bottom right panel*) for results from the grid of 252 isothermal isobaric models. Each plot shows all models, with lighter colours indicating higher pressure values in the plot against temperature (*top left panel*), and lighter colour indicating higher temperature for the plots against pressure and slab thickness.

Plotting k/h against temperature (Figure 5.20, *top left panel*) reveals that, for all pressures, the k/h ratio increases approximately linearly with temperature up to around 25000 K, where the k/h ratio saturates between 2 and 2.4. This suggests that for lower (more realistic) temperatures the k/h ratio is a close analogy to temperature, regardless of slab thickness or pressure. The plots of k/h against pressure (Figure 5.20, *top right panel*) and slab thickness (Figure 5.20, *bottom left panel*) do not

show any significant correlations. There are some correlations but they are very much model dependent, so nothing general can be said about those relationships. The bottom right panel of Figure 5.20 shows the k/h ratio against optical thickness of the h line – k/h ratio against k line optical thickness is not shown as it is almost identical. There is a general trend that shows lower optical thickness has a larger k/h ratio, with higher optical thicknesses corresponding to lower k/h ratios. The transition between the two cases is at τ values around the transition between optically thin and optically thick. There are some diversions from this trend (so there is some model dependence) but generally the k/h ratio does appear to depend on the optical thickness, and when the lines are optically thin ($\tau < 1$) the k/h ratio is larger than 2.

As mentioned in §5.5.2, the reversal level of the h and k lines is heavily dependent on the optical thickness of the lines, as seen in Figure 5.12 (page 183). Exploring how the line reversal is related to other parameters is useful for narrowing down the physical prominence conditions that gave rise to the observed profiles. Figure 5.21 shows plots of h and k line reversal against temperature (*top panels*), gas pressure (*middle panels*), and slab thickness (*bottom panels*). The most informative of these is the reversal level vs. temperature plots (*top panels*). These show that the reversal of both h and k lines is heavily dependent on temperature, but also on gas pressure (shown by the green colour gradient). In terms of temperature the reversal level is greatest at around 8000 – 10000 K, dependent on the model. These plots also generally show that larger reversal levels indicate higher pressures. That sentiment is echoed in the middle panels of Figure 5.21, which show reversal level against pressure. The bottom panels of Figure 5.21 show that, for reversed profiles, the slab thickness does have an effect on the amount of reversal seen in the emergent profile, with the largest line reversals only being found for the thickest prominence slabs. Reversal level as a function of optical thickness was already discussed in §5.5.2 (Figure 5.12), where only models with optical thickness higher than ~ 10 show any central reversal.

It is useful to compare the results of isothermal isobaric models to those of models with a PCTR. Figures 5.22, 5.23, and 5.24 recreate the plots of reversal against optical thickness, k/h ratio against model parameters, and reversal against model parameters (respectively) for models with a PCTR. Panels are in the same order as those for the isothermal isobaric models (Figures 5.12, 5.20, and 5.21), with slab thickness in the isothermal isobaric plots being replaced by column mass, M , in the PCTR case.

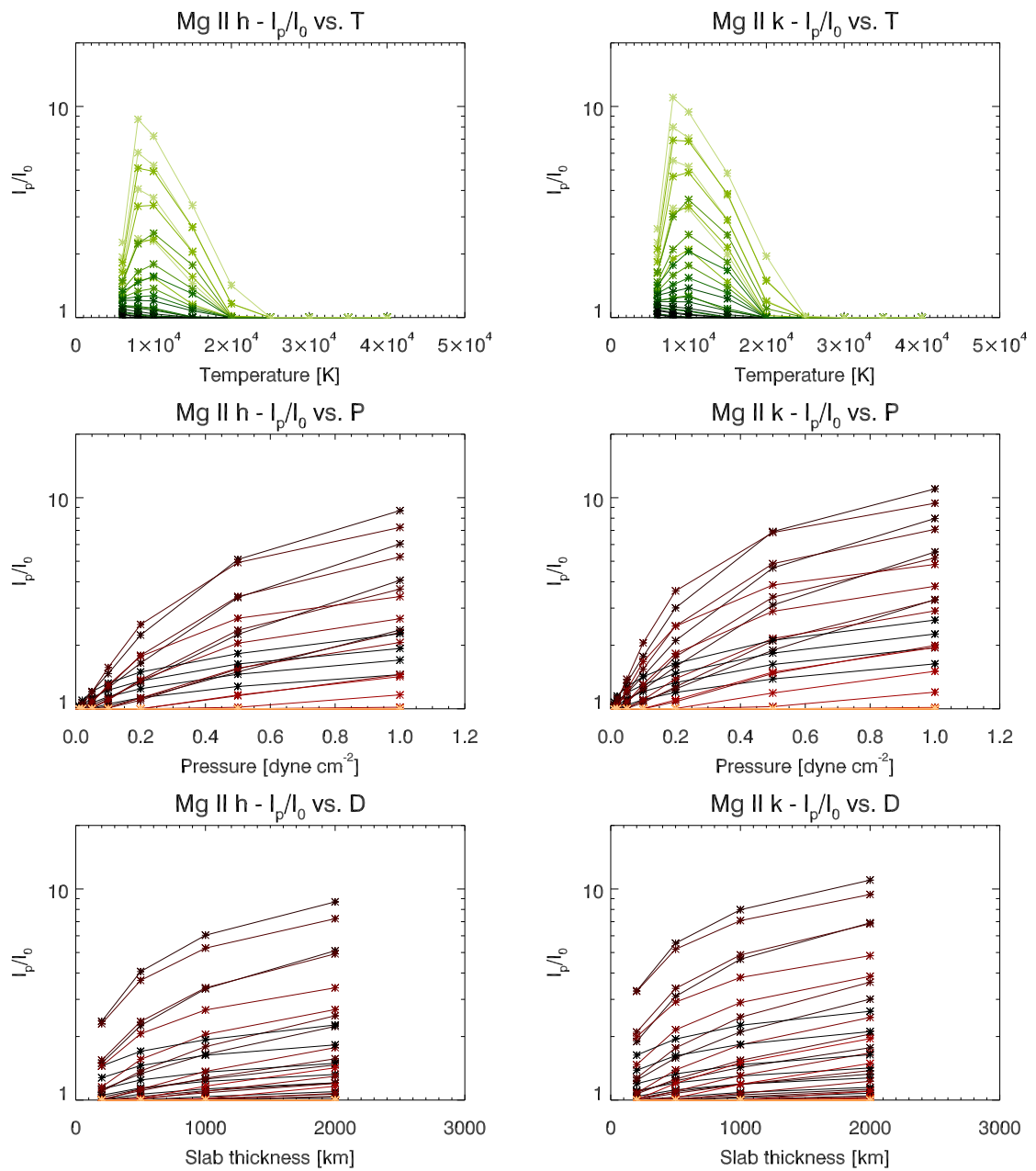


Figure 5.21: Plots of reversal level of the Mg II h (*left*) and k (*right*) lines against physical parameters for the 252 isothermal isobaric models. *Top:* Reversal vs. T , colour scale indicates pressure. *Middle:* Reversal vs. P , colour scale indicates temperature. *Bottom:* Reversal vs. D , colour scale indicates temperature.

Only the PCTR models where $\gamma = 2$ are presented here, as these represent the most extreme PCTR case.

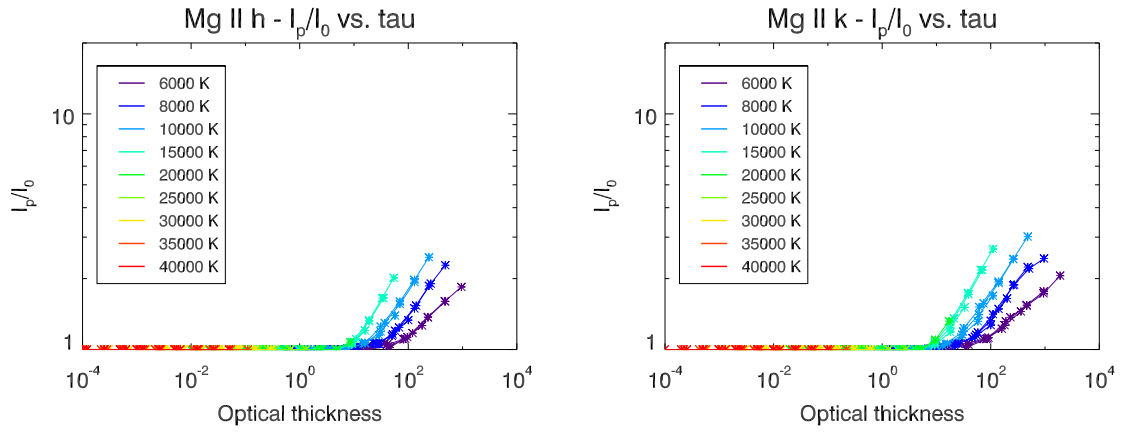


Figure 5.22: Reversal level against optical thickness for models with a PCTR and $\gamma = 2$. Colours indicates temperature. *Left:* Mg II h. *Right:* Mg II k.

Figure 5.22 shows reversal against optical thickness for the PCTR models. A similar pattern is found to the isothermal isobaric case, with reversals only appearing where $\tau > 10$ and for models with $T_{\text{cen}} < 25000$ K. The inclusion of a PCTR inhibits the creation of deep central reversals, as discussed in §5.6, and this can be seen by comparing Figures 5.12 and 5.22.

The k/h ratio for all models is plotted against model parameters (T_{cen} , P_{cen} , M , and τ_{h}) in Figure 5.23. The k/h ratio responds to temperature in a similar way to the isothermal isobaric case (Figure 5.23, *top left panel*), with an approximately linear relationship before saturation at a k/h ratio of between 2 – 2.4 for central temperatures above 25000 K. The central pressure has a larger effect on the k/h ratio for PCTR models than in the isothermal isobaric case (Figure 5.23, *top right panel*). At low temperatures, the k/h ratio increases with central pressure, whereas for high temperature models the opposite is true. It is also interesting to note that the observed values of k/h ratio in the prominence on 15 July 2014, 1.41, are only seen for the lowest pressure PCTR models, where $P_{\text{cen}} = 0.01, 0.02$ dyne cm^{-2} . The relationship between k/h ratio and column mass for PCTR models is considerably different to that of the k/h ratio and slab thickness for isothermal isobaric models (Figure 5.23, *bottom left panel*). This is due to the empirical relationship between column mass and slab thickness, which is dependent on the gas density (Anzer & Heinzel 1999). Notably the relationship between k/h and column mass for each temperature is similar to that of the k/h ratio and optical thickness (Figure 5.23, *bottom right panel*).

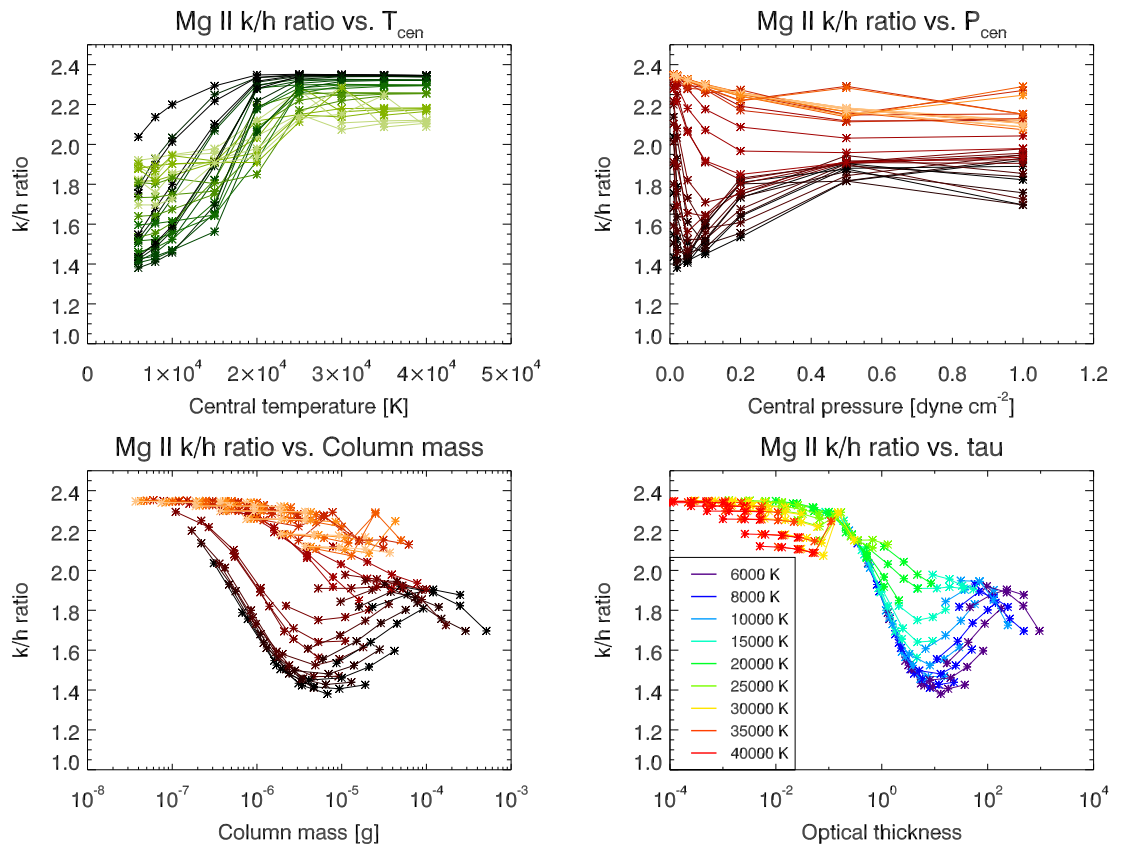


Figure 5.23: Plots of the Mg II k/h ratio against physical parameters for the PCTR models with $\gamma = 2$. *Top left:* k/h vs. T_{cen} , colour scale indicates pressure. *Top right:* k/h vs. P_{cen} , colour scale indicates temperature. *Bottom left:* k/h vs. M , colour scale indicates temperature. *Bottom right:* k/h vs. τ_h , colours indicate temperature.

The optical thickness affects the k/h ratio similarly in PCTR models to isothermal isobaric models. However, there are less models at the observed k/h ratio of 1.41 where the models are optically thick – that ratio appears to correlate only to a few models where the optical thickness is around 10, corresponding to those models with low P_{cen} , mentioned previously.

Figure 5.24 shows the reversal of the Mg II h and k lines against the other PCTR model parameters – central temperature (*top panels*), central pressure (*middle panels*), and column mass (*bottom panels*). Again, immediately noticeable in all plots is the lower maximum reversal level as compared to Figure 5.21 for isothermal isobaric models. Other than that, plots of reversal against T_{cen} and P_{cen} are nearly identical to the isothermal isobaric cases. Central reversals are largest for temperatures of

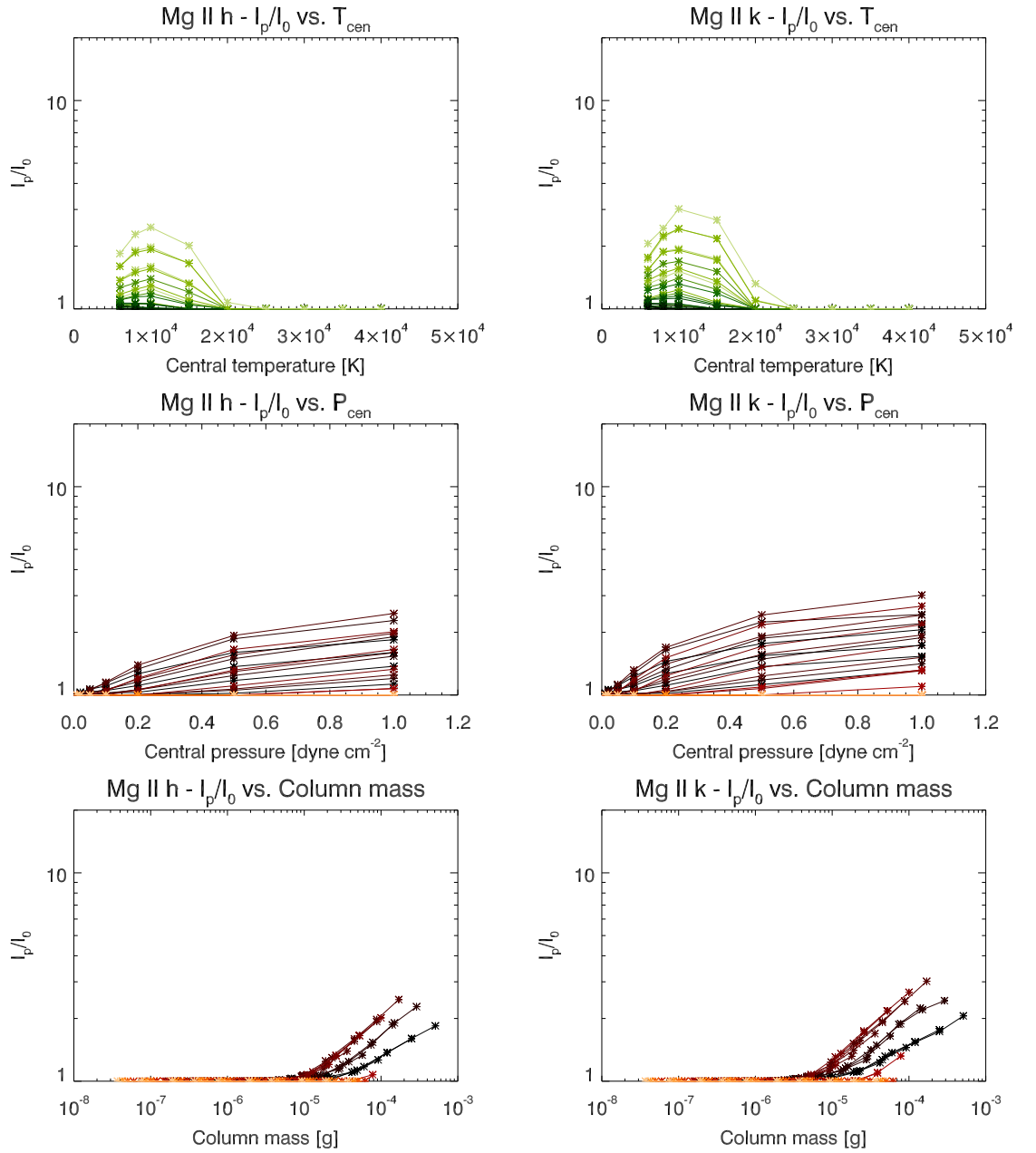


Figure 5.24: Plots of reversal level of the Mg II h (*left*) and k (*right*) lines against physical parameters for the PCTR models where $\gamma = 2$. *Top:* Reversal vs. T_{cen} , colour scale indicates pressure. *Middle:* Reversal vs. P_{cen} , colour scale indicates temperature. *Bottom:* Reversal vs. M , colour scale indicates temperature.

~ 10000 K and the level of reversal increases with pressure. Column mass is related to reversal level in a similar way to optical thickness. Only column masses above

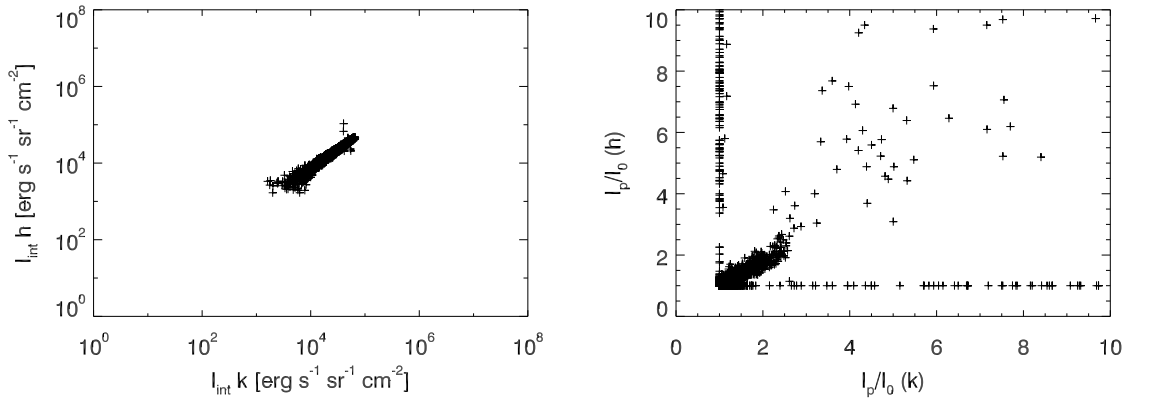


Figure 5.25: Correlations between Mg II h and k observed line parameters from *IRIS* profiles. Data is from the *IRIS* raster starting at 10:21 UT on 15 July 2014. *Left:* Correlation between integrated intensities of the Mg II h and k lines. Power law index is 0.99 *Right:* Correlation between Mg II h and k reversal level.

5×10^{-6} g have a central reversal, and again it is only lower temperature models that show any reversal.

5.7.2 Comparison to observations

The results from these model grids can be compared with observations, such as those made in 2014 with *IRIS* (Chapters 3 and 4). Comparison to the [Heinzl et al. \(2014\)](#) grid of 27 models (§3.4.4) revealed that, for expected prominence temperatures (6000 K) and slab widths (1000 km), the most reversed line profiles could have optical thickness as high as 820 with gas pressures of 0.5 dyne cm^{-2} . Using the grid of models computed here, a more detailed comparison can be drawn.

The first thing that can be checked is the observed relationship between the h and k line integrated intensities and the relationship between the reversal level of the h and k lines. Figure 5.25 shows these correlations using *IRIS* data from the raster starting at 10:21 UT on 15 July 2014. These plots are made from a selection of prominence pixels from the raster – some spicules and some corona was visible at the bottom and top the raster, respectively, so these parts were not included. Comparing the plots in Figure 5.25 to the results from the models in Figure 5.10 (isothermal isobaric) and Figure 5.17 (PCTR) there are some noticeable differences, but also some similarities. The left panel of Figure 5.25 shows the integrated intensity of h against

the integrated intensity of k. The overall trend of the line is nearly the same as found for the models (power law index = 0.99), but there is some deviation from a power law, especially at intensities lower than $10^4 \text{ erg s}^{-1} \text{ sr}^{-1} \text{ cm}^{-2}$ for both lines. There are also no observed profiles with both $I_{\text{int}}(\text{k})$ and $I_{\text{int}}(\text{h}) < 10^3 \text{ erg s}^{-1} \text{ sr}^{-1} \text{ cm}^{-2}$, nor with both $I_{\text{int}}(\text{k})$ and $I_{\text{int}}(\text{h}) > 10^5 \text{ erg s}^{-1} \text{ sr}^{-1} \text{ cm}^{-2}$. This indicates that models with intensity values in those ranges are not accurate. Looking again at Figures 5.15 and 5.16 (similarly for PCTR models) indicates that the models where $I_{\text{int}}(\text{k}) < 10^3 \text{ erg s}^{-1} \text{ sr}^{-1} \text{ cm}^{-2}$ are those with high central temperatures ($> 25000 \text{ K}$). This matches the indication from line profile behaviour at high temperatures (discussed in §5.5.2) where, contrary to observations, there are no reversed profiles.

The right panel of Figure 5.25 shows the reversal of h against the reversal of k from the *IRIS* observation. The majority of the points from the *IRIS* raster do show a similar relationship between the reversal of h and the reversal of k – a roughly linear relationship with most of the points clustered at reversal values $\sim 1 - 2$. Immediately noticeable, however, are parts of the prominence where one of k or h are reversed but the other line is not. These pixels create the horizontal and vertical lines at $I_p/I_0 = 1$, which are not seen in the right panels of Figure 5.10 or 5.17 – this indicates that, in the models, whenever one of h or k is reversed, so is the other. Neither the isothermal isobaric nor the PCTR models can account for this observed phenomenon. There are also a number of points scattered at higher reversal levels, and the plot in Figure 5.25 cuts off many of the points that show extremely large central reversals in either line. These extreme cases are again not recreated by any of the current models, suggesting that improvements to the models need to be made.

The divergence of the ratio of intensities from a power law at low h and k intensities in the observed profiles, and the differences between the observed and modelled h to k reversal level, indicates that there are still inaccuracies in the models. These discrepancies, along with the complexity of observed line profiles, highlight the fact that more complex prominence models are needed to account for observed profiles, with multi-thread models being the natural next step to this. The multi-thread models presented by [Gunár et al. \(2007, 2008\)](#) can recreate some of the observed asymmetries of the Ly- α line by using threads with random small velocities along the line of sight, which could be implemented in this code for Mg II – the asymmetries observed in the Mg II h and k lines are similar to those seen in Ly- α .

5.8 Conclusion

This chapter is dedicated to developing prominence models of the Mg II h and k resonance lines. With the large amount of high spatial, spectral and temporal resolution data available from the *IRIS* satellite, understanding the formation and behaviour of these lines in prominences has become extremely important. Using a 1D radiative transfer code for prominences, PROM, from Gouttebroze et al. (1993, GHV) – updated for hydrogen by Gouttebroze & Labrosse (2000), and altered to include calcium (Gouttebroze et al. 1997) and helium (Labrosse & Gouttebroze 2001) – the model for the emission and absorption of magnesium in prominence slabs has been constructed. Due to similarities in the atomic structure of Mg II and Ca II it was the calcium code developed by Gouttebroze et al. (1997) that was used as a basis for this work. Since the launch of *IRIS*, the Mg II h and k lines have been well studied and modelled in the chromosphere (Leenaarts et al. 2013a,b) and in flares (e.g. Kerr et al. 2016), but recent prominence models have been more limited (Heinzl et al. 2014, 2015). The Heinzl et al. (2014, HVA) grid of prominence Mg II models represents a good basis, which explored 27 isothermal isobaric models and investigated the inclusion of a PCTR to some of their models too. The goal of the work presented in this chapter is to extend that grid of models in order to more fully understand the behaviour of the Mg II h and k lines.

The atomic model of magnesium used here has been constructed using atomic data from a number of sources (see Table 5.1, page 169). Here a five-level plus continuum Mg II atom is used, and level population due to transitions from Mg I is not considered. Incident radiation has been calculated using *IRIS* quiet-sun profiles for the Mg II h and k lines, as well as continuum-level intensities for the three Mg II subordinate lines.

In order to understand if the updates to the PROM code provide reasonable results, a direct comparison to the HVA grid of isothermal isobaric models can be made. This is done by solving the radiative transfer and statistical equilibrium equations for prominence models with input parameters the same as those used in HVA: $T = 6000, 8000, 10000$ K, $P = 0.01, 0.1, 0.5$ dyne cm⁻², $D = 200, 1000, 5000$ km. Emergent line profiles and calculated line optical thicknesses can then be compared, which reveal that there are some differences between the models computed here and those from HVA. In low T and low P cases there is no difference between emergent

profiles from the two codes but in other cases, especially for high pressure models, there are 30–40% differences between this code and the results from the HVA models. The recovered optical thicknesses are more closely matched to those from HVA, with less than 10% differences for all models. The reason for the differences is not entirely clear. Although care was taken to use the same atomic data as in HVA, it was not always possible. There are also differences in the incident radiation between the two codes – HVA used RASOLBA profiles whereas *IRIS* has been used here – but the fact that the lower P/D models are similar indicates that the incident radiation is not the cause of the differences. For low P/D values the emergent profile is more heavily influenced by the incident radiation, so any changes to that incident profile would be noticeable in the emergent emission. Regardless of the differences between the resulting profiles, the trends seen in the HVA grid of models are reproduced here, so it is worth investigating an extended grid of 1D isothermal isobaric and PCTR models using this code.

An extended grid of 1D models was designed in order to investigate the effects of higher temperatures and pressures on the emergent h and k line profiles. Temperatures of 6000, 8000, 10000, 15000, 20000, 25000, 30000, 35000, and 40000 K were used to achieve this, along with gas pressures of 0.01, 0.02, 0.05, 0.1, 0.2, 0.5, and 1 dyne cm⁻² and slab thicknesses of 200, 500, 1000, and 2000 km. There are therefore 252 possible parameter combinations for these models. The aim is then to find links between observable line parameters (line integrated intensity, k/h ratio, reversal level) and the model parameters T , P , D , and τ . The integrated intensity of the h and k lines is closely related for all models, displaying a power law relationship with a small ‘bump’ which is caused by the differences in the optical thickness of the h and k lines. Line reversal of both h and k is found to be closely related to optical thickness, with only models where $\tau > 10$ showing any central reversal of the lines. Integrated intensity is also related to the optical thickness of the lines for both h and k, with the relationship changing at the transition between optically thin and optically thick.

Investigating higher temperature models ($T \geq 15000$ K) reveals a number of things. Firstly, there are no central reversals found for models above 20000 K. Secondly, the line centre intensity decreases with temperature, down to intensities that are not observed in real prominences (within the instrumental sensitivity of *IRIS*). The cause of this decreased intensity is the increased amount of ionisation to

Mg III at these temperatures. Therefore there is relatively less Mg II in the relevant energy states to produce photons that contribute to the h and k lines, causing a lower intensity in those lines. This indicates that extending the HVA grid of isothermal isobaric models much past ~ 20000 K is not necessary, as the computed emergent line profiles do not reflect those observed. However, it would be useful to have a finer grid of models between $\sim 6000 - 15000$ K to properly investigate the differences in low-temperature cases.

Models with a prominence-corona transition region (PCTR) represent a significant improvement on isothermal isobaric slab models due to their temperature and pressure gradients between the cool prominence core and the hot surrounding atmosphere. Temperature and pressure gradients from Anzer & Heinzel (1999) are used here to represent the PCTR. The Mg II h and k lines from PCTR models show similar inter-line relationships, and also similar correlation with the line optical thickness to the isothermal isobaric cases. Considering the emergent line profiles themselves there are some notable changes. Primarily at low central temperatures (< 10000 K) there is a much larger range of line-centre intensities recovered than in the isothermal case with the same central temperature. This is caused by the presence of higher temperature plasma in the PCTR, which causes more collisional excitation within the slab.

Some correlations are found between observable parameters of the Mg II h and k lines (namely the k/h ratio and the reversal level) and the temperature of the plasma slab, for both isothermal isobaric and PCTR models. For all pressures and slab thicknesses, the k/h ratio increases approximately linearly with temperature, up to a point where the k/h ratio saturates somewhere between 2 and 2.4, depending on the model. There is also some correlation between the k/h ratio and the line optical thickness. In the isothermal isobaric case, for optically thin slabs (at higher T) the k/h ratio is high, around 2 to 2.4, switching around $\tau = 1$ to lower values of around 1.4, mostly for low T models. There are models that deviate from this trend, but generally there is a correlation seen. This is interesting in comparison with the *IRIS* observations presented in §4.3.2, where k/h values closely scattered around a value of 1.41 were found. From the model results shown here this indicates that the observed profiles are all optically thick, and the prominence temperatures are low ($\sim 6000 - 8000$ K). A similar trend is seen for models with a PCTR, but there is some deviation for models with high optical thickness. The observed trend indicates that

only a small number of PCTR models can explain the observed k/h ratio of 1.41 – those with low pressure (0.01 or 0.02 dyne cm^{-2}) and an optical thickness of around 10. It remains to be seen which of these scenarios is more likely, however the PCTR models are generally better at explaining observed line profiles (Schmieder et al. 2014; Heinzel et al. 2015).

Reversal level of the h and k lines can also be used as an indicator of both the plasma temperature and pressure, with the largest peak-to-core ratios coming from models (isothermal isobaric and PCTR) with temperatures of 8000–10000 K. Higher pressure models generally show higher reversal levels too, however there is some model dependence of this.

Finally, the model observable parameters are compared to actual prominence observations from *IRIS*, finding that there are some significant deviations from the results of both isothermal isobaric and PCTR models. The plot of observed h to k integrated intensity shows a similar trend at higher intensity values ($> 10^4 \text{ erg s}^{-1} \text{ sr}^{-1} \text{ cm}^{-2}$), but at lower intensities there are diversions from the power law described by the model intensities. There are no observed profiles where both $I_{\text{int}}(k)$ and $I_{\text{int}}(h) < 10^3 \text{ erg s}^{-1} \text{ sr}^{-1} \text{ cm}^{-2}$ indicating that models which show h and k intensities in that region are not representative. The models that do have those values of $I_{\text{int}}(k)$ and $I_{\text{int}}(h)$ are mostly those with temperatures $> 25000 \text{ K}$, which do not match with observations in other ways previously discussed. There are also deviations between observed and modelled reversal levels of the h and k lines. No models are recovered where one of h or k is reversed and the other is not, however this situation is seen in the *IRIS* data.

These models represent a significant simplification of the physical conditions of prominence plasma, but are nonetheless a useful tool for investigating the prominence conditions with respect to the observed $\text{Mg II } h$ and k profiles. Although there is some improvement in moving from isothermal isobaric models to those with a PCTR, there are still a number of situations observed by *IRIS* that cannot be explained by these simple models. It will therefore be necessary to move to more complex multi-thread models for future comparisons to observations. The 1D isothermal isobaric and PCTR models presented here can be used as a base for these more complex prominence models, including ones that include 1D/2D multi-thread structures to attempt to replicate the fine structure and small-scale prominence dynamics that are observed (Gunár et al. 2007, 2008; Labrosse & Rodger 2016).

Chapter 6

Conclusions

Solar tornado-like prominences have presented one of the biggest mysteries of recent years in the field of prominence research. Although tornado prominences have been identified for a long time (Pettit 1925, 1932), the recent interest in them has sparked debate as to their true nature (e.g. Su et al. 2012; Li et al. 2012; Orozco Suárez et al. 2012; Wedemeyer et al. 2013a; Panasenco et al. 2014; Su et al. 2014; Levens et al. 2015, 2016a; Schmieder et al. 2017b). Are they rotating? What is the magnetic structure? How is the plasma behaving? Are the plasma motions linked to the magnetic field? These questions require answers if the apparent tornado motions are to be quantified and fully understood, and it is these questions that this thesis has aimed to address. Another important question regarding tornadoes is: can they trigger prominence eruptions? Twisting motions have been observed in prominence eruptions (Nicholson 1944; Li & Zhong 1997), and quiescent tornadoes have been observed to erupt suddenly (Su et al. 2012), so understanding tornado-like prominences has become important in relation to the Sun-Earth interaction through space weather.

Tornado plasma diagnostics: Tornado-like prominences are a relatively common occurrence, but targeting them with telescopes and satellites that have a small field of view is challenging, because predicting their appearance in advance of them crossing the limb is difficult. Therefore there have been relatively few successful dedicated tornado studies. The first in the satellite era of solar astronomy was made in 2013 using the EIS spectrometer on *Hinode*, which was studied by Su et al. (2014) and

forms part of the analysis presented here in Chapter 3 and published in [Levens et al. \(2015\)](#). That observation, on 14 September 2013, caught a tornado at the west limb of the Sun over the course of one raster and a three hour sit-and-stare. [Su et al. \(2014\)](#) had previously shown that the tornado column appeared to be rotating by measuring the Doppler shift of the Fe XII 195.12 Å and Fe XIII 202.04 Å lines, finding that there was a split Doppler pattern across the tornado's axis which persisted for at least three hours. The analysis presented in Chapter 3 looks at that observation in more detail, showing a range of plasma diagnostics that were available from the EIS study. Beginning with a Doppler shift analysis, the results of [Su et al. \(2014\)](#) have been recreated for the high-temperature lines that they used (≥ 1.5 MK), and extended to lower temperatures of around 1 MK with the Fe IX 197 Å line. All lines formed above 1 MK, where the tornado is seen as a dark column against the bright background corona, show the split Doppler pattern. At lower temperatures there is no clear structure in the Doppler maps. It is recognised that the spectral lines formed below 1 MK observed by EIS mostly are weak in prominences or are heavily blended, so Doppler shifts cannot be derived from them with enough precision for a detailed velocity study. It is also important to note that the split Doppler pattern seen in the EIS raster could be the result of an instrumental effect. [Young et al. \(2012\)](#) have reported that an artificial Doppler shift could be introduced to EIS data by a tilted and elliptical point spread function, similar to that seen in *SOHO/CDS* ([Haugan 1999](#)). The effect of this is an instrumental Doppler shift on the order of 5 km s^{-1} , which would be created with a pattern exactly like those seen in the tornado observed by EIS. However, in some lines the observed Doppler shifts are on the order of 15 km s^{-1} , so even removing the 5 km s^{-1} instrumental shift the pattern would still be seen. It is worth noting the results of [Schmieder et al. \(2017b\)](#), where they showed that certain cuts through a tornado (observed in H- α) could give the impression of prolonged rotation, but when considered as a whole the Doppler pattern suggested slow oscillation.

Other plasma diagnostics are available from the EIS observation. Electron densities have been calculated using density-sensitive line ratios. Using this method, densities of $\log n_e = 8.5 - 9$ are recovered in the tornado from lines formed at 1.5 MK, and it is found that the density is generally lower in the tornado than in the surrounding corona. This scenario points towards a situation where there is a 'sheath' of hot plasma surrounding the tornado at a similar temperature to the corona but

at a lower density. The range of electron densities recovered is at the lower end of those found previously in prominences, but at a much higher temperature than is typically probed for prominence diagnostics. Non-thermal line widths have been investigated for the Fe XII 195.12 Å and Fe XIII 202.04 Å lines, which show those lines are slightly broader in the tornado than in the nearby corona. This indicates some additional broadening mechanism at the tornado. A different magnetic field structure in the tornado than the surrounding corona could cause this broadening, where a ‘turbulent’ magnetic field component as suggested by [Schmieder et al. \(2014\)](#) could cause additional non-thermal broadening. Another possibility is the presence of Kelvin-Helmholtz instabilities at the boundary between the tornado and the corona. It has been found that these instabilities could cause non-thermal broadening ([Zaqarashvili et al. 2015](#)) at the boundary between two plasmas of different densities, where there is a shear velocity between them (as might be expected at the boundary between a rotating tornado and the corona surrounding it). Both of these possibilities would require further studies using other instruments to investigate – high resolution spectroscopy of (e.g.) H- α should also show line broadening if a Kelvin-Helmholtz instability exists between the tornado and the corona, and improved magnetic field observations from CLASP ([Kano et al. 2012](#); [Kobayashi et al. 2012](#)) or the updated THEMIS ([Gelly et al. 2016](#)) will help to improve our understanding of the tornado magnetic field.

The EIS observation from 14 September 2013 was also used to calculate the differential emission measure (DEM) for the first time in a tornado-like prominence, along with DEMs from points in the prominence and in the corona nearby. Nine EUV spectral lines were used to constrain the DEM, formed at temperatures from $\log T = 5.4 - 6.2$. The DEMs reveal that the tornado and prominence body have more emission at lower plasma temperatures than the corona at similar distances from the solar limb, as is expected. They also show that there is slightly more emission at higher temperatures along the tornado and prominence body lines of sight, supporting the idea that the velocity, density, and non-thermal line width measurements are coming from the tornado itself. However, it must be noted that the DEM is very sensitive to emission from hot loops in the foreground of the prominence, so the presence of any such loops could be influencing the calculated DEM. No hot loops were detected in the foreground of the 14 September 2013 dataset, but the DEM technique can require a careful selection of points to avoid such foreground

structures.

Despite the wealth of information available from the EIS observation alone, there were many questions that remained open on the low temperature plasma and the structure of the magnetic field. These questions required further, multi-instrument studies to answer. A coordinated observing campaign was run in 2014 using the *Hinode* and *IRIS* satellites along with the THEMIS telescope in the Canary Islands. The spectrometer of *IRIS* allows for observations of lines formed at chromospheric plasma temperatures, and THEMIS can provide spectropolarimetry of prominence structures, allowing for a measurement of the magnetic field. The second part of Chapter 3 presents plasma diagnostics from an observation of two tornado-like prominence legs on the 15 July 2014, mostly concentrated on the Mg II h and k lines from *IRIS*. The results of this part of Chapter 3 (and the first part of Chapter 4) have been published in [Levens et al. \(2016a\)](#). Those optically thick lines are formed at chromospheric temperatures and are bright in prominences, but show much more complex profiles than the predominantly optically thin coronal emission observed by EIS. A first estimate of the Doppler velocity has been made using a Gaussian fit to the Mg II k line, which indicates that the overall line shifts are relatively small, on the order of $\pm 5 \text{ km s}^{-1}$. No evidence of a rotational pattern is found in the *IRIS* Mg II lines. It is clear, however, that a simple Gaussian approximation for the Mg II h and k lines is not valid for most pixels, and to properly understand the profiles seen requires a model that includes full treatment of the radiative transfer and statistical equilibrium in the prominence. A small sample of 1D isothermal isobaric models was presented by [Heinzel et al. \(2014\)](#), which gives a grid of models to compare the observed line profiles to. The model parameters give an estimate of the physical parameters necessary to create the observed line profiles. The central reversal of the Mg II h and k lines is sensitive to the model parameters, and comparing the observed line reversals to the grid of models suggests that the prominence on 15 July 2014 has high optical thickness, up to 820 for the k line in regions with the highest reversal. These highly reversed profiles also suggest a relatively high gas pressure, around 0.5 dyne cm^{-2} . Parts of the prominence with lower reversal levels suggest optical thicknesses nearer 100 and gas pressures around 0.1 dyne cm^{-2} . This is the first time highly reversed profiles have been reported in the Mg II lines from *IRIS* in a prominence – previous prominence observations with *IRIS* have only shown non-reversed profiles ([Schmieder et al. 2014](#); [Vial et al. 2016](#)). There are also a large

number of pixels that show non-reversed profiles in the prominence on 15 July 2014, and in these regions the optical thickness and gas pressure could be much lower. The complexity of the observed profiles suggest that the simple grid of 1D isothermal isobaric models from [Heinzel et al. \(2014\)](#) does not fully represent the physical characteristics of the real prominence, so larger grids and more complex models are required to explain the observations.

Tornado magnetic field: The magnetic field in the tornado-like prominence observed on 15 July 2014 is discussed in Chapter 4. Observations from THEMIS were used to derive the magnetic field strength and orientation in the tornadoes from the polarisation of the He I D₃ line at 5876 Å. Magnetic field strengths of up to 60 G are seen in places in the tornadoes, with the average field strength being lower, around 30 G. The magnetic field inclination is found to be mostly around 90° everywhere in the tornadoes, horizontal with respect to the solar surface. The azimuth, with respect to the line of sight, is between 60° and 100°. These results are contrary to the vertical or twisted tornado magnetic field models that have been suggested ([Su et al. 2012, 2014](#); [Luna et al. 2015](#)), indicating that the more likely scenario is that of the plasma being supported against gravity in dips in the field ([Aulanier & Demoulin 1998](#); [Heinzel & Anzer 1999](#)). It also gives counter-evidence against the rotational model of tornadoes, suggesting instead that the perceived rotation seen in AIA movies is due to the projection effect of oscillations onto the plane of sky, similar to the LALO model explored by [Luna et al. \(2016\)](#). This conclusion is enhanced by the tornado observation of [Schmieder et al. \(2017b\)](#), where it was found (from Doppler shifts in the H- α line) that apparent tornado-like velocity patterns were transient, and that the evolution of the Doppler pattern suggests slow oscillation rather than rotation.

Comparing plasma and magnetic field: Although the evidence from the 15 July 2014 observations suggests that the tornadoes are not rotating, it is still important to understand the plasma motions seen, and how they are related to the magnetic field in the prominence. The second part of Chapter 4 investigates the relationship between observable parameters from the *IRIS* and *Hinode* satellites and the magnetic field parameters observed by THEMIS, and this work has recently been published in [Levens et al. \(2017\)](#). Plasma motions and the magnetic fields are closely linked,

so understanding that link is important in interpreting the motions observed. A better knowledge of how they are related can also help to constrain prominence models, which can in turn give a more accurate view of the physical parameters of the prominence. In order to investigate correlations between parameters on a pixel-by-pixel basis, a robust spatial co-alignment has been performed on the data sets. Although the spatial offsets between instruments can be reconciled using post-processing techniques, the temporal offset between the space-based satellites and THEMIS remains. However, it is noted that the morphology of the prominence does not change dramatically in the hours between the *IRIS/Hinode* observations and the THEMIS data. This is a quiescent prominence, so the problem of the temporal offset is minimal because the prominence was stable as it crossed the limb. For a more dynamic prominence, such as an eruption or active prominence with fast flows, any temporal offset between data sets will have more of an impact on the analysis.

Comparisons between the magnetic field parameters from THEMIS (field strength, inclination, and azimuth) and observable parameters from the Mg II lines from *IRIS* (reversal level, k/h ratio, and k_3 Doppler shift) have been investigated, but no correlations were found. The electron density from the EIS observation has also been compared to the magnetic field parameters from THEMIS and the Mg II parameters from *IRIS*, but again no correlations were found. The lack of correlations between data sets for the 15 July 2014 prominence highlights several factors that need to be considered when comparing data sets from different instruments at different wavelengths. Comparing lines formed at different temperatures, or with different optical thicknesses, is to compare emission from different parts of the solar atmosphere/prominence. Any comparison between data sets must therefore make careful consideration of these factors.

Despite there not being any notable correlations between the magnetic parameters and the observable plasma parameters for the 15 July 2014 prominence, the analysis presented in Chapter 4 and [Levens et al. \(2017\)](#) still provide detailed measurements of the observed parameters from the various instruments. The magnetic field is found to be stronger in the tornadoes, with an average value of 30 G, than in the rest of the prominence, which has an average value of around 20 G. The field inclination is horizontal everywhere, again not showing any signs of the vertical, twisted field that was outlined by [Su et al. \(2012\)](#).

Line parameters from the Mg II h and k lines observed by *IRIS* can provide

comparisons to prominence models such as those by [Heinzel et al. \(2014\)](#). The reversal of the Mg II k line varies from non-reversed to a peak-to-core ratio of 2.8. It is found that the reversal is generally higher in the tornadoes than in the rest of the prominence, with average values of 1.23 and 1.14 respectively. Regions of the prominence with a large Mg II k central reversal (> 2) have a high optical thickness. It has been found, however, that the Mg II lines can be optically thick in prominences even when no reversal is present ([Heinzel et al. 2015](#)). The k/h integrated intensity ratio is found to have a mean value of 1.41 everywhere, which is similar to previously observed prominences with *IRIS* (e.g. [Schmieder et al. 2014](#); [Vial et al. 2016](#)). Optically thin, collisionally excited emission would give a k/h ratio of 2 ([Leenaarts et al. 2013a](#)), so any departure from this ratio indicates a departure from the optically thin case. The position of the central reversal has been used to infer a Doppler velocity for the frontmost layers of the prominence. The Doppler shifts are found to be between $\pm 10 \text{ km s}^{-1}$ everywhere, a similar order to the Doppler shift derived from the Gaussian approximation in Chapter 3.

The electron density in one of the tornadoes observed on 15 July 2014 has been calculated in the same way as in the tornado of 13 September 2014 in Chapter 3, using lines from *Hinode*/EIS. For plasma temperatures of 1.5 MK the electron density is found to have mean values of $\log n_e = 8.98$ and $\log n_e = 9.06$ in the tornado and surrounding corona respectively. Those values are similar to those found for the tornado of 13 September 2014.

The coordinated observations presented in Chapters 3 and 4 represent the first multi-instrument observing campaign that was dedicated to investigating the plasma and magnetic field structure of tornado-like prominences. There were a number of limitations to that study, however, so future observing campaigns using more instruments would be beneficial in fully understanding the link between the plasma and the magnetic field in tornado-like prominences. Using future observations of the CLASP sounding rocket instrument ([Kano et al. 2012](#); [Kobayashi et al. 2012](#)) could provide plasma and magnetic field measurements in the Ly- α line. These would be complementary to THEMIS observations in He I D₃, especially when THEMIS becomes operational again with its new adaptive optics system ([Gelly et al. 2016](#)). New *IRIS* studies could also be beneficial, focusing on the C II and Si IV lines which are in emission in prominences but have not been explored for their diagnostic potential. Creating new models for these lines in prominences will become necessary

if such observations are made, as it has been with Mg II in order to explain the complexity of the observed line profiles.

Prominence Mg II models: The high resolution spectra of the Mg II h and k lines observed by *IRIS*, presented in Chapters 3 and 4, underline the necessity of having prominence models capable of explaining the complex range of profiles seen. Chapter 5 presents an update to the PROM code originally written by Gouttebroze et al. (1993, GHV) to include a model for Mg II emission in prominences. The code is a 1D radiative transfer code that solves the full radiative transfer and statistical equilibrium in a prominence slab, which is irradiated from below by the solar disc. In its simplest form the code treats a 1D isothermal isobaric prominence slab, but can be used to explore models with a PCTR. Intrinsically the PROM code calculates the hydrogen emission profiles, but can also calculate emergent profiles for lines of helium (Labrosse & Gouttebroze 2001) and calcium (Gouttebroze et al. 1997), and can now calculate emission of Mg II lines. Heinzel et al. (2014) presented a limited grid of 27 isothermal isobaric models of the Mg II h and k lines, which were used in Chapter 3 to compare to *IRIS* observations. The aim of the updated PROM code in Chapter 5 is to have an extended grid of models and to have the ability to freely explore more complex models, such as those with a PCTR, to better explain the range of observed line profiles.

The atomic model of magnesium used in Chapter 5 consists of a five-level plus continuum Mg II atom. Incident radiation comes from *IRIS* quiet-sun observations, with the profiles of Mg II h and k and continuum-level intensities for the three Mg II subordinate lines being provided to the code.

The first models explored in Chapter 5 were a replication of the grid of models from Heinzel et al. (2014) as a check that the updated PROM code was giving reasonable results. Emergent profiles and optical thicknesses of the h and k lines could be directly compared, revealing that there were some differences between the calculations here and those in Heinzel et al. (2014). In some models differences of up to 30–40% were present between the resulting integrated intensities from two codes, but in other models the intensities were identical. Generally it is higher pressure, higher slab thickness models that diverge the most, where the emergent profiles are most affected by collisions in the plasma. The emergent intensity from lower

pressure/slab thickness models is more heavily influenced by resonant scattering of the incident radiation, and the collisional effects play less of a role. The resulting optical thicknesses themselves are in good agreement with those from HVA, with values from the two codes within 10% of each other. Despite these differences the trends seen in the [Heinzel et al.](#) models and the models from the updated PROM code are the same, so an extended grid of 1D isothermal isobaric models and PCTR models have been investigated.

A grid of 252 isothermal isobaric models was computed in Chapter 5 in order to investigate the effects of higher pressures and temperatures on the emergent Mg II h and k line profiles. These have then been used to compare physical model parameters (T , P , D , τ) to observable line parameters (integrated intensities, k/h ratio, reversal level). The h and k line intensities are found to be closely related, and the reversal of both lines is highly dependent on optical thickness, with only models where $\tau > 10$ showing any central reversal. Integrated intensities of h and k are also related to the optical thickness, with the relationship clearly changing at the transition between optically thin and optically thick. High temperature isothermal isobaric models, with $T \geq 15000$ K, have been investigated, showing that there are no central reversals for models with temperatures over 20000 K. Line-centre intensities decrease for all models as slab temperature increases above 15000 K, to the point where intensities are lower than those observed in real prominences. The decrease is caused by the higher level of Mg II ionisation at those temperatures, meaning that Mg II is less populated. There is therefore relatively less Mg II in the correct energy states to produce h and k photons. However, as has been repeatedly shown by numerous authors for a range of prominence emission lines, an isothermal isobaric slab model is not the most realistic representation of a prominence, especially at such high temperatures. Therefore it is natural to consider models with a PCTR, which represent a slightly more realistic scenario.

The inclusion of a PCTR introduces temperature and pressure gradients between the cool prominence core and the hot surrounding corona. In this model, temperature and pressure gradients that are taken are those described in [Anzer & Heinzel \(1999\)](#). The most notable difference between the results of the PCTR models and the isothermal isobaric models is at low temperatures (< 10000 K), where line-centre intensities take a much larger range of values. This is caused by the presence of higher temperature plasma deeper into the slab, which in turn causes more radiative

excitation at lower core temperatures.

Correlations between the observable parameters of the Mg II h and k lines and the model parameters have been investigated for both the simple isothermal isobaric models and for the PCTR models. For both models it is found that the k/h ratio increases approximately linearly with temperature for all pressures and slab thicknesses, saturating somewhere between 2 and 2.4 at temperatures above ~ 25000 K. The k/h ratio is also related to the optical thickness of the lines, with optically thin slabs at higher temperature having k/h larger than 2, switching to a value around 1.4 at $\tau = 1$, mostly for low temperature models. This result is notable in light of the observed k/h ratio from *IRIS* in Chapter 4, where values are scattered closely around 1.41 – this indicates that the observed profiles are all optically thick with low temperatures ($\sim 6000 - 8000$ K). The reversal of the h and k lines is also dependent on plasma temperature and the pressure, with the largest reversal levels appearing in models where $T \sim 8000 - 10000$ K.

Finally in Chapter 5, observable parameters from models are compared to actual observed line properties from *IRIS*. In both the isothermal isobaric models and the PCTR models there are deviations from the observed profiles. Comparing integrated intensity of h to the integrated intensity of k, a similar power law is found at higher intensity values, but at lower intensities the observations deviate significantly from the models. This again indicates that the higher temperature models, with $T > 25000$ K are not a good description of the actual prominence plasma. The plot of observed reversal of h against reversal of k show a similar trend to all the models, with most points scattered between reversal values of 1 – 2. There are also a number of points in the prominence where one of the lines is reversed and the other is not, and others where extremely large reversal levels are found. These situations are not replicated in any models, so further modelling is required to attempt to explain this observation.

The models presented in Chapter 5 represent an update on the work of [Heinzel et al. \(2014\)](#), but there is clearly more complexity needed in order to describe the prominence conditions accurately. For this it will be necessary to turn to 2D (and eventually 3D) multi-thread models, which will do a better job of simulating the fine structures and dynamics that are observed in real prominences. The models presented here only handle the plasma in the prominence, and do not have any dependence on the magnetic field. In order to properly recreate the physics of promi-

nences it will become necessary to develop 3D radiative magneto-hydrodynamic (RMHD) models, which can fully describe the interaction between the plasma and the magnetic field. 3D modelling codes are not trivial, however, so prominence models of such complexity cannot currently be performed.

Closing remarks: This thesis has primarily been concerned with investigating the nature of solar tornado-like prominences. Through multi-instrument analysis and dedicated coordinated observations it has been possible to answer some of the open questions regarding these tornadoes. Although some observations presented here do indicate that the tornado is rotating, such as those from EIS on the 14 September 2013, on balance the evidence points away from the rotational model. It seems more likely that the observed tornado-like motions are caused by the projection of oscillations onto the plane of the sky, and that the cool plasma is suspended above the solar surface by a dipped horizontal magnetic field. The research presented in this thesis is not exhaustive, however, so these intriguing phenomena warrant further dedicated studies. Tornadoes, and the prominences that host them, are still far from being well understood. Some remaining open questions on tornadoes are: If they are not rotating, what is driving the observed oscillations? Are they linked to prominence eruptions, and if so can they be used to predict when a prominence will erupt? Answering these questions is key to fully understanding tornado-like prominences, and their link to the rest of the solar atmosphere.

Bibliography

- Allen, C. W. 1964, *Astrophysical Quantities*
- Allred, J. C., Kowalski, A. F., et al. 2015, *The Astrophysical Journal*, 809, 104
- Ambastha, A. 2010, *Astrophysics and Space Science Proceedings*, 18, 15
- Anzer, U. & Heinzel, P. 1999, *Astronomy and Astrophysics*, 349, 974
- Anzer, U. & Heinzel, P. 2005, *The Astrophysical Journal*, 622, 714
- Artzner, G., Bonnet, R. M., et al. 1977, *Space Science Instrumentation*, 3, 131
- Artzner, G., Vial, J. C., et al. 1978, *The Astrophysical Journal, Letters*, 224, L83
- Aulanier, G. & Demoulin, P. 1998, *Astronomy and Astrophysics*, 329, 1125
- Aulanier, G., Demoulin, P., et al. 1998, *Astronomy and Astrophysics*, 335, 309
- Avrett, E. H. & Loeser, R. 1992, in *Astronomical Society of the Pacific Conference Series*, Vol. 26, *Cool Stars, Stellar Systems, and the Sun*, ed. M. S. Giampapa & J. A. Bookbinder, 489
- Babcock, H. W. & Babcock, H. D. 1955, *The Astrophysical Journal*, 121, 349
- Bates, B., Bradley, D. J., et al. 1969, *Nature*, 224, 161
- Bates, B., Bradley, D. J., et al. 1970, in *IAU Symposium*, Vol. 36, *Ultraviolet Stellar Spectra and Related Ground-Based Observations*, ed. R. Muller, L. Houziaux, & H. E. Butler, 274
- Berger, T. 2014, in *IAU Symposium*, Vol. 300, *Nature of Prominences and their Role in Space Weather*, ed. B. Schmieder, J.-M. Malherbe, & S. T. Wu, 15–29

- Berger, T. E., Shine, R. A., et al. 2008, *The Astrophysical Journal, Letters*, 676, L89
- Boerner, P., Edwards, C., et al. 2012, *Solar Physics*, 275, 41
- Bonnet, R. M., Blamont, J. E., et al. 1967, *The Astrophysical Journal, Letters*, 148, L115
- Bonnet, R. M., Lemaire, P., et al. 1978, *The Astrophysical Journal*, 221, 1032
- Brayely, E. W. 1869, *Monthly Notices of the Royal Astronomical Society*, 29, 91
- Brown, C. M., Feldman, U., et al. 2008, *The Astrophysical Journal, Supplement*, 176, 511
- Casini, R., López Ariste, A., et al. 2003, *The Astrophysical Journal, Letters*, 598, L67
- Chae, J. 2003, *The Astrophysical Journal*, 584, 1084
- Clearman, H. E. 1953, *The Astrophysical Journal*, 117, 29
- Culhane, J. L., Harra, L. K., et al. 2007, *Solar Physics*, 243, 19
- Cunto, W., Mendoza, C., et al. 1993, *Astronomy and Astrophysics*, 275, L5
- de La Rue, W. 1869, *Monthly Notices of the Royal Astronomical Society*, 30, 22
- de Pontieu, B., McIntosh, S., et al. 2007, *Publications of the ASJ*, 59, S655
- De Pontieu, B., Title, A. M., et al. 2014, *Solar Physics*, 289, 2733
- Del Zanna, G. 2013, *Astronomy and Astrophysics*, 555, A47
- Del Zanna, G., Dere, K. P., et al. 2015, *Astronomy and Astrophysics*, 582, A56
- Del Zanna, G., Landini, M., et al. 2002, *Astronomy and Astrophysics*, 385, 968
- Dere, K. P., Landi, E., et al. 1997, *Astronomy and Astrophysics, Supplement*, 125
- Domingo, V., Fleck, B., et al. 1995, *Solar Physics*, 162, 1
- Doschek, G. A. & Feldman, U. 1977, *The Astrophysical Journal, Supplement*, 35, 471
- Durand, E., Oberly, J. J., et al. 1949, *The Astrophysical Journal*, 109, 1

- Engvold, O., Hirayama, T., et al. 1990, in *Lecture Notes in Physics*, Berlin Springer Verlag, Vol. 363, IAU Colloq. 117: Dynamics of Quiescent Prominences, ed. V. Ruzdjak & E. Tandberg-Hanssen, 294
- Feldman, U. & Doschek, G. A. 1977, *The Astrophysical Journal, Letters*, 212, L147
- Fletcher, L., Dennis, B. R., et al. 2011, *Space Science Reviews*, 159, 19
- Fredga, K. 1966, *The Astrophysical Journal*, 144, 854
- Fredga, K. 1969, *Solar Physics*, 9, 358
- Freeland, S. L. & Handy, B. N. 1998, *Solar Physics*, 182, 497
- Gelly, B., Langlois, M., et al. 2016, in *Proceedings of the SPIE*, Vol. 9906, Ground-based and Airborne Telescopes VI, 99065A
- Gilbert, H. R., Hansteen, V. H., et al. 2002, *The Astrophysical Journal*, 577, 464
- Gilman, P. A. 2000, *Solar Physics*, 192, 27
- Golub, L., Deluca, E., et al. 2007, *Solar Physics*, 243, 63
- Gouttebroze, P. 2004, *Astronomy and Astrophysics*, 413, 733
- Gouttebroze, P. 2005, *Astronomy and Astrophysics*, 434, 1165
- Gouttebroze, P. 2006, *Astronomy and Astrophysics*, 448, 367
- Gouttebroze, P. & Heinzel, P. 2002, *Astronomy and Astrophysics*, 385, 273
- Gouttebroze, P., Heinzel, P., et al. 1993, *Astronomy and Astrophysics, Supplement*, 99, 513
- Gouttebroze, P. & Labrosse, N. 2000, *Solar Physics*, 196, 349
- Gouttebroze, P., Vial, J.-C., et al. 1997, *Solar Physics*, 172, 125
- Graham, D. R. 2014, PhD thesis, University of Glasgow
- Graham, D. R., Fletcher, L., et al. 2015, *Astronomy and Astrophysics*, 584, A6
- Graham, D. R., Hannah, I. G., et al. 2013, *The Astrophysical Journal*, 767, 83

- Grant, R. 1852, History of physical astronomy. From the earliest ages to the middle of the 19th century
- Gudiksen, B. V., Carlsson, M., et al. 2011, *Astronomy and Astrophysics*, 531, A154
- Gunár, S., Heinzl, P., et al. 2008, *Astronomy and Astrophysics*, 490, 307
- Gunár, S., Heinzl, P., et al. 2007, *Astronomy and Astrophysics*, 472, 929
- Gunár, S., Mein, P., et al. 2012, *Astronomy and Astrophysics*, 543, A93
- Hale, G. E. & Ellerman, F. 1903, *Publications of the Yerkes Observatory*, 3, I.1
- Handy, B. N., Acton, L. W., et al. 1999, *Solar Physics*, 187, 229
- Hannah, I. G. & Kontar, E. P. 2012, *Astronomy and Astrophysics*, 539, A146
- Hansteen, V. H., De Pontieu, B., et al. 2006, *The Astrophysical Journal, Letters*, 647, L73
- Harra, L. K., Matthews, S. A., et al. 2014, *The Astrophysical Journal*, 792, 93
- Harrison, R. A., Sawyer, E. C., et al. 1995, *Solar Physics*, 162, 233
- Haugan, S. V. H. 1999, *Solar Physics*, 185, 275
- Heasley, J. N. & Mihalas, D. 1976, *The Astrophysical Journal*, 205, 273
- Heasley, J. N., Mihalas, D., et al. 1974, *The Astrophysical Journal*, 192, 181
- Heasley, J. N. & Milkey, R. W. 1976, *The Astrophysical Journal*, 210, 827
- Heasley, J. N. & Milkey, R. W. 1978, *The Astrophysical Journal*, 221, 677
- Heasley, J. N. & Milkey, R. W. 1983, *The Astrophysical Journal*, 268, 398
- Heinzl, P. 2015, in *Astrophysics and Space Science Library*, Vol. 415, Solar Prominences, ed. J.-C. Vial & O. Engvold, 103
- Heinzl, P. & Anzer, U. 1999, *Solar Physics*, 184, 103
- Heinzl, P. & Anzer, U. 2001, *Astronomy and Astrophysics*, 375, 1082
- Heinzl, P., Gouttebroze, P., et al. 1987, *Astronomy and Astrophysics*, 183, 351

- Heinzl, P., Schmieder, B., et al. 2008, *The Astrophysical Journal*, 686, 1383
- Heinzl, P., Schmieder, B., et al. 2015, *The Astrophysical Journal, Letters*, 800, L13
- Heinzl, P., Schmieder, B., et al. 2001, *Astronomy and Astrophysics*, 370, 281
- Heinzl, P., Vial, J.-C., et al. 2014, *Astronomy and Astrophysics*, 564, A132
- Henze, W. & Stenflo, J. O. 1987, *Solar Physics*, 111, 243
- Herald, D. 1976, *Moon*, 15, 91
- Hirayama, T. 1963, *Publications of the ASJ*, 15, 122
- Hopfield, J. J. & Clearman, H. E. 1948, *Physical Review*, 73, 877
- Hubeny, I. & Mihalas, D. 2014, *Theory of Stellar Atmospheres*
- Huggins, W. 1869, *Monthly Notices of the Royal Astronomical Society*, 30, 36
- Ivanov-Kholodnyi, G. S. & Nikol'Skii, G. M. 1961, *Soviet Astronomy*, 5, 31
- Janssen, M. 1869a, *Astronomical register*, 7, 107
- Janssen, M. 1869b, *Astronomical register*, 7, 131
- Johnson, F. S., Purcell, J. D., et al. 1953, *The Astrophysical Journal*, 117, 238
- Kanno, M., Withbroe, G. L., et al. 1981, *Solar Physics*, 69, 313
- Kano, R., Bando, T., et al. 2012, in *Proceedings of the SPIE, Vol. 8443, Space Telescopes and Instrumentation 2012: Ultraviolet to Gamma Ray*, 84434F
- Kerr, G. S., Fletcher, L., et al. 2016, *The Astrophysical Journal*, 827, 101
- Kerr, G. S., Simões, P. J. A., et al. 2015, *Astronomy and Astrophysics*, 582, A50
- Ko, Y.-K., Doschek, G. A., et al. 2009, *The Astrophysical Journal*, 697, 1956
- Kobayashi, K., Kano, R., et al. 2012, in *Astronomical Society of the Pacific Conference Series, Vol. 456, Fifth Hinode Science Meeting*, ed. L. Golub, I. De Moortel, & T. Shimizu, 233
- Kosugi, T., Matsuzaki, K., et al. 2007, *Solar Physics*, 243, 3

- Kucera, T. A. & Landi, E. 2006, *The Astrophysical Journal*, 645, 1525
- Labrosse, N. & Gouttebroze, P. 2001, *Astronomy and Astrophysics*, 380, 323
- Labrosse, N. & Gouttebroze, P. 2004, *The Astrophysical Journal*, 617, 614
- Labrosse, N., Heinzl, P., et al. 2010, *Space Science Reviews*, 151, 243
- Labrosse, N. & Rodger, A. S. 2016, *Astronomy and Astrophysics*, 587, A113
- Labrosse, N., Schmieder, B., et al. 2011, *Astronomy and Astrophysics*, 531, A69
- Landi, E. & Landini, M. 1997, *Astronomy and Astrophysics*, 327, 1230
- Landi, E., Young, P. R., et al. 2013, *The Astrophysical Journal*, 763, 86
- Lang, J., Kent, B. J., et al. 2006, *Applied Optics*, 45, 8689
- Leake, J. E., Lukin, V. S., et al. 2013, *Physics of Plasmas*, 20, 061202
- Leenaarts, J. & Carlsson, M. 2009, in *Astronomical Society of the Pacific Conference Series*, Vol. 415, *The Second Hinode Science Meeting: Beyond Discovery-Toward Understanding*, ed. B. Lites, M. Cheung, T. Magara, J. Mariska, & K. Reeves, 87
- Leenaarts, J., Pereira, T. M. D., et al. 2013a, *The Astrophysical Journal*, 772, 89
- Leenaarts, J., Pereira, T. M. D., et al. 2013b, *The Astrophysical Journal*, 772, 90
- Lemaire, P., Choucq-Bruston, M., et al. 1984, *Solar Physics*, 90, 63
- Lemaire, P., Gouttebroze, P., et al. 1981, *Astronomy and Astrophysics*, 103, 160
- Lemaire, P. & Skumanich, A. 1973, *Astronomy and Astrophysics*, 22, 61
- Lemen, J. R., Title, A. M., et al. 2012, *Solar Physics*, 275, 17
- Levens, P. J., Labrosse, N., et al. 2015, *Astronomy and Astrophysics*, 582, A27
- Levens, P. J., Labrosse, N., et al. 2017, *Astronomy and Astrophysics*, 607, A16
- Levens, P. J., Schmieder, B., et al. 2016a, *The Astrophysical Journal*, 818, 31
- Levens, P. J., Schmieder, B., et al. 2016b, *The Astrophysical Journal*, 826, 164

- Li, K. & Zhong, S. 1997, *Astronomy and Astrophysics, Supplement*, 126
- Li, X., Morgan, H., et al. 2012, *The Astrophysical Journal, Letters*, 752, L22
- Liang, G. Y., Whiteford, A. D., et al. 2009, *Journal of Physics B Atomic Molecular Physics*, 42, 225002
- Liu, W., De Pontieu, B., et al. 2015a, *The Astrophysical Journal*, 803, 85
- Liu, W., Heinzel, P., et al. 2015b, *Solar Physics*, 290, 3525
- López Ariste, A. 2015, in *Astrophysics and Space Science Library*, Vol. 415, *Solar Prominences*, ed. J.-C. Vial & O. Engvold, 179
- López Ariste, A., Asensio Ramos, A., et al. 2009, *Astronomy and Astrophysics*, 501, 729
- López Ariste, A. & Casini, R. 2002, *The Astrophysical Journal*, 575, 529
- López Ariste, A. & Casini, R. 2003, *The Astrophysical Journal, Letters*, 582, L51
- López Ariste, A., Rayrole, J., et al. 2000, *Astronomy and Astrophysics, Supplement*, 142, 137
- Luna, M., Moreno-Insertis, F., et al. 2015, *The Astrophysical Journal, Letters*, 808, L23
- Luna, M., Terradas, J., et al. 2016, *The Astrophysical Journal*, 817, 157
- Mackay, D. H., Karpen, J. T., et al. 2010, *Space Science Reviews*, 151, 333
- Madjarska, M. S., Vial, J.-C., et al. 1999, in *ESA Special Publication*, Vol. 446, *8th SOHO Workshop: Plasma Dynamics and Diagnostics in the Solar Transition Region and Corona*, ed. J.-C. Vial & B. Kaldeich-Schü, 467
- Mariska, J. T., Doschek, G. A., et al. 1979, *The Astrophysical Journal*, 232, 929
- Markwardt, C. B. 2009, in *Astronomical Society of the Pacific Conference Series*, Vol. 411, *Astronomical Data Analysis Software and Systems XVIII*, ed. D. A. Bohlender, D. Durand, & P. Dowler, 251
- Martínez González, M. J., Asensio Ramos, A., et al. 2016, *The Astrophysical Journal*, 825, 119

- Matthews, S. A., Harra, L. K., et al. 2015, *The Astrophysical Journal*, 812, 35
- Mercier, C. & Heyvaerts, J. 1977, *Astronomy and Astrophysics*, 61, 685
- Mghebrishvili, I., Zaqarashvili, T. V., et al. 2015, *The Astrophysical Journal*, 810, 89
- Milkey, R. W. & Mihalas, D. 1974, *The Astrophysical Journal*, 192, 769
- Moe, O. K., Cook, J. W., et al. 1979, *Solar Physics*, 61, 319
- Morrill, J. S. & Korendyke, C. M. 2008, *The Astrophysical Journal*, 687, 646
- Nasmyth, J. 1852, *Monthly Notices of the Royal Astronomical Society*, 13, 5
- Newton, H. W. 1934, *Monthly Notices of the Royal Astronomical Society*, 94, 472
- Nicholson, S. B. 1944, *Publications of the ASP*, 56, 162
- Ning, Z., Cao, W., et al. 2009, *Astronomy and Astrophysics*, 499, 595
- Noyes, R. W., Dupree, A. K., et al. 1972, *The Astrophysical Journal*, 178, 515
- Öhman, Y. 1969, *Solar Physics*, 9, 427
- Orozco Suárez, D., Asensio Ramos, A., et al. 2012, *The Astrophysical Journal, Letters*, 761, L25
- Orrall, F. Q. & Schmahl, E. J. 1976, *Solar Physics*, 50, 365
- Orrall, F. Q. & Schmahl, E. J. 1980, *The Astrophysical Journal*, 240, 908
- Paletou, F., Vial, J.-C., et al. 1993, *Astronomy and Astrophysics*, 274, 571
- Panasenco, O., Martin, S. F., et al. 2014, *Solar Physics*, 289, 603
- Panesar, N. K., Innes, D. E., et al. 2013, *Astronomy and Astrophysics*, 549, A105
- Parenti, S., Schmieder, B., et al. 2012, *The Astrophysical Journal*, 754, 66
- Parenti, S. & Vial, J.-C. 2007, *Astronomy and Astrophysics*, 469, 1109
- Parker, E. N. 1988, *The Astrophysical Journal*, 330, 474
- Patsourakos, S. & Vial, J.-C. 2002, *Solar Physics*, 208, 253

- Pereira, T. M. D., Carlsson, M., et al. 2015, *The Astrophysical Journal*, 806, 14
- Pereira, T. M. D., Leenaarts, J., et al. 2013, *The Astrophysical Journal*, 778, 143
- Pereira, T. M. D. & Uitenbroek, H. 2015, *Astronomy and Astrophysics*, 574, A3
- Pesnell, W. D., Thompson, B. J., et al. 2012, *Solar Physics*, 275, 3
- Pettit, E. 1919, *The Astrophysical Journal*, 50, 206
- Pettit, E. 1925, *Publications of the Yerkes Observatory*, 3, 4.iii
- Pettit, E. 1932, *Contributions from the Mount Wilson Observatory / Carnegie Institution of Washington*, 451, 1
- Pettit, E. 1936, *The Astrophysical Journal*, 84, 319
- Pettit, E. 1941, *Publications of the ASP*, 53, 289
- Pettit, E. 1943a, *Contributions from the Mount Wilson Observatory / Carnegie Institution of Washington*, 679, 1
- Pettit, E. 1943b, *Publications of the ASP*, 55, 184
- Pettit, E. 1946, *Publications of the ASP*, 58, 150
- Pettit, E. 1950, *Publications of the ASP*, 62, 144
- Pike, C. D. & Mason, H. E. 1998, *Solar Physics*, 182, 333
- Pikel'Ner, S. B. 1971, *Solar Physics*, 17, 44
- Pojoga, S. 1994, in IAU Colloq. 144: Solar Coronal Structures, ed. V. Rusin, P. Heinzel, & J.-C. Vial, 357–360
- Poland, A. I. & Tandberg-Hanssen, E. 1983, *Solar Physics*, 84, 63
- Pottasch, S. R. 1963, *The Astrophysical Journal*, 137, 945
- Purcell, J. D., Garrett, D. L., et al. 1963, in Space Research Conference, ed. W. Priester, 781
- Rathore, B. & Carlsson, M. 2015, *The Astrophysical Journal*, 811, 80

- Richardson, R. S. 1940, *Publications of the ASP*, 52, 326
- Rutten, R. J., Hammerschlag, R. H., et al. 1997, in *Astrophysics and Space Science Library*, Vol. 225, SCORE'96 : Solar Convection and Oscillations and their Relationship, ed. F. P. Pijpers, J. Christensen-Dalsgaard, & C. S. Rosenthal, 289–292
- Saito, K. & Tandberg-Hanssen, E. 1973, *Solar Physics*, 31, 105
- Scherrer, P. H., Schou, J., et al. 2012, *Solar Physics*, 275, 207
- Schmahl, E. J. & Orrall, F. Q. 1986, in *NASA Conference Publication*, Vol. 2442, NASA Conference Publication, ed. A. I. Poland
- Schmieder, B., Chandra, R., et al. 2010, *Astronomy and Astrophysics*, 514, A68
- Schmieder, B., Gunár, S., et al. 2007, *Solar Physics*, 241, 53
- Schmieder, B., Kucera, T. A., et al. 2013, *The Astrophysical Journal*, 777, 108
- Schmieder, B., López Ariste, M. Z. A., et al. 2017a, *ArXiv e-prints*
- Schmieder, B., Malherbe, J. M., et al. 1984, *Astronomy and Astrophysics*, 136, 81
- Schmieder, B., Mein, P., et al. 2017b, *Astronomy and Astrophysics*, 597, A109
- Schmieder, B., Tian, H., et al. 2014, *Astronomy and Astrophysics*, 569, A85
- Schweizer, M. 1853, *Monthly Notices of the Royal Astronomical Society*, 13, 171
- Secchi, A. 1875, *Le Soleil*
- Secchi, P. A. 1877, *Le Soleil*, Vol. 2
- Shimizu, T. 2009, in *Astronomical Society of the Pacific Conference Series*, Vol. 415, The Second Hinode Science Meeting: Beyond Discovery-Toward Understanding, ed. B. Lites, M. Cheung, T. Magara, J. Mariska, & K. Reeves, 1
- Sigut, T. A. A. & Pradhan, A. K. 1995, *Journal of Physics B Atomic Molecular Physics*, 28, 4879
- Staath, E. & Lemaire, P. 1995, *Astronomy and Astrophysics*, 295, 517

- Stephenson, F. R. 1990, *Philosophical Transactions of the Royal Society of London Series A*, 330, 499
- Su, Y., Gömöry, P., et al. 2014, *The Astrophysical Journal, Letters*, 785, L2
- Su, Y., Wang, T., et al. 2012, *The Astrophysical Journal, Letters*, 756, L41
- Suematsu, Y., Tsuneta, S., et al. 2008, *Solar Physics*, 249, 197
- Sviatsky, D. 1923, *L'Astronomie*, 37, 418
- Tandberg-Hanssen, E. 1970, *Solar Physics*, 15, 359
- Tandberg-Hanssen, E. 1974, *Geophysics and Astrophysics Monographs*, 12
- Tandberg-Hanssen, E., Cheng, C. C., et al. 1981, *Advances in Space Research*, 1, 275
- Terradas, J., Soler, R., et al. 2015, *The Astrophysical Journal, Letters*, 802, L28
- Tousey, R. 1963, *Space Science Reviews*, 2, 3
- Tsuneta, S., Ichimoto, K., et al. 2008, *Solar Physics*, 249, 167
- Uchida, Y. & Kaburaki, O. 1974, *Solar Physics*, 35, 451
- Uitenbroek, H. 2001, *The Astrophysical Journal*, 557, 389
- Vernazza, J. E., Avrett, E. H., et al. 1981, *The Astrophysical Journal, Supplement*, 45, 635
- Vial, J. C. 1982a, *The Astrophysical Journal*, 253, 330
- Vial, J. C. 1982b, *The Astrophysical Journal*, 254, 780
- Vial, J. C., Gouttebroze, P., et al. 1979, *Solar Physics*, 61, 39
- Vial, J.-C., Pelouze, G., et al. 2016, *Solar Physics*, 291, 67
- Vial, J. C., Salm-Platzer, J., et al. 1981, *Solar Physics*, 70, 325
- Vyssotsky, A. N. 1949, *Meddelanden fran Lunds Astronomiska Observatorium Serie II*, 126, 3

- Warren, H. P., Ugarte-Urra, I., et al. 2014, *The Astrophysical Journal, Supplement*, 213, 11
- Wedemeyer, S., Scullion, E., et al. 2013a, *The Astrophysical Journal*, 774, 123
- Wedemeyer, S., Scullion, E., et al. 2013b, in *Journal of Physics Conference Series*, Vol. 440, *Journal of Physics Conference Series*, 012005
- Wedemeyer-Böhm, S., Scullion, E., et al. 2012, *Nature*, 486, 505
- Wentzel, D. G. 1974, *Solar Physics*, 39, 129
- West, E., Cirtain, J., et al. 2011, in *Proceedings of the SPIE*, Vol. 8148, *Solar Physics and Space Weather Instrumentation IV*, 81480F
- Widing, K. G., Feldman, U., et al. 1986, *The Astrophysical Journal*, 308, 982
- Wiik, J. E., Dere, K., et al. 1993, *Astronomy and Astrophysics*, 273, 267
- Wiik, J. E., Schmieder, B., et al. 1997, *Solar Physics*, 175, 411
- Wilhelm, K., Curdt, W., et al. 1995, *Solar Physics*, 162, 189
- Williams, D. R., Baker, D., et al. 2013, *The Astrophysical Journal*, 764, 165
- Woods, T. N., Eparvier, F. G., et al. 2012, *Solar Physics*, 275, 115
- Young, C. A. 1896, *The sun*
- Young, P. R., O'Dwyer, B., et al. 2012, *The Astrophysical Journal*, 744, 14
- Young, P. R., Watanabe, T., et al. 2009, *Astronomy and Astrophysics*, 495, 587
- Zaqarashvili, T. V., Zhelyazkov, I., et al. 2015, *The Astrophysical Journal*, 813, 123
- Zhong, S. & Li, K. 1994, *Publications of the Yunnan Observatory*, 4, 1
- Zirker, J. B., Engvold, O., et al. 1994, *Solar Physics*, 150, 81